Fabrication and Characterization of Lithium–Sulfur Batteries

Von der Fakultät Energie-, Verfahrens- und Biotechnik der Universität
Stuttgart zur Erlangung der Würde eines Doktor-Ingenieurs (Dr.-Ing.)
genehmigte Abhandlung

Vorgelegt von

Natalia Andrea Cañas

aus Córdoba, Argentinien

Hauptberichter: Prof. Dr. rer. nat. K. Andreas Friedrich

Mitberichter: Prof. Dr. rer. nat. Maximilian Fichtner

Tag der mündlichen Prüfung: 24.07.2015

Institut für Thermodynamik und Wärmetechnik

der Universität Stuttgart

2015

A mi hermano, Federico

Eidesstattliche Erklärung

I hereby declare that I have written the submitted dissertation myself and in this process have used no other sources or materials than those indicated.

Hiermit erkläre ich, dass ich die beigefügte Dissertation selbstständig verfasst und keine anderen als die angegebenen Hilfsmittel genutzt habe.

Natalia A. Cañas

Stuttgart, den 25.08.2015

Abstract

The lithium–sulfur battery is a promising system for the future generation of rechargeable batteries. Its main advantages are the high theoretical capacity (1675 Ah $\mathrm{kg_S}^{-1}$), high energy density (~2500 Wh $\mathrm{kg_S}^{-1}$), and low cost of sulfur. So far, the commercial application of this battery has been hindered by the reduced cycle-life. The isolating properties of sulfur as well as the formation of polysulfides in a complex reaction mechanism, which is not completely understood, are mainly causes for battery degradation.

This work is focused on the characterization of the Li–S battery by application of several characterization techniques under *in situ* and *ex situ* conditions. Using X–ray diffraction, the reaction of sulfur was monitored during discharge and charge, and the formation of nano–crystalline lithium sulfide as end product of discharge was identified for the first time *in operando*. The structural changes of sulfur and its partial amorphization were observed after charge and analyzed using the Rietveld method. Furthermore, electrochemical impedance spectroscopy was applied during cycling to measure the impedance characteristics of the cell. For this, an electrical equivalent circuit was designed to describe specific physical and electrochemical process. Thus, the resistance of the electrolyte, the charge transfer resistance in the electrodes, as well as the reaction and dissolution of isolating products were simulated and quantified. The polysulfides, as well as S_8 and Li_2S, were investigated in an organic electrolyte using UV–vis spectroscopy. Here, the species S_6^{2-} and $S_3^{\bullet -}$ were identified and semi–quantified at several states of discharge. Further characterization methods, like scanning electron microscopy, atomic force microscopy, and thermal analysis coupled with mass spectroscopy were used to understand the degradation processes that caused morphological changes in the cathode.

The output obtained through the application of the different characterization techniques was compared with a physico–chemical model in order to obtain a deeper knowledge in the reaction mechanisms occurring in the battery. Moreover, through further developments on the fabrication process of the battery, main factors influencing the battery capacity were identified. Thereby, the capacity of the battery was increased from ~275 Ah $\mathrm{kg_S}^{-1}$ to 800 Ah $\mathrm{kg_S}^{-1}$ (after 50 cycles, at a discharge rate of 0.18 C).

This thesis provides new insights into the electrochemical and degradation processes of Li–S batteries and will hopefully contribute to enhance the energy density of future Li–S batteries.

Kurzfassung

Die Lithium–Schwefel-Batterie (Li–S) ist ein vielversprechendes Energiespeichersystem der nächsten Generation von Akkumulatoren. Wesentliche Vorteile dieser Batterien sind die hohe theoretische Kapazität (1675 Ah kg^{-1}), die hohe Energiedichte (~2500 Wh kg^{-1}) und die geringen Kosten des Schwefels. Bis heute ist eine kommerzielle Anwendung aufgrund der starken Degradation der Batterien bei der Zyklisierung nicht erreicht. Grund hierfür sind die mangelnde Leitfähigkeit der Aktivmaterialien sowie die komplexen elektrochemischen Prozesse mit der Bildung von vielen Zwischenprodukten, welche bislang noch nicht vollständig verstanden sind.

Der Fokus dieser Arbeit liegt auf der Charakterisierung von Li–S-Batterien durch Anwendung unterschiedlicher *in situ*- und *ex situ*- Techniken. Mithilfe der Röntgendiffraktometrie konnten die Reaktionsvorgänge von Schwefel während der Entladung und Ladung beobachtet werden. Dabei konnte erstmalig *in operando* die Bildung von nanokristallinem Lithiumsulfid als Endprodukt der Entladung identifiziert werden. Nach der Ladung der Batterien konnten strukturelle Veränderungen und teilweise eine Amorphisierung des Schwefels festgestellt und mittels Rietveld–Analyse quantifiziert werden. Durch die Anwendung der elektrochemischen Impedanzspektroskopie konnten die während des Zyklierens ablaufenden Zellprozesse untersucht werden. Hierzu wurde ein elektrisches Ersatzschaltbild entwickelt, um die physikalischen und elektrochemischen Prozesse zu beschreiben. Dafür wurde der Widerstand des Ladungsdurchtritts der Elektroden, der Widerstand des Elektrolyten sowie die Bildung und Auflösung der isolierenden Produkte als einzelne Impedanzbeiträge simuliert und quantifiziert. Die sich bildenden Polysulfide beim Entladevorgang sowie die Endprodukte S_8 und Li_2S wurden mittels UV–vis–Spektroskopie unter Ar–Atmosphäre untersucht. Hierbei wurden die Spezies S_6^{2-} und $S_3^{\bullet -}$ bei unterschiedlichen Entladungstiefe semi–quantitativ analysiert. Darüber hinaus wurden die Degradationsprozesse, die die morphologischen Veränderungen in der Kathode verursachen mittels Rasterelektronenmikroskopie, Rasterkraftmikroskopie und thermogravimetrischen Methoden (DTA–MS) untersucht.

Um ein tieferes Verständnis der in der Batterie ablaufenden Reaktionsmechanismen zu erhalten, wurden die experimentellen Charakterisierungsergebnisse mit einem physikalisch–chemischen Modell verglichen. Durch die Weiterentwicklung des Herstellungsverfahrens konnten wichtige Faktoren für die Steigerung der spezifischen Kapazität identifiziert werden. Dabei konnte die Kapazität der Batterie von ca. 275 $\text{Ah kg}_\text{S}^{-1}$ auf 800 $\text{Ah kg}_\text{S}^{-1}$ erhöht werden (nach 50 Zyklen, Entladungsrate: 0,18 C).

Diese Arbeit liefert neue Einblicke in die elektrochemischen Vorgänge sowie in den Degradationsmechanismus von Li–S-Batterien und soll dazu beitragen die neuartigen Sekundärbatterien weiterzuentwickeln.

Contents

Abstract vii

Kurzfassung ix

Contents xi

List of symbols and abbreviations xv

Symbols xv

Abbreviations xviii

1 Introduction 1

1.1 Motivation 1

1.2 Organization of the thesis 2

2 Fundamentals 5

2.1 Lithium–sulfur batteries 5

2.1.1 Operating principles 5

2.1.2 Main problems and challenges 8

2.1.3 State of art 9

2.1.4 Importance of characterization 13

2.2 X–ray diffraction (XRD) 13

2.2.1 Generation of X–rays and its interaction with materials 13

2.2.2 Rietveld–Method 15

2.3 Electrochemical Impedance Spectroscopy (EIS) 17

2.3.1 The transfer function: impedance 18

2.3.2 Equivalent circuit for modeling 19

2.4 Ultraviolet–visible (UV–vis) spectroscopy 20

2.5 Atomic force microscopy (AFM) 22

2.6 Scanning electron microscopy (SEM) 23

2.7 Thermal analysis and mass spectroscopy 24

3 Battery fabrication and electrochemical characterization 27

3.1 Experimental procedures 27

3.1.1 Cathode materials 27

3.1.2 Fabrication of the cathode 28

3.1.3 Mixing and milling 29

3.1.4 Coating and drying 30

3.1.5 Cell construction and electrochemical testing 31
3.2 Result and discussion 32
3.2.1 Morphology of the cathode 32
3.2.2 Influence of cathode fabrication on the capacity fading 34
3.2.3 Influence of $LiNO_3$ as co–salt for the electrolyte 37
3.3 Conclusion 40
4 *In situ* X–ray diffraction 43
4.1 Experimental procedures 44
4.1.1 Design considerations for *in situ* X–ray cells 44
4.1.2 In situ cell 45
4.1.3 Electrochemical test and configuration of diffractometer 47
4.1.4 Rietveld analysis 48
4.2 Results and discussion 48
4.2.1 Diffractograms of cathode components 48
4.2.2 *In situ* XRD during the first cycles 50
4.2.3 Structural mapping of cathodes 55
4.2.4 Rietveld refinement of diffractograms 56
4.2.5 Semi–quantification of crystalline and amorphous phase 59
4.2.6 Discussion and comparison with further investigations 61
4.3 Conclusions 62
5 Electrochemical impedance spectroscopy 63
5.1 Experimental procedures 64
5.2 Results and discussion 64
5.2.1 EIS during cycling 64
5.2.2 Equivalent circuit (EC) for Li–S batteries 67
5.2.3 Assignment of processes to the EC–elements 69
5.2.4 Simulation of EIS during the first cycle 70
5.2.5 Degradation during cycling 73
5.3 Conclusions 76
6 UV–vis spectroscopy 79
6.1 Experimental procedures 80
6.1.1 Set up of UV–vis absorption measurements 80
6.1.2 Preparation of reference solutions 81
6.2 Results and discussion 81
6.2.1 Sulfur and lithium sulfide 81
6.2.2 Polysulfide reference solutions 83

6.2.3 Discharge process: changes in the absorption spectra 87
6.3 Conclusions 91
7 Morphological changes and degradation 93
7.1 Experimental procedures 93
7.1.1 Scanning electron microscopy (SEM) 93
7.1.2 Atomic force microscopy (AFM) 93
7.1.3 Thermal analysis and mass spectroscopy 94
7.2 Results and discussion 94
7.2.1 Morphological changes on the surface (SEM) 94
7.2.2 Formation of isolating layers (AFM) 96
7.2.3 Stability of the binding between particles (DSC–MS) 98
7.3 Conclusions 103
8 Simulations 105
8.1 Description of the model 105
8.1.1 Model parameters 108
8.2 Simulations and correlation with experimental results 111
8.2.1 Discharge profile 111
8.2.2 Formation, dissolution and reaction of end products 113
8.2.3 Formation and reaction of intermediate products 116
8.3 Conclusions 119
9 Summary and conclusions 121
10 Outlook 125
11 Additional information 127
11.1 Battery fabrication and electrochemical characterization 127
11.1.1 Swagelok® cells for electrochemical testing of Li–batteries 127
11.1.2 Images of cathodes and substrate 128
11.1.3 Krypton adsorption measurements 131
11.1.4 Influence of the temperature on the discharge capacity 132
11.1.5 Sulfur structure and Li_2S reactivity 133
11.2 Electrochemical impedance spectroscopy 134
11.2.1 Finite diffusion 134
11.2.2 EIS simulation results 135
11.3 Additional absorbance spectrum and TG analysis 137
11.4 Reduction mechanisms of Li–S batteries and simulations 138
11.4.1 Review of sulfur reduction mechanisms for Li–S batteries 138
11.4.2 Parameters used in the simulation. 140

Literature..**143**
List of figures..**153**
List of tables **161**
Publications **163**
Acknowledgements **167**
Curriculum vitae..**169**

List of symbols and abbreviations

Symbols

Greek alphabet		
Symbol	Units	Definition
α (Chapter 5)		Characteristic factor of the CPE semicircle (EIS)
α (Chapter 8)		Symmetry factor of charge transfer reactions
ΔH_f^0	kcal mol^{-1}	Enthalpy of formation
ΔG	J mol^{-1}	Molar Gibbs reaction enthalpy
ε	L mol^{-1} cm^{-}	Extinction coefficient
ε_i		Volume fraction of phase *i*
ε_i'		Maximum volume fraction of phase *i* (S atoms present in form *i*)
η		Mixing parameter
θ	°	Angle between the incident ray and the scattering
θ_k		Calculated position of reflex k
θ_i		Position of the observed intensity i
λ	nm	Wavelength of incident wave
λ_{max}	nm	Absorption maxima
ρ_i	kg m^{-3}	Density of phase *i*
σ_i		Standard deviation of y_i
τ	nm	Average of crystalline primary particles
τ_i		Tortuosity of a porous phase *i*
ν_i		Stoichiometric coefficient of species *i*
ϕ	V	Electric potential
$\Delta\phi$	V	Electric potential difference between electrode and electrolyte
$\varphi(\omega)$		phase
ω		angular frequency
ω_f		normalization factor
ω_o		Excitation frequency

Roman alphabet		
Symbol	Units	Definition
A		Absorbance
A_{dl}	$m^2 m^{-3}$	Total volume specific area of an electrode
$A_m{}^V$	$m^2 m^{-3}$	Volume–specific surface area: surface at which reaction *m* happens.
B		Full width of the peak at half maximum
c	$mol L^{-1}$	Concentration
c_i	$Mol m^{-3}$	Concentration of species *i*
C_{dl}	$F m^{-2}$	Area–specific double layer capacitance
d	pm	Spacing between the planes in the atomic lattice
d_a	cm	Path length of the absorbing solution
d_N	µm	Diffusion layer thickness
D_i, $D_{i,eff}$	$m^2 s^{-1}$	(Effective) transport coefficient of species *i*
D_k		Constant of diffusion
E	V	Cell voltage
E_f^{act}	$J mol^{-1}$	Activation energy of forward and reverse reactions
U	V	Voltage
F	$As mol^{-1}$	Faraday’s constant: 96485 $Asmol^{-1}$
g_i	$J mol^{-1}$	Molar Gibbs free enthalpy of species *i*
G		Reflex function: profile function of the reflex k
G_{UA}		Gaussian function
F_k		Structure factor
fwhm		Full width at half maximum
H(ω)		Transfer function
hkl		Miller indices
i_{tot}, i_{dl}, i_F	$A m^{-3}$	Volume–specific cell current density (indices: total current, double layer current, Faradaic current)
I	A	Current
I_f		Instrumental factors
I_t		Transmitted intensity
$\vec{J}_i$	$mol m^{-2} s^{-1}$	Flux of species *i*
k		Shape function/factor (Scherrer equation)
k_N	s^{-1}	Diffusion time constant
k_f, k_r		Forward and backward rate constants

k_0		Pre–exponential factor in Arrhenius equation
$K_{\alpha1}$, $K_{\alpha2}$,		Characteristic lines emitted by an X–ray tube
L_k		Lorentz polarization factor
L_{UA}		Lorentzian function
m		Index of chemical reactions
M		Function to minimize in Rietveld Refinement
M_i	kg mol^{-1}	Mean molar mass of phase *i*
M_{Li2S}	g mol^{-1}	Molar mass of sulfur
M_S	g mol^{-1}	Molar mass of sulfur
n		Integer (Bragg´s reflection law)
n_e		Number of electrons
R	J mol^{-1} K^{-1}	Ideal gas constant: 8.3145 J mol^{-1} K^{-1}
s		Scale factor
$\dot{s}_{i,m}$	mol m^{-2} s^{-1}	Chemical production rate of species *i* in reaction *m*
t	s, h	Time
T	K	Absolute temperature
T_s	°C	Temperature of the sample
T_r	°C	Temperature of the reference
P		Sample factor
PV_{UA}		Pseudo–Voigt function
R	Ohm	Resistance
R_{wp}		Weighted profile of the “residue” parameter
$X(\omega_o)$		Sinusoidal wave input
y	m	Spatial position
y_b		Intensity of the background (XRD)
y_{ic}		Calculated intensity in the position i (XRD)
y_{io}		Measured intensity in the position i (XRD)
$Y(\omega_o)$		Sinusoidal output signal
w_i		Profile parameter
W	Ohm $s^{-1/2}$	Warburg parameter
z		Number of electrons transferred in charge–transfer
Z	Ohm	Impedance
Z`		Real part of impedance
Z``		Imaginary part of impedance
Z_C	Ohm	Capacitance element

Z_L	Ohm	Inductance element
Z_N	Ohm	Nernstian diffusion impedance
Z_R	Ohm	Resistance element
Z_S	Ohm	Finite diffusion impedance

Abbreviations

Abbreviation	Description
AC	Alternating electrical current
AE	Auger electrons
α–S_8	Orthorhombic cyclo–octasulfur
β–S_8	Monoclinic cyclo–octasulfur
TEGDME	Tetraethylene glycol dimethyl ether
AFM	Atomic force microscopy
BMIM	1–butyl–3methylimidaolium
BSE	Backscattered electrons
C_4mim DCA	1–n–butyl–3–methyl–imidazolium dicyanamide
CL	Cathodoluminescence
CB	Carbon black
CPE	Constant phase element
COD	Crystallography Open Data Base
DME	1,2–dimethoxyethane
DMF	N,N–dimetilformamida
DMSO	Dimethylsulfoxide
DOL	1,3–dioxolane
DOD	Depth of discharge
DOC	Depth of charge
DSC	Differential scanning calorimetry
EIS	Electrochemical impedance spectroscopy
ESW	Electrochemical stability window
EDX	Energy dispersive X–ray spectroscopy
GPE	Gel polymer electrolytes
IL	Ionic liquid
LiTFSI	Lithium bis(tri–fluoromethanesulfonyl)imide
MS	Mass spectroscopy

PVDF	Polyvinylidene fluoride
PDF	Power Diffraction File
rGO	Reduced graphene oxide
NMP	N–methyl–2–pyrrolidone
OCV	Open circuit voltage (V)
PEDOT	Poly(3,4)–ethylenedioxythiophene
PEEK	Polyether ether ketone
PEO	Polyethylene oxide
PYR14	1–ethyhl–3methylpyrrolidinium
PiP14	1–butyl–1–methylpiperidinium
S, S_8	Sulfur, cyclo–octasulfur
SE	Secondary electrons
SEM	Scanning electron microscopy
SATP	Standard ambient temperature and pressure (25 °C, 1 bar)
STA	Simultaneous thermal analysis
TFSI	Bis(trifluoromethan–sulfonyl)imide
TFSA	Bis(trifluoromethansulfonyl)amide
TG	Thermogravimetry
UV–vis	Ultraviolet–visible
XRD	X–ray diffraction

1 Introduction

1.1 Motivation

Electrical energy storage systems are becoming important to support renewable energy generation and electro–mobility. They should help to compensate the discrepancy of demand and supply of electricity produced by e.g. solar or wind based electrical generation. Furthermore, the electrification in the transportation sector is crucial for future mobility to reduce the dependence on oil and minimize emissions [1]. Current lithium–ion batteries do not meet the expectation of tomorrow´s energy storage system. New batteries with significantly higher energy density and long cycle life would have significant benefits for mobile and stationary storage applications.

In 1962, Herbet and Ulam [2] introduced the concept of using elemental sulfur as a positive electrode in alkali–metal sulfur batteries. Especially in the last ten years, the investigation of Na–S and Li–S batteries has gained considerable interest. Sulfur has many advantageous characteristics such as low cost and toxicity, natural abundance, and low equivalent weight. Moreover, Li–S batteries have a high theoretical capacity (1675 Ah $\mathrm{kg_S}^{-1}$) and energy density (2500 Wh $\mathrm{kg_{Li2S}}^{-1}$, equivalent to 2800 Wh L^{-1}). They are expected to provide 2–4 times higher specific energy than conventional lithium–ion batteries and for this reason, they are considered great candidates as future energy storage systems.

Figure 1.1 presents a comparison of the main battery systems in regards to the specific energy, mileage, and cost; this is based on practical assumptions [3]. Li–S batteries can provide significantly increased energy density at a lower cost. Considering its use in electric cars, the energy density would be sufficient to deliver a driving range of more than 400 km, scaled to the driving range of the Nissan Leaf. For Li–O_2 batteries the theoretical energy density is much higher than that of the current batteries and of the one under development. Nevertheless, these practical values are questionable because of the difficult estimation due to the existence of few realistic prototypes.

The main problems of Li–S batteries are low cyclability and high self–degradation. In order to understand these problems and improve the battery, it is important to gain a deeper knowledge of the electrochemical and physical processes that occur during charge and discharge. Hence, this work is motivated by the necessity of a deeper understanding of the processes occurring in Li–S batteries.

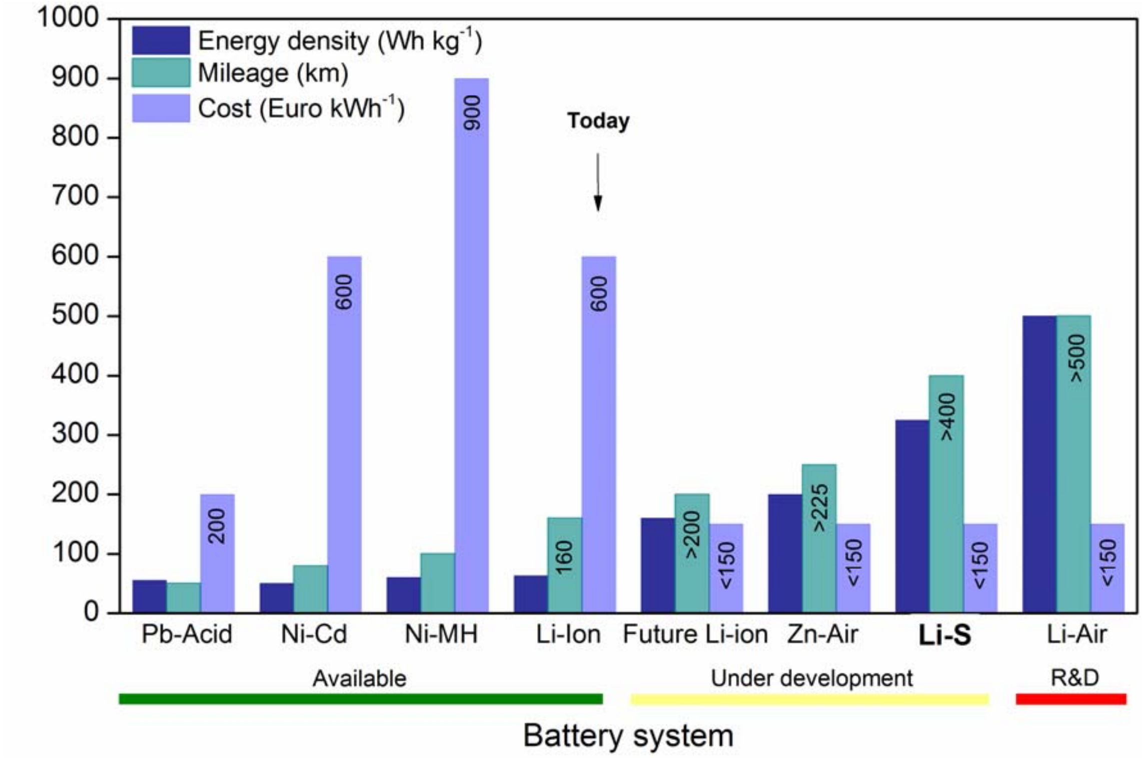

Figure 1.1: Battery systems: comparison of practical specific energy, mileage and cost [3]**. The mileage are based on the minimum specific energy for each system and scaled to the specific energy of Li–ion cells (140 Wh kg^{-1}) and driving range of the Nissan Leaf (160 km)** [4]**. The cost for technologies under development are targets of the US Advanced Battery Consortium** [5]**.**

1.2 Organization of the thesis

This work aims to understand the critical issues associated with the electrochemical processes occurring in Li–S batteries, establishing methods and procedures necessary to investigate this system. This has been reflected in the development of the research throughout the thesis, as outlined in Figure 1.2. This provides a schematic overview on the focus and the interconnections of the chapters.

To begin with, a general background about Li–S batteries and an overview of the most relevant research done on this field in the last decades is provided in Chapter 2. The working principles of the characterization techniques used in this work are also described here. The description of the experimental work, as well as the results and discussion are presented in chapters 3 to 7. Chapter 3 begins with the investigations into the preparation of the positive electrode and the influence of the fabrication steps on the cycling performance of the battery. Besides, it shows the effect of $LiNO_3$ as electrolyte additive and the improvements on the cyclability. In chapter 4 the application of *in situ* X–ray diffraction (XRD) on the study of the products of discharge and charge (sulfur and lithium sulfide) are presented [6]. Furthermore, using electrochemical impedance spectroscopy (EIS), physical and chemical processes can be monitored during cycling of the battery and the impedance contribution can be determined [7]. The application of this method on Li–S batteries is covered in chapter 5.

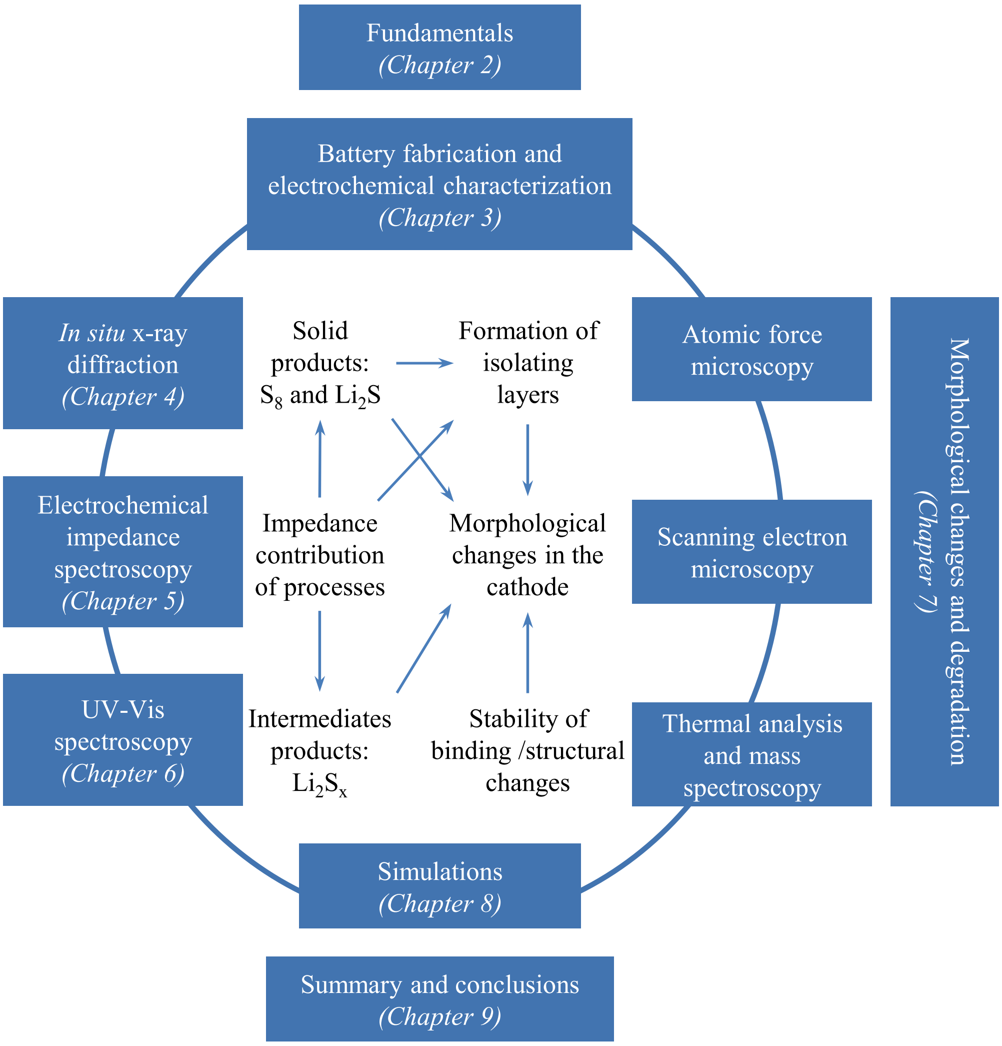
Fundamentals
(Chapter 2)
Battery fabrication and electrochemical characterization
(Chapter 3)
In situ x-ray diffraction
(Chapter 4)
Electrochemical impedance spectroscopy
(Chapter 5)
UV-Vis spectroscopy
(Chapter 6)
Atomic force microscopy
Scanning electron microscopy
Thermal analysis and mass spectroscopy
Morphological changes and degradation
(Chapter 7)
Simulations
(Chapter 8)
Summary and conclusions
(Chapter 9)
Solid products: S8 and Li2S
Formation of isolating layers
Impedance contribution of processes
Morphological changes in the cathode
Intermediates products: Li2Sx
Stability of binding /structural changes

Figure 1.2: Organization of the thesis, main focus and interconnection of the chapters.

The intermediate products of the batteries are dissolved in the electrolyte and are extremely reactive in air. Not many techniques are applicable for its detection. In this work, ultraviolet–visible (UV–vis) spectroscopy was chosen for the study of these species and this is shown in chapter 6 [8]. Furthermore, chapter 7 describes the degradation of the battery in relation with the morphological and structural changes in the cathode. This was investigated using atomic force microscopy (AFM), scanning electron microscopy (SEM) and the combination of thermal analysis (TG/DSC) and mass spectroscopy (MS). A physico–chemical model for Li–S batteries is presented in chapter 8 and the results obtained using experimental analytical techniques are compared with the simulations in order to obtain a deeper knowledge in the reaction mechanisms occurring in the battery. Finally, the summary of this thesis with the conclusions and recommendations for future work is described in chapter 9.

2 Fundamentals

This chapter introduces Li–S batteries, describing the electrochemistry of the system and the main degradation problems. In addition, a literature review summarizes the efforts of the last years in improving the cycling stability through the use of new materials and concepts for electrodes and electrolytes. Afterwards, the main characterization techniques used in this work are explained.

2.1 Lithium–sulfur batteries

2.1.1 Operating principles

The most investigated Li–S battery system consists of a lithium anode, an organic liquid electrolyte containing a lithium salt, a porous polymeric membrane, and a sulfur composite cathode (Figure 2.1). A high electrical conductive material is necessary in the cathode to be in contact with the low conductor sulfur. For this purpose, carbon black, graphite or carbon nanotubes are normally chosen.

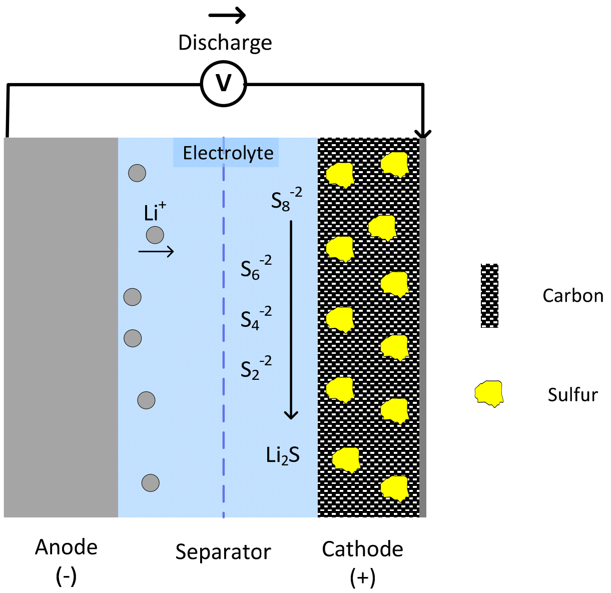

Figure 2.1: Illustration of the Li–S battery components.

The electrical energy is generated by several redox reactions (2.6–2.12). During discharge, lithium (anode) is oxidized to Li^+ ion at the anode/electrolyte interface and the electron is transferred to the outer circuit. Sulfur is reduced at the cathode side where electrons are added. While the electrolyte provides Li^+ ions to allow the electrons to keep flowing and the reactions to continue; the separator allows ions to flow between electrons, while isolating them electrically. Overall, the electrochemical reaction can be described with the followings reactions:

$$\text{Oxidation: } S_{8(s)} + 16\ e^- \rightarrow 8S^{2-} \tag{2.1}$$

$$\text{Reduction: } Li \rightarrow Li^+ + e^- \tag{2.2}$$

$$S_{8(s)} + 16\ Li \rightleftarrows 8\ Li_2S_{(s)}\ ;\ E = 2.1\ V \tag{2.3}$$

The discharge and charge profiles of the Li–S battery, considering complete reaction at room temperature, are schematically shown in Figure 2.2. The discharge curve presents two distinguishable stages or plateaus, one steep and short at high potential between 2.5 and 2.2 V, and other relative flat and longer at about 2 V. The reaction of sulfur to high order polysulfides is expected in the first plateau while in the second plateau the reaction to form Li_2S occurs. When charging, reverse reactions follows and sulfur is formed at the end of charge at 2.5 V.

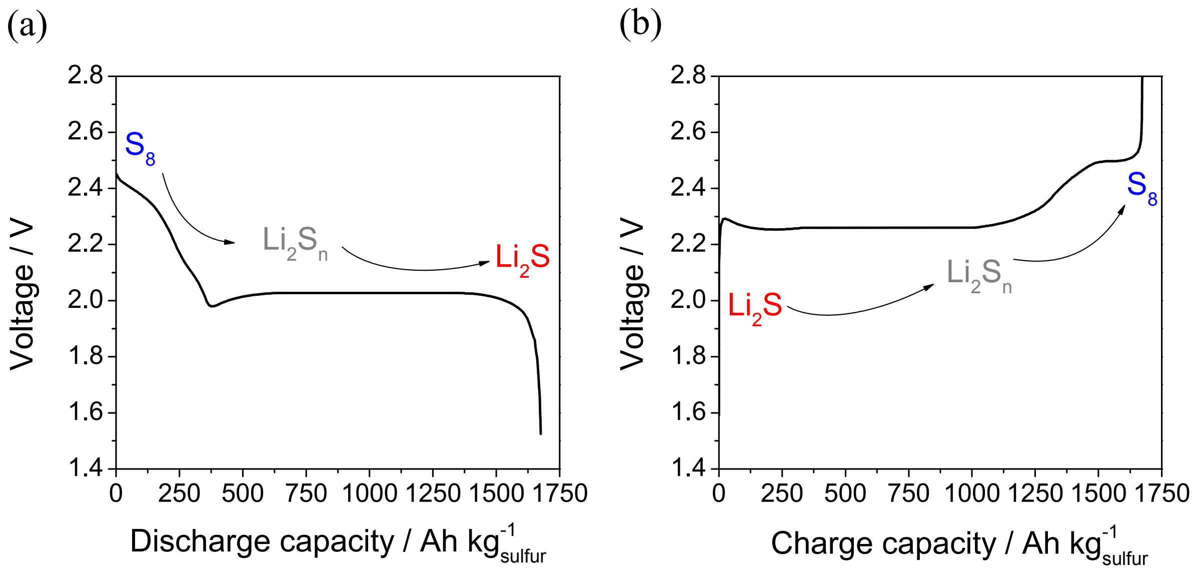

Figure 2.2: Schematic discharge (a) and charge (b) profile expected for a fully cycled Li–S battery.

The enthalpy of formation of Li_2S, ΔH_f^0 (at 298 K) is –106.5 kcal mol^{-1}[9]. The specific capacity of sulfur is calculated in equation (2.4), where n_e is the number of electrons per atom of sulfur (2), F the Faraday constant (96485 C), and M_s the molar mass of sulfur (32 g mol^{-1}).

$$\text{Specific capacity} = \frac{n_e \cdot \mathrm{F}}{\mathrm{M_S}}\,(\mathrm{As\ g^{-1}}) = \frac{1000 \cdot n_e \cdot \mathrm{F}}{3600 \cdot \mathrm{M_S}}\,(\mathrm{Ah\ kg^{-1}}) = 1675\ \mathrm{Ah\ kg^{-1}} \tag{2.4}$$

Based on the discharge profile, the average discharge potential (E) is at around 2.1 V vs. Li^+ / Li (2.5) and the specific energy can be calculated as follows:

$$\text{Energy density} = \mathrm{E} \cdot \frac{n_e \cdot \mathrm{F}}{\mathrm{M_s}}\,(\mathrm{As\ g^{-1}}) = \mathrm{E} \cdot \frac{1000 \cdot n_e \cdot \mathrm{F}}{3600 \cdot \mathrm{M_{Li2S}}}\,(\mathrm{Wh\ kg^{-1}}) = 2445\ \mathrm{Wh\ kg^{-1}} \tag{2.5}$$

After cell assembling (charged cell) sulfur exists mostly in the orthorhombic crystalline form as cyclo–S_8 and a low percentage is dissolved in the electrolyte. During discharge, the partially dissolved sulfur reduces to polysulfide ions with progressively lower states of oxidation, according to the electrochemical reactions (2.6)–(2.13). As the discharge proceeds, the dissolved $S_{8(diss)}$ in the electrolyte is consumed by the electrochemical reaction (2.8), the concentration of $S_{8(diss)}$ decreases, enhancing further dissolution of crystalline sulfur into the liquid phase. While Li_2S precipitates during discharge, the intermediate polysulfides are soluble in the electrolyte.

$$2Li \rightleftarrows 2Li^+ + 2e- \tag{2.6}$$

$$S_{8(s)} \rightleftarrows S_{8(diss)} \tag{2.7}$$

$$S_{8(diss)} + 2\,e- \rightleftarrows + S_8^{2-} \tag{2.8}$$

$$^3/_2\, S_8^{2-} + e- \rightleftarrows 2S_6^{2-} \tag{2.9}$$

$$S_6^{2-} + e- \rightleftarrows {}^3/_2\, S_4^{2-} \tag{2.10}$$

$$^1/_2\, S_4^{2-} + e- \rightleftarrows S_2^{2-} \tag{2.11}$$

$$^1/_2\, S_2^{2-} + e- \rightleftarrows S^{2-} \tag{2.12}$$

$$2Li^+ + S^{2-} \rightleftarrows Li_2S_{(s)} \downarrow \tag{2.13}$$

Here, a simple reaction mechanism was presented. Nevertheless, there are still many discussions about the reactions steps occurring during cycling. Different hypothesis were presented in the last years which includes often several additional reactions and radical intermediates. Regarding the solid end product of reactions, some authors mention the formation of solid $Li_2S_{2(s)}$, besides $Li_2S_{(s)}$. However, in the phase diagram of Li–S only Li_2S is shown as stable phase [10] and $Li_2S_{2(s)}$ may exist as metastable solid compound [10,11]. The main mechanisms of reactions proposed in the last years for the Li–S system [12–17] are summarized in additional information (section 11.4.1).

2.1.2 Main problems and challenges

In spite of the intensive research of the last decades, Li–S batteries are still not commercially available. This is explained by the numerous limitations of the system, which are basically related to the isolating properties of the reaction products, the dissolution of the intermediates of reaction, and the high reactivity of the lithium anode. These are explained as follows:

- Sulfur, the product of charge, is an electronic insulator and no reaction is possible without the use of an additive electronic conductor. High carbon content increases electrical conductivity; however, it also reduces the energy density. Furthermore, sulfur is partially soluble in several organic solvents used in Li–S batteries. It diffuses through the electrolyte, reaches the anode surface, which is in most all the cases lithium metal. Here, sulfur can reacts chemically with the unprotected surface reducing to polysulfides and corroding lithium. Moreover, the morphology of the cathode can change upon cycling due to the changes on state of aggregation, and the formerly well–dispersed sulfur can aggregate and become isolated for further reaction.
- The dissolution of polysulfides (Li_2S_x with $2 \leq x \leq 8$) is also one of the causes of degradation. Polysulfide can diffuse to the anode and react directly with lithium metal and be reduced to lower order polysulfides. This is called shuttle mechanism and leads to irreversible loss of sulfur in the battery, corrosion of lithium metal, self–discharge, and poor Coulombic efficiency [18,19]. In the extreme case, the polysulfides react with Li to form Li_2S, which deposits on the negative electrode, partially blocking it for further reactions [20]. Furthermore, the dissolution of lithium polysulfides causes an increase in viscosity of the electrolyte and the concentration can rise up to 10 mol L^{-1}, decreasing the ion mobility between electrodes [21].
- Lithium sulfide, the product of discharge, is also non–conductive, precipitates during discharge and is almost insoluble in organic electrolytes. It generates inactive areas over the electrode which reduces the capacity of the battery. Volume changes occurs in the cathode during cycling due to the density difference between sulfur (α–phase, 2.07 g cm^{-3}) and Li_2S (1.66 g cm^{-3}) [22]. Thus, sulfur composites electrodes are expanded during discharge and

contracted during charge. Thickness change of the electrode of about 22% was measured by Paris and collegues [23]. This can lead to failure of batteries caused by crack formation in the cathode matrix.

- Lithium metal is the standard material in Li–S batteries. It is extremely reactive in air and water, this leads to severe security problems for example in mobile applications. Lithium can form dendrites during cycling, which can conduct to short circuits in the battery. Lithium reacts also with impurities present in the electrolyte and generates a passivation layer between anode and electrolyte [24]. If the ion conductivity of this layer is not high enough, it can block the electrode, and the battery fails. Moreover, if this layer is continuously formed during cycling, it consumes the anode material, which will not be available anymore for further reactions.
- Decomposition of electrolyte occurs by reaction of polysufides with several common electrolyte solvents: esters, carbonates and phosphates [25]. Conventional lithium salts such as lithium hexafluorophosphate ($LiPF_6$), lithium tetrafluoroborate ($LiBF_4$), lithium bisoxalatoborate (LiBOB) and lithium difluoro(oxalato)borate ($LiBF_2C_2O_4$) can also react with polysulfides producing LiF.

2.1.3 State of art

In the last two decades, researchers have been investigating new concepts for Li–S batteries in order to overcome the limitations listed above. In the following paragraphs, the most important approaches related with improvements on the cathode, electrolyte and anode are presented.

Cathode materials

Most attempts to improve the electrochemical performance of Li–S batteries have been focused on the positive electrode. Due to the low electrical conductivity of sulfur, the incorporation of a conductive material in the cathode of Li–S batteries is one of the main issues related to the fabrication of the electrode. Different strategies were developed associated to the selection of the conductive material and the method of incorporating sulfur in the composite. Carbon black [19,23,26–31], active carbon [32,33] carbon nanotubes [26], and graphene [34,35] are common conductive materials applied in Li–S batteries. The sulfur composite is prepared by mechanical mixing/milling of both components, by melting or sublimation of sulfur, or by *in situ* reaction of sulfur. These last strategies facilitate the incorporation of sulfur in nano materials. The incorporation of sulfur in a nano–porous conductive matrix were first presented by Wang and coworkers [32,33]. The pore size was around 2.5 nm and resulted in batteries with a reversible capacity of 400 Ah kg_S^{-1} (current density: 0.3 mA cm^{-2}, max. 25 cycles). Ji and coworkers [20] obtained better cyclability with the utilization of high order meso–porous carbon; 6.5 nm diameter carbon tubes separated by 3–4 nm wide channel voids. This configuration should help to trap the polysulfides and facilitate the conduction of ions and electrons in the matrix. Reversible capacity of 1005 Ah g_S^{-1} was achieved (current density: 0.37 mA cm^{-2}, max. 20 cycles). Further attempts were made using the same approach to encapsulate sulfur in an conductive matrix , among others: [36–39].

Li–S batteries fabricated by Wang and coworkers [40] achieved discharge capacities of 800 Ah kg_S^{-1} up to 400 cycles at a discharge rate of 0.2 C. They created hollow carbonized polypyrolle spheres of around 450 nm diameter, in which melted sulfur was embedded. High cycling performance until now were demonstrated by Seh and colleagues [41]. They generated a TiO_2 yolk shell with internal void to encapsulate sulfur and retain intermediate products. This configuration showed capacity retention of 67% after 1000 cycles.

The binder plays also an important role in creating a good electric network structure and maintaining the cathode morphology during cycling. Polyethylene oxide (PEO) and polyvinylidene fluoride (PVDF) are often chosen as binders for Li–S batteries. Because of the poor adhesion of PEO [42] and the oft used toxic solvent N–methyl–2–pyrrolidone (NMP) for PVDF, alternative binders have been tested in the last years. Some of these are gelatin [28,43,44], Nafion® [45] and also conductive polymers such as poly(3,4)–ethylenedioxythiophene (PEDOT) [46]. Binder free electrodes, with moderate capacity retention, have been also investigated recently to avoid the use of solvents in the industrial fabrication [47–50].

Other approach to retain the active material during cycling is the use of protective layers. Polyaniline [51], graphene nano–sheets [52–54], carbon fiber cloth [48], Nafion® [55] are some of the materials used to coat the surface of the cathode. High capacity retention was achieved by a cell with an interlayer consisting of reduced graphene oxide (rGO) and CB, showing an initial discharge capacity of 1260 Ah kg_S^{-1} and 895 Ah kg_S^{-1} after 100 cycles [54]. When considering the use of interlayers, it is important to calculate the full cell capacity, because the application of interlayers normally involved an increase of the total weight of the cell while lowering its capacity.

Electrolyte

High ionic conductivity (> 10^{-4} S cm^{-1}), electrochemical stability, and safety are the most important characteristics required in the electrolyte [56]. A lower electrochemical stability window (ESW) is required for Li–S batteries compared with Li–ion batteries, 2.5 V vs. 4 V. As it was already described, polysulfides dissolve in conventional organic electrolytes, generating a chemical shuttle. In order to avoid this, the use of additives, as well as the substitution of conventional organic electrolytes by polymer electrolytes or ionic liquid (IL) based electrolytes, has been implemented during the last decade.

A common liquid electrolyte for Li–S batteries is a binary mixture, normally 1:1 (v/v) of 1,3–dioxolane (DOL) and 1,2–dimethoxyethane (DME) [50,57–60] doped with 1M lithium bis(tri–fluoromethanesulfonyl)imide ($Li[N(SO_2CF_3)_2]$, LiTFSI). Moreover, glycol ethers (glymes, Gn) such as diglyme, triglyme, and specially tetraglyme (TEGDME) has also been applied as a single solvent [40,61–63], or in mixtures with DOL [64–66] or IL [67]. The mixture of electrolytes, like TEGDME/DOL [68] or DOL/DME [69], enhances the ion transportation, lowers the viscosity, and improves the wettability of the electrode [68,69].

The utilization of solid electrolytes is attractive mainly due to safety reasons and the better control of polysulfide dissolution, contrary to flammable organic solvents. Batteries based on PEO electrolytes show limitation in operation above 70 °C to avoid the crystallization of polymer, which induces low ionic conductivity [70]. Alternative gel polymer electrolytes (GPEs) can be used [30,33,56,71,72]. Usually, Li–GPE–S cells suffer from capacity fading due to the poor liquid electrolyte retention of the membrane. High performance was achieved by using a functional poly(methyl–methacrylate) containing inorganic trimethoxysilane domains synthesized and blended with poly(vinylidenefluoride–co–hexafluoropropylene) [73]. The capacity retention obtained was around 88% after 100 cycles (1050 Ah kg_S^{-1}).

ILs have been used to replace liquid electrolytes due to the following advantages: non–volatility, non–flammability, large ESW, and large solubility power [56]. Drawbacks are their high viscosity, which reduces the ion mobility, and the high material costs. The application of ILs in Li–S started in 2006 [74] and their investigation continues until now [75–77]. Bis(trifluoromethan–sulfonyl)imide/amide

[TFSI/TFSA] is often used as an anion, while some examples of cations are 1–butyl–3methylimidaolium [BMIM], 1–ethyhl–3methylpyrrolidinium [PYR14], and 1–butyl–1–methylpiperidinium [PiP14] [78–80]. Among the IL–based electrolytes, low viscosity TFSA–based ILs reach high capacity (around 700 Ah kg_S^{-1} after 50 cycles) and high Coulombic efficiency.

Anode materials

Lithium is a suitable anode material because of its light weight and low standard reduction potential. Nevertheless, it remains as the main safety problem for application of Li–S batteries in mobile applications due to its high reactivity and the formation of dendrites. New concepts of Li–S batteries must be developed for addressing the safety concerns of metallic Li anodes. In order to replace the anode by an intercalation material, sulfur must be replaced by its lithiated counterpart. By starting with Li_2S as active material in the cathode [81–85], the metallic lithium can be replaced by a silicon, tin or graphite anode, where Li can be intercalated. Moreover, the stability of the cathode may be enhanced using Li_2S as starting active material because further expansion of the cathode is avoided. Nevertheless, Li_2S has also a low electrical conductivity and has the additional disadvantage that it reacts extremely fast in air atmosphere, and the fabrication of such cathodes must be carried out under Ar–atmosphere. Discharge capacities of around 300 Ah kg_S^{-1} were presented using cathodes made of micro–sized carbon–Li_2S composite [86]. Higher capacity was achieved combining this electrode with a solid electrolyte [87]. Pre–lithiated sulfur composite as a cathode and graphite as an anode have been also proposed by He and coworkers [23]. This type of cathode was also tested with a gel electrolyte and a Sn–C–Li composite anode with moderate capacities [82]. Si nanowire [81], Li–Al [88], and $Li_{2,6}BMg_{0,05}$ [89] were also investigated as anode materials. Furthermore, Visco and colleagues proposed the use of Li–conducting ceramic electrolytes to protect lithium electrodes [90]. All solid state batteries were fabricated: In/Li_2S–P_2S_5 and glass–ceramic/Li_2S–Cu showed an initial capacity of about 490 Ah kg^{-1} [91].

Magnesium is also one of the most attractive anode materials for sulfur cathodes. This is abundant in the earth´s crust and also safer than lithium, because no dendrite formation occurs. Mg–S batteries have a higher theoretical capacity (3200 Wh L^{-1}) than Li–S batteries; this is based on the two–electron conversion reaction: $Mg^{2+} + S + 2e^- \leftrightarrow MgS$ [92]. Currently, the main research is focused in finding an appropriate electrolyte [93–95]. Recently, a simple aproach to synthesis electrolyte solutions for recheargable magnesium batteries consisted of binuclear magnesium aluminate complexes was presented by Zhao-Karger et. al.[96].

A new concept was presented recently by Duan and colleagues [97]. They fabricated a sulfur/lithium–ion battery that consists of a lithium/Sn–C composite anode, a carbyne polysulfide cathode, and a carbonic ester electrolyte. The battery delivers a reversible capacity of 500 Ah kg_S^{-1} after 50 cycles at a current density of 200 A kg_S^{-1}.

These new concepts developed to replace the "classical Li–S" system, which substitute the lithium anode by safer materials, define a trend for reaching a sulfur battery with real perspective in the industrial fabrication and its application in a wide consumer market.

2.1.4 Importance of characterization

The development of Li–S cells requires a deeper understanding of the electrochemical processes. Changes of composition and structure in the electrodes, as well as the processes occurring in the interface electrode/electrolyte during cycling are very complex. Characterization studies must be carried out to create a robust basis of fundamental knowledge that allows the generation of new ideas to improve this system. In the next section the basic principles of the main characterization techniques used in this work are presented. The application of these techniques on the Li–S system will be described in chapters 4–7.

2.2 X–ray diffraction (XRD)

XRD is an important technique for the quantitative and qualitative investigation of crystalline materials. This technique has been intensively applied in the last decades for the investigation of structural changes occurring in batteries. Thank to modern X–ray diffractometers, diffractogramms can be taken in few minutes; allowing, with a proper experimental layout, the investigation of electrodes materials during cycling (*in situ/operando*).

2.2.1 Generation of X–rays and its interaction with materials

X–rays are electromagnetic waves with a wavelength between 10^{-3} and 10^{-1} nm and a technical energy interval of 3–500 keV. Their use allows the investigation of crystalline materials since their wavelengths are lower than the atomic distance in the lattice structure (~1 Å). In order to produce X–rays, a tungsten filament (the cathode) is heated at high temperature. Electrons are emitted and accelerated in an electric field located between the cathode and a copper or cobalt anode. The X–rays are produced in the focal spot of the anode. Two spectra are obtained: the bremsspectrum and the characteristic spectrum. The first one is produced by the deceleration of the electrons in the electrical field of the atoms in the anode. The atoms of the anode material are ionized in the most internal shells by the electrons produced in the cathode. Then a radiation of quantum energy occurs when an electron jumps from an external orbital into the free place of an internal orbital with lower energy level. The quantum energy differences are characteristic for each element and provide a discontinuous characteristic spectrum (Figure 2.3 (a)). Three characteristics lines are emitted: $K_{\alpha1}$, $K_{\alpha2}$ and K_{β}. For standard XRD measurement the characteristic line $K_{\alpha1}$ is used.

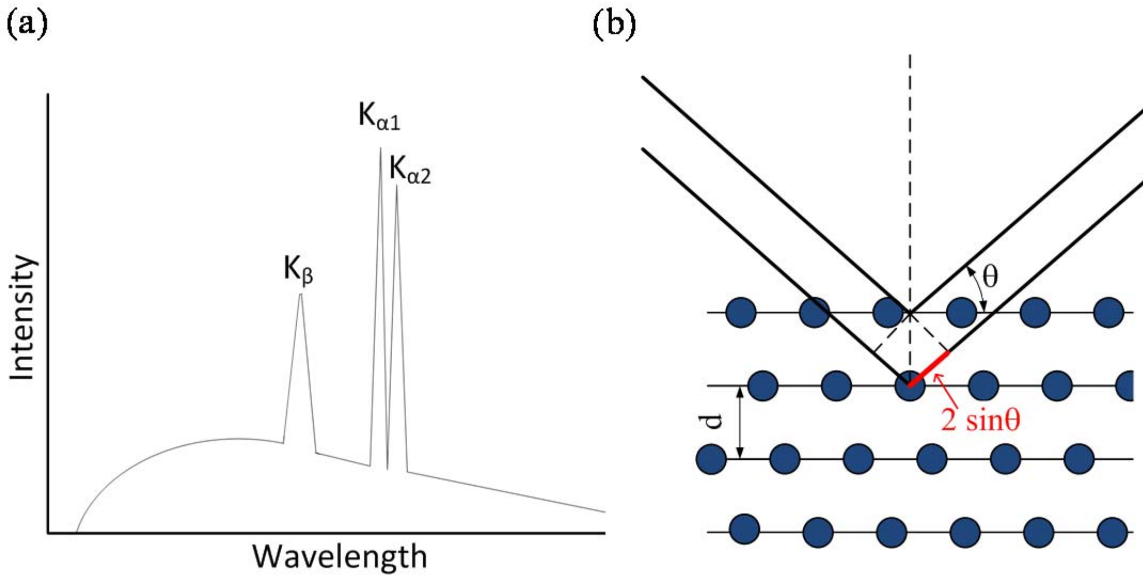

Figure 2.3: (a) Schematic representation of the spectrum emitted by an X–ray tube: the smooth continuous curve is due to bremsstrahlung and the spikes are characteristic k lines. (b) Elastic scattering of X–ray in the lattice of a crystalline solid.

To obtain monochromatic radiation for the measurements, the characteristic lines $K_{\alpha2}$ and K_{β} have to be eliminated or reduced. The elimination of the K_{β} line as well as the parallelization of $K_{\alpha1}/K_{\alpha2}$ can be done by using a Göbel mirror. A thin monocrystal, as monocromator and slit apertures can be applied to cut out lines $K_{\alpha2}$ and K_{β}. The monocrystal is set in a position where the Bragg`s law applied only to $K_{\alpha1}$; consequently, other wavelengths are eliminated. A characteristic Cu $K_{\alpha1}$ radiation is obtained at the end of this process [98]. When a material is radiated by X–rays; the energy and intensity of the radiation decrease and the direction of propagation changes. For crystalline or long range order materials, the incident radiation is diffracted, when the wavelength λ multiplied by an integer n is equal to $2d\ sin\theta$ (Bragg´s reflection law: $n\lambda = 2d\cdot sin\theta$), where d is the distance between the planes and θ the angle between the incident ray and the scattering planes (Figure 2.3 (b)). The reflected X–rays are detected at several θ and they are represented in diffractograms, in which the intensity is plotted versus 2θ. By analyzing the diffractograms, the distribution of lattice plane in the crystal can be predicted and the properties of the crystal structure can be obtained [99].

The main information that can be obtained from a XRD analysis is related to:

- Identification of crystalline phase: the space group and unit cell of the crystal structure can be determined by analyzing the peak position and peak intensity of the sample.
- Crystallinity: sharp peaks in the diffractogram are related to the crystallinity of the phases. Amorphous phase are present as broad bands. The crystallinity of the sample can be calculated by comparing the area under the peaks and bands, which is proportional to the volume of the crystalline and amorphous volume respectively.
- Crystallite size: the width of the peaks becomes larger when the crystalline size decreases. The average size of crystalline primary particles (τ) can be calculated by the Scherrer equation: $\tau = k\lambda/Bcos\theta$, where k is the shape function and B is the full width of the peak at half maximum. Modern refinement programs allow calculating the crystallite size by the use of mathematical refinements.
- Orientation of particles in a sample: preferred orientations of a phase in a sample are related to the relation between the intensity of the *hkl*–peaks.

A refinement method must be applied when quantitative analysis of a diffractogram is desired. A short review of the structure refinement method developed by the physician Hugo Rietveld is described below [100,101].

2.2.2 Rietveld–Method

The Rietveld method, firstly implemented to analyze neutron diffractograms, is frequently applied to evaluate XRD diffractograms. The advantage of this method is that employs directly the profile intensities instead of the integrated intensity;

considering, in this way, each intensity–point of the diffractogram. First, the diffractogram is indexed, the Miller indices are correlated to observed reflexes, and the lattice parameters are calculated. Thus, indexing of a diffractogram can be very complicated, when some reflexes overlap. The approach of this method is basically the use of analytical profile´s functions and least squares algorithm, in which the theoretical line profile is refined with the measured profile. A function M compares the measured intensity y_{io} with the calculated intensity y_{ic} from the structural model (2.14). This function is minimized with respect to the profile parameter $w_i = \sigma_i^{-2}$ [101], where σ_i is the standard deviation of y_i.

$$M = \sum_i w_i \, (y_{io} - y_{ic})^2 \tag{2.14}$$

The observed intensity is hence the sum of the contributions of all the Bragg–reflexes k in the position i and the background y_b. Here, s is a scale factor; m_k, the multiplicity factor; L_k, the Lorentz polarization factor; F_k, the structure factor; G, the profile function of the reflex k; θ_i position of the observed intensity i; and θ_k, the calculated position of reflex k.

$$y_{ic} = s \sum_k m_k L_k |F_k|^2 \, G\left(2\theta_i - 2\theta_k\right) + y_b \tag{2.15}$$

The least–squares refinement is applied by a computer program using approximate values for the first refinement. Subsequent refinement is carried out until a certain convergence criterion is achieved. Some parameters can be kept constant during refinement, and constraints can be introduced as well between them. The progress and quality of a Rietveld refinement, i.e. the minimization of the function M, is evaluated by a “residue” parameter, calculating also the standard deviation for each refined parameter [102]. It is important to clarify that this “residue” parameter describe only how good is the agreement between observed and calculated intensities; however, it does not state if the values calculated are physical possible or not. The weighted profile of the “residue” parameter (R_{wp}) is described in (2.16), where $\Delta_i = y_{io} - y_{ic}$.

$$R_{wp} = \left[\sum_i (w_i \Delta_i^2) \Big/ \sum_i (w_i \, y_{io})^2 \right]^{1/2} \tag{2.16}$$

The principal interest in applying the Rietveld analysis is to obtain physical parameters of the structure like lattice constant, atom positions, and phase composition, in case of mixtures. One of the main issues related to this method is finding a suitable profile functions and background curve. Additionally, the shape of the reflex is influenced by instrumental factors (e. g. intensity distribution of the X–ray source, the dimension of the slit filter, etc.) and by sample properties, like crystallite size, lattice defect, and strains. Each of these factors requires a function that describes the intensity distribution of each reflex. Basically, the profile of the reflex function (G) can be described as a convolution of the instrumental factors (I_f) and the sample (P), this means $G = P \cdot I_f$. The emission profile is then described by the following parameters: area under the emission profile line, wavelength of the emission profile (in Å), and the Lorentzian and Gaussian half width of the emission profile. Generally, the instrument function is represented by a Lorentzian function, while the sample contribution using a Gaussian (Table 1). Voigt functions [103,104] are applied successfully for reflex profiles in which the particle size and strain are studied. An approximation of this function, carried out using Rietveld programs, results in a Pseudo–Voigt function (PV_{UA}). For asymmetric peaks split functions, such as Split–Pearson and Split–Pseudo functions, are often used. They allow the fitting of reflexes with asymmetric profiles [105].

Table 1: Unit area peak types for the Gaussian, Lorentzian and Pseudo Voigt symmetric functions [105]**. fwhm is the full width at half maximum, $x = 2\theta - \theta_k$, and η: mixing parameter.**

Profile function	Definition
Gaussian, $G_{UA}(x)$	$G_{UA}(x)=\left(\frac{g_1}{\text{fwhm}}\right)\exp\left(\frac{-g_2x^2}{\text{fwhm}^2}\right)\quad g_1=2\sqrt{\frac{\text{Ln}\,(2)}{\pi}}\ ;\ g_2=\text{Ln}\,(2)$
Lorentzian, $L_{UA}(x)$	$L_{UA}(x)=\left(\frac{2}{\pi\, fwhm}\right)\left(\frac{1+4x^2}{fwhm^2}\right)^{-1}$
Pseudo–Voigt, $PV_{UA}(x)$	$PV_{UA}(x)=\eta L_{UA}(x)+(1-\eta\, G_{UA}(x))$

2.3 Electrochemical Impedance Spectroscopy (EIS)

EIS has become one of the most powerful techniques for investigating processes occurring in electrochemical power sources. An important advantage of this method is the capability to characterize and identify in a single measurement, without external influences, different physical or chemical steps taking place in a complex system.

2.3.1 The transfer function: impedance

The impedance spectroscopy is based on the classical method of the Transfer Function (TF). If a system is perturbed by a sinusoidal wave input $X(\omega_o)$, it results in a sinusoidal output signal $Y(\omega_o)$ with the same frequency (ω_o) but with different phase and amplitude. The ratio between output and input signal is the complex transfer coefficient $H(\omega_o) = Y(\omega_o)/X(\omega_o)$. The transfer coefficient describes the properties of linear steady–state systems and is affected by the frequency and also by the properties of the analyzed system. If the input signal includes a set of frequencies (ω), the transfer function is described by $H(\omega) = Y(\omega)/X(\omega)$. The Fourier transform is employed to move from the time domain to the frequency domain back and forward [106].

EIS can be applied either galvanostatic or potentiostatic. In the galvanostatic mode, the input signal is an alternating electrical current (AC), and the output voltage is measured. The potentiostatic mode is conducted in the opposite way; a sinusoidal voltage is applied in the system and the response measured is the electrical current. The transfer function is called in this case complex impedance (Z) and is obtained from the changes in amplitude and phase according with:

$$Z(\omega)=\frac{\Delta U(\omega)}{\Delta I(\omega)}=\frac{U_0(\omega)}{I_0(\omega)}e^{j\left(\varphi_u(\omega)-\varphi_i(\omega)\right)}=Z^{\prime}(\omega)+jZ^{\prime\prime}(\omega) \tag{2.17}$$

where:

Z: Impedance

ΔU: input voltage

ΔI: output current

$\varphi(\omega)$: phase

$Z^{\prime}$: Real part of impedance

$Z^{\prime\prime}$: Imaginary part of impedance

ω: angular frequency

The transfer function is measured with a small amplitude perturbation signal in order to keep the state of the system stable. For this, only the linear part of the response is considered. The selection of the amplitude depends on the degree of non–linearity at the selected working point. For electrochemical kinetic studies, amplitudes between 1 mV and 10 mV are normally acceptable [106]. The use of very low signal amplitude can increase the level of noises in the measurement, while very high signal amplitude can produce errors due to non–linearity of the system.

The measurements generate a three–dimensional data set: ω_i, Z_i` and Z_i`` for each frequency. Commonly, the real part of the impedance is plotted on the X axis and the imaginary part on the Y axis (Nyquist plot) for each frequency (ω). Another common representation is the Bode plot, which describes the dependency of both log $|Z_i|$ and φ on log $|\omega_i|$ [106].

2.3.2 Equivalent circuit for modeling

To analyze the impedance spectra, the parameters of the system can be modeled either with a physicochemical model or with an equivalent electrical circuit (EC). When applying an EC, the aim is to correlate the individual contribution of the single components in the impedance to each element of the EC. The most common circuit elements and the corresponding impedance equation are summarized in Table 2 and represented in the Nyquist plot on the right.

Table 2: Circuit components, their respective symbols and impedance equations. On the right a schematic explanation of the behavior of the impedance for each element. (W: Warburg parameter).

Circuit component	Symbol	Impedance equation	Schematic view
Resistance	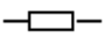	$Z_R = R$	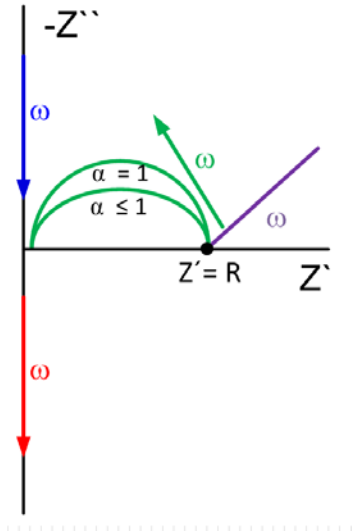
Inductance	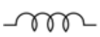	$Z_L\ (\omega)= j\omega L$	
Capacitance	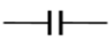	$Z_C\ (\omega)= -(j\omega C)^{-1}$	
R||C Element	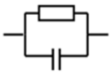	$Z_{RC}(\omega)= R\ (1+j\omega C)^{-1}$	
R||CPE Element (α ≤ 1)	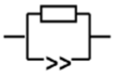	$Z_{R\|\|CPE}(\omega)= R\ (1+j\omega C)^{-\alpha}$	
Warburg–Element	— W —	$Z_w\ (\omega) = W(j\omega)^{-1/2}$	

A resistive element R can be correlated to an electrolyte resistance, charge transfer resistance or resistive behavior of barriers in activation processes. The inductance element describes the magnetic field originated from the pass of current through coils Z_L. In an electrochemical cell, the impedance appears sometimes to be inductive due to adsorption of reactants on the surface. Besides, inductive behavior is commonly observed in an electrochemical cell as result of non–uniform current distribution, inductance of cell cables or slow response of reference electrodes. The capacitance is a function of the frequency with only an imaginary part and a phase shifted –90° with respect to voltage. Electrochemical phenomena like double layer capacitance at the electrode/electrolyte interface are described using this element. This double layer is commonly produced by the charging occurring across the interface, which originates a charge separation and thus a potential difference. Capacitance can also be applied for describing adsorption or crystallization of phases. The combination of resistance and capacitance in parallel (RC) is commonly applied as a sub–model in more complex models to describe the charge transfer resistance of a layer.

The constant phase element (CPE) is one of the most commonly applied elements to define frequency–dependent behavior. The replacement of the capacitance in the RC element by CPE generates a depressed semicircle, which is commonly found in real systems due to inhomogeneity of the sample, like roughness or non–uniform layer thickness. The variable α is dimensionless and defines the grade of compression of the CPE semicircle. Thus, the limit value of $\alpha = 1$ represents ideal capacitive behavior.

The diffusion of species is described here by the Warburg impedance [107]. This represents a linear semi–infinite diffusion layer, which obeys the second Fick´s law, and explains general diffusion affected by charge transfer reactions [107]. The real and imaginary components are equal and hence the phase shift is –45° and it is frequency independent. Nevertheless, diffusion length is finite in electrochemical systems, like batteries. This is normally represented by "General Warburg Impedance", also called "Nernstian diffusion impedance" when the concentration is assumed as constant at certain distance from the electrode, or by the "Finite diffusion impedance", when a phase boundary is present. These are explained in more detail in section 11.2.1.

2.4 Ultraviolet–visible (UV–vis) spectroscopy

UV–vis spectroscopy uses the light in the ultraviolet (200–400 nm) and visible (400–800 nm) wavelength ranges to detect and quantify molecules which absorb at defined wavelengths. Modern spectrometers cover normally a greater range until near infrared (NIR) region (200–2000 nm).

The absorption of light by a material occurs due to the excitation of valence electrons of the compound from the normal (ground) state to a higher energy (excited) state [108]. Valence electrons can be found in single bonds (σ), double or triple bonds (π), and non–bonding (n) orbitals. A transition of an electron, from one of these orbitals to an empty orbital (normally anti–bonding orbital: σ^*, π^*), occurs when electromagnetic radiation in a defined frequency is absorbed (Figure 2.4). The energy difference between the orbitals is determined by the nature of bonding system and the number of atoms. Most of the absorptions measured comprise only $\pi\rightarrow\pi^*$, $n\rightarrow\sigma^*$, and $n\rightarrow\pi^*$ transitions.

The light source for the UV–region is usually a deuterium lamp and for the Vis–NIR, tungsten or halogen lamp. The sample is prepared normally as solution at low concentration and filled in a small square–section cuvette, usually 1 cm wide. Ideally, the solvent should not absorb in the same absorption region as the investigated species. When testing on transmission mode, the UV–vis radiation passes through the sample and the radiation across the whole UV–vis range is scanned simultaneously or step by step. This radiation can be compared simultaneously with a reference cell containing the solvent. Photocells detect the radiation transmitted and the spectrometer registers the absorption by comparing the initial intensity (I_o) with the transmitted intensity (I_t).

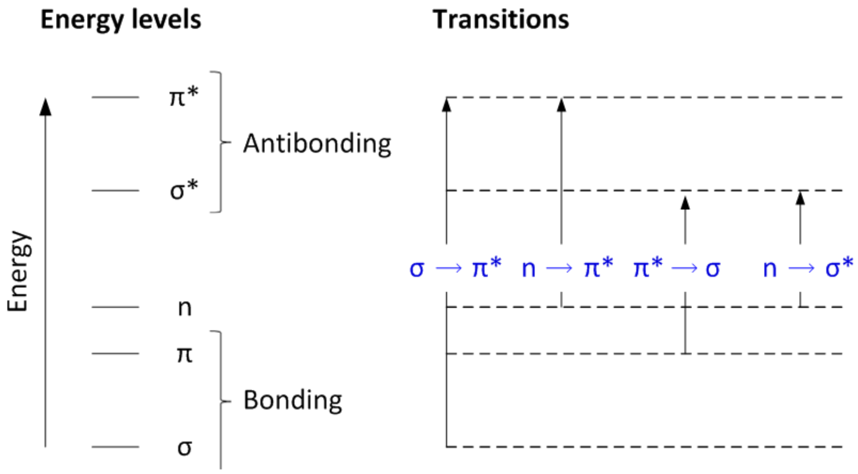

Figure 2.4: Energy levels of bonding orbitals and electron transitions in UV–vis spectroscopy [108].

For the quantification of low concentration solutions the Lambert–Beer´s law can be applied (2.18), where ε, the extinction coefficient (L mol^{-1} cm^{-1}); λ, wavelength (cm); A is the absorbance; d_a, path length of the absorbing solution (cm); and c, concentration of the absorbing species (mol L^{-1}).

$$A=\log\frac{I_o}{I_t}=\varepsilon d_a c \tag{2.18}$$

Although the energies of the orbitals involved in electronic transitions have fixed values, the absorption peaks in UV–vis spectroscopy in condensed matter are normally broad and not very sharp. This is due to the several numbers of vibrational energy levels available at each electronic energy level, in which the transitions occur.

2.5 Atomic force microscopy (AFM)

AFM provides a 3D surface profile of materials with a spatial resolution up to the atomic scale. Forces between a sharp probe supported by a flexible cantilever (<10 nm) and surface are measured at very short distance (0.2–10 nm) (Figure 2.5). Repulsive forces result when the tip of the probe is brought close to sample due to the negative charge of the electrons on the surface. This results in a deflection of the cantilever. A laser focuses on the extreme of the cantilever, where the probe is located, and photodiodes measure the intensity reflected from the cantilever. The repulsive force is described using the Hooke´s law ($F = kz$), where k is the spring constant and z the cantilever deflection.

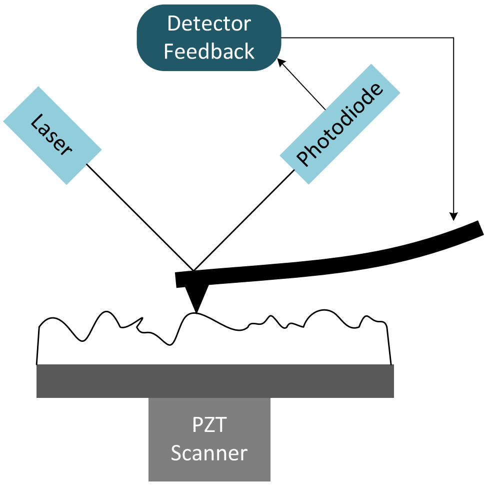

Figure 2.5: Schematic of AFM instrument. PZT: piezoelectric tube.

AFM can be applied to measure all materials, isolators or conductors. Topography and mechanical properties like adhesion force, electrical conductivity, deformation, and stiffness can be also evaluated by this technique. Furthermore, the microscope can operates in several modes such as contact, friction, tapping, and conducting mode [99]. Tapping mode was used in this work (section 7.1.2). Here, the cantilever is oscillated at its resonance frequency using piezoelectric element drives. The advantage of this mode is that it diminishes the damages of the surface and tip compared with the contact mode, which maintains physical contact between tip and surface.

2.6 Scanning electron microscopy (SEM)

SEM produces images by focusing accelerated electron beams onto the surface of the sample. The images can reveal details in the order of 1 nm size. Electrons are generated in a tungsten filament cathode, a high voltage is applied, the temperature of the filament increases to over 2500 K, and electrons are emitted. The electrons are focused by one or two condensers lenses, accelerated to around 60 to 100 keV, and focused onto the surface using an objective lens (Figure 2.6, left) [99]. The sample chamber with the lens system is under vacuum to prevent scattering of electrons due to collisions with molecules of the air. The electrons interacts with the sample material and several signals are produced including Auger electrons (AE), secondary electrons (SE), backscattered electrons (BSE), characteristic X–rays (EDX), continuum X–ray, and cathodoluminescence (CL) (Figure 2.6, right).

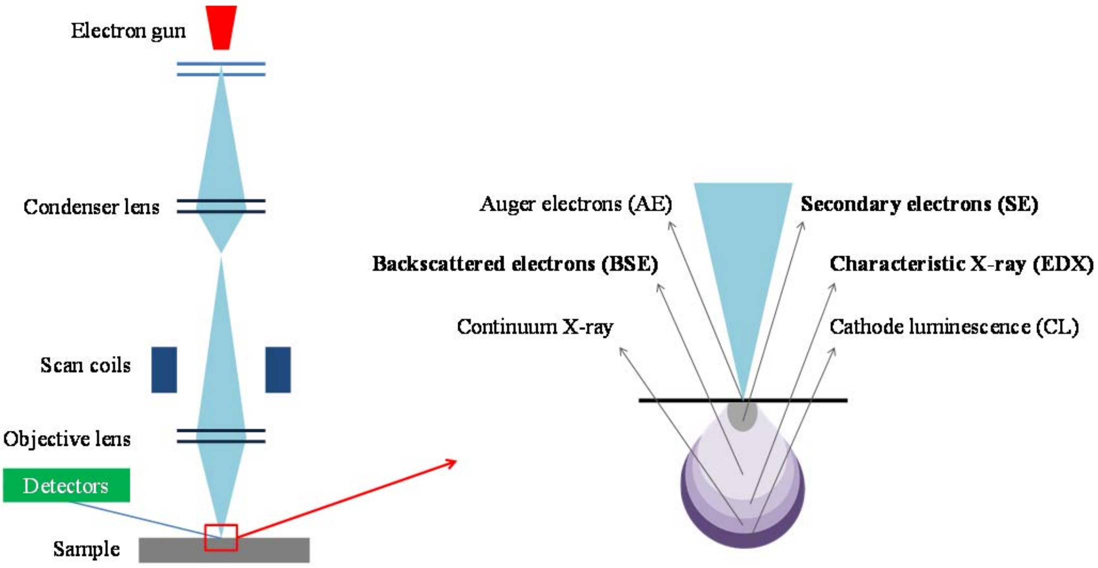
Electron gun
Condenser lens
Scan coils
Objective lens
Detectors
Sample
Auger electrons (AE)
Secondary electrons (SE)
Backscattered electrons (BSE)
Characteristic X-ray (EDX)
Continuum X-ray
Cathode luminescence (CL)

Figure 2.6: Schematic of SEM instrument and signals generated by the interaction of electron beam and sample [99]**.**

SE and BSE detectors are the most common detectors integrated in the equipment. High resolution images are obtained using the SE detector. SE are produced by inelastic interactions of beam electrons with valence electrons of atoms in the sample which cause the expulsion of the electrons from the atoms. On the contrary, BSE are produced by elastic interaction of beam electrons with nuclei of atoms in the sample; hence, they are proportional to the mean atomic number of the sample (z). Thus, a "brighter" intensity correlates with higher average z in the sample, and "dark" areas have lower average z. For this reason BSE images are very helpful for distinguishing different phases in the sample. Furthermore, the measurement of energy dispersive X–rays (EDX) allows the elemental analysis of a sample.

2.7 Thermal analysis and mass spectroscopy

Common methods used for thermal analysis are thermogravimetry (TG) and differential scanning calorimetry (DSC). TG measures weight changes in the material as a function of temperature under controlled atmosphere. It consists in a pan or a plate loaded with the sample placed over a high precision balance (Figure 2.7 (a)) [109]. The furnace is equipped with a thermocouple for precise temperature measurements and specific gases are purged into the atmosphere. DSC allows measuring the heat absorbed or released by a sample relative to a reference. DSC is useful to detect endothermic and exothermic processes, which are not necessary associated with loss of weight (e.g. melting, crystallization, amorphization). DSC consists of a sample and a normally empty reference pan, both connected to a thermocouple and placed over a balance; this last, in case of TG/DSC analysis (Figure 2.7 (a)).

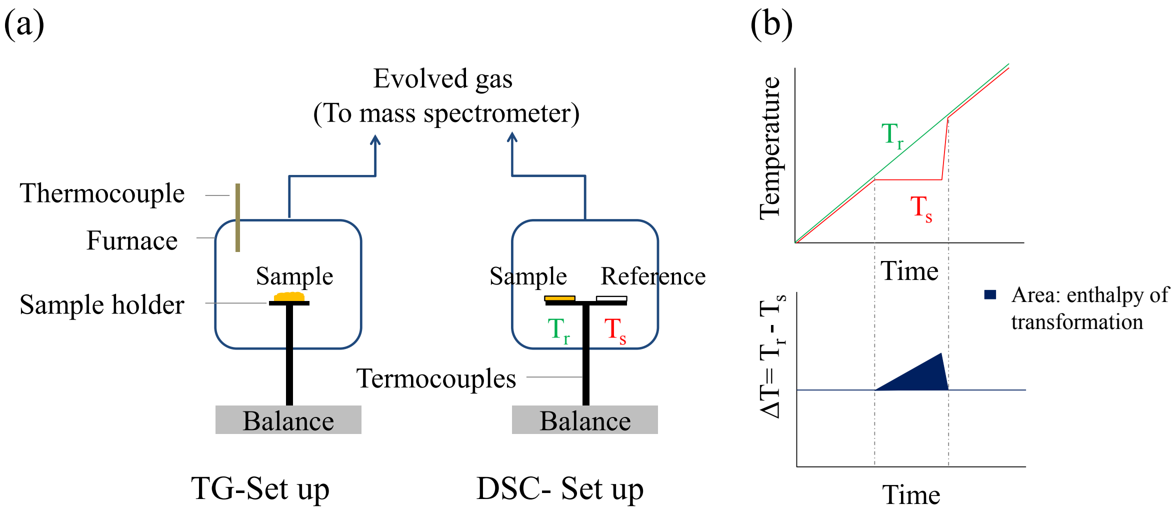
(a)
Evolved gas
(To mass spectrometer)
Thermocouple
Furnace
Sample holder
Sample
Balance
Sample
Reference
T_r
T_s
Termocouples
Balance
TG-Set up
DSC- Set up
(b)
Temperature
T_r
T_s
Time
$\Delta T = T_r - T_s$
■ Area: enthalpy of transformation
Time

Figure 2.7: (a) TG and DSC configurations. (b) Schematic determination of the enthalpy by measuring the temperature of the sample (T_s) and the reference (T_r).

The difference of temperature between reference and sample (ΔT) is measured over time, when the temperature drops; power is supplied to maintain the temperature constant. The heat realeased or absorbed is correlated to the area of the peak seen in the DSC thermogram, which corresponds to the enthalpy of the process, exothermic or endothermic (Figure 2.7 (b)). During heating of the sample in the TG–DSC, the gas evolved can be analyzed by running the equipment in couplings with a mass spectrometer (MS). With the MS fragmentation patterns of substances in the gaseous phase are obtained by electron ionization of the molecules at high energy. By analyzing the relation of the mass number of the particles and molecules detected, the chemical structures of molecules can be resolved.

3 Battery fabrication and electrochemical characterization

The processes included in the cathode fabrication, like mixing, milling, coating and thermal treatments, play an important role in the electrochemical performance of the battery. Furthermore, the preparation of a homogenous cathode layer is required to characterize properly the electrode before, during, and after cycling. This chapter introduces the cathode materials used in this work and the fabrication steps of the battery. Moreover, the influence of selected preparation steps on the capacity fading of the battery is presented.

3.1 Experimental procedures

3.1.1 Cathode materials

The cathode components used for the fabrication of the cathode layer were sulfur powder (S, 99.5% purity, Alfa Aesar), Super P carbon black (CB, 99% purity, Alfa Aesar) as conductive material, and polyvinylidene fluoride (PVDF, Alfa Aesar) as binder. Figure 3.1 shows SEM pictures of the raw powders. The cathode layer in the electrode was composed by 50 wt. % S, 40 wt. % CB, and 10 wt. % PVDF. The composition of the cathode was maintained constant for all the experiments in this work.

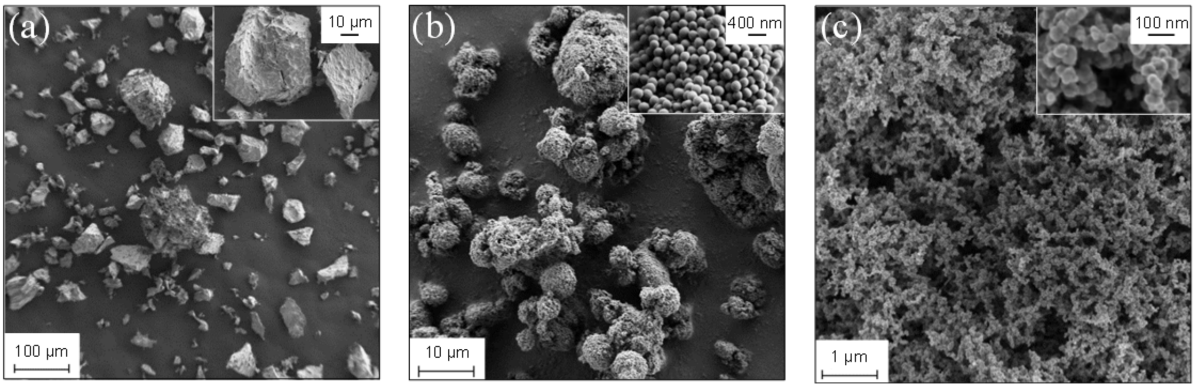

Figure 3.1: Raw materials (a) sulfur, (b) PVDF and (c) CB. SEM pictures, SE detector, EHT: 1 kV, 0.5 kV (PVDF).

The sulfur had an initial average particle size of 39 µm and an orthorhombic crystal structure (Figure 4.4). CB was selected as conductive material for its high specific surface area of 60 m^2 g^{-1} (see section 11.1.3), low particle size (ca. 70 nm), and high electrical conductivity; necessary properties to improve the electron transfer between sulfur and collector. Furthermore, CB nano–particles create a conductive carbon network with a complex arrangement and high porosity, so called "structure", which allows electrical conductive paths from the current collector to the active sites of reactions. These structures are basically aggregations of primary spherical particles (see magnification on top of Figure 3.1 (c)) with particle size smaller than 100 nm. An important aspect to consider during processing of raw powders is that the primary structure of CB can be destroyed when intensive shearing forces are applied. This results in a reduction of the electric conductivity due to the destruction of conductive paths. As binder, PVDF was chosen for its electrochemical, thermal, chemical stability, and its high adherence. The powder consists of agglomerations of well–defined nano particles with a diameter of around 200 nm (Figure 3.1 (b)).

As cathode collector, carbon coated aluminum foil was used (Showa Denko SDX™ [110]; see morphology of substrate in Figure 11.2). The high conductive carbon coating improves the adherence of the layer with the current collector, reducing the contact resistance between the cathode layer and collector by approximately 50% [110]. The stability of the layer over the substrate was also especially important for the *ex situ* analysis of the samples. With the use of conventional aluminum foil, the cathode layer was easily released from the collector while dissembling the cell.

3.1.2 Fabrication of the cathode

The main objective of the cathode fabrication was to obtain a homogenous electrode layer in which the sulfur particles are covered and in contact with the CB nano–particles, while PVDF create bindings between particles and with the current collector. Moreover, the cathode had to be easily reproduced and industrially scalable. It is worth mentioning that the cathode should present high capacity at the beginning of its cycle life in order to assure a high conversion of the active material. Thus, reactions and physicochemical processes are not interrupted due to a low conversion, and the complete cycle of the battery can be studied.

Several parameters and steps of the cathode fabrication were modified in the course of this dissertation. An overview is presented in Table 3 showing the main parameters of mixing, coating, and drying procedures. These will be explained in more detail in the following sections.

3.1.3 Mixing and milling

Cathode I was prepared by mixing all the solid components (S, PVDF, and CB) together and after that, solvents were added. The use of the roll mixer resulted in cathodes with large agglomerates of sulfur in the cathode, as well as the presence of PVDF particles after spraying, which were not dissolved during processing (see Figure 11.3). For this reason the roll mixer was replaced by a tumbling mixer, working at higher angular velocity; and PVDF was dissolved separately in the solvents before adding CB and S. In the tumbling mixer a more intensive mixing effect is expected due to a permanent shifting of product areas. In the new procedure (Cathode II), S and CB were mixed for twelve hours in a tumbling mixer. PVDF was dissolved separately in a 50:50 (v/v) mixture of DMSO and ethanol. Although N–Methyl–2–pyrrolidone (NMP) is a better solvent for PVDF, it was not chosen due to its high toxicity.

Table 3: Comparison of mixing, coating and drying procedures.

Mixing/Milling	Coating	Drying
Initial procedure (Cathode I)		
Roll mixer[‡]	Suspension spray	In vacuum oven
1) Mix of S, CB and PVDF (5 rpm, t= 12 h) 2) Mix with solvents[†] (5 rpm, t= 12 h)	– Internal mixing nozzle – Coating in one step – Heating plate under substrate (100 °C)	80 °C (48 h)
New procedure (Cathode II)		
Tumbling mixer[‡]	Suspension spray	In vacuum oven
1) Mix of S and CB (20 rpm, t= 24 h) 2) Dissolution of PVDF in solvents (magnet stirring) 3) Mix of S and CB with dissolution (2) (20 rpm, t = 24 h)	– External mixing nozzle – Coating in 3 steps or more – No heating plate – Drying between each sprayed layer	Between sprayed layers, 60 °C (1.5–3 h) At the end of coating: 60 °C (24 h) In vacuum in the glove box

[†]Solvents: 1:1 (v/v) mixture of ethanol and DMSO. [‡]In both cases ceramic balls of 8 mm diameter were added in the tank.

3.1.4 Coating and drying

Suspension spraying

The cathodes were fabricated using a wet–powder spraying system (Figure 3.2). In this process, the cathode suspension is applied onto a substrate by means of pressurized air. The suspension was placed in a pressurized tank and it was directed to the nozzle in a polypropylene tube. The movement of the nozzle as well as the sample holder was controlled by a 3D axis robot (Janome JR 2400N GLT). The axis with the nozzle moves in perpendicular direction (y) to the substrate holder at 300 mm s^{-1}, while the substrate holder advances step by step in x–direction so all the surface of the substrate is coated.

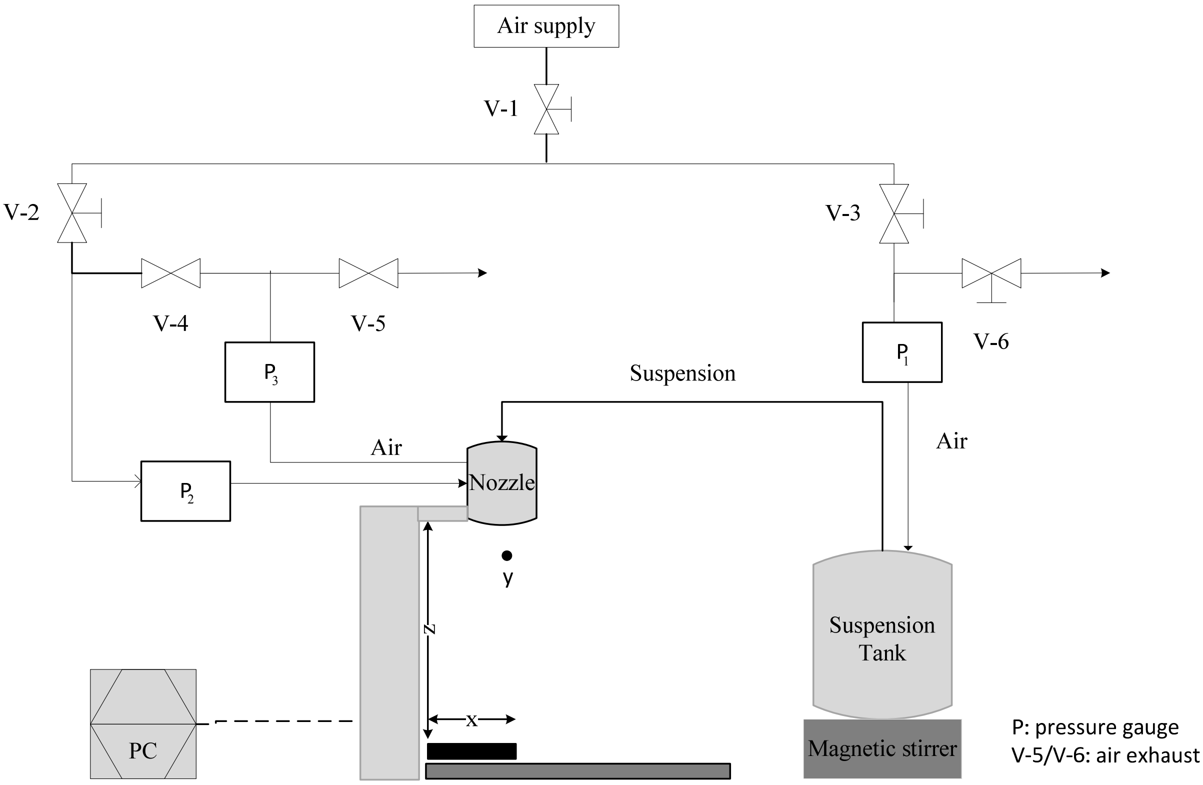

Figure 3.2: Wet–powder spraying system for cathode fabrication.

The internal mixing nozzle used in the first tests was replaced by an air–atomizing external mixing nozzle (LECHLER GmbH). This avoided blocking of suspension in the nozzle, while the slurry mixes with the air outside the nozzle. The pressure of air and suspension, as well the distance between nozzle and layer, were adjusted to obtain a uniform spraying. Homogenous layers were obtained by injecting the suspension at low pressures (between 0.2–0.4 bar) and atomizing externally with air at 0.5 bar pressure. The distance between nozzle and substrate was set at z = 180 mm. Each cathode was prepared by spraying three to four layers over an aluminum foil. The thickness of the cathode can be increased according with demand, by inclusion of furthers spraying/drying steps. However, the electrode thickness is limited by the diffusional resistance or loss of adhesion. Lower sulfur utilization is observed in Li–S batteries for sulfur cathodes with increasing cathode thickness [111] and the formation of discharge and charge products may be concentrated at the surface of the electrode. A drawback in this fabrication process is the large amount of solvent (96 wt.%) used in the slurry preparation, which increases the manufacturing costs as well as the time of drying.

Drying

Between each spraying, the cathode was dried in an oven at 60 °C. At this temperature sulfur volatilization and formation of cracks in the layer due to rapid drying are avoided (Figure 11.5). Especially, the inclusion of a drying step between each sprayed layer improves the stability of the cathode, the adherence on the aluminum collector during spraying, and the homogeneity of the layers. The thickness of the cathode layer, without substrate, varied between 15–20 µm (Figure 11.4). In Figure 3.3 (a) the sprayed cathode after drying is shown, around 22 batteries can be built up from each of them (Figure 3.3 (b)). In the microscopic picture, the homogeneous layer and distribution of sulfur particles can be seen as light points (Figure 3.3 (c)).

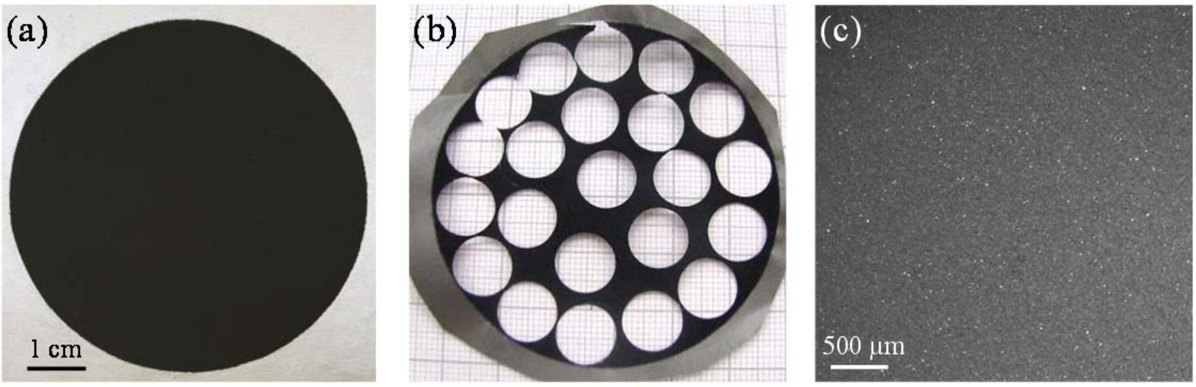

Figure 3.3: Cathode after spraying and drying (a) and after individual cathodes were punched out for cell preparation (b). Microscopic picture of the cathode surface (c), where the white spots are the non–totally covered sulfur particles.

3.1.5 Cell construction and electrochemical testing

The battery was built and tested in a so–called Swagelok® cell (Figure 3.4 (a)) to assure the hermetic sealing and to avoid reaction of the battery components with air. The selected material for the testing Swagelok® cell was polyether ether ketone

(PEEK®) for the body, and stainless steel for the electrodes bolts and nuts. More information concerning the selection of material for the Swagelok® cell is described in section 11.1.1. The battery was assembled in a glove box under an argon atmosphere. First, a 10 mm diameter cathode was punched out and placed on the cathode collector: an aluminum disk over the spring located inside the Swagelok cell. The separator, a 25 μm thick polypropylene microporous membrane (Celgard 2500), was placed on top of the cathode and soaked with 14 μL electrolyte, 1 M $LiPF_6$ (99.99%, Sigma–Aldrich) in TEGDME (99.9%, Sigma–Aldrich). Next, a 1.5 mm thick lithium anode (99.9%, Sigma–Aldrich) was placed on the separator. To complete the construction, the cell was tightened until there was no gap between the nut and body hexes of the Swagelok® cell. To avoid a short circuit, the diameters of the lithium foil and cathode were 10 mm, while the separator diameter was 2 mm larger.

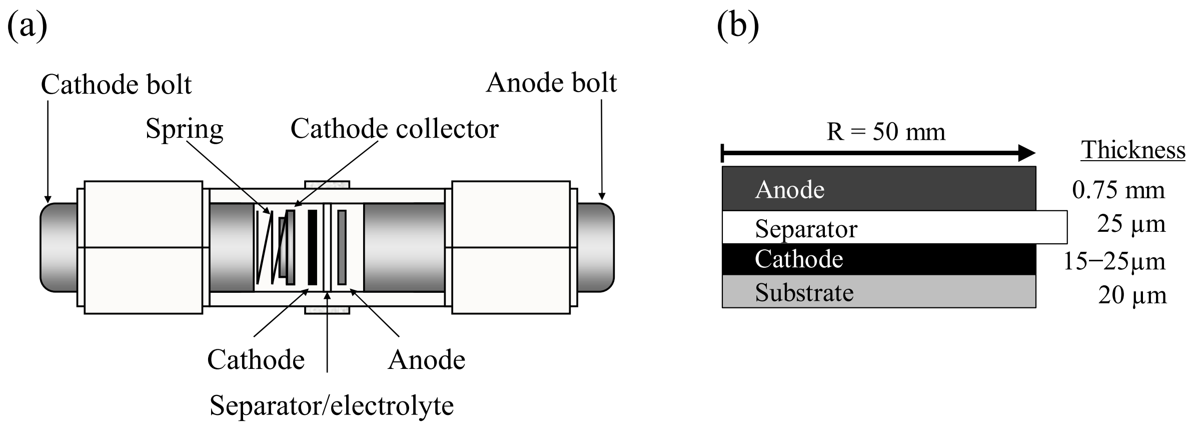

Figure 3.4: (a) Scheme of Swagelok®–cell with inside view of the battery components. (b) Components of the battery and dimensions.

The electrochemical testing or cycling of the batteries was carried out with the battery test equipment BaSyTec. The charge–discharge proceeded galvanostatic at 0.18 C (300 A kg_S^{-1}). The battery was first discharged until 1.5 V, charged at constant current density up to 2.8 V, and then a potentiostatic period followed for 15 min before starting the next cycle.

3.2 Result and discussion

3.2.1 Morphology of the cathode

High resolution SEM pictures show that the uses of different fabrication procedures result in dissimilar cathode morphologies (Figure 3.5).

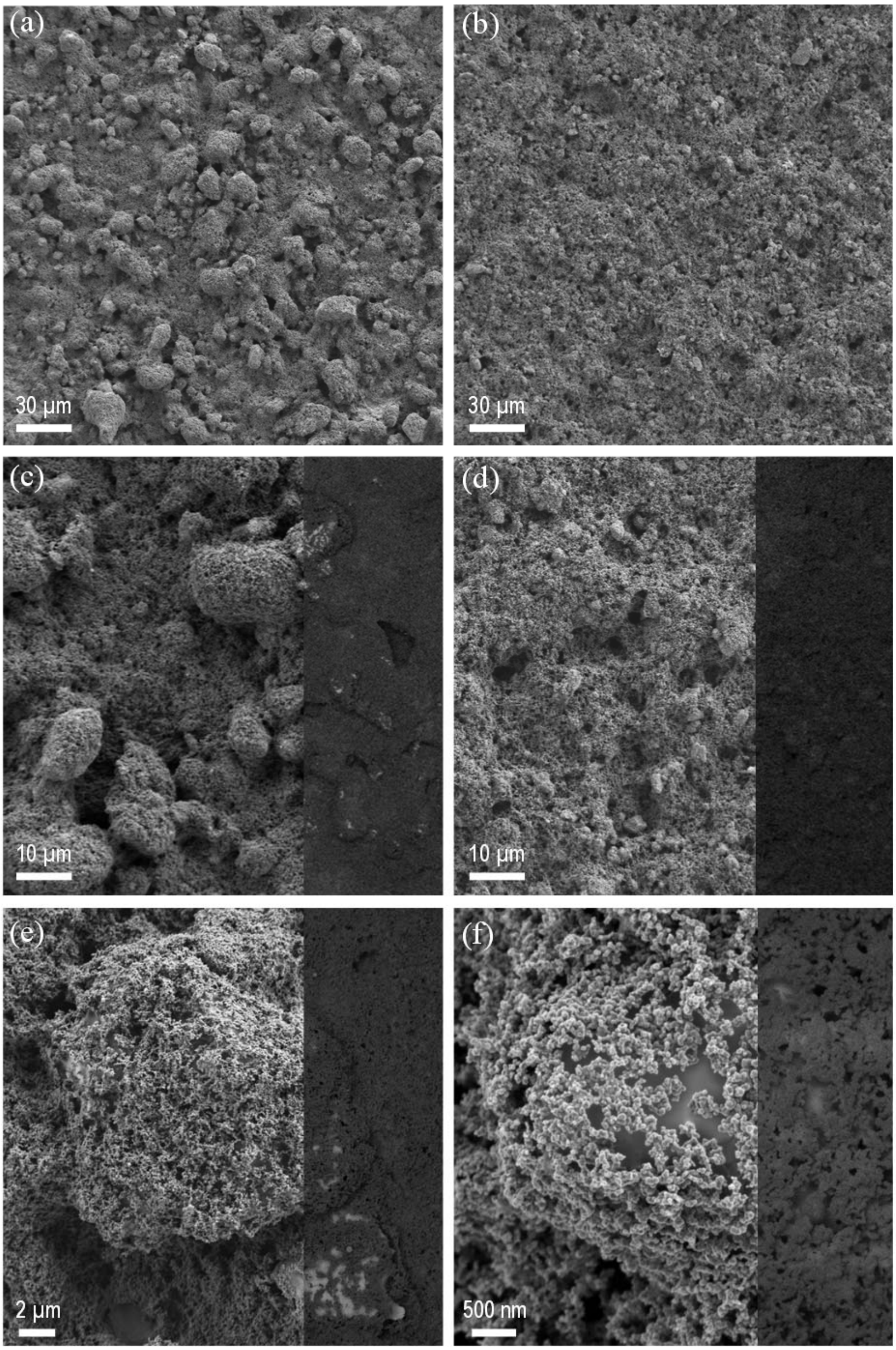

Figure 3.5: Surface of cathodes fabricated using different fabrication procedure. (a, c, e) Cathode I (initial procedure) and (b, d, f) Cathode II (new procedure).

Cathode I presents larger particle size (up to ca. 20 µm) than Cathode II. Moreover, no homogenous particle size is obtained in Cathode I, probably by the agglomeration of S crystallites. This evidences that the roll mixer disperses the sulfur particles without destroying agglomerates of sulfur or reducing the particle size. On the other hand, the tumbling mixer reduces the sulfur particle to less than 4 µm, and only some larger particles are present.

The insets on the right side of Figure 3.5 (c–f) are the corresponding BSE pictures. Due to the higher atomic weight of sulfur, it is identified in light color. Thus, it can be seen that Cathode II has a surface completely covered by CB particles. Some CB particle seems to be embedded in the sulfur and some wrapped around the sulfur (Figure 3.5 (e,f)). The built CB network and the close contact between the conductive carbon and sulfur are responsible for providing electron pathways for the insulating sulfur. In case of Cathode I, the uncovered area of sulfur particle is higher.

3.2.2 Influence of cathode fabrication on the capacity fading

Figure 3.6 shows the discharge capacity vs. cycle number for Cathode I and Cathode II. Throughout this work, the discharge capacity is based on the mass of sulfur present in the battery. It should be keep in mind, that S represents 50 wt.% of the cathode layer; thus, the specific capacity considering the total mass of cathode is the half.

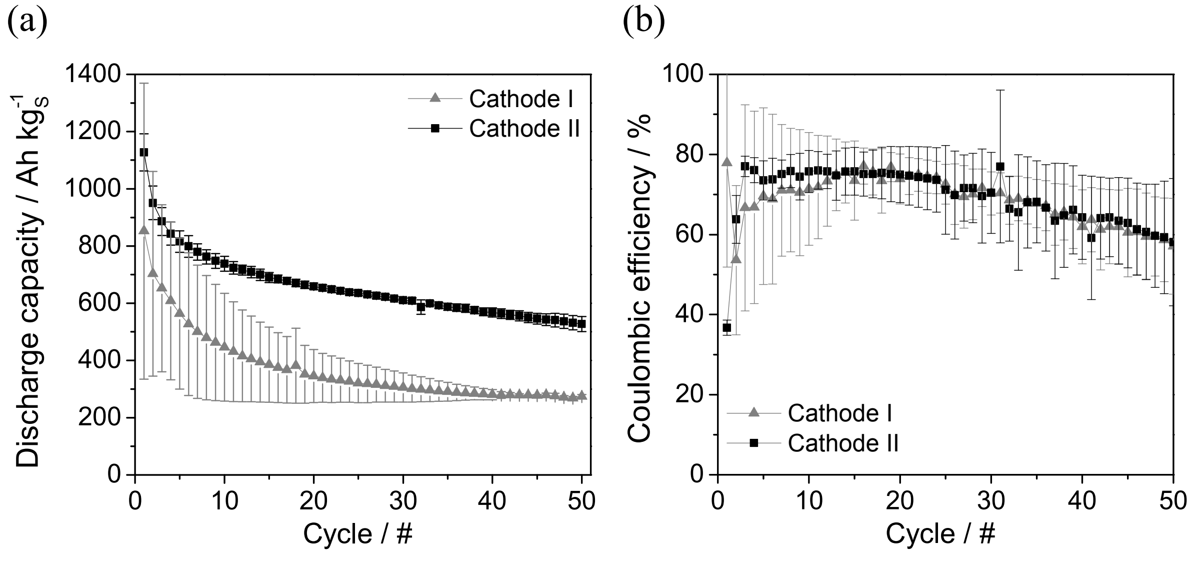

Figure 3.6: Cyclability of batteries using Cathode I and Cathode II. (a) Discharge capacity vs cycle. (b) Coulombic efficiency. The average and error bars are calculated based on the results of 3 tested batteries.

The improved dispersion of S particles, the high contact with carbon black network, as well as the reduction of S particle size, are responsible for the increase in the discharge capacity of batteries fabricated with Cathode II. This is related to the increase of active surface area which allows higher sulfur dissolution and utilization for the electrochemical reactions. Nevertheless, both systems display similar capacity retention. This means that improvements on the cathode morphology do not avoid the degradation of the batteries by mechanisms already described in section 2.1.2, like deposition of isolating products covering the active surface and the shuttle mechanisms occurring in the electrolyte and anode interface.Batteries fabricated with Cathode II have a higher discharge capacity, in the first cycle 850 Ah kg_S^{-1} compared to 1150 Ah kg_S^{-1} for Cathode I. Moreover, the reversible discharge capacity after 50 cycles remains at 528 Ah kg_S^{-1} while for Cathode I is 275 Ah kg_S^{-1}, this represents 32% and 47% capacity retention respectively. The Coulombic efficiency, ratio between discharge and charge capacity (expressed in percentage), is in both cases not stable during cycling with values lower than 100%. The high values of the error bars demonstrate the instability of the batteries due to the charge process.

In Figure 3.7, discharge and charge profiles of the batteries fabricated with Cathode I and Cathode II are displayed. Both discharge plateaus, at high and low voltage, are larger for Cathode II. The charge capacity is in almost all cases higher than the discharge capacity. This is caused by the shuttle mechanism. According to these charge profiles, shuttling effect does not start at the beginning of the charge process. On the one hand, Li_2S is oxidized in the cathode generating long–chain lithium polysulfides and elemental sulfur step by step. On the other hand, polysulfides are reduced chemically on the lithium surface. When the concentration of long–chain lithium polysulfides increases, the shuttle phenomenon is enhanced. Thus, at the high plateau (~ 2.5 V) two processes would be in competition: the electrochemical oxidation of polysulfide on the cathode surface and the chemical reduction of polysulfide on the anode. The active shuttle phenomenon prolonged consequently the charge process, which reduce the cycling performance of the batteries.

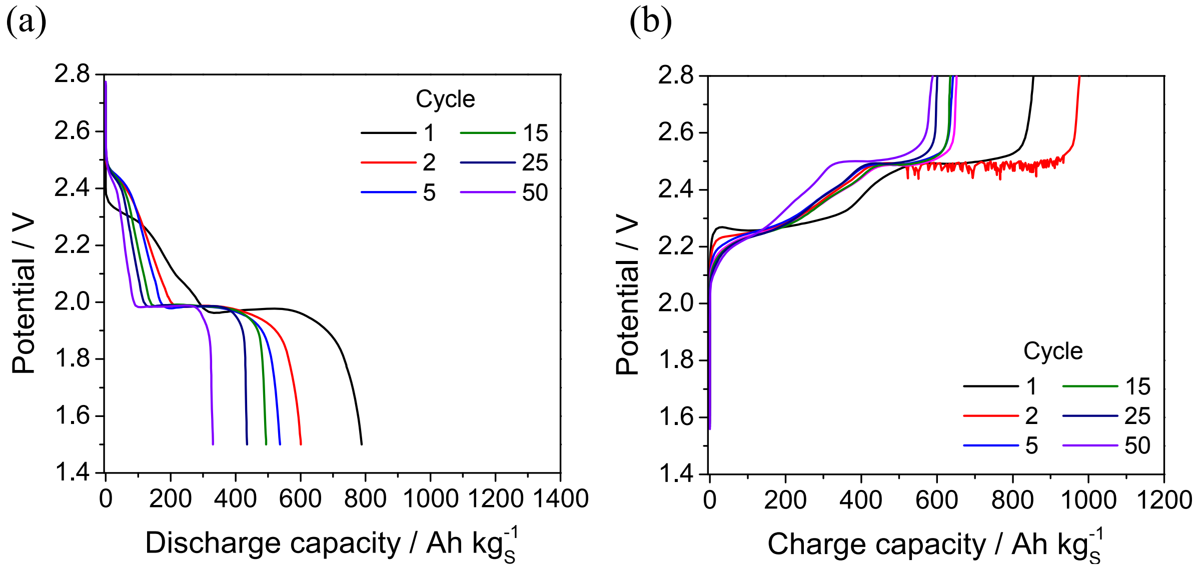

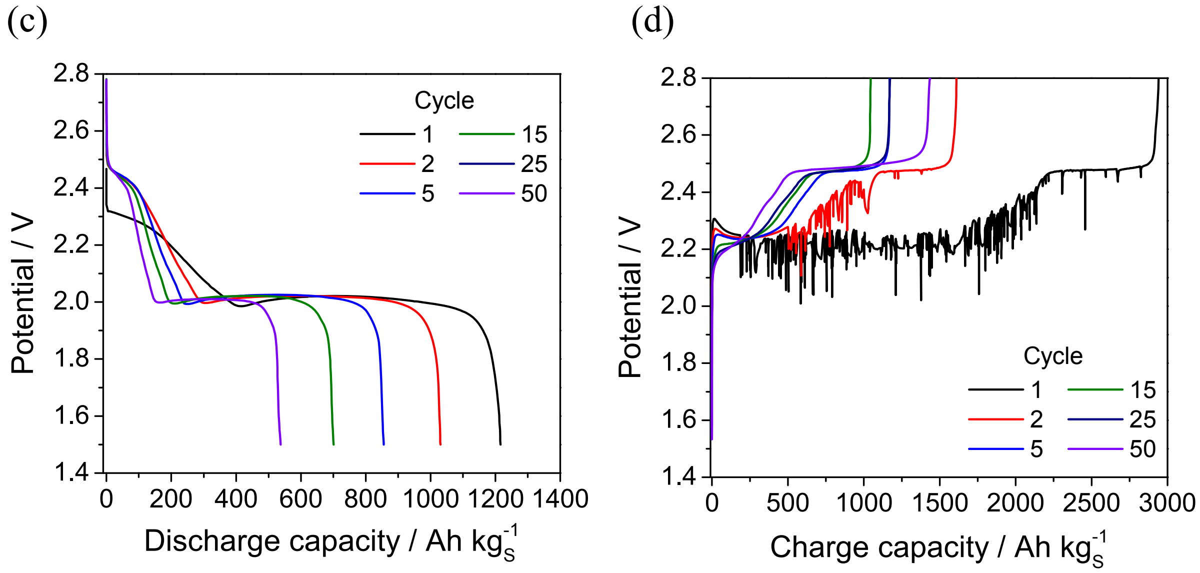

Figure 3.7: Discharge and charge profiles for cathode I (a,b) and cathode II (b,c). Cycling was performed between 1.5 and 2.8 V and current density of 300 A kg_S^{-1} (0.18 C).

Other phenomenon caused by the dissolution of active species is the self–discharge of the cell. The open circuit voltage (OCV) of the cell decreases with the time, as shown in Figure 3.8, and it is stabilized after 30 days at 2.1 V. This happens due to the chemical reaction of dissolved sulfur with lithium metal to form polysulfide: $Li + {}^{x}/_{8} S_8 \rightarrow Li_2S_x$. Similar results were observed by Ryu and colleagues [112], they observed a decrease from 2.54 to 2.08V after 7 days, and then a slower but continuous drop of potential. Moreover, they declared that the self–discharge rate of Li/TEGDME/S battery depends on the materials of current collectors, linking a corrosion of the collector due to formation of polysulfides.

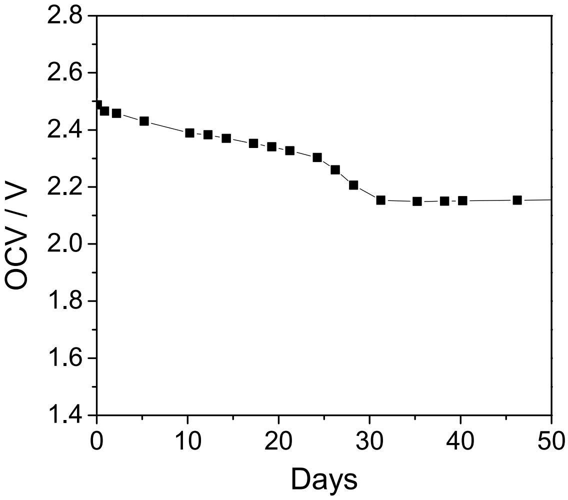

Figure 3.8: Self discharge of Li–S batteries.

The formation of polysulfides cannot be avoided in this type of cell configuration due to the dissolution of sulfur and its diffusion to lithium surface. Self–degradation of the battery should be more influenced by the dissolution of sulfur in the electrolyte. Thus, it is expected that the amount of electrolyte has a higher impact on the self–discharge as well as the collector material.

3.2.3 Influence of $LiNO_3$ as co–salt for the electrolyte

In 2008, Mikhaylik [113] studied the influence of lithium bis(trifluoromethane sulfonyl) imide (LiTFSI) in a 50:50 ratio mixture of 1,3–dioxolane (DOL) and dimethoxyethane (DME) as well as in a solution of trifluoromethyl sulfonate. He postulated that N–O chemical bond was the responsible for inhibition of the shuttle mechanism. To demonstrate this; he tested salts containing the N–O bond like potassium nitrate, cesium nitrate, ammonium nitrate, potassium nitrite, and dinitro–toluene. The highest Coulombic efficiency and discharge capacity upon cycling were achieved with $LiNO_3$ concentrations between 0.2 M and 1.0 M. After this, several studies have shown the benefits of $LiNO_3$ [114–118]. $LiNO_3$ avoids the large charging cycles, increasing the Coulombic efficiency to 100%. This is attributed to elimination of the shuttle mechanisms due to the formation of a “protective” and Li^+ ion conductive layer on the anode surface. This layer is composed of Li_xNO_y and/or Li_xSO_y components [119] which are responsible to prevent the reaction of polysulfides with lithium metal and thus to eliminate the shuttle effect during charge.

In this section, $LiNO_3$ is used as a co–salt in the electrolyte to stabilize the Coulombic efficiency and to increase the cyclability of the Li–S battery. Electrolyte solutions with different $LiNO_3$ concentration (0, 0.1, 0.5, 0.75, and 1 M) (99.99%, Sigma–Aldrich) were prepared. The concentration of $LiPF_6$ was constant at 1 M in TEGDME. The electrolyte components were mixed with a magnetic stirrer for 24 h in the glove box under Ar atmosphere. The results of the electrochemical tests for different concentrations of $LiNO_3$ are summarized in Figure 3.9. The capacity fading[1] is affected by the concentration of the co–salt and reaches a minimum of around 35% for 0.75 M $LiNO_3$ (Figure 3.9 (b)). By further increase of concentration the capacity fading rises again. This last behavior may be explained by the formation of a thicker protective layer on the anode, which reduces the mobility of Li^+, and thus its availability for further reactions. Although the Coulombic efficiency reaches already values near to 100% with 0.1 M $LiNO_3$, by increasing the concentration the Coulombic efficiency is more stable (lower error bars). Considering both the capacity fading and the Coulombic efficiency, the optimal concentration of $LiNO_3$ for this cell configuration is found to be 0.75 M.

---

[1] Capacity fading (%) = (Discharge Capacity$_{(\text{cycle } x-1)}$ −Discharge Capacity$_{(\text{cycle } x)}$)·(Discharge Capacity$_{\text{cycle } x-1)}$) ·

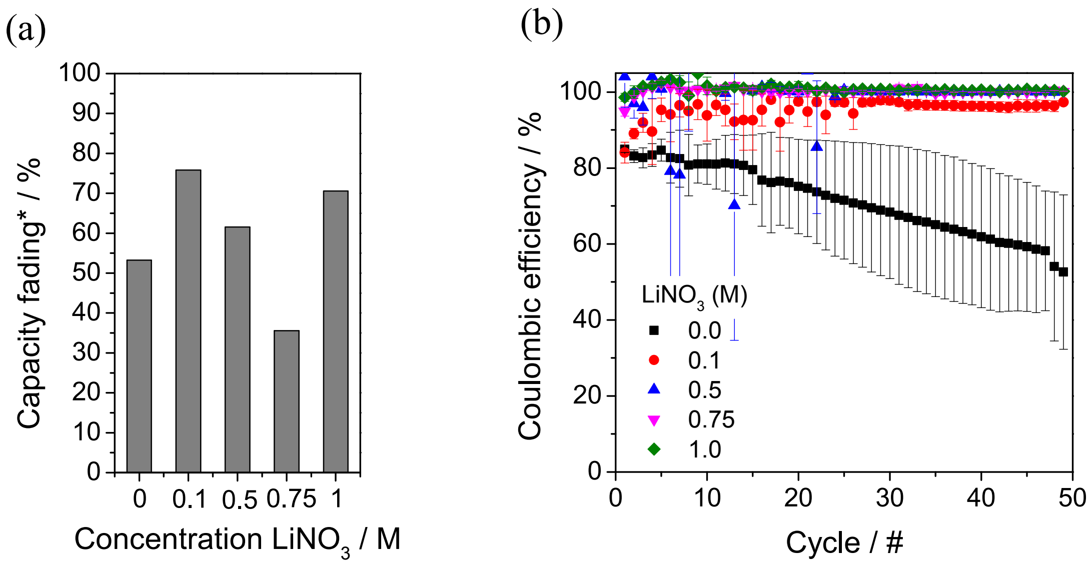

Figure 3.9: Influence of concentration of $LiNO_3$ in the capacity fading of batteries after 50 cycles (a) and the Coulombic efficiency (b). *Calculated between cycle 1 and 50. The average and error bars are calculated based on the results of 3 tested batteries.

In Figure 3.10, the improvements on capacity regarding cathode fabrication (Cathode I → Cathode II) and electrolyte modification (Cathode II without → with 0.75 M $LiNO_3$) are presented.

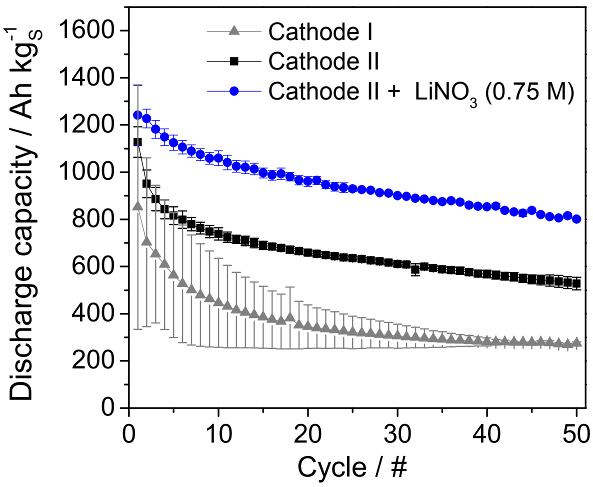

Figure 3.10: Improvements on the cyclability of the cell by modification of cathode and electrolyte. The average and error bars are calculated based on the results of 3 tested batteries.

The reduction of sulfur particle size and its homogenous distribution in the cathode layer influence mainly the initial discharge capacity (852 Ah kg_S^{-1} for Cathode I, 1127 Ah kg_S^{-1} for Cathode II). The co–salt reduces the shuttle mechanism which is reflected by the lower capacity fading and thus a higher capacity at the 50th cycle (527 Ah kg_S^{-1} Cathode II without $LiNO_{3,}$ 800 Ah kg_S^{-1} with 0.75 M $LiNO_3$). Figure 3.11(a) shows the performance of the battery (Cathode II, 0.75 M $LiNO_3$, 1M $LiPF_6$) when discharging at 0.18 C and 2 C up to 1000 cycles. The red inset in the picture shows an example of the variation of the capacity caused by changes in the environmental temperature. The dependency of the capacity with the temperature can be seen in Figure 11.12. The capacity increases 12 Ah kg_S^{-1} per + 1 °C. As expected, the initial values of capacity are much lower for higher C–rate. However, the charge capacity increases in the first cycles reaching it maximum at cycles. This may be explained by the lower dissolution of sulfur at the initial stages of discharge and lower crystallization of Li_2S at the end of discharge. The discharge reaction mechanism includes first the dissolution of sulfur in the electrolyte and second the reaction with Li ions to build up the polysulfides; when the discharge rate is fast, sulfur cannot dissolve completely and lower formation of polysulfides is reached. Moreover, the crystallization of Li_2S is a slower process and this must favored after several cycles when polysulfides have been accumulated in the electrolyte.

For both C–rates the Coulombic efficiency maintains constant confirming that the protective effect of $LiNO_3$ against the shuttle mechanisms prevails up to 1000 cycles. Some investigations have shown that the effect of $LiNO_3$ disappears at higher cycle number [116]; however, this is not observed in the cell tested through this work. After 500 cycles both capacity curves meets and the capacity fading comes independent of the discharge rate. It is expected that inactive cores of S_8 or Li_2S are built up, and lower the utilization of active material in the subsequent cycles. Moreover, according with the similar discharge profile observed in Figure 3.11 (b), the reaction mechanisms at different C–rates seems to be similar after 500 cycles. The first discharge plateau is shorter due to the less amount of crystalline sulfur present in the charge state. Therefore, it is expected that most of the reactions occurs in the liquid phase; this means oxidation and reduction of polysulfides with less formation of S_8 or Li_2S. The difference on capacity for cathode II (Fig. 3.10 and Fig. 3.11), with electrolyte: 0.75 M $LiNO_3$, 1 M $LiPF_6$ in TEGDME, tested at 0.18 C is caused by a difference of sulfur loading (–30% for cahode in Fig. 3.11) because they were coated in different production lots. The standard deviation (average of the first 50 cycles) between both production lots was 59 Ah kg_S^{-1}.

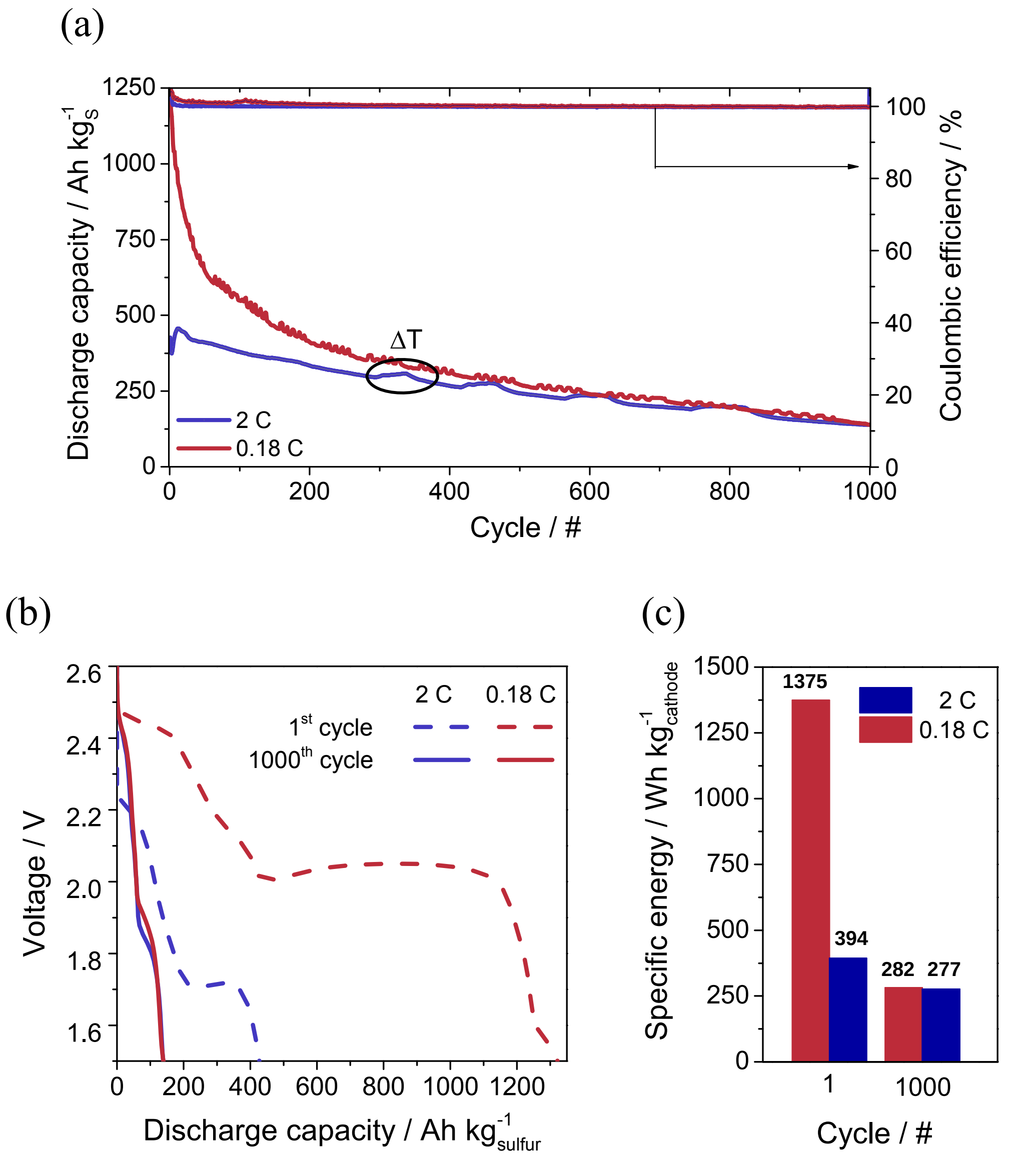

Figure 3.11: (a) Discharge capacity and Coulombic efficiency of Li–S batteries at 0.18 C and 2 C. (b) Comparison of discharge profile between batteries tested at 0.18 C and 2 C. (c) Specific energy density based on the cathode mass for cycle 1, 50, and 1000.

The average energy density of the cell calculated based on the total mass of cathode, is presented for cycle 1, and 1000 in Figure 3.11 (c).

3.3 Conclusion

The use of wet–powder spraying allows the fabrication of homogenous sulfur–composite layers. However, the use of large amount of solvents is a disadvantage, and a solvent recuperation system should be implemented for industrial applications.

Improvements on the mixing and milling processes showed that well–dispersed and small sulfur particles, surrounded by CB particles, improves the sulfur utilization during the first cycles, which results in an increased of battery performance from 275 to 528 Ah $\mathrm{kg_S}^{-1}$ after 50 cycles. Nevertheless, the capacity fading of the battery is still high (47 %) and it is caused among others by the low Coulombic efficiency generated by the shuttle mechanisms. This can be improved by the utilization of $LiNO_3$ as co–salt in the electrolyte. With this electrolyte additive and cell configuration discharge capacities of 800 Ah $\mathrm{kg_S}^{-1}$ were achieved (after 50 cycles, 0.18 C–rate). However, the capacity fading of the battery is still high (35% between the 1st and 50th cycle). This simple but industrially viable cell configuration can be further improved by the use of protective layers and electrolyte additives [45,51,114,120–122]. In the next chapters, the processes responsible for the degradation of the battery will be studied.

4 *In situ* X–ray diffraction

XRD is an important characterization method to follow structural and composition changes occurring in battery electrodes. This technique can be applied *in situ* or *operando*, this means that measurements are performed under operating conditions of the electrochemical cell, without exposure to the external environment. In the past, *in situ* XRD experiments were already performed successfully on lithium–ion batteries, bringing new insights into the lithium intercalation process [123–127]. However, there has been little application of this method to Li–S batteries to evaluate the crystalline reaction products S_8 and Li_2S [82,128]. On the contrary, many groups studied the Li–S system by carrying out *ex situ* measurements [44,61,63,114,129,130]. They evidenced the reduction of sulfur to polysulfides and the formation of Li_2S at the end of discharge [61,63], but until the date it was not clear if Li_2S converts back to soluble polysulfides in the following charge step or if it becomes inaccessible due to its isolating properties after the first discharge. Moreover, no information about the rate of formation was available. Nelson and colleagues [128] carried out the first *in situ* XRD study of Li–S batteries throughout the entire first cycle of the battery. They detected the reaction of sulfur during discharge and its recrystallization during charge; nevertheless, the formation of the discharge product Li_2S was not detected.

It is important to highlight that the high reactivity of Li_2S is a problematic issue during measurements, because it hydrolyses easily in air, producing H_2S and LiOH. Probable reasons why Li_2S may not be detected are: a) the *in situ* cell is not air–tight, b) the discharge capacity of the cell is too low, Li_2S does not precipitate and only soluble polysulfides are present at discharge state, or c) the penetration depth of the X–ray is not high enough and the structural information comes from a deeper region of the bulk cathode material. If this occurs, no information is obtained from the interface cathode/separator, where probably the main quantity of Li_2S is formed.

In this chapter, the reactions of crystalline phases in the Li–S battery were monitored for the discharge and charge process using *in situ* XRD. The dissolution and reaction of sulfur during discharge, as well as its recrystallization during charge were followed. In contradiction to the results presented by Nelson et al. [128], it was found that lithium sulfide does build up during the first discharge cycle and reacts back in the following charge. In addition, this work is complemented with semi–quantitative analysis of the crystalline species, the Rietveld refinement of the spectra, and 2D mapping of the cathode. Most of the results presented in this work were published in the Journal of Power Sources [6].

Sulfur and its allotropes

Sulfur is the element with the largest number of solid allotropes; around 30 allotropes were already identified. In general they consist of cyclic molecules without ramifications and with ring sizes of 6 to 20 atoms. In addition, sulfur can be polymeric when long S–chain are conformed in random coils or helical conformation [131]. The stable form of sulfur at standard conditions for temperature and pressure is the orthorhombic α–S_8 modification (space group 70). The octamers are organized in two layers each perpendicular to the crystal c axis forming a so called “crankshaft structure”. At around 96 °C α–S_8 transforms reversibly to monoclinic β–S_8; this is stable up to ~120 °C (melting temperature) [132]. The phase diagram of sulfur can be seen in additional information (Figure 11.13).

4.1 Experimental procedures

4.1.1 Design considerations for *in situ* X–ray cells

An *in situ* or also called *operando* analysis of a battery refers to the characterization of one or more of its components using a spectroscopic or microscopic technique under potential or current control, e.g. during discharge or charge. For *in situ* XRD measurements, an *in situ* cell is necessary, where the battery is placed and connected to a potentiostat for electrochemical measurement. Moreover, the *in situ* cell has to enable XRD analysis without dissembling the cell. Its fabrication approach depends on the battery technology to be considered (aqueous vs. non–aqueous batteries), the type of X–ray sources (X–ray spectrometer vs. synchrotron sources), and the type of collecting modes (reflection vs. transmission modes). For the assembling of the cell and selection of the main components, the following aspects have to be considered:

- An X–ray transmission window is necessary; the X–ray must be transmitted through a window into the material to be analyzed, then reflected and transmitted back to the detector. A suitable material for this purpose must be not only mechanical robust but also chemical stable in order to protect the sample and avoid undesirable reactions. To avoid peak overlapping, it is preferable that the hkl–peaks of the window´s material are not present in the same region of the spectra where peaks of the sample appear. Beryllium is one of the most used materials as window for *in situ* XRD cells. Nevertheless, it can be dangerous by studying of highly oxidizing compounds, for example with materials operating at potentials greater than 4.2 V vs. Li metal. Be–windows oxidize and become porous at such high operating voltage. Mylar (Polyethylenterephthalat) is an alternative material due to its high stability and high transmission of X–rays. Aluminum foil is advantageous for investigation of components at low theta–angle, where no peaks of aluminum can interfere with the sample peaks.

- Cell has to be hermetic (air–proof). Because of the high reactivity of Li and some Li–based components mainly with water and air, measurements must carry out in a moisture– and oxygen free environment. Gaskets are normally used to prevent electrical contact and ensure a hermetic seal.
- The cell should be friendly to use. The assembly of batteries occurs in the glove–box; for this reason it is important that the active materials are easy to load in the cell. The *in situ* cell must be easy to tight, to align on the diffractometer´s sample holder, and also to dismantle and clean.
- Electric contact to control the current and potential are necessary for both electrodes. Aluminum is used often as cathode collector, when measurements on reflection mode are carried out due to the low absorption of X–rays. When analysis through all battery components are carried out on transmission mode, copper and nickel can be used as anode collector. Nevertheless, they show higher absorption. In case lithium is used as anode (low X–ray absorption), this can be used at the same time as collector.

4.1.2 In situ cell

An *in situ* cell was specially built up for the continuous collection of diffractograms during electrochemical test of the battery. For the design, the fabrication aspects described in above were considered. An exploded illustration of the cell components is shown in Figure 4.1. The cell consisted of two holed aluminum plates, the cathode plate with a thin aluminum window, and the anode plate. A 6 µm thick aluminum foil was chosen as X–ray window and fixed onto the cathode plate with a conductive epoxy. Although a thicker Al–window is more stable, the X–ray absorbance is too high, decreasing the intensity of the Bragg peaks of the active materials. Each plate (component 1 and 9 in Figure 4.1.) acts as electrode collector and is connected directly to the potentiometer using banana jacks connectors in the hole located on the side of each plate. A tube made of polyether ether ketone (PEEK) was placed in the middle (component 3) to insulate electrically the battery from the interior walls of the cell. A 0.75 mm thick polymer gasket is positioned between the two plates to seal the cell airtight. This avoids also a short circuit between both electrode plates. A metal spring inside the cell applies mechanical pressure of the stack (see components 5–8, Figure 4.1) against the Al–window. The combination of a thin X–ray window and a thin cathode layer (~ 20 µm) allows to obtain information of the entire cathode´s volume located between collector and separator.

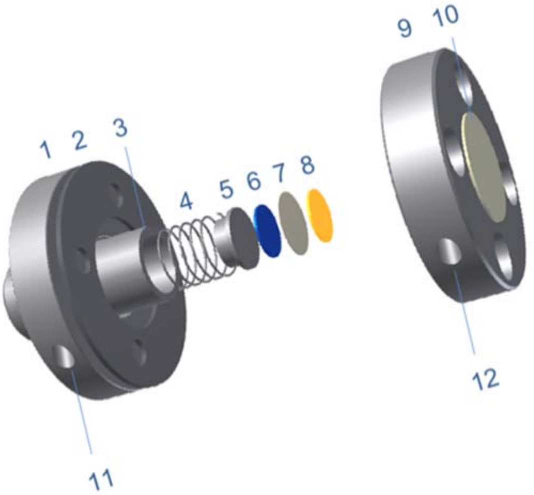

Figure 4.1: Exploded illustration of the *in situ* XRD cell. Components: 1) Anode plate, 2) polymer gasket, 3) insulator plastic tube, 4) spring, 5) stainless steel anode collector, 6) anode, 7) separator, 8) cathode, 9) cathode plate, 10) Al–window, and 11–12) holes for connecting the banana jacks.

The battery was assembled in the glove box under Argon atmosphere. The 1.5 mm thick lithium anode (99.9%, Sigma Aldrich) was placed on a stainless steel disk over the spring. The separator, a 25 µm thick polypropylene microporous membrane (Celgard 2500), was set on top of the anode and soaked with 14 µL electrolyte, 1 M $LiPF_6$ (99.99%, Sigma Aldrich) in TEGDME (99.9%, Sigma Aldrich). The cathode was then placed on the separator. The cell–stack was positioned in the *in situ* cell and this was finally closed with plastic screws. The diameter of the lithium foil and cathode was 10 mm, while the separator diameter was dimensioned 2 mm larger to avoid short circuit.

4.1.3 Electrochemical test and configuration of diffractometer

The cycling performance of the battery was investigated using an electrochemical workstation (Zahner IM6) with cycling software (Zahner Thales) [13]. The charge–discharge procedure was carried out galvanostatic at a current density of 300 mA g_{sulfur}^{-1} between 2.8 V and 1.5 V.

X–ray diffractograms were recorded with an X–ray diffractometer, D8 Discover Bruker GADDS, equipped with a VÅNTEC–2000 area detector (Figure 4.2). Exposures were made on reflection mode using a tuned monochromatic and parallel X–ray beam (Cu–K_{α}). The tube collimator aperture was 1 mm. The X–ray source was filtered by one Göbel mirror and two pinhole collimators. The accelerating voltage was 45 kV and the tube current was 0.650 mA. Each diffraction pattern was measured in four frames with a step size of $2\Theta = 23°$, starting with $\Theta_1 = \Theta_2 = 12°$ (Bragg–Brentano condition). The exposure time for each frame was 180 s. A script was written in order to record the diffractograms continuously.

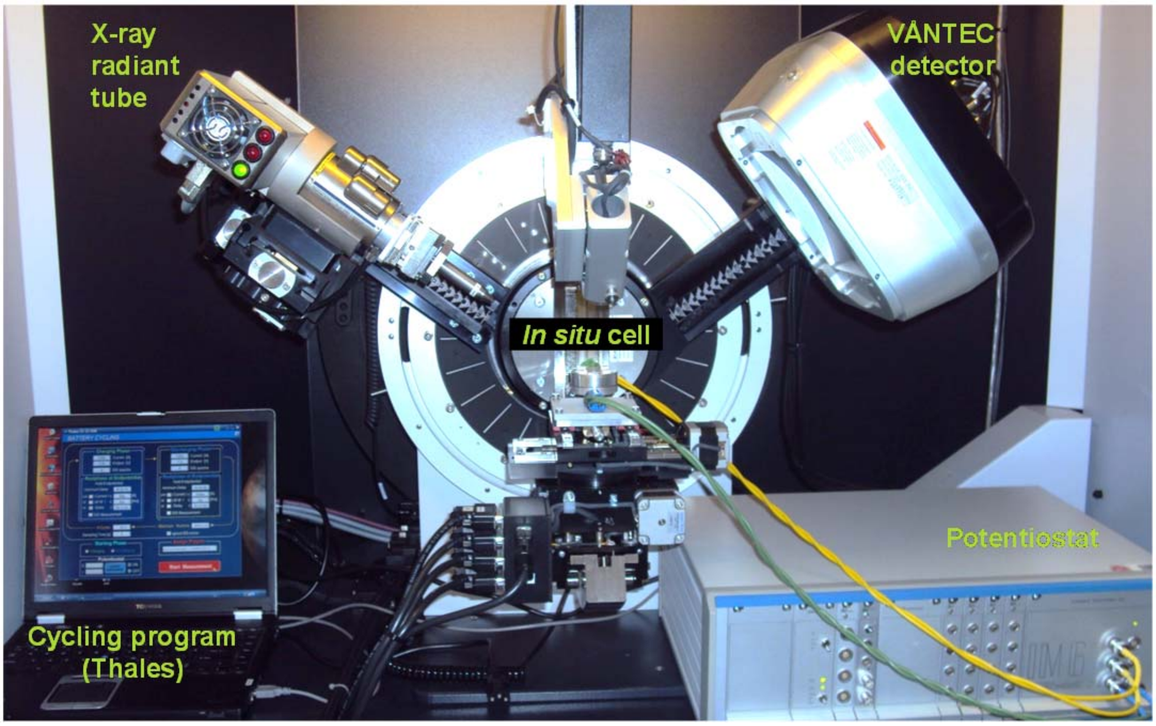

Figure 4.2: Configuration of the *in situ* XRD experimental set–up. The radiant tube and the VÅNTEC detector are shown. The *in situ* cell is mounted on a motorized goniometric head and connected to the potentiostat, in which the electrochemical experiment is controlled by the cycling program (Thales).

The *in situ* cell was placed on the sample stage as shown in Figure 4.2 and connected to the potentiostat. The cell starts to discharge at the same time as the first frame of the diffractograms is taken with XRD. Twelve minutes were required to record each *in situ* XRD pattern and the measurements were performed without interruption until the end of each cycle. For this reason the XRD pattern represents averaged values of the reflected X–ray during the exposure time.

4.1.4 Rietveld analysis

Phase analysis

The refinement of the crystalline phase was made with the software Diffracplus Topas 4.2 [133]. Before starting the refinement, the instrument contributions were discriminated. The instrumental function was calculated based on the measurement of a well crystallized specimen, in this case, α–Al_2O_3. Additional convolutions were selected to parameterize the profile shape with different Lorentzian and Gaussian functions (see Table 1). After, the instrument function was fixed and the refinement of the sample could be started. First, the background function was determined. The active materials were fitted with structural information obtained from the Crystallography Open Data Base (COD) (COD ID: 9011362 [134], COD ID: 9009060 [135]) whereas the inactive components such as C, PP–separator, and Al–substrate were fitted with Pseudo Voigt (PV) functions (peak phase analysis). The following parameters were sequentially fitted: scale (intensity), crystalline size, and lattice parameters (a,b,c).

Quantification of amorphous phase

The quantification of the amorphous phase was determined by combining a refinement of the crystalline phase with a single line fitting for the amorphous phase. The background is fitted with a 1st order function and the amorphous phase is fitted with a single Split–PseudoVoigt function (spv) located at the maximum of the amorphous bump. The sequence of refinement was first the large amorphous bump; second, the high intensity reflections of crystalline peaks; and final, the smaller reflections.

4.2 Results and discussion

4.2.1 Diffractograms of cathode components

XRD patterns of raw powders of sulfur, CB, PVDF, and sulfur are presented in Figure 4.3 as comparison basis for the diffractograms measured of the cathode. Sulfur pattern corresponds to the pattern of α–S_8 face centered orthorhombic sulfur (PDF: 00–008–0247).

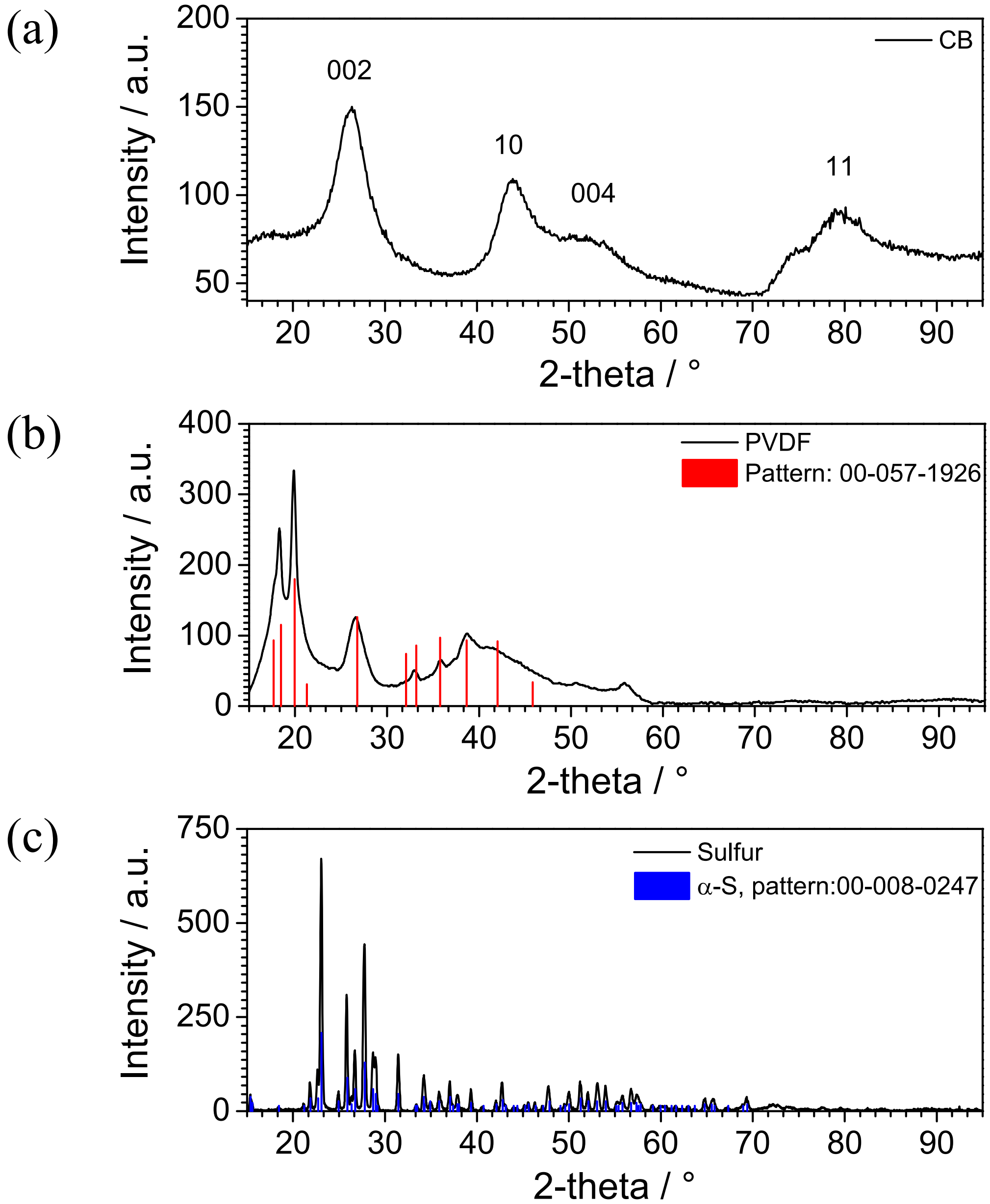

Figure 4.3: Diffractograms of the raw materials as powder: carbon black (a), PVDF (b) and sulfur (c).

Carbon black consists of parallel layer groups with 4 or 5 roughly parallel graphite layers. According to Warren [136], the distance between parallel layers L_c is in the order of 12 Å, while the normal to layer L_a 20 Å. Carbon black pattern consist of the *(00l)* crystalline reflexions (002) at $2\Theta = 26^\circ$ and (004) at $2\Theta = 51^\circ$, and the 2 dimensional *(hk)* reflexions *(10)* at $2\Theta = 44^\circ$ and *(11)* at $2\Theta = 74^\circ$. While the *(00l)* reflections evidence that several graphite layers are roughly parallel, the two dimensional lattice reflections are originated by randomly oriented graphite layers.

Two dimensional reflections are characterized by asymmetric shapes of peak that sharply increase of intensity like a crystalline peak and then decrease their intensity slowly in form of a shoulder. The sharpening of reflections is related with an increase of size of the parallel groups. This has been already observed after heat treatment of CB [136]. After cathode preparation only a sharp peak at 2Θ = 24° is observed. This reflex is correlated with carbon, and assumed to be of the type *(00l)*, meaning that graphite layers of CB lie near parallel to one other after cycling.

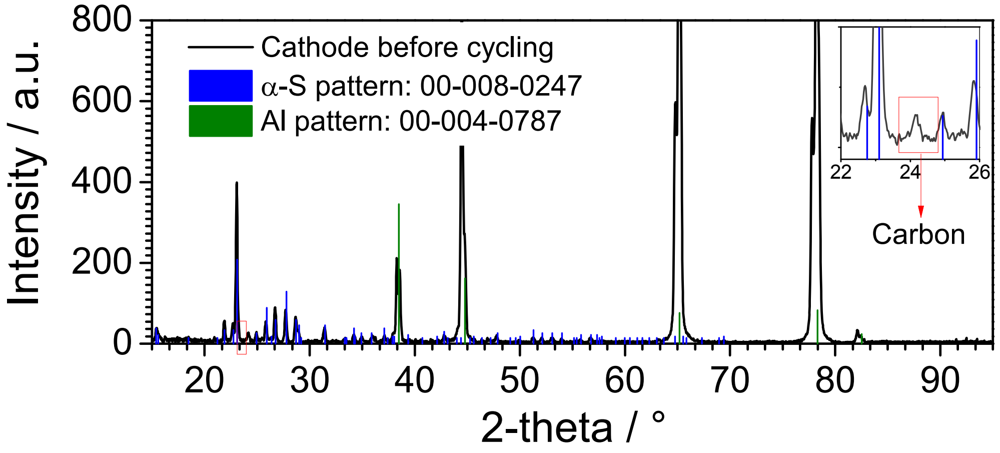

Figure 4.4: Diffractogram of the cathode before cycling. The aluminum reflexes correspond to the aluminum collector.

The crystalline peaks corresponding to the PVDF powder disappears after cathode preparation, because after dissolution with solvent, PVDF form thin amorphous films.

4.2.2 *In situ* XRD during the first cycles

First discharge

Figure 4.5 shows the X–ray patterns measured during the first discharge at different depths of discharge (DOD). On the top of the curve, the discharge profile is displayed; each point corresponds to a diffractogram on the main figure. Thereby, only the range where the main reflections of the active components appears is shown (2θ = 20° – 35°) and here the background of the diffractograms was eliminated for better visualization. The progression of discharge is plotted from the top to the bottom. The complete measured diffractograms can be seen in Figure 4.8. Here the reflections of the PP–separator 040 and 130 can be seen at 17° and 18° respectively (PDF: 00–054–1936 [137]). This is noteworthy because it means that the cathode was radiated through its whole thickness. The Bragg peaks of sulfur can be clearly detected in the first diffractogram. As expected, the structure of sulfur is orthorhombic face centered, which is the stable modification of sulfur below 96 °C [138] (PDF: 00–008–0247). The reflection at 2θ = 24° is related to carbon black.

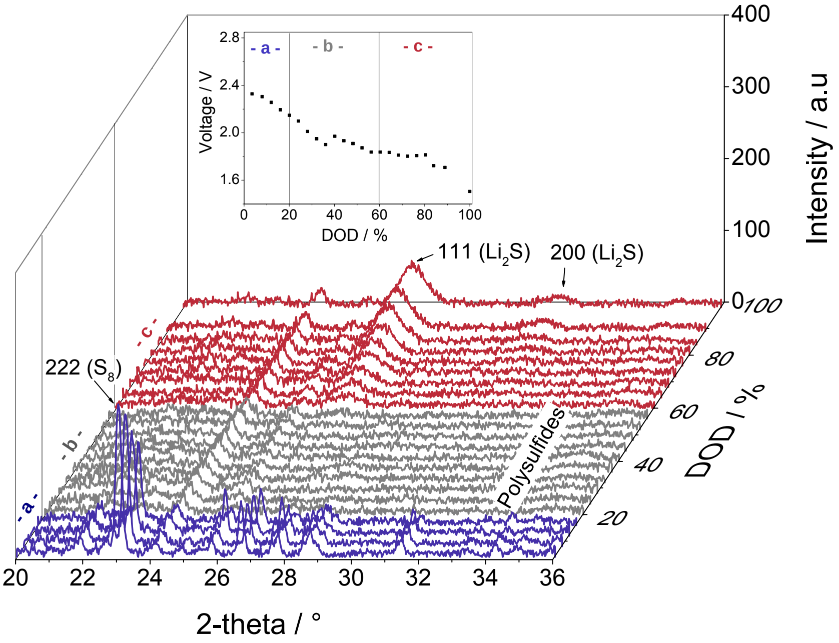

Figure 4.5: ***In situ*** **XRD data collected during discharge of Li–S battery at a rate of 300 A kg_s^{-1} (0.18 C). Background was subtracted for clarity, original XRD diffractograms can be seen in Figure 4.8. Three different regions are shown: (a) reaction of sulfur to high order polysulfides (blue), (b) reactions of high order polysulfides (gray), and (c) formation of Li_2S (red). The discharge curve is shown on the top. The average discharge capacity is 1276 Ah kg_S^{-1}.**

According to these measurements, the corresponding discharge curve in Figure 4.5 can be divided in three periods: (a) between 0 and 20%, DOD crystalline sulfur is detected and its peaks intensities gradually decrease, (b) between 20 and 60%, DOD no crystalline phase of the active material is detected, and (c) between 60 and 100%, DOD Li_2S built up progressively. During stage (a), the upper plateau region; sulfur successively dissolves and starts to reduce to high order polysulfides. At the beginning of the discharge step, sulfur is mostly in the $S_{8(s)}$ crystalline phase due to its low solubility in TEGDME. The dissolution of sulfur in TEGDME can be calculated according to equation of Sciamanna et al. [139]: wt.% of sulfur = exp [–10.994(T_m/T) +12.584). Thus, the solubility of sulfur at room temperature is 0.19 wt.%. Although, the value is low, the weight relation between the sulfur present in the cathode and the electrolyte is also low. This means that at the beginning 18.4% of sulfur is dissolved. As the discharge proceeds, the dissolved $S_{8(diss)}$ in the electrolyte is consumed by the electrochemical reaction $2Li + S_{8(diss)} \rightleftarrows 2Li^+ + S_{8(diss)}^{2-}$; the concentration of $S_{8(diss)}$ decreases, enhancing further dissolution of crystalline sulfur into the liquid phase

[140]. In the interval between 20% and 60% DOD no diffraction peaks of active phases are present. The diffraction peaks abruptly disappear at 20% DOD because of the dissolution of sulfur and the formation of high order polysulfides. During this period it is expected that the concentrations of $S_{8(diss)}$, ${S_{8(diss)}}^{2-}$, ${S_{6(diss)}}^{2-}$ and ${S_{4(diss)}}^{2-}$ decrease and the reduction of the polysulfides down to ${S_{(diss)}}^{2-}$ starts. From 60% DOD on, Li_2S diffractions peaks are detected for the first time and their intensity increase continuously until the end of discharge. Li_2S has a cubic face centered structure (PDF number: 00–023–0369). The peaks are broad, e. g. 111–peak has a full width at high maximum (FWHM) of 0.904 ° ± 0.027 °. Broad peaks signalize clearly the presence of nano–sized crystallites. The analysis of Li_2S is difficult when the volume fraction is low, because the broad peaks are not well distinguishable from the background of the diffractogram and the reflections cannot be accurately quantified. Considering this, the precipitation of $Li_2S_{(s)}$ may start at a lower rate than 60% DOD, even though no crystalline phase is observable in the XRD pattern.

First charge

The X–ray patterns measured during charge are displayed in Figure 4.5. Right after the battery starts to charge, Li_2S reacts back to high order polysulfides. The progress of the reaction can be followed with the continuous decrease in intensity and area under the 111–reflection of Li_2S.

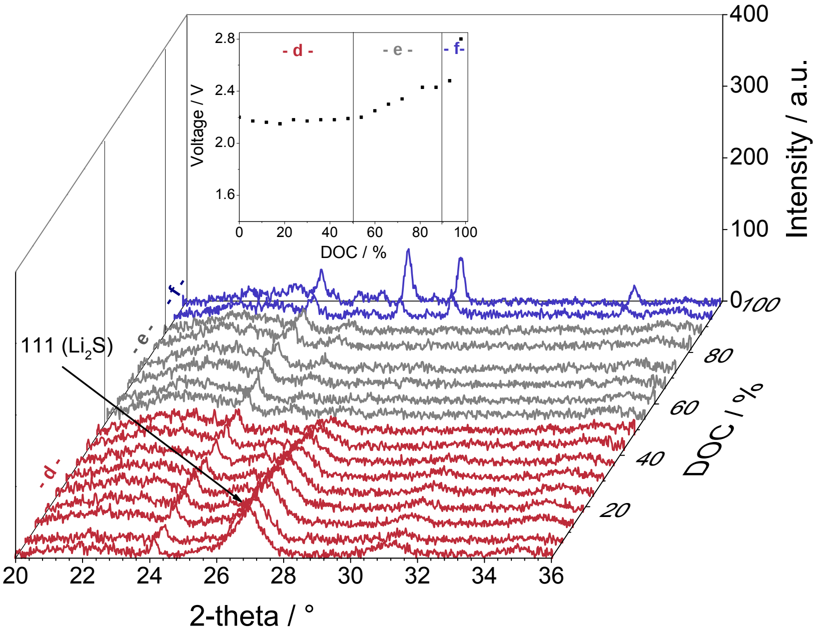

Figure 4.6: *In situ* XRD data collected during charge of Li–S battery at a current density of 300 A kg_S^{-1} (0.18 C). Three different regions are shown: (d) reaction of Li_2S (blue), (e) reactions of high order polysulfides (gray), and (f) formation of sulfur (red). The charge curve is shown on the top. Charge capacity: 1283 Ah kg^{-1}.

Mainly the reverse reactions (2.13)–(2.12) are expected to occur during this period. At around 50% depth of charge (DOC), the reflections of Li_2S are no longer detectable. Between 50 and 95% DOC no crystalline active phases are found. Here, high order polysulfides are formed and dissolved in the electrolyte according to reverse reactions ((2.12)–(2.9)).

New Bragg peaks related to the formation of crystalline sulfur appear up to 95% DOC. Nevertheless, the position and relative intensity of the reflections changes respect to the spectra before cycling, e.g, the 222–reflection of S_8, identified before cycling, cannot be detected after the first charge.

Second discharge and charge

During the second cycle (Figure 4.7) the crystalline products S_8 and Li_2S are also detected, reacting completely during discharge and charge respectively. Nevertheless, the intensity of reflections is lower with respect to the first cycle and the increase of the amorphous phase can be clearly seen between 20°–24°.

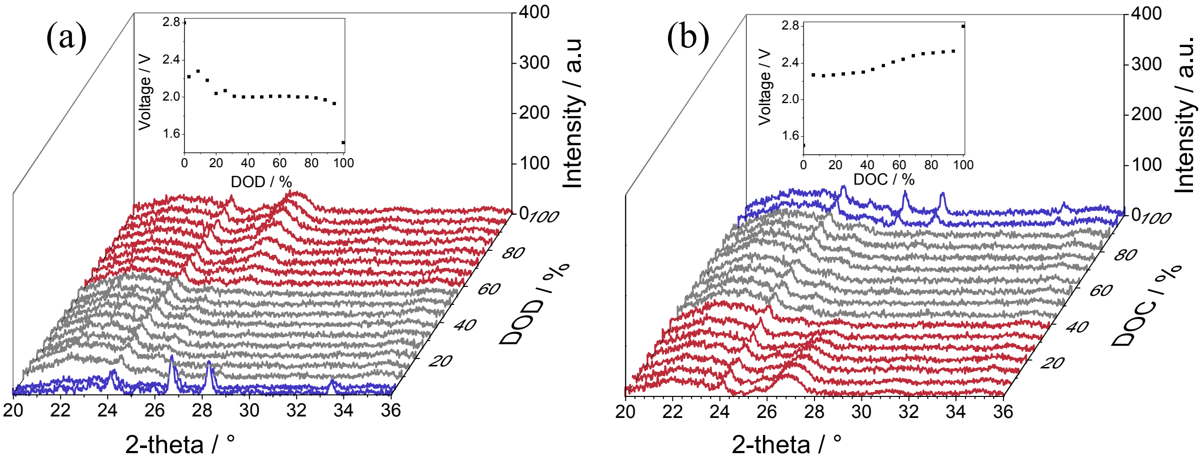

Figure 4.7: *In situ* XRD data collected during the second cycle. (a) 2^{nd} discharge and (b) 2^{nd} charge of Li–S battery at a current density of 300 A kg_S^{-1} (0.18 C).

The *in situ* measurement was carried out in a specific position of the sample with a tube collimator aperture of 1 mm. Therefore, an inhomogeneous growth of crystallites in the cathode could not be detected under these measurements conditions. For this reason, a XRD mapping of the cathode was carried out before cycling and at different cycle number to study the distribution of sulfur in the electrode (section 4.2.3).

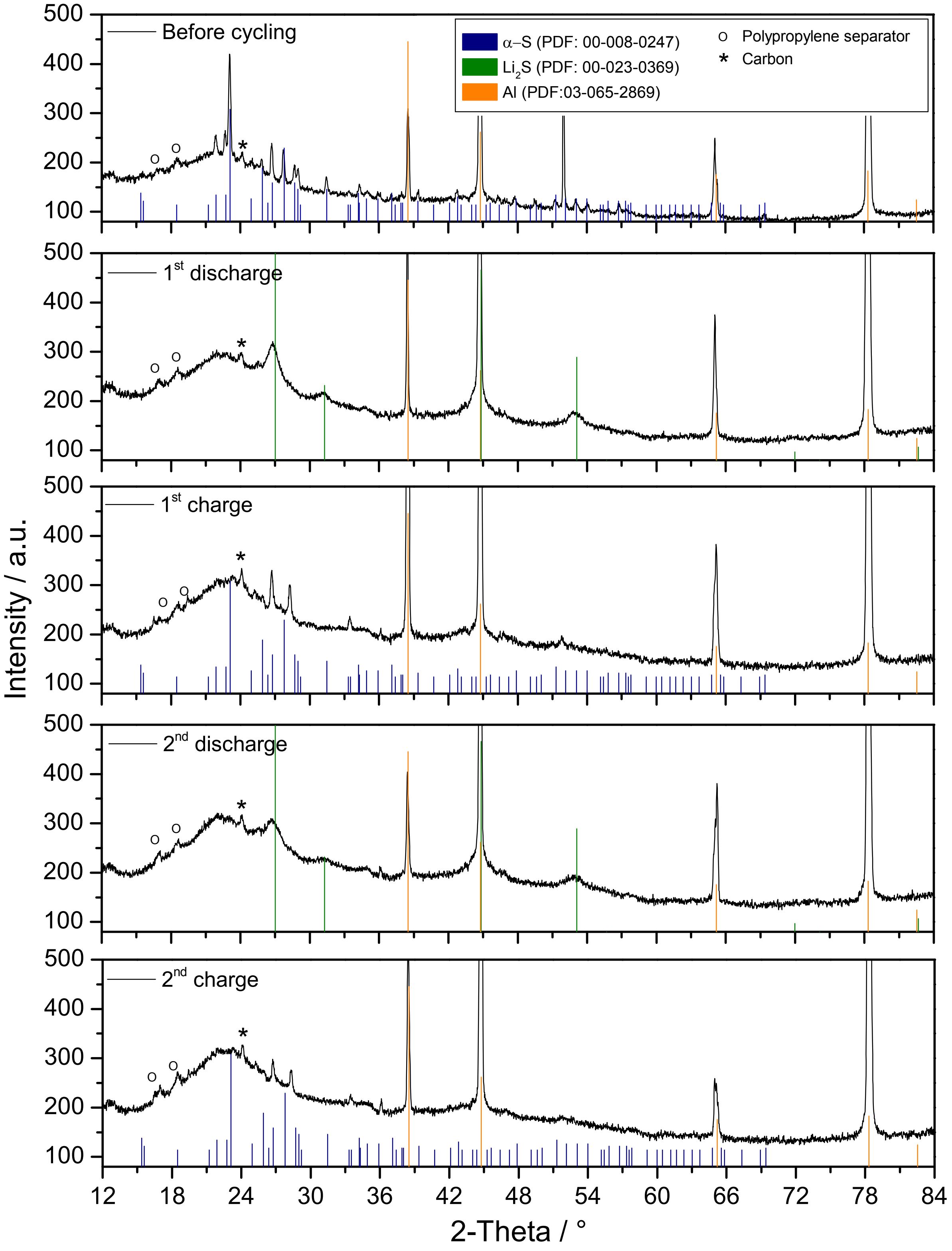

Figure 4.8: ***In situ*** **XRD data collected before cycling, after the 1st discharge, after the 1st charge, after the 2nd discharge, and after the 2nd charge.**

4.2.3 Structural mapping of cathodes

A schematic view of the raster grid for the XRD mapping is shown in Figure 4.9. Here the beam spots are illustrated as circles, although in reality they are elliptical and their size depends on the θ incident angle. The cathode was measured in 13 positions and during the measurement the sample stage oscillated in 0.5 mm XY to obtain higher statistic information of the sample. In Figure 4.10 the integrated area of the sulfur reflexes are represented in the 13 positions of the cathode. The distribution of sulfur is inhomogeneous and the highest amount is located in the center of the cathode, in the side positions almost no crystalline sulfur was measured.

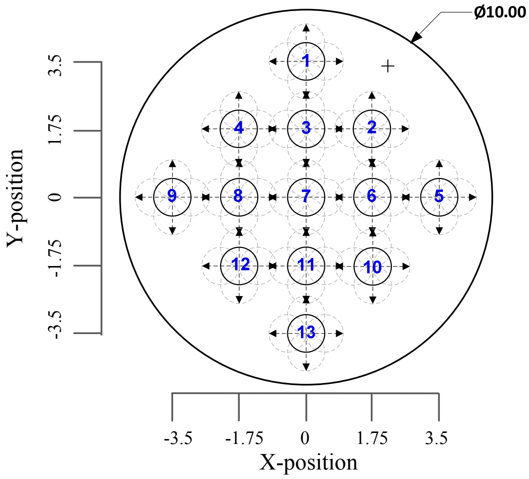

Figure 4.9: Schematic raster grid for analyzing 10 mm diameter cathodes. 13 target positions were selected.

Before cycling, the cathode shows a homogenous dispersion of sulfur, this is illustrated in Figure 4.11 for the raster position 1, 3, 7, 11, and 13. This implies that through the selected mixing procedure the cathode components are well mixed and that the coating procedure generates cathode with uniform thickness. In contrast, cathode after cycling show an inhomogeneous distribution of sulfur which is reflected by changes in the intensity of the reflections. Moreover, variation in the position of the peaks reveals changes of the orientation of the sulfur crystallites in different location of the cathode.

The inhomogeneous distribution of sulfur in the cathode has been also confirmed by microscopic pictures of the electrode after charge (see Figure 11.7 and Figure 11.8).

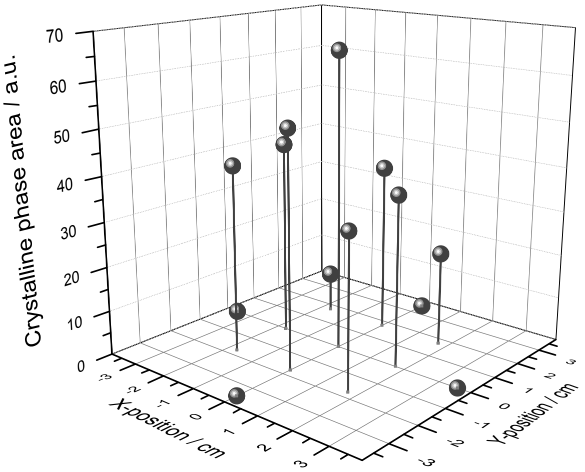

Figure 4.10: Spatial distribution of the sulfur crystalline phase after charge (1st cycle).

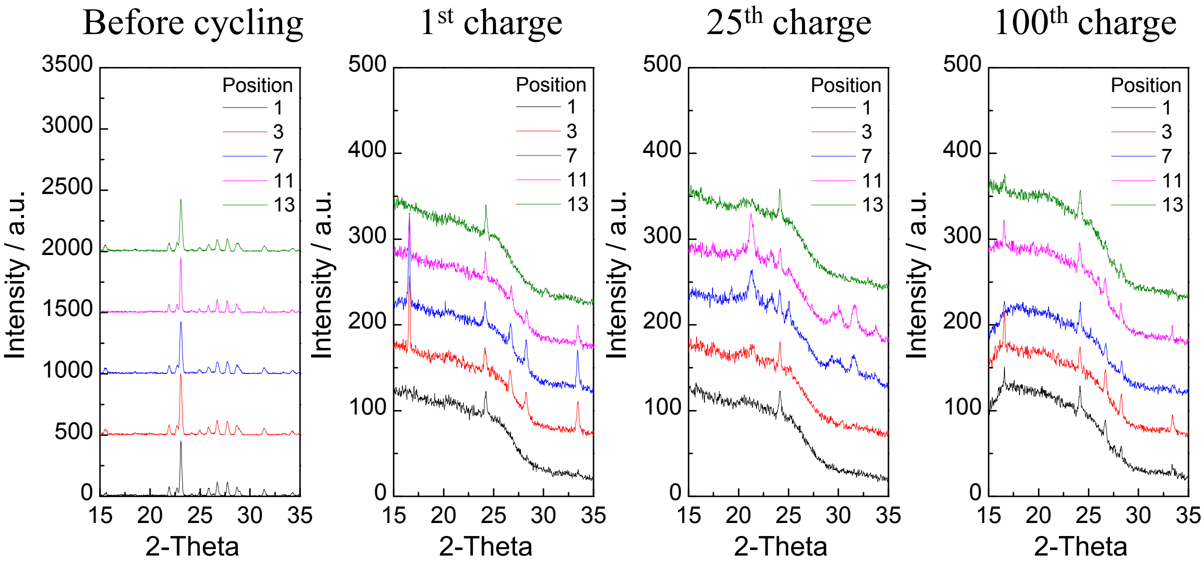

Figure 4.11: Diffraction data of the cathode before cycling, after the 1st, 25th, and 100th cycle for the positions 1, 3, 7, 11 and 13.

4.2.4 Rietveld refinement of diffractograms

Rietveld analysis was used to gain more information about the structural properties of the active components. Figure 4.12 illustrates the *in situ* measured and calculated diffractograms before cycling (a), after the first charge (b), and after the first discharge (c). Only diffractograms of the active phases (sulfur and Li_2S) are shown. The reflexes of the other cathode components were fitted as a peak phase (i.e Al at 2θ = 40° and 47°). According to the changes in the position and intensity of the reflections, only some planes of sulfur can be seen in the diffractograms after cycling.

This is related to a preferred orientation of the particles in the cathode during charge. Calculated structure parameters are summarized in Table 4.

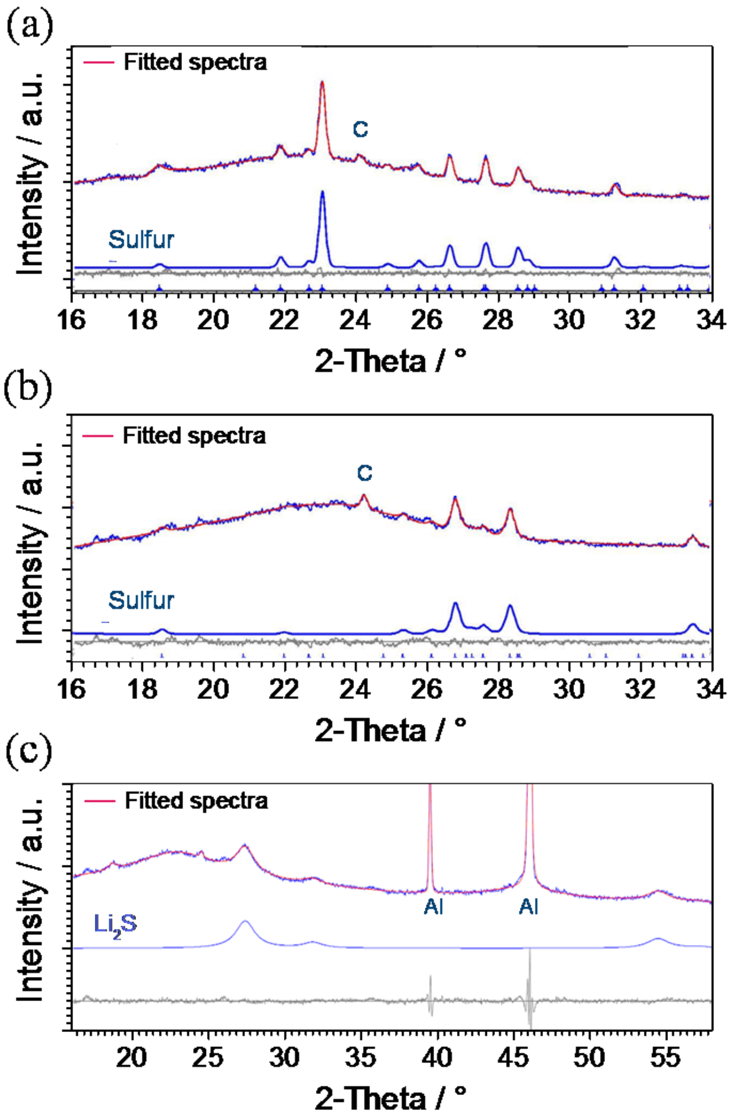

Figure 4.12: Measured and refined diffractogram for cathode before cycling (a), after 1st charge (b), and after 1st discharge. The subtracted curve between measured and calculated diffractogram is the grey curve in the bottom).

The orientation of sulfur crystallites was also observed by *ex situ* SEM measurements of the cathode and separator surface after charge (Figure 4.13). Here, two different sections of the separator surface are displayed from the cathode side after cycling and cell dissembling. Figure 4.13 (a) shows sulfur agglomerates over the separator (cathode side). These agglomerates consist of needle shaped particles not larger than 2 µm (Figure 4.13 (b)), which seems to be aligned perpendicular to the separator surface (Figure 4.13 (c)). In some areas sulfur needles are disordered and the form of the particle can be clearly identified (Figure 4.13 (b)). Additionally, some amorphous material can be seen in the right side of (Figure 4.13 (b)). The small sized crystallites allow them to growth up throughout the separator as it can be clearly seen in Figure 4.13 (d). Some sulfur crystallites were found to be arranged in large agglomerates over the cathode surface (Figure 4.13 (e)).

Table 4: Structure parameters refined with Rietveld–method for diffractograms before and after cycling: crystallite size, cell volume, and lattice parameter a, b, c, for the orthorhombic structure of sulfur (phase group: Fddd) and Li_2S (phase group: Fm-3m).

Parameters	Sulfur before cycling	Sulfur after cell charge	Li_2S after discharge
Phase group	Fddd	Fddd	Fm–3m
Crystallite size (nm)	–	142 (27)	6.07 (30)
Cell Volume (Å^{-3})	3295.7 (13)	3360.9 (30)	189.99 (23)
a (Å)	10.4715 (11)	10.4695 (20)	5.7488 (23)
b (Å)	12.8665 (25)	12.7150 (11)	–
c (Å)	24.4610 (83)	25.2474 (49)	–

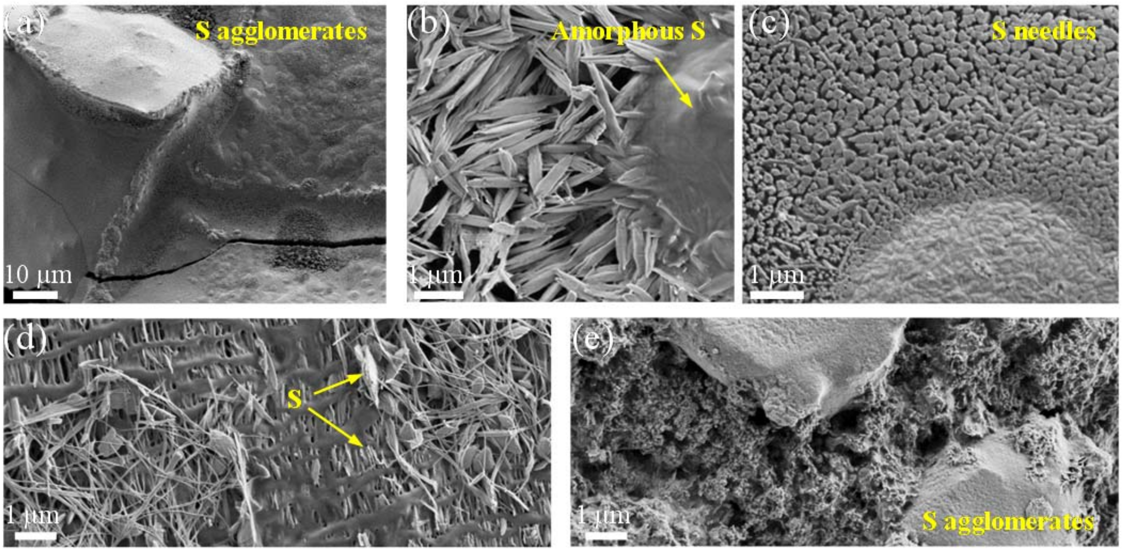

Figure 4.13: SEM micrographs of a separator section viewed from the cathode side (a–d) and of cathode after charge (e).

The particle size observable in the SEM pictures is similar to the one obtained by the Rietveld analysis. After cycling, the unit cell of sulfur is larger mostly due to an increase of the lattice parameter c (24.46 → 25.24 Å), while the other lattice parameters remain approximately constant. The broad Li_2S reflexes evidence the formation of nano–sized crystallites, which was calculated to be around 6 nm. The orientation of sulfur particles is probably due to epitaxial growth of sulfur crystallites on the carbon substructure. The carbon particles may act as nucleation centers and the deposited layer show preferential crystallographic orientations.

4.2.5 Semi–quantification of crystalline and amorphous phase

The integrated intensity of the Bragg reflections, area under peaks, is directly proportional to the crystallite volume. Therefore, the crystalline phase of the cathode can be semi–quantified considering the maximum integrated intensity as 100% of crystalline volume. For sulfur, the 222–reflection was chosen for peak integration during discharge and the 311–reflection at $2\theta \sim 26.5°$ during recrystallization for the first and second charge, because the 222–reflection does not appear any longer after the first charge. This change in the structural phase limits the quantification of sulfur before and after cycling. Figure 4.14 (a, c, e, g) shows the integrated intensity of the main reflections of sulfur (222 before cycling, 311 after cycling) and lithium sulfide (111) at different DOD and DOC. Moreover, the amorphous area was also evaluated, Figure 4.14 (b, d, f, h). The dissolution and reaction of sulfur is only observed in the first 20% DOD of the discharge cycle (Figure 4.14). The formation of lithium sulfide and can be detected in the last 60% DOD of the discharge time. During charge, the reaction of Li_2S is slower compared with the recrystallization rate of sulfur. By the second discharge, almost 50% less crystalline Li_2S is formed compared with the first discharge. At the end of the second charge, the peaks of sulfur appear at the same positions, indicating a similar orientation of particles as the one after the first charge.

It is interesting to observe the evolution of the amorphous area during cycling. Before cycling almost no amorphous phase is present in the cathode, while during discharge, this increases and almost triplicates it value at around 70% DOD. Next, when the formation of crystalline Li_2S increases, the amorphous phase reduces back but only to the double of its initial values. During the initial period of the first charge, the amorphous phase remains constant and starts to increase at around 30% DOC, when almost 50% of the crystalline Li_2S already reacted to polysulfides. The highest amorphous area is measured between 50–80% DOC and then slightly decreases with the formation of crystalline sulfur. From this evidence, it is expected that the formation of crystalline sulfur follows similar transition processes than the slow solidification of melted sulfur (polymeric$_{(amorphous)}$ → monoclinic → orthorhombic). This would means that first the sulfur chain molecule is build up according to the reaction of Li_2S_8 ($xLi_2S_8 \rightarrow 2xLi + S_{8x(chain,\ amorphous)}$) and after the formation of crystalline sulfur occurs ($S_{8(\text{chain, amorphous})} \rightarrow S_{8(\text{cycle 1st monoclinic, 2nd orthorhombic})}$). This process seems not to be completely reversible, and only the crystalline phase reacts back in the next discharge process. In the second cycle, the amorphous phase remains almost constant along the cycle. The presence of the amorphous phase is also observed after 100 cycles (see Figure 4.11).

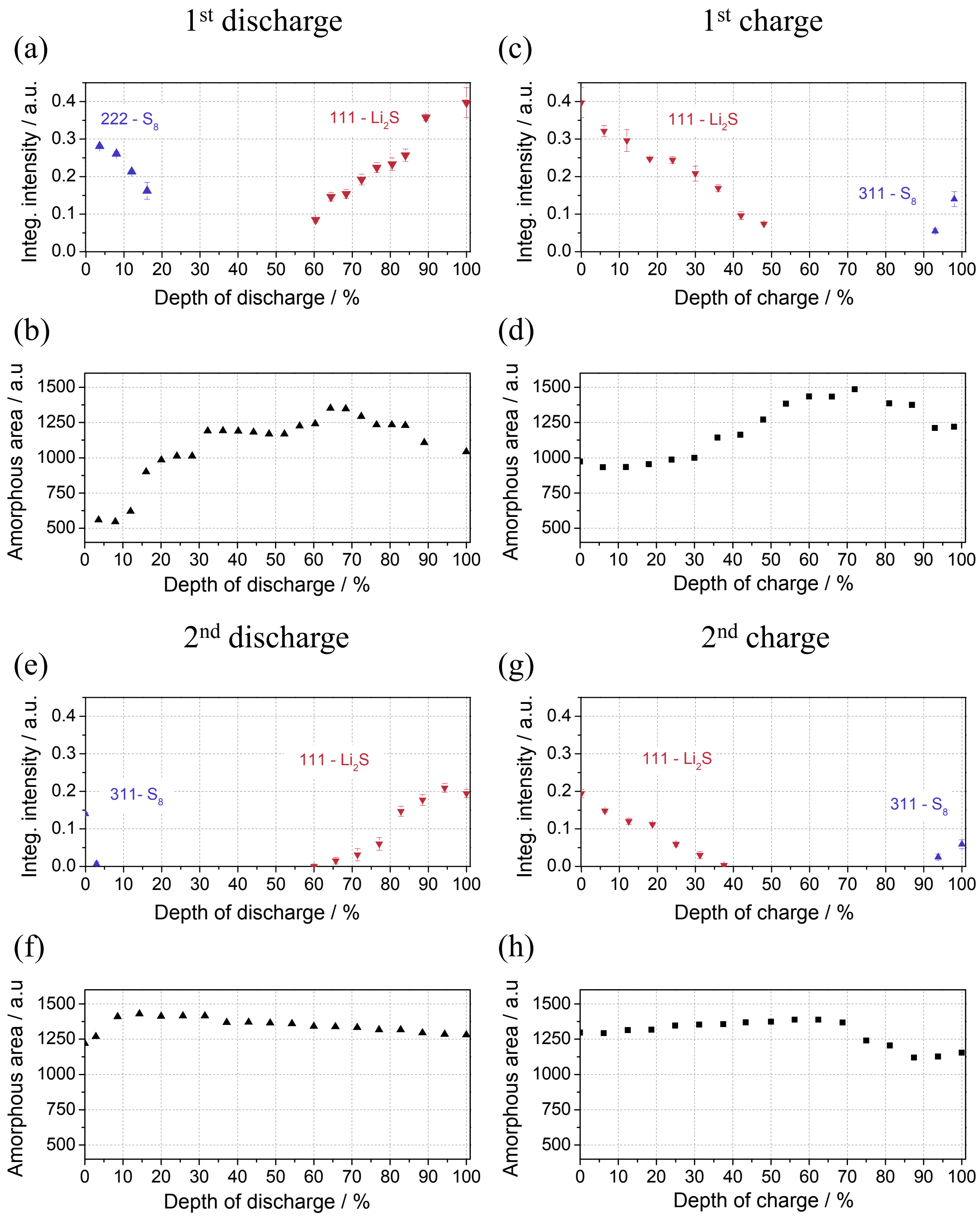

Figure 4.14: Semi–quantitative X–ray analysis for the first two discharges (a) and charge cycles (b) of a Li–S battery.

It is well known that polymeric of amorphous sulfur does not dissolve in organic solvents like crystalline sulfur does. For this reason, it is expected that the loss of capacity is caused by amorphous sulfur that build up an isolating film over the conductive CB particles. Moreover, it is important to notice that after discharge the amorphous phase increases by 100% (from around 500 to 1000 a.u of amorphous area) and after this cycle it does not decrease any further. This means that the isolating layer formed during discharge does not disappear after charge; but rather it increases by 25% due to the contribution of amorphous sulfur.

4.2.6 Discussion and comparison with further investigations

Previously work of Nelson and colleagues [128] carried out *in situ* XRD measurements on Li–S batteries at similar current density. Similar to this work, they found crystalline sulfur at the beginning of the discharge cycle (until ~ 23% DOD). They observed some changes in the position of sulfur Bragg Peaks, which was interpreted as an anisotropic orientation of S_8 particles. Contrary to the present results, no Li_2S was detected at the end of discharge. Considering the low discharge capacity (~750 Ah kg_S^{-1}) of the tested battery, the formation of Li_2S may not have been detected due to incomplete reduction of polysulfide.

Preceding publication confirmed the results shown in this chapter. Waluś and coworkes [141] used synchrotron–based in situ XRD to monitor the electrodes and complete cell during the first two cycles at C/20. During the initial stages of discharge the intensities of sulfur peaks gradually decrease until their complete disappearance at the end of the first plateau. Contrary to the results presented in this work, the Li_2S signal appears exactly at the beginning of the second discharge plateau, this is explained by the higher resolution of the synchrotron XRD and the lower discharge rate. Moreover, they reported, besides the presence of α–sulfur after charge, the appearance of monoclinic β–sulfur. They postulated this after matching the measured diffractograms of the recrystallized sulfur with the pattern of monoclinic β–sulfur (PDF: 01–071–0137). However, no structural refinement was performed in these diffractograms and considering the high number of S–reflexes in the reference patterns of sulfur, the confirmation of the β–sulfur just by simple matching of the measured diffractogram with a reference pattern is not trustful. Moreover, it is known that β–sulfur is stable above 95 °C, and although its formation maybe possible during crystallization in the electrochemical cell, this would be expected by high C–rate where the transformation β–S → α–S cannot be completed. This would be analog to the formation of monoclinic sulfur by quenching melted sulfur with cold water.

4.3 Conclusions

In this chapter, a suitable cell for *in situ* XRD analysis was designed to study the structural modifications on the cathode of Li–S batteries during electrochemical cycling. As a result, the formation and reaction of sulfur Li_2S were monitored *operando* during charge and discharge. It was demonstrated that at a low discharge rate sulfur reduces consecutively during the first discharge to Li_2S. The formation of Li_2S was observed for the first time at a depth of discharge of 60% in the second discharge plateau at 1.8 V. During the first charge cycle, crystalline Li_2S reacts entirely and sulfur recrystallizes with a different oriented structure and smaller particle size. The reaction of Li_2S is slower as the recrystallization rate of sulfur and after the second discharge, almost 50% less crystalline Li_2S is formed compared with the first discharge. At the end of the second charge, the peaks of sulfur appear at the same positions, indicating a similar orientation of the particles as the one after the first charge. However, an amorphous phase appears during first discharge and does not disappear completely in the further cycles. The non–homogenous distribution of active material in the cathode observed after cycling, the diminution of crystalline phase between cycle, the increase of isolating amorphous phase in the electrode contributes to the reduction of cell capacity, by the non–completely utilization of the active material.

5 Electrochemical impedance spectroscopy

EIS is a powerful technique to investigate the physical and electrochemical processes occurring in batteries during cycling. This method is used in the characterization of Li–S batteries to study, amongst other topics, the influence of electrode protective layers [61,142,143], cathode materials [28,29,144–147] and electrolyte compositions [44,112,115,148,149] on the impedance of the cell.

Few studies have applied EIS at different depths of charge or discharge [31,150–152]. In these studies, such measurements were performed using potentiostatic mode with an amplitude signal of 5 mV at different frequency ranges (100 kHz–100 mHz [150], 1 MHz–10 mHz [151], 65 kHz–1 Hz [152], 200 kHz–1 mHz [31]). The processes described by the proposed equivalent circuits (ECs) in [150] are electrolyte resistance (R_e), the formation of the conductive agent/electrolyte interface ($Rct||CPE_1$), Li_2S film formation ($Rg||CPE_2$) and polysulfide diffusion (Warburg–Element, W_0). The element R||CPE is defined as a resistance (R) connected in parallel to a constant phase element (CPE). Similar ECs were applied for the fitting of the impedance spectra in [152]. The processes analyzed here were electrolyte resistance (R_{el}), surface layer formation on lithium and sulfur electrodes ($R_1||CPE_1$), the electrochemical reaction of sulfur ($R_r||CPE_r$) and polysulfide diffusion (W). C. Barchasz and coworkers [31] did not analyzed the spectra at high frequencies, and therefore, no electrolyte resistance was considered. The boundary electrode/electrolyte was also described by a $R_{ct}||CPE_{dl}$ element, new phase formation was represented by a $R_{ct}||CPE_f$ element, and the liquid–state diffusion of soluble polysulfides was defined by a CPE_l rather than a Warburg Element.

The models described above can fit impedance spectra either at high or low frequency regions, but none of these have been applied over a wide frequency range. In this chapter, changes in the impedance of Li–S batteries were studied by means of EIS at different depths of discharge/charge over a wide frequency range. A simple but consistent EC is proposed to quantify the impedance contributions related to each physical or electrochemical process occurring in the battery. Moreover, the impedance spectra of Li–S batteries were evaluated in discharge and charge states for up to 50 cycles. Most of the results presented in this work were published in Electrochimica acta [7].

5.1 Experimental procedures

The battery was built up in the Swagelok cell as described in Figure 3.4. The cycling performance of the battery was investigated using an electrochemical workstation (Zahner® IM6) with proprietary battery evaluation software (Zahner®). The charge–discharge procedure was performed galvanostatically at a current density of 300 mA g_{sulfur}^{-1} in a voltage range of 2.8–1.5 V. After reaching the final charge voltage of 2.8 V, a potentiostatic period occurred for 15 min before the next cycle began.

EIS measurements were performed at the same electrochemical workstation during cycling in equidistant charge intervals of 50 mC. Each spectrum was measured in the frequency range of 1 MHz to 60 mHz and with an excitation voltage of 5 mV. The experimental data were fitted with an EC created with Thales software.

5.2 Results and discussion

5.2.1 EIS during cycling

Figure 5.1 (a) and Figure 5.2 (a) show the first discharge and charge curves of the Li–S battery respectively. Each point in the curve represents a recorded EIS spectrum. For clarity, a selection of spectra is presented. The frequency–dependent impedance of the cell represents the response of several parallel processes occurring in the battery. During cycling, these processes are revealed in the form of two or three depressed semicircles in the impedance plots. It can be seen that not only the diameter of the semicircles, the charge transfer resistance respectively, but also the number of semicircles that appear in the spectra changes with the state of charge or discharge. Moreover, a distinct additional process is observed at low frequencies, which is shown by a bended slope line. At high frequencies, no inductance is observed in the EIS spectra up to 1MHz.

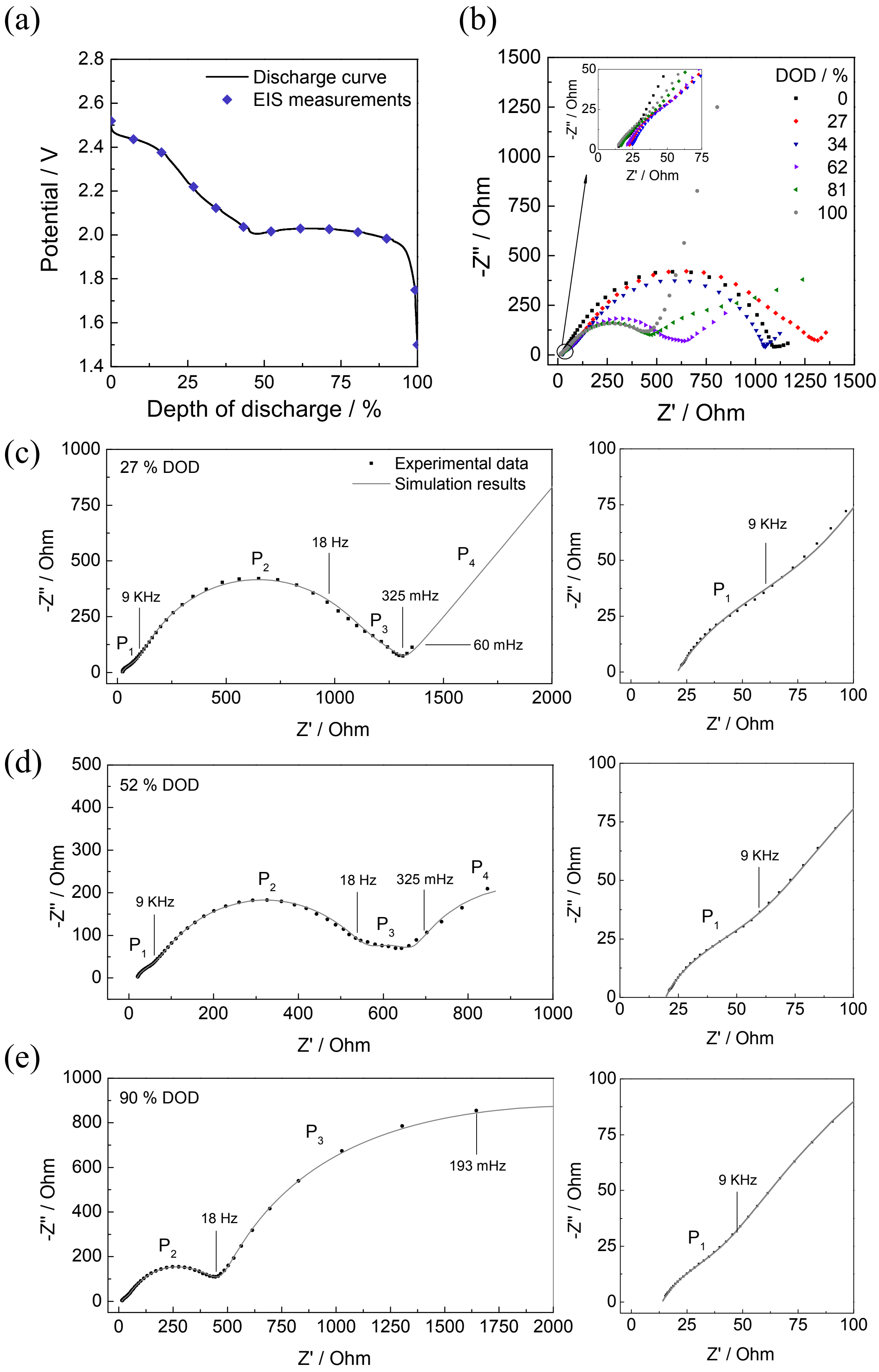

Figure 5.1: Discharge curve of a Li–S battery; each point represents an EIS measurement (a). Selected Nyquist plots in the frequency range of 60 mHz–1 MHz at different depths of discharge, DOD (b). Experimental and fitting results at 27% (c), 52% (d), and 90% DOD (e). The high frequency regions of the spectra are amplified on the right.

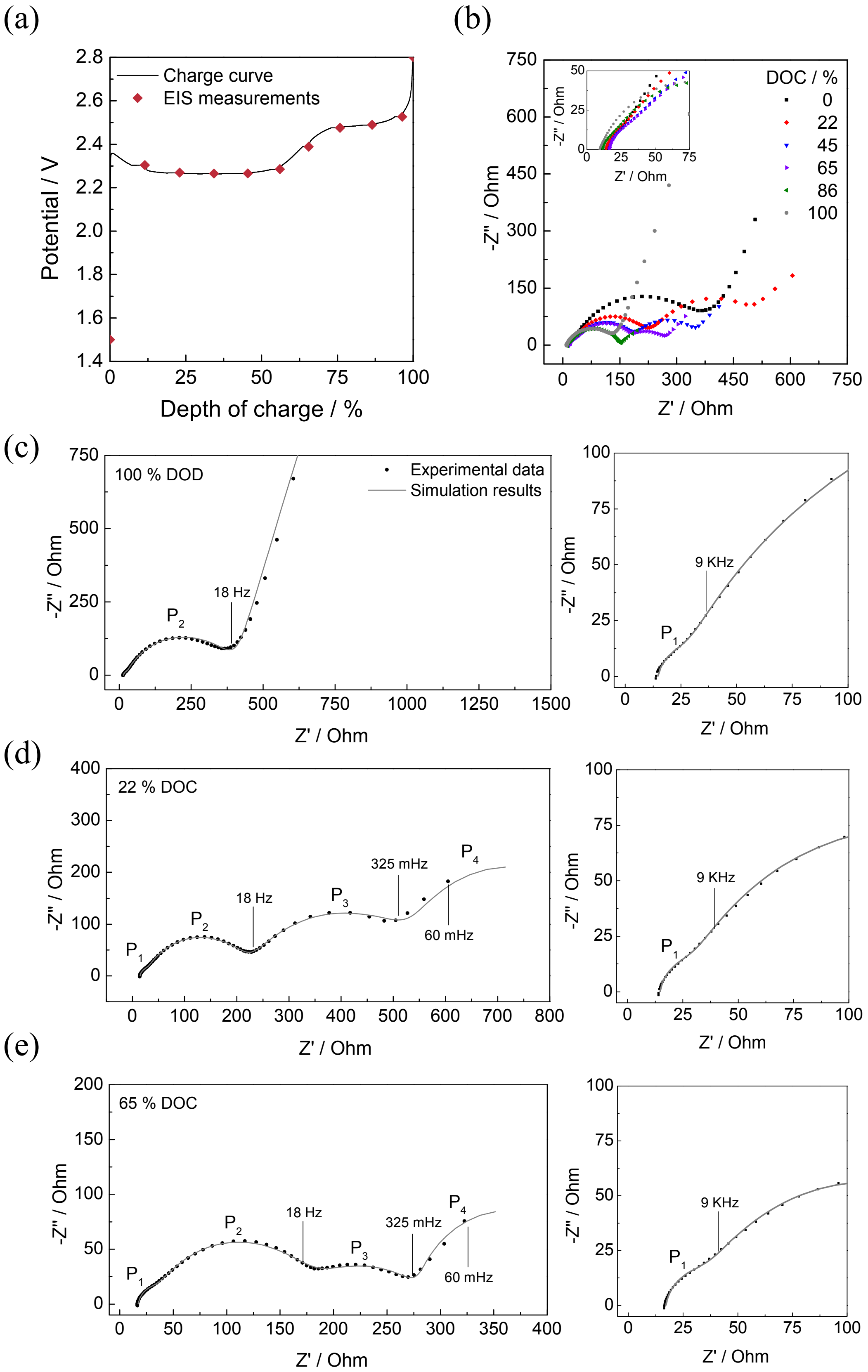

Figure 5.2: Charge curve of a Li–S battery; each point represents an EIS measurement (a). Selected Nyquist plots in the frequency range of 60 mHz–1 MHz at different depths of charge, DOC (b). Experimental and fitting results at 100% DOD (c), 22% DOC (d), and 65% DOC (e). The high frequency regions of the spectra are amplified on the right.

During discharge, a semicircle with a relatively small diameter (low resistance) can be observed at high frequencies. This process named here P_1 is present in all EIS measurements and can be seen, for example, in the magnified images in Figure 5.1(c–d). In the middle frequency range, a larger depressed semicircle (P_2) is observed during cycling. This larger semicircle is accompanied by a short bended line at low frequencies (P_4). From a 16% DOD, a new semicircle (P_3) appears between P_2 and P_4. P_3 vanishes after 27% of DOD (Figure 5.1 (c)) and reappears at approximately 50% DOD, growing continuously, like it can be seen in Figure 5.1 (d–e), until the end of discharge. At higher states of discharge, P_3 becomes more significant, whereas P_4 (at low frequencies) is suppressed (see Figure 5.1 (e)). The processes P_1–P_4 are observed at specific cutoff frequencies in the MHz–, kHz–, Hz– and mHz– domains, respectively.

During charge, the processes $P_{1\text{–}4}$ can also be discerned. P_1 is present during charge in the high frequency range and semicircle P_2 decreases with increasing DOC. The semicircle corresponding to P_3 diminishes continuously with an increasing depth of charge (DOC) (compare loop P_3 in Figure 5.2 (d) and (e)). At the end of charge, a small increase is observed (see modeling results). Finally, the process P_4 behaves concurrently with P_3.

5.2.2 Equivalent circuit (EC) for Li–S batteries

To simulate the results of the EIS spectra, an equivalent electrical circuit was designed. First, the spectrum was expanded in the lower frequency range down to 1 mHz (Figure 5.3) in order to identify the form of the short bended line that appears at high frequency. This was necessary to correlate this last slow process with a proper element of an EC. As it can be seen in Figure 5.3, this measurement reveals that the process (P_4) in the low frequency region take the form of a semicircle. This cannot be described by neither a Warburg element nor a capacitive element, contrary to proposed by [150–152].

An equivalent electrical circuit consisting of an ohmic resistance R_0 in series with four R||CPE Elements (R and CPE connected in parallel) was chosen to model the EIS results (Figure 5.4). A CPE was selected instead of a capacitor because of the non–ideal behavior of the system, reflected as depressed semicircles in the Nyquist plots. As described in chapter 2.3.2, CPE is similar to an ideal capacitive element, but has an absolute phase angle of less than 90°. The CPE impedance is defined by the Thales program as $Z = 1/(\omega_f T(j\omega/\omega_f)^{\alpha}$, where ω is the angular frequency, ω_f is a normalization factor, and T and α are constants. The variable α is dimensionless ($\alpha \leq 1$) and defines the grade of compression of the CPE semicircle. The limit value of $\alpha = 1$ represents ideal capacitive behavior. In these measurements, α varies between 0.48 and 1.

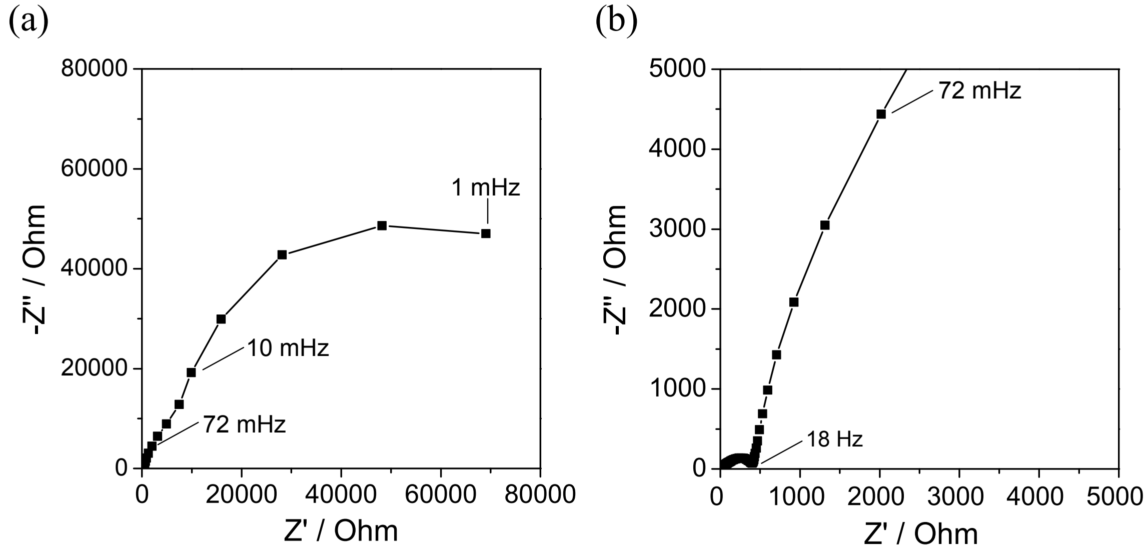

Figure 5.3: Nyquist plot of a Li–S Battery, frequency range: 1 mHz–1 MHz (a) with magnification in the frequency range: 72 mHz–1 MHz (b).

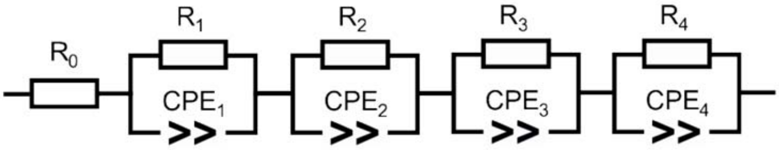

Figure 5.4: Equivalent electrical circuit of a Li–S battery used to fit the experimental data.

Depressed semicircles such as P_3 could be the result of the superposition of many semicircles, as several parallel reactions occur in the battery. Nevertheless, these depressed semicircles cannot be identified separately and the EC must be simplified in one depressed semicircle. Non–ideal behavior can also be explained by heterogeneities of the electrode material, roughness and gradient concentrations.

In Figure 5.5, an example of an EIS spectrum at 81% DOD and its fitting to the EC are shown. The blue semicircles in the image are only guides to the eye. As shown, the experimental points fitted with the equivalent circuit with a fitting error of 1.19% (calculated as average error of all elements). The different processes described previously ($P_{1\text{–}4}$) are now described by the corresponding R||CPE elements of the EC. Depending on the depth of charge or discharge, $R_3||CPE_3$ and/or $R_4||CPE_3$ may not be present or may be indistinguishable in the frequency range of measurement.

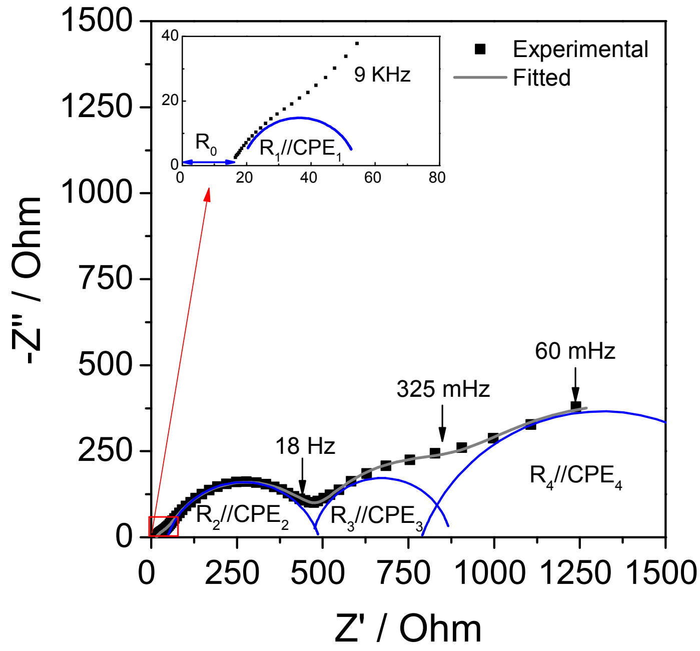

Figure 5.5: Nyquist plot of the impedance response of the battery at 81% DOD. The blue semicircles are schematics to clarify the domain of each EC element. The high frequency region of the spectrum is magnified at the top.

5.2.3 Assignment of processes to the EC–elements

Each element of the EC should describe a physical, chemical or electrochemical process occurring in this battery. The assignment of a process to each element is probably one of the most difficult and controversial part in the EIS. This results of the combination of previous knowledge about the system, the observation of the changes in the EIS spectra, and the comparison with the results obtained using other characterization techniques, like the used in this work: XRD, AFM and UV–vis spectroscopy. These results support the following assignment of the elements in the EC, which are summarized in Table 5.

Table 5: Assignment of processes to the elements of the EC.

Element of the EC	Chemical and physical cause
R_0	Ohmic resistance, electrolyte resistance
R_1||CPE_1	Anode charge transfer
R_2||CPE_2	Cathode process: charge transfer of sulfur intermediates
R_3||CPE_3	Cathode process: reaction and formation of S_8 and Li_2S
R_4||CPE_4	Nernst–diffusion

The first loop at high frequency, $R_1||CPE_1$, is associated with the charge transfer occurring at the anode surface. This interpretation is based on analysis of the simulation results that will be presented in the following chapter. First, the clear, concurrent behavior of R_0 and R_1 as a function of DOD or DOC is observed. This implies that P_1 is also affected by the concentration of polysulfides that can be reduced at the anode, which leads to charge transfer inhibition. Second, the resistance values of P_1 are much lower than those of P_2 (related to the charge transfer resistance of the cathode, see explanation below). This is attributed to the faster reaction kinetics occurring in the anode ($Li \leftrightarrow Li^+ + e^-$).

The $R_2||CPE_2$ element is attributable to the charge transfer of sulfur intermediates, and $R_3||CPE_3$ is attributable to the formation and dissolution of S_8 and Li_2S. The correlation of these EC–elements with specific chemical processes occurring in the battery was conceived after analysis of the simulation results. Note that R_2 is highest at 0% discharge where the concentration of sulfur intermediate is minimized. On the contrary, R_3 obtains its highest value at full discharge where accessible S_8 is unavailable and obtains its lowest values after sulfur dissolution. R_3 is visible when the formation of Li_2S starts. Both the electrochemical reactions and the resistance of each EC–element exhibit a distinct DOD/DOC dependence. Finally, diffusion of species in the electrolyte is detected at low frequencies. In the EC, this process is simulated using the element $R_4||CPE_4$. This could be replaced by using the “General Warburg Impedance” described in section 11.2.1.

5.2.4 Simulation of EIS during the first cycle

The circuit elements (ohmic resistance, charge transfer resistances, and associated double layer capacitance) were calculated by fitting the experimental data points with the EC. A complete overview of the simulation results are presented in the supplemental information (Table 13, Table 14, and Table 15). The resistance contributions as functions of DOD and DOC for the first cycle are illustrated in Figure 5.6. The electrolyte resistance (R_0) changes during discharge and is influenced by the concentration of soluble polysulfides (Figure 5.6 (a)). High resistances are observed from 34–52% DOD, indicating states with high concentration of polysulfides corresponding to the end of the first plateau in the discharge curve. When the reduction of polysulfides to lithium sulfide is complete, R_0 reduces back to approximately its original values.

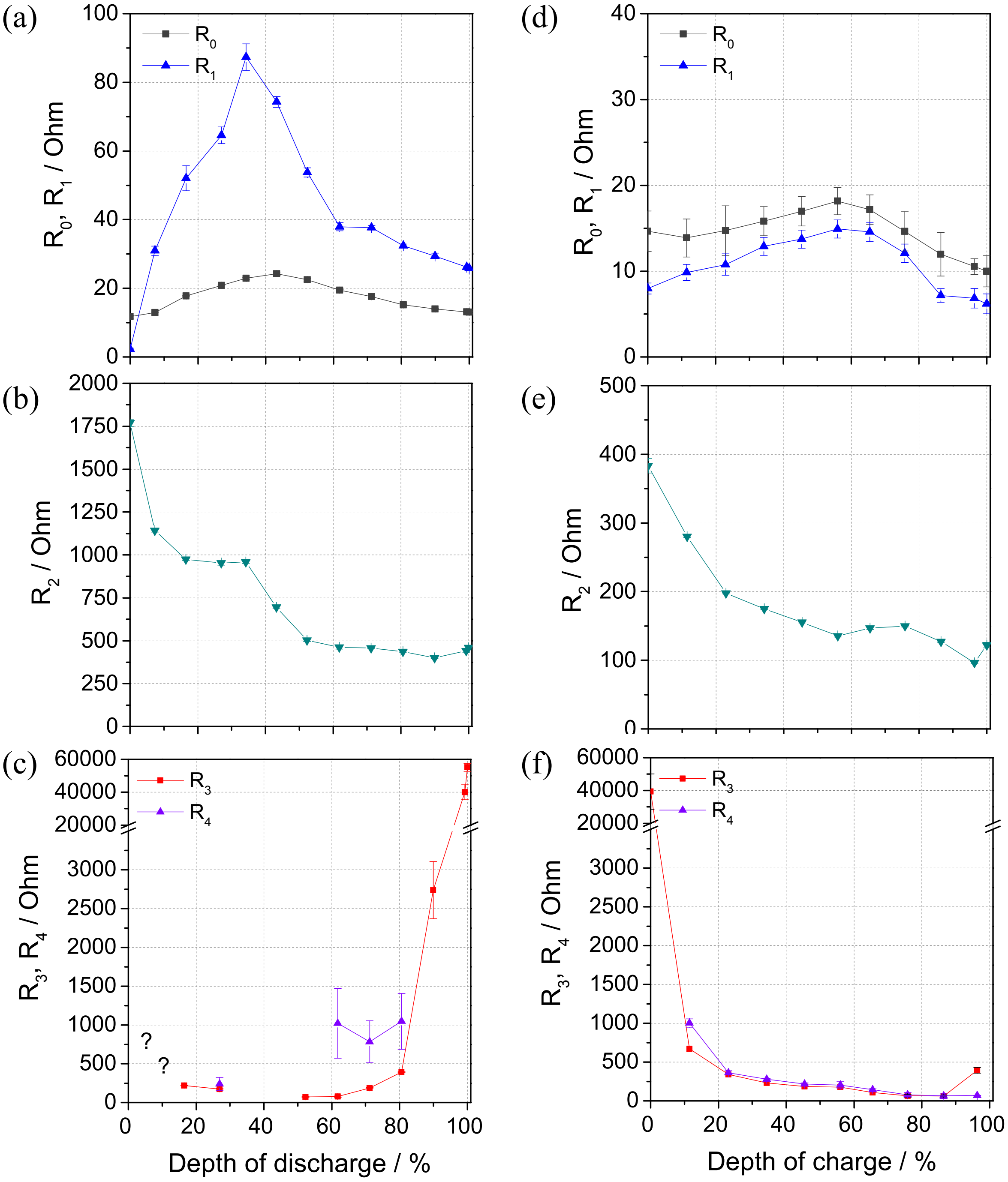

Figure 5.6: Changes of charge transfer resistances during first discharge (a–c) and first charge (d–f) of the Li–S battery.

The charge transfer resistance in the anode (R_1) shows a trajectory similar to R_0 but more pronounced, with a maximum at around 34% DOD. These both show similar behavior, because a high concentration of dissolved polysulfides in the electrolyte not only increased the viscosity (R_0) but it also hinders the charge transfer of lithium ions (R_1) due to the presence of polysulfides, which diffuse through the separator to the anode surface. The charge transfer resistance on the cathode side, described by R_2, decreases during discharge (Figure 5.6 (b)). The drastic diminution of resistance R_2 during the first stages of discharge may be caused by the changes in composition and morphology occurring in the cathode during this period. As a consequence of the dissolution and reaction of sulfur, the content of solid sulfur in the cathode diminishes; a more porous structure remains, with a higher surface area and greater conductivity. The charge transfer of polysulfide ions is enhanced as a result of these factors. In the interval between 16% and 34% DOD, the resistance remains constant. At this stage, process P_3 can be recognized at 16% and 27% DOD (see fitting curve Figure 5.1 (c)). The reason for the appearance of process P_3 may be the slowing of an electrochemical step, which is seen as a new CPE element in the spectrum. The presence of this element at the first stages of discharge is related to the dissolution of the remaining sulfur in the cathode.

The dissolution and progressive reaction of sulfur was already monitored during the first stage of discharge by means of *in situ* XRD in chapter 4.2.2. At 0% DOD, a small loop associated with P_3 can be observed between P_2 and P_4. Nevertheless, the small quantity of measured points results in an imprecise quantification. For this reason the spectrum of the completely charged battery (0% DOD) was simulated with three R||CPEs. After sulfur dissolves and reacts, P_3 cannot be observed until 52% DOD is reached. The reappearance of this process at this discharge state is then now attributable to the formation of Li_2S. The resistance of this element increases continuously until the end of discharge, due to the gradual formation of this solid and low electrically conductive end product of the Li–S discharge reaction (Figure 5.2 (c)). Moreover, R_2 stabilizes at the final stages of discharge with the progressive reduction of polysulfides.

R_4, which is attributed to diffusion, could not always be determined as a result of an insufficient number of measured points at low frequencies. However, it is observed that R_4 follows the tendency of P_3 (Fig. 6 (c)). The dissolution or formation of solid isolating materials can influence the diffusion of species, negatively in the case of solid products formation. Diffusion is suppressed by the dominant process P_3 at values higher than 81% DOD, and it is displaced out of the measured frequency range. This can be clearly observed in Figure 5.2 (e), at 90% DOD, where the large P_3 semi–circle is present in the low frequency range.

During the charge step (Figure 5.6 (d–f)), an overall decrease in the absolute values of the resistance elements is observed in comparison with the discharge step. The maximum values of R_0 and R_1 occur at approximately 60% DOC. In contrast to the discharge process, the maximum concentration of polysulfides in the electrolyte occurs in the second half of the charging process, at the end of the first plateau. At this point, lithium sulfide has been completely reacted to high order polysulfides according with the results of the *in situ* XRD Figure 4.6. The resistance related to the charge transfer in the cathode, R_2, decreases and stabilizes after approximately 40% DOC. The most important changes in the cathode morphology may occur during the first discharge, when the sulfur particles dissolve and leave the CB structure. Afterwards, the formation of solid products may occur primarily at the surface of the cathode, and not in the bulk. For this reason the charge transfer of the cathode during the first charge does not induce such pronounced changes as it does during the first discharge. Moreover, using XRD it has been observed that less crystalline sulfur is formed at the end of charge (Figure 4.14), a general reduction of the isolating solid species reduce the resistance on the cathode, and therefore the charge transfer on the cathode is enhanced.

The reaction of Li_2S in the first stages, and thus the reduction of the isolating phase in the cathode, can be followed by the diminution of R_3. The most drastic changes in R_3 occur in the range between 100% DOD and 22% DOC (Figure 5.6 (f)). This can be observed in Figure 5.2 (c–d). At the end of the charging cycle, an increase in R_3 is observed due the formation of solid S_8. The resistance related to diffusion (R_4) can be clearly linked to the dissolution of Li_2S and the formation of sulfur, with both following the same trajectory.

5.2.5 Degradation during cycling

EIS spectra were taken over 50 cycles to investigate the degradation of the battery. As in can be seen in Figure 5.7, the specific discharge capacity of the cell is high at the beginning of the cycling (approximately 1200 mAh g^{-1}) and decreases continuously with the number of cycles. The degradation of the cell is greater than the one observed in the cycling tests of the same battery before (Figure 3.6). This may be caused by an aging of the cell due to extra time necessary for the EIS measurements.

The simulated resistances of the EC elements up to 50 cycles are presented in Figure 5.8. In the high frequency region, the low ohmic resistance R_0 and charge transfer resistance R_1 do not change appreciably with an increased number of cycles (Figure 5.8 (a,b)). Contrariwise, the resistance associated with the charge transfer of the cathode (R_2) decreases drastically in the first few cycles, 50% between the 1st and 10th cycles (Figure 5.8 (c)). Although the charge transfer resistance in the cathode reduces, the degradation of the cell increases, resulting in lower discharge capacities. The rate of loss of resistance is similar to the rate of the fading of capacity (49%). The battery loses 83% of its specific discharge capacity in 50 cycles, while the major decrease occurs in the first 10 cycles (49%). From the 10th to the 20th cycle, a more gradual diminution is observed. In conclusion, the loss of discharge capacity behaves concurrently with the diminution of charge transfer resistance in the cathode; the high reduction of R_2 is most likely associated with the better accessibility of active material by electronic conduction; related to the less formation of non–conductive Li_2S upon cycling.

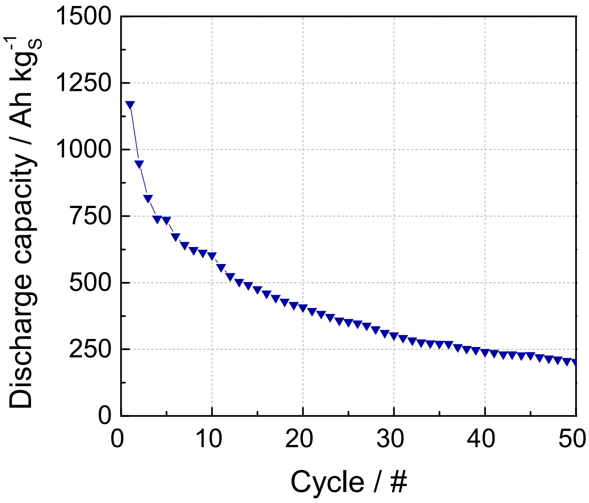

Figure 5.7: Cycle performance of a Li–S battery at room temperature for up to 50 cycles.

The resistance R_3 cannot be precisely fitted in the same manner as the other circuit elements (Figure 5.8 (e)). Evaluation of this element shows larger errors due to the fewer available measurement points at low frequencies. The formation of Li_2S, which is linked to this element, decreases during cycling. This diminution is reflected by the reduction of the resistance at the beginning of the cycle. Nevertheless, the resistance increases gradually after 10 cycles. This may be a result of a gradual degradation of the cathode due to the growth of an isolated film at the boundary between cathode and separator, composed of solid reaction products. On the contrary, the bulk of the cathode may consist, at the end of the 50th cycle, essentially of carbon black and some isolated particles of active material.

The concentration of non–conductive reaction products may increase in the direction of the surface of the cathode. This can be explained by the reduction of charge transfer resistance related to the reaction of soluble polysulfides, R_2, and the high resistance R_3 due to the formation of a non–conductive layer on the surface.

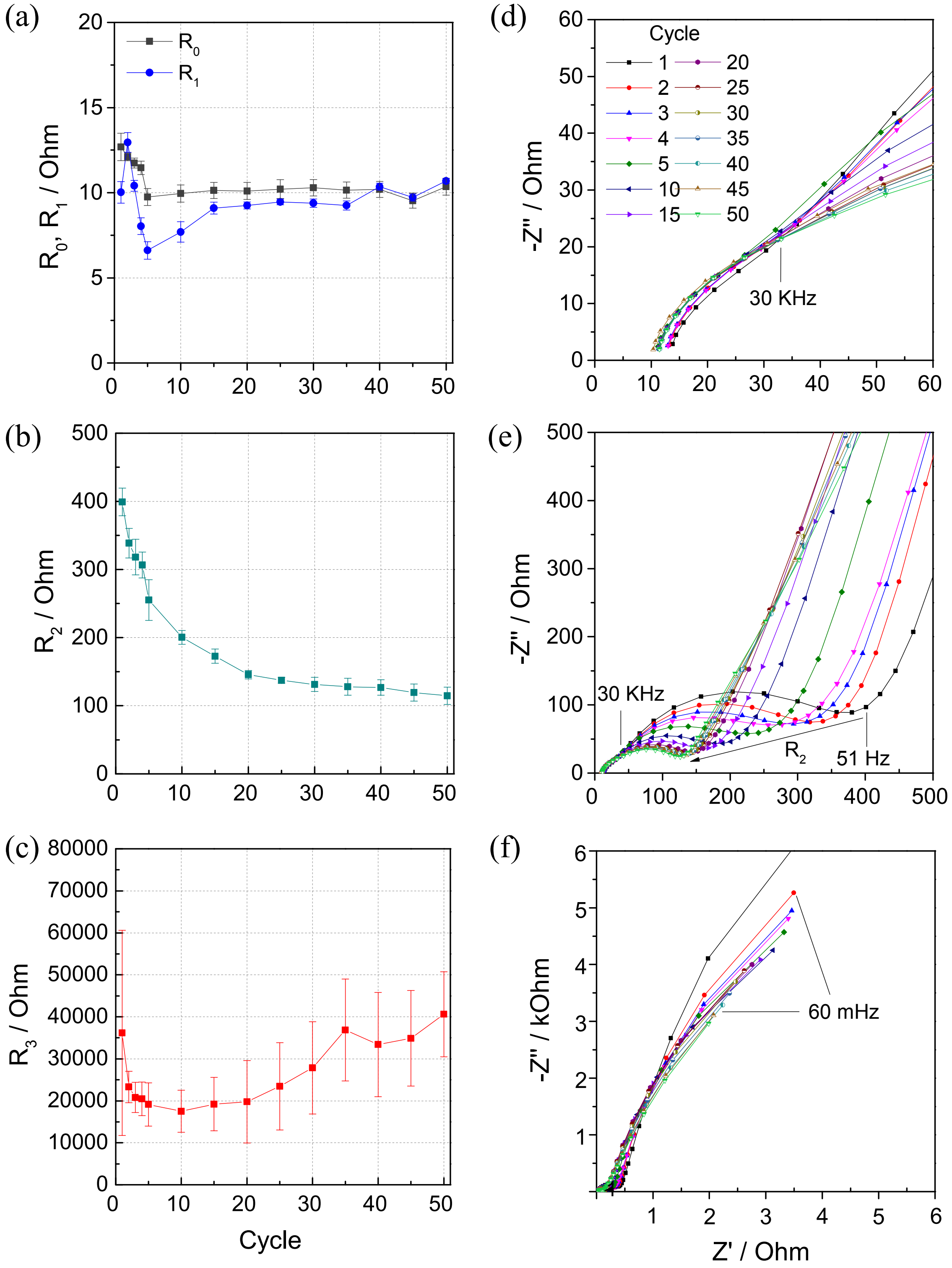

Figure 5.8: Charge transfer resistances calculated by modeling of the impedance spectra up to 50 cycles (a–c) and Nyquist plots of the corresponding frequency regions (d–f).

If the contribution of each element to the total resistance of the cell is analyzed, the formation of non–conductive phase (Li_2S) (R_3) contributes with around 99% to the total resistance. To follow the relative changes in resistance of the other elements, only R_0, R_1 and R_2 are considered in Figure 5.9. Major contribution of resistance is associated to charge transfer resistance in the cathode (~ 80–95%). This reduces considerably until the 20th cycle and then remains almost constant.

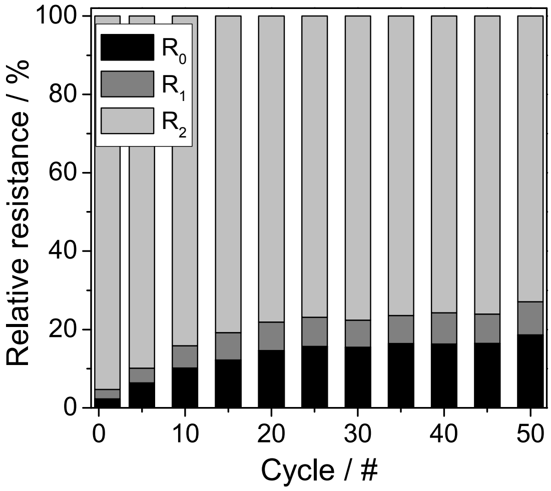

Figure 5.9: Relative values of the charge transfer resistance related to the electrolyte (R_0), anode charge transfer resistance (R_1), and cathode charge transfer resistance (R_2).

5.3 Conclusions

In this chapter, the Li–S battery was investigated measuring EIS spectra during cycling of the battery. The use of EIS allows *operando* investigations of Li–S batteries where several processes can be monitored: the formation and dissolution of solid products, changes in the viscosity of the electrolyte due to the dissolution of polysulfides, and the behavior of the charge transfer resistance in the electrodes. Moreover, an equivalent circuit was proposed for the evaluation of Li–S batteries, which can be applied in a broad frequency domain. The elements of this circuit have been related to physical and chemical processes occurring in the anode, cathode and electrolyte. The impedance contributions associated with these processes are strongly dependent on the depths of discharge and charge of the cell. During the first cycle, the dissolution and formation of solid reaction products can be detected and evaluated through the appearance of an additional semicircle in the middle frequency region of the Nyquist impedance plot. This is in agreement with the results obtained using *in situ* XRD analysis. The highest electrolyte resistance, related to the highest concentration of polysulfides, is detected at around 40% DOD and 56% DOC, at the end of the first discharge and charge plateau, respectively. The study of the degradation of the cathode for up to 50 cycles shows that the impedance contributions related to the electrolyte and the anode side present only small changes, while the charge transfer resistance in the cathode is reduced by 71% after 50 cycles. This diminution is related to the rate capacity loss of the battery as a result of the lessened formation of non–conductive solid products in the cathode bulk. The battery loses 83% of its specific discharge capacity in 50 cycles, while the major decrease (49%) occurs in the first 10 cycles. Finally, the formation of S_8 and Li_2S represents the greatest contribution to the resistance of the cell, thus it is also the determining factor in the degradation of this battery.

6 UV–vis spectroscopy

The formation, dissolution, and reaction of the solid products (S_8 and Li_2S) were analyzed *operando* using XRD (chapter 2.2). However, the polysulfides could not be detected due to their high solubility in the electrolyte, which was reflected in the increase of the electrolyte resistance and anode charge transfer resistance measured using EIS (Chapter 2.3). In the present chapter, the use of ultraviolet–visible (UV–vis) spectroscopy is chosen to analyze the polysulfide species and to bring new insights into understanding the reduction process of sulfur in the Li–S battery.

UV–vis spectroscopy has been frequently used for analyzing polysulfides in aqueous and non–aqueous media [153–161]. Nevertheless, only few studies focused on the polysulfides at different state of charge in lithium sulfur batteries [160,162,163]. Furthermore, the quantification of these components was not included in these investigations and the number of polysulfides involved in the reaction of Li–S batteries is still unclear. To my knowledge, the first *in situ* UV–vis analysis on Li–S batteries carried out using UV–vis spectroscopy in transmission mode was presented by D. Mamorstein [164]. This work shows a profound analysis of the polysulfides in a Li–S battery with ionic liquid electrolyte. Recent work shows *in situ* experiments measurements in reflection mode [163]. The main disadvantage of this configuration is that the area of the cathode analyzed was free of an opposite lithium anode, so the electrochemical activity is reduced and limited almost to the diffusion of polysulfides from active area to the radiated area. The authors observed changes of the peak wavelength in the range between 479–572 nm for polysulfides Li_2S_x with x = 8–2). The investigation of polysulfides by means of *ex situ* techniques is difficult due to the high reactivity of these components when in contact with air. For this reason measurements have to be conducted in an inert atmosphere to obtain accurate and trustful results.

This chapter presents an experimental setup for the investigation of polysulfides under argon atmosphere and proposes a new approach for their identification and quantification during cycling of Li–S batteries. It comprises the analysis of UV–vis absorption polysulfide intermediates and end products as well as the study of the spectra at different depths of discharge in Li–S batteries.

It is reproduced with permission from [8] with copyright [2014] owned by the American Chemical Society.

6.1 Experimental procedures

6.1.1 Set up of UV–vis absorption measurements

A miniature spectrometer Maya2000Pro (Ocean Optics) was used to measure the optical absorbance of the samples. The light source (DH–2000bal, Ocean Optics) combines the continuous spectrum of a deuterium and a halogen lamp with wavelength ranges of 215–400 nm and 360–2000 nm, respectively. A schematic configuration of the setup is shown in Figure 6.1. The solutions were measured in quartz cuvettes (Hellma) with a path width of 1 cm. The light source and the detector were placed outside the glove box, while the cuvette holder was inside the glove box. Light was transmitted between these components using fiber optics, which were connected to the glove box using a vacuum feed through. The fiber optics and the focusing lenses of the cuvette holder transmit light of wavelengths between 200–2000 nm and the optimal range of the detector for this configuration is 200–800 nm. The experimental setup has two main advantages: first, it enables measurements under argon atmosphere, avoiding undesirable reactions with air and water; second, a wide wavelength range can be analyzed in short integration times (6 ms).

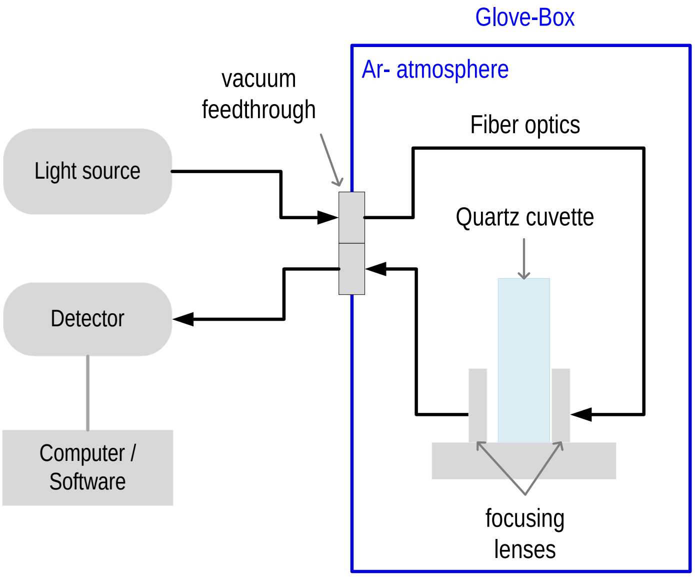

Figure 6.1: Set–up for UV–vis spectroscopic measurements.

6.1.2 Preparation of reference solutions

Preliminary spectroscopic experiments of reference solutions were necessary to identify the absorption maxima (λ_{max}) of the polysulfides. Based on the results, the spectra at different DOD can be interpreted. Therefore, a set of different polysulfide reference solutions was prepared under argon atmosphere. First, the end products of the reaction were measured in TEGDME as a solvent. The absorbance spectrum of TEGDME was subtracted from the sample measurements (Figure 11.15). In contrast to the intermediate reaction products, S_8 and Li_2S can be acquired as pure crystalline powder. Each powder was mixed in a glove box with TEGDME for at least 48 hours using a magnetic stir bar to obtain 50 mM solutions.

The study of the intermediate polysulfides is complicated by the fact that no polysulfide standards exist and disproportion reactions occur rapidly [165]. Additionally, the absorbance peaks change with the use of different solvents (Table 6). Polysulfide solutions can be prepared in non–aqueous solvents in different ways: first, by direct reaction of S_8 with lithium metal: $Li + {}^{x}/_{8}\, S_8 \rightarrow Li_2S_x$; second, by reacting with lithium sulfide (Li_2S): $Li_2S + (x+1)\, S \rightarrow Li_2S_x$; and third, electrochemically by reducing S_8 at a constant potential. According to *Rauh et al.* [158], the direct reaction of S_8 with Li_2S is faster and more easily controllable and is therefore chosen to obtain references of each polysulfide Li_2S_x with $x = 3 – 8$; to this, Li_2S and S_8 were mixed in stoichiometric proportions in TEGDME. While this technique does not necessarily yield a pure solution of the desired polysulfide, it will result in a mixture of polysulfides in equilibrium with the desired stoichiometric polysulfide.

6.2 Results and discussion

6.2.1 Sulfur and lithium sulfide

The absorption spectra of the colorless S_8 solution show an absorbance peak in the low wavelength range between 200 and 350 nm (Figure 6.2 (a)). No peaks in the visible region are observed. The overlapping sub–bands hidden in the non–symmetrical, broad peak can be determined by calculating the 2nd derivative of the absorbance curve. In the 2nd derivative spectrum, three sharp bands can be recognized at 245, 265 and 289 nm (Figure 6.2 (b)). The characteristic absorption maximum (λ_{max}) of S_8 is assigned to the 265 nm band. The linear dependency of the absorbance with the concentration is shown in Figure 6.2 (c).

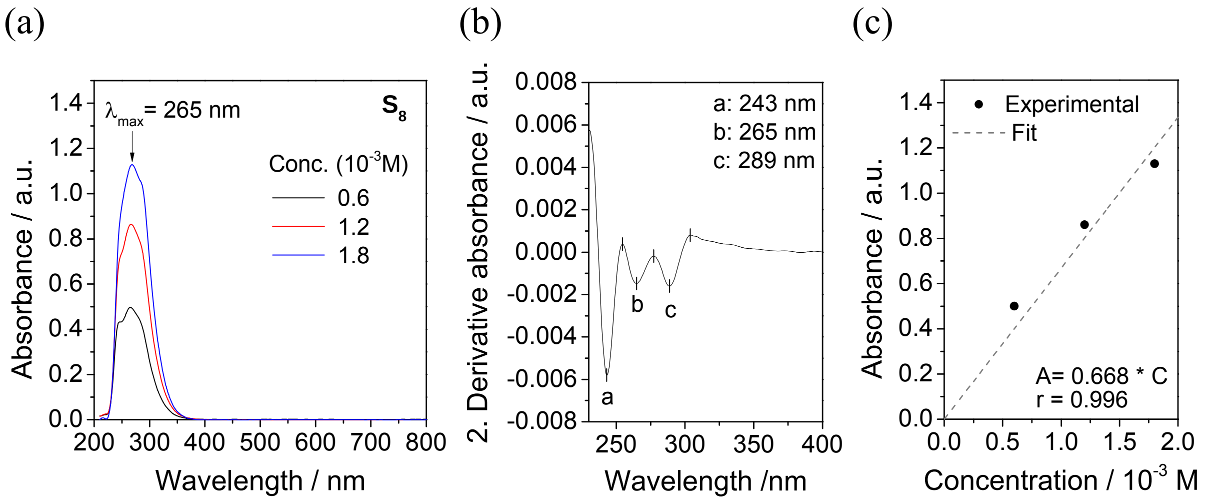

Figure 6.2: (a) Absorption spectra of S_8 dissolved in TEGDME, (b) the 2nd derivative spectra, and (c) changes in absorbance at λ_{max} with concentration

The spectral bands of dissolved S_8 in TEGDME are similar to the ones found for S vapor below 250 °C (210, 265, 285 nm) [166]. These absorbance bands are related to electronic transitions of cyclo–S_8, whereas the acyclic species S_2, S_3 and S_4 mainly absorb in the visible region. Given these facts, it can be concluded that the first step in the discharge mechanism of Li–S batteries is the dissolution of S from cyclo–$S_{8(s)}$ to cyclo–$S_{8(diss)}$ and that the opening of the S_8 ring only occurs during the redox reaction with lithium. However, the amount of S_8 dissolution as well as the predominant sulfur species may change with the use of different solvents or for heat pre–treated sulfur cathodes.

Contrary to S_8, Li_2S has a low solubility in TEGDME. However, spectra of this compound were obtained for highly dilute samples (Figure 6.3 (a)).

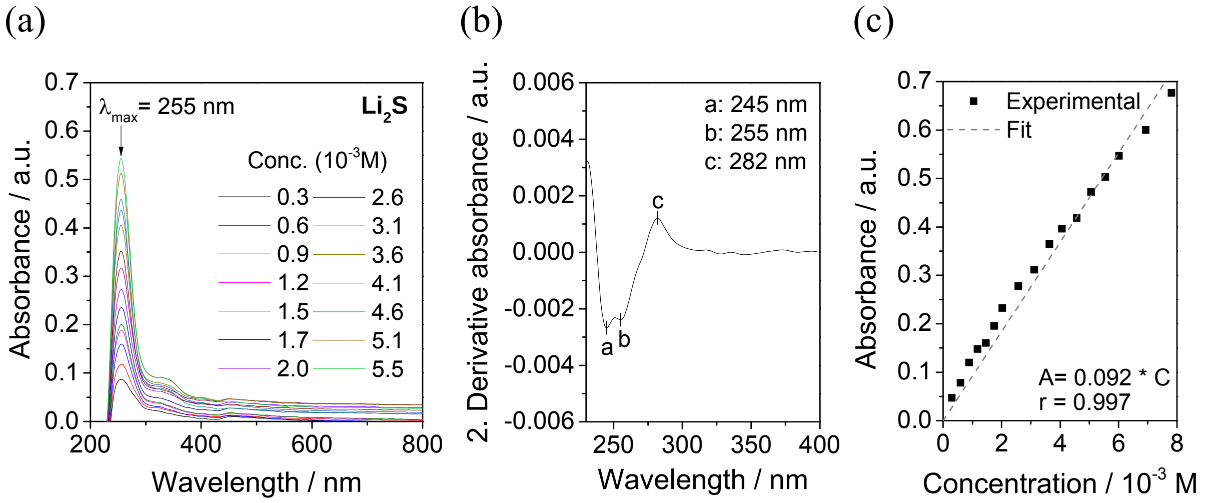

Figure 6.3: (a) Absorption spectra of Li_2S dissolved in TEGDME, (b) the 2nd derivative of the absorbance, and (c) changes in absorbance at λ_{max} with concentration.

Li_2S exhibits a sharper absorbance peak at λ_{max} = 255 nm with a small shoulder between 300– 370 nm. In the second derivative, bands at 245, 255 and 282 nm are identified. In the second derivative, bands at 245, 255 and 282 nm are identified (Figure 6.3 b). Figure 6.3 (c) shows the absorbance as a function of concentration and the results of the linear regression calculation.

6.2.2 Polysulfide reference solutions

During the electrochemical reduction of cyclo–octasulfur (S_{8c}) several polysulfides are formed. Various reduction mechanisms of sulfur have been proposed based on electrochemical and/or spectroscopic studies [153–155,158–160,167,168]. The stable form of the reduced polysulfides (S_x^{2-}) depends on the number of sulfur atoms in the molecule [169]. Polysulfides with x = 3–4 are stable in the chain form. When x is six or seven, the polysulfides can be either present as a chain or as a cyclic molecule. For x > 7, they are stable in the cyclic form [169].

Polysulfides dissolved in different solvents were already analyzed using UV–vis spectroscopy [153–161]. However, different absorption maxima are assigned to each polysulfide by different authors. Table 6 summarizes the absorption maxima assigned to sulfur species and the solvents used in past studies.

Table 6: Summary of absorption maxima estimated in the literature for polysulfides and radicals.

Ref.	Solvent	Polysulfides anions								Polysulfides radicals		
		S_8^{2-}	S_7^{2-}	S_6^{2-}	S_5^{2-}	S_4^{2-}	S_3^{2-}	S_2^{2-}	S^{2-}	$S_4^{\cdot-}$	$S_3^{\cdot-}$	$S_2^{\cdot-}$
[153]	DMSO	492		475		420	618					
[159]	DMF	490^{l}, 355^{c}	470	340, 450	435	420	334	280	250	~700	600	
[161]	DMF	500									617	
[160]	[C_4mim] [DCA]			350, 460		440	620				620	
[157]	DMSO									512		395
[12]	DMSO	490		340, 450		310	260			770	610	

c: cyclic; l: linear.

The spectra of the polysulfide references recorded in this study at different concentrations are shown in Figure 6.4. Small insets show the different colors of the polysulfide solutions. High order polysulfides (Li_2S_x with $x > 4$) show an intensive red or orange color, while Li_2S_4 and Li_2S_3 are yellow–green.

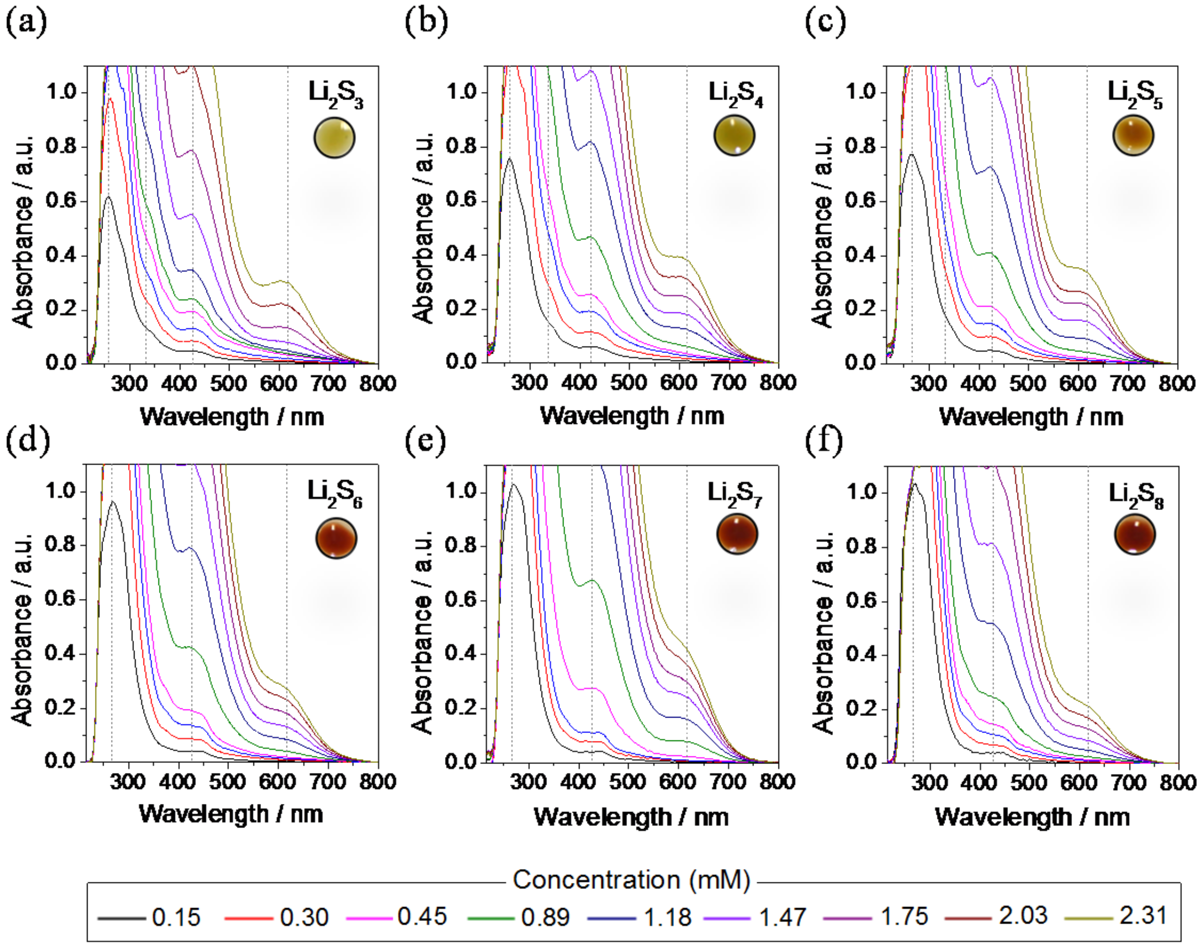

Figure 6.4: Absorption spectra of polysulfide solutions at different concentration Small insets show the visible color of the concentrated polysulfide solutions.

At low concentrations, a broad band is observed at around 265 nm. With increasing concentration, additional absorbance bands appear at higher wavelengths. This may be caused by a lower absorbance coefficient of compounds absorbing at this wavelength region. Another explanation may be related to the type of transitions occurring in these components: Polysulfides absorb light due to the excitation of valence electrons in their single bonds (σ), double bonds (π) and non–bonding (n) orbitals. In fact, it was already proposed that polysulfides have different resonance forms due to the presence of double bonds in the molecule [170]. In the wavelength region that it was measured, the transitions to be expected for polysulfides are: $\pi \rightarrow \pi^*$ and $n \rightarrow \pi^*$. The maximum absorbance was measured at a low wavelength range, usually associated with the transition $\pi \rightarrow \pi^*$, which typically occurs in the UV–region. With increasing concentration, more absorption bands are observed at higher wavelengths. They may be related to weaker $n \rightarrow \pi^*$ transitions (less light absorbed) of the non–bonding electron pairs of the polysulfides. Because of the saturation of the detector at around 1.3 a.u. in the low wavelength region (200–300 nm), it is important to measure a wide concentration range in order to detect all absorbance bands. Each wavelength region is analyzed at a specific concentration, which is chosen to be as high as possible without showing saturation.

The spectra in Figure 6.4 (a–g) are difficult to analyze without quantifying the absorbance and measuring the exact wavelength of absorption. Values of λ_{max} were obtained by fitting the curves with Gaussian functions (see examples in Figure 6.5). Furthermore, Figure 6.6 (a) compares the spectra at the lowest concentration in the region between 225–325 nm. λ_{max} shifts progressively from 257.4 nm for Li_2S_3 to 269.4 nm for Li_2S_8. This shift is explained by the effect of the non–bonding electrons of sulfur atoms. With increasing chain length, the number of non–bonding electrons of sulfur and thus the resonance of the π–system increases. This moves the primary absorption band towards a longer wavelength. At higher concentration, absorption bands are observed in the Vis–region. The main absorbance bands appear at 425 and 615 nm for all solutions. An additional band is observed for Li_2S_4 and Li_2S_3 at around 330 nm. For the analysis, the absorbance at 615 nm and 425 nm was evaluated relative to the absorbance at λ_{max} in the UV–region (~265 nm) (see Figure 6.6 (b)). For $\lambda_{max} = 615$ nm the absorbance rises linearly with the decrease of polysulfide order for Li_2S_8 to Li_2S_4, while a significantly lower absorption was measured for Li_2S_3. The maximum value of absorbance for $\lambda_{max} = 425$ nm is reached for the Li_2S_4 polysulfide reference solution. At 615 nm the absorbance follows a similar tendency. The band at 425 nm is clearly related to S_4^{2-}, in accordance with previous studies [153,159]. The band close to 615 nm is assigned to the anion radical $S_3^{\bullet -}$ by many authors [12,159–161] but also to S_3^{2-} by others [153,160]. Here, this band is observed for all the solutions, but it has its maximum value (in relation to the band at 425 nm) for Li_2S_3 solution.

In order to study the effect of dissolution on the samples, the changes in the absorbance ratio between the bands at 615 nm (A_{615}) and 425 nm (A_{425}) were analyzed in the concentration range of 0.45−1.47 mM (Figure 6.6 (c)). The ratio A_{615}/A_{425} increases with decrease order of polysulfide. Considering that extinction coefficient of the bands should be constant at this concentration range, changes in the ratio A_{615}/A_{425} would mean a variation in the equilibrium of the disproportion reaction of polysulfides. The error bars in Figure 6.6 (c) shows no significant changes in the relation of the absorbance between these bands, meaning that the equilibrium of the disproportion reactions is not significantly affected in this concentration range.

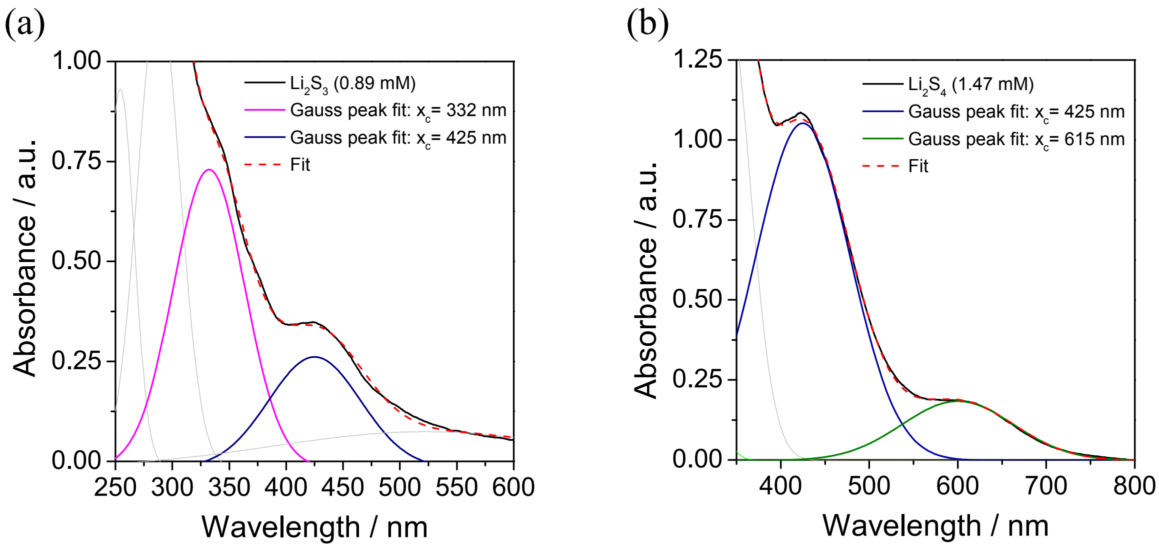

Figure 6.5: Example of fitted spectra at different wavelength regions with Gaussian functions to estimate the absorption maxima.

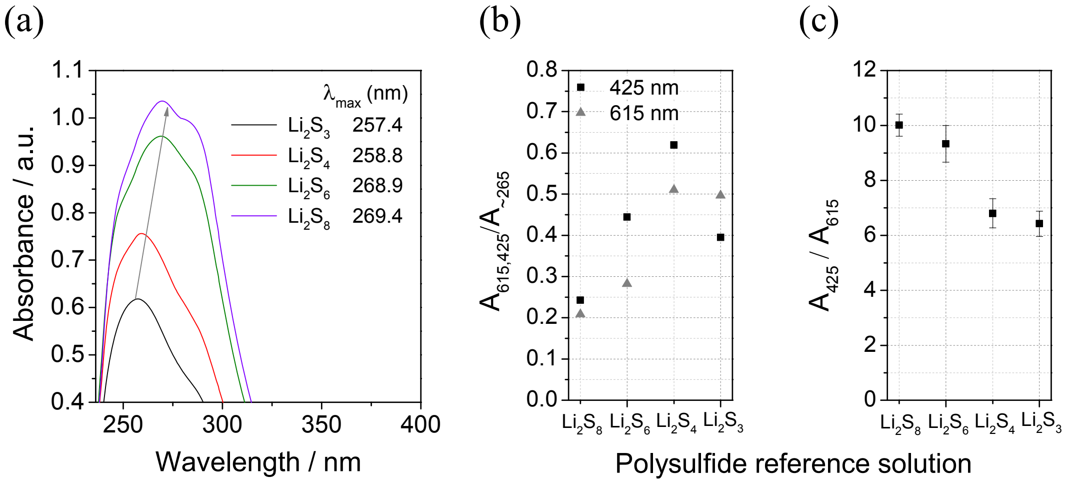

Figure 6.6: (a) Spectra of polysulfide solutions at the lowest concentration. The grey arrow indicates the changes in $\lambda_{max.}$ (b) Changes in absorbance of polysulfide solutions at 425 nm and 615 nm for the different polysulfide solutions relative to maximum absorbance at 265 nm; and (c) changes in the absorbance ratio between the bands at 615 nm and 425 nm in the concentration range of 0.45 – 1.47 mM.

The use of high diluted samples cannot be avoided by applying UV–vis spectroscopy in transmission mode. Although this may affect the equilibrium of the disproportion reactions of polysulfides, all samples were studied systematically in a wide range of concentrations, which allow observing relative changes between the samples accurately.

To summarize, polysulfide solutions prepared by mixing stoichiometric amounts of Li_2S and S_8 in TEGDME have rather similar UV–vis spectra, with the main absorption bands at ~265 nm (observable at low concentration), as well as 332, 425 and 615 nm (at higher concentration). Unfortunately, the assignment of one characteristic spectrum to each polysulfide solution is not possible, because of the coexistence of different polysulfides, continuously created by disproportionation reactions. Nevertheless, the shift of the absorption band at low concentration and also the changes in the absorbance of the bands at 615 and 425 nm clearly show the variation of the polysulfide composition. The characteristic absorbance bands identified in this study for S_8, Li_2S and Li_2S_x are summarized in Table 7.

Table 7: Absorbance bands assigned to S_8, Li_2S and various polysulfides in TEGDME.

Wavelength / nm	Species (in TEGDME)
245, $\underline{255}$, 282	S^- (Li_2S)
243, $\underline{265}$, 289	cyclo S_8
332	S_6^{2-}
425	S_4^{2-}
615	$S_3^{\bullet-}$

6.2.3 Discharge process: changes in the absorption spectra

UV–vis spectra at different depths of discharge (DOD) are shown in Figure 6.7. At the initial stages of discharge (12.5% DOD), only absorption in the UV–region of the sample occurs (Figure 6.7 (a)). New absorbance bands appear in the Vis–region with increasing DOD at higher concentrations (Figure 6.7 (b–h)). The absorption at 425 nm and 615 nm rises between 25−37.5% DOD (Figure 6.7 (b,c)). At 50% DOD, the absorption band at 330 nm appears (Figure 6.7 (c)). This band reaches it maximum by 62.5% DOD and drops again after 75% DOD. Contrary, the band at 425 nm diminishes continuously until the end of discharge and a slight growth of the band at 615 nm is observed (Figure 6.7 (h)).

The discharge profiles of the batteries tested until a specific depth of discharge are shown in Figure 6.8. The electrochemical tests show a good reproducibility of the discharge profile, which is especially significant when measuring under *ex situ* conditions. The second plateau starts when reaching 2.0 V near to 37% DOD, considering (100% DOD = 1200 Ah kg_S^{-1}).

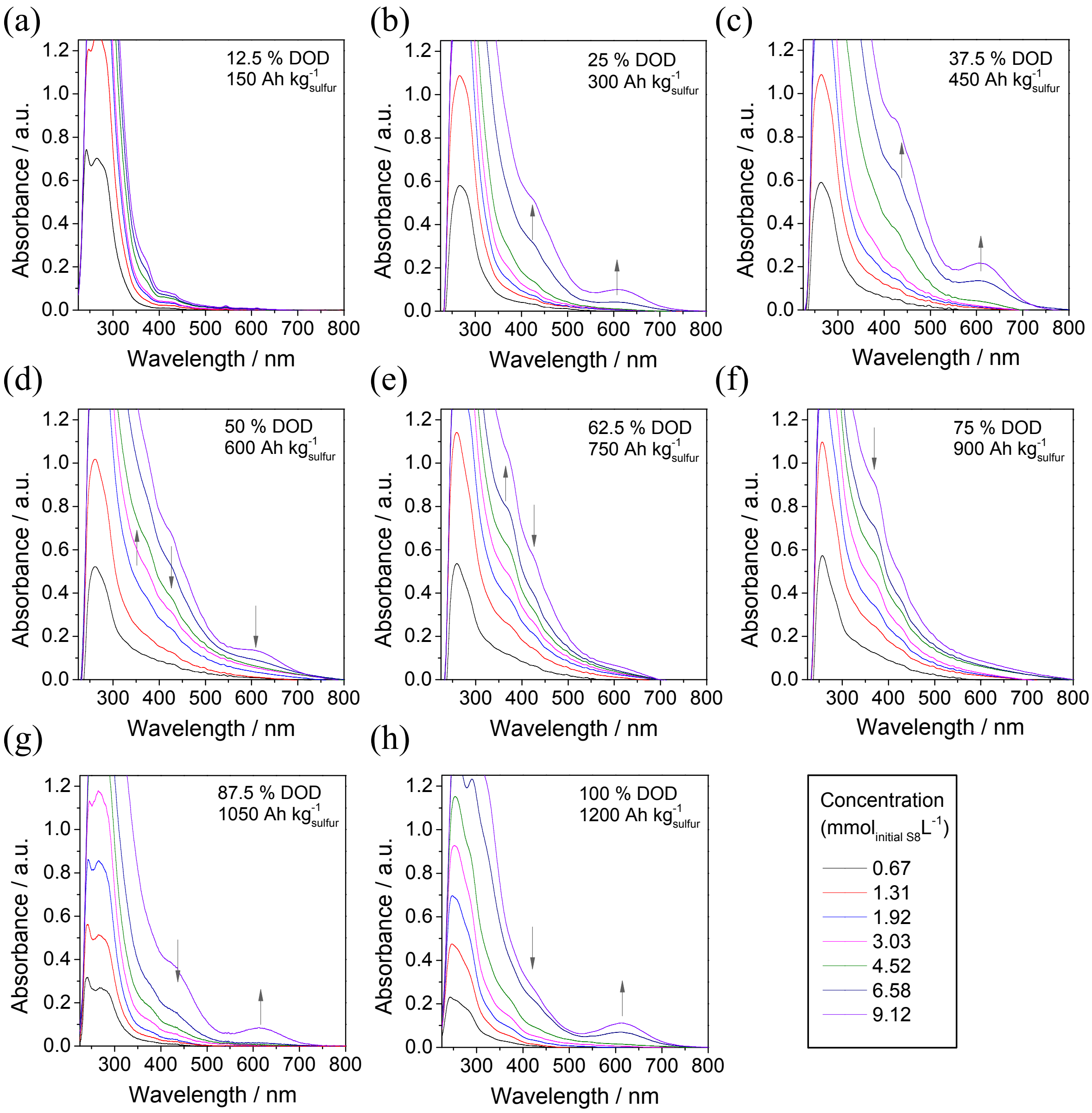

Figure 6.7: UV–vis spectra of cathode samples at different depths of discharge.

The UV–region of the samples was analyzed at low concentration and the Vis–region at higher concentrations. The absorbance bands identified in the spectra are: ~257–267 nm (at low concentration, UV–region) and 332, 425 and 615 nm (at high concentrations, Vis–region). For the analysis, the area under the curve and also the change in λ_{max} are determined for the spectra at the lowest concentration for each DOD (Figure 6.9). At this range, the detector is not saturated and the total absorbance can be measured from 200 to 800 nm. The area of absorbance is proportional to the quantity of species in the solvent that absorb light. It is important to mention that this does not only include the soluble polysulfides but also the absorbance caused by S_8 (and Li_2S) in solution.

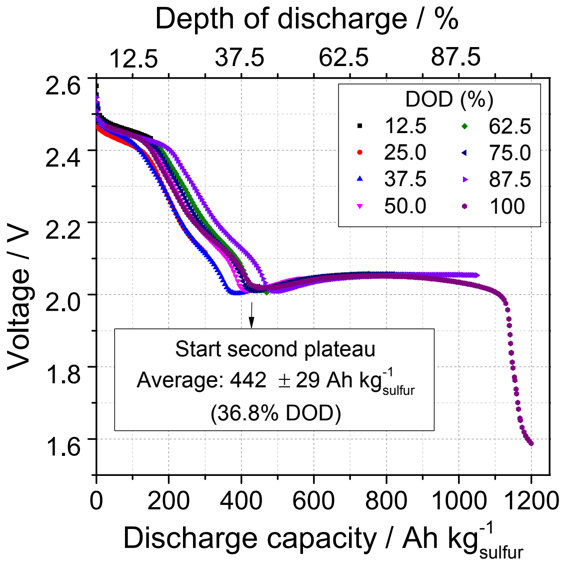

Figure 6.8: Discharge profiles of batteries used for the *ex situ* measurements.

It was already demonstrated by means of *in situ* XRD that only sulfur and lithium sulfide are crystalline during discharge and the polysulfides are dissolved in the electrolyte during cycling. The dissolution of sulfur in TEGDME can be calculated according to equation of Sciamanna et al. [139]: wt.% sulfur = exp [–10.994 (T_m/T) + 12.584). Thus, the solubility of sulfur at room temperature is 0.19 wt.%. Although, the value is low, the weight relation between the sulfur present in the cathode and the electrolyte is also low. This means that at the beginning 18.4 wt.% of sulfur is dissolved and the rest is solid in the cell. Nevertheless, when the cathode and separator is immersed in a greater volume of TEGDME (300 µL), sulfur should be completely dissolved. This explains the highest absorbance at the beginning of the discharge (17.5% DOD) caused by the presence of dissolved S_8 (Figure 6.9, left y–axis). However, the presence of polysulfides can be identified separately from the sulfur because they present additional peaks at higher wavelengths (Vis–region). Between 25% and 87.5% DOD, it remains almost constant. At the last stage of discharge, the absorbance falls rapidly. Due to the very low solubility of Li_2S and the low concentration of polysulfides, the absorbance value is extremely low at the end of discharge.

Changes in λ_{max} are also shown in Figure 6.9 (right y–axis). The reference polysulfide solutions already showed that λ_{max} decreases with reduced polysulfide order. For the samples analyzed at different DOD, the same behavior was found in the range of 25–75% DOD. During the first discharge plateau (12.5% DOD), λ_{max} is 265.7 nm. At higher concentrations, spectra show no significant absorbance at high wavelengths, which is related to low order polysulfides. Thus, it is expected that the major contribution to the absorbance is due to soluble S_8 ($\lambda_{max} = 265$ nm). When the cell is fully discharged, the concentration of dissolved components is lowest and the identification of λ_{max} is no longer possible.

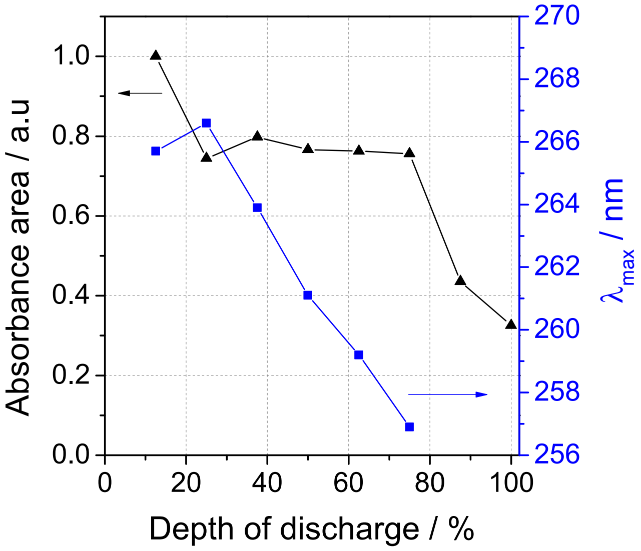

Figure 6.9: Changes of absorbance area (left axis) and maximal wavelength λ_{max} (right axis) during discharge at lowest concentration (0.67 $mmol_{initialS}L^{-1}$).

In Figure 6.10 the absorbance changes at 425 and 615 nm are shown during discharge. At 37.5% DOD, the highest absorbance is obtained for the bands at 425 and 615 nm and the maximum concentration of polysulfides is detected. At this point, the maximum concentration of polysulfides is reached. The band at 425 nm was already observed in the spectra of all polysulfide reference solutions and the maximum value was detected with the solution of Li_2S_4.The absorbance of this band can be considered to be representative of the middle order polysulfides. The maximum concentration is located around the end of the first plateau, where the formation Li_2S is expected. After this, the concentration decreases until the end of discharge.

The absorbance related to $S_3^{\bullet -}$ is detected for the first time at 25% DOD. After the maximum at 37.5% DOD, it remains almost constant until just before the end of discharge, where a slight increase in absorbance is observed. The formation of $S_3^{\bullet -}$ can be associated with the disproportionation reactions of polysulfide (6.1), proposed by [155].

$$S_x^{2-} \leftrightarrow \left(\frac{2x-2}{5}\right) S_3^{\bullet -} + \left(\frac{6-x}{5}\right) S^{2-} \tag{6.1}$$

The disproportionation of middle and low order polysulfides occurs in parallel to the reduction reactions of S_8 to Li_2S. For this reason $S_3^{\bullet-}$ is observed almost during the whole discharge process.

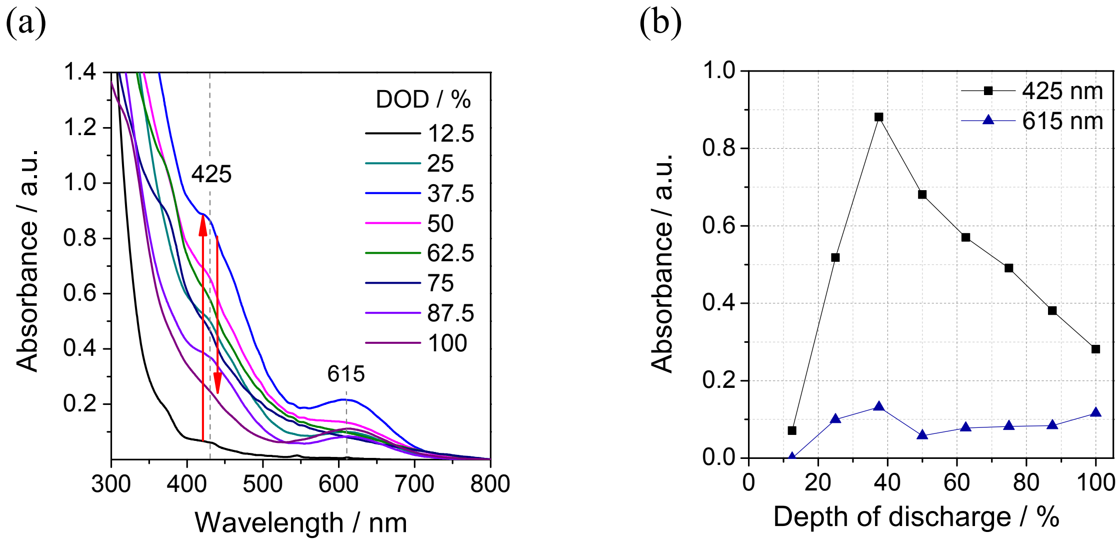

Figure 6.10: Absorbance changes in the bands at 425 and 615 nm at the highest concentration (9.12 $mmol_{initialS8}L^{-1}$).

6.3 Conclusions

An approach to investigate the formation of polysulfides in the liquid electrolyte of a lithium–sulfur battery during discharge has been demonstrated using UV–vis spectroscopy under argon atmosphere. Absorbance maxima of dissolved sulfur and polysulfide species were determined at various concentrations. It was found that sulfur and lithium sulfide dissolved in TEGDME absorb light at 265 nm and 255 nm, respectively. The bands at 425 and 615 nm were identified in the spectra of the reference polysulfide solutions and for the samples at different depths of discharge. These bands are suggested to be the characteristic bands for S_4^{2-} and $S_3^{\bullet-}$. Using these as a reference, the evolution of several species could be followed during discharge. λ_{max} of the band at the UV–region diminishes linearly with increasing DOD in the range between 25–75% DOD. This confirms the decrease of polysulfide chain length during discharge. Moreover, the highest concentration of polysulfides was found at around 37% DOD, around 450 Ah kg_S^{-1}. This experiment shows the possibility to not only detect the polysulfide intermediates but also to quantify them using UV–vis spectroscopy, at least semi–quantitatively. Nevertheless, it also demonstrates the limitation of this method to verify the existence of individual polysulfide species. For this reason these results will be compared with the output of a physicochemical model as well as experimental data obtained from XRD and EIS in chapter 8 to gain more information about the electrochemical reactions of polysulfides.

7 Morphological changes and degradation

This chapter focuses on changes in the morphology and stability of the cathode caused by degradation during cycling. First, changes on the cathode surface caused during cycling are analyzed using SEM at several states of charge and discharge. Second, the electrical conductivity and topography of the electrode surface are examined using AFM. Finally, the stability of the layer is studied after several cycles using TG/DSC and evolved gas analysis with a mass spectrometer. Part of the work presented in this chapter was already published in [6,7].

7.1 Experimental procedures

7.1.1 Scanning electron microscopy (SEM)

Analysis of the morphological changes on the cathode surface was carried out at different states of discharge/charge (DOD/DOC). For this, a scanning electron microscope (Zeiss ULTRA plus with charge compensation) was used. After cycling the battery until the desired DOD/DOC, the cathodes were demounted from the Swagelok cell, dried, cut, and fixed properly with conductive tape on the sample holder. High resolution images were taken using an accelerating voltage of 1 kV, and both secondary electron and backscattered electron (SE and BSE) detectors were applied.

7.1.2 Atomic force microscopy (AFM)

The topography and electrical conductivity of the cathode surface were studied using AFM. Cathodes were demounted from the Swagelok cell, dried, and fixed with conductive silver paste onto a conductive sample holder of an atomic force microscope (Multimode 8, Bruker Corp.). The sample was not cleaned after cycling to avoid chemical or physical elimination of active materials from the surface. Cathodes showed no significant differences when measured with or without cleaning (to remove $LiPF_6$ salt). The current over the surface was measured with a Pt–coated conductive tip working in tapping mode at frequency of 1 KHz and a scan rate of 0.5 Hz. A voltage of 100 mV was applied between the tip and the sample holder, and the average steady state current was measured at each tip–surface contact. Each tip–sample interaction was analyzed with Peak Force–TUNA™ mode, which averages the non–continuous current measured with the intermittent contacts in tapping mode [171,172].

7.1.3 Thermal analysis and mass spectroscopy

The samples were further characterized with TG–DTA/DSC–Apparatus STA–476 (NETZSCH) connected with a mass spectrometer MS–403C (NETZSCH). With the DSC configuration (Chapter 2, Figure 2.7), the mass and enthalpy changes of the single components of the cathode were measured. Two Pt crucibles protected with an Al_2O_3 layer, for sample and reference, were used to avoid reaction of the sample with Pt. Cathodes before and after cycling were analyzed on a plate crucible made of Al_2O_3 (T_{max}=1700 °C) with a diameter of 17 mm (Figure 2.7, TG–set up). The cathode diameter was 16 mm in order to analyze a greater content of active material; thus, batteries were built in Swagelok® cells with a larger internal diameter than the ones employed in the other characterization methods (XRD, EIS, UV–vis spectroscopy). For this, the sample carrier was placed in a furnace under controlled atmosphere and heated from room temperature until 1000 °C at 5 K min^{-1}.

7.2 Results and discussion

7.2.1 Morphological changes on the surface (SEM)

Figure 7.1 illustrates the changes on the morphology of the cathode surface during first cycle. A non–tested cathode was immersed in electrolyte, removed, and dried to observe the influence of the electrolyte. Before cycling the micro–sized sulfur particles are covered with carbon black nano–particles; however, some of them show partial dissolution of sulfur. After 20% DOD, the particles of sulfur are not identified any longer and instead of that some cavities are present due to dissolution and reaction of sulfur. This is in agreement with the results of the *operando* XRD: no peaks of crystalline sulfur are detected after 20% DOD. However, this does not exclude that some small quantity of sulfur is still present in the bulk of the electrode.

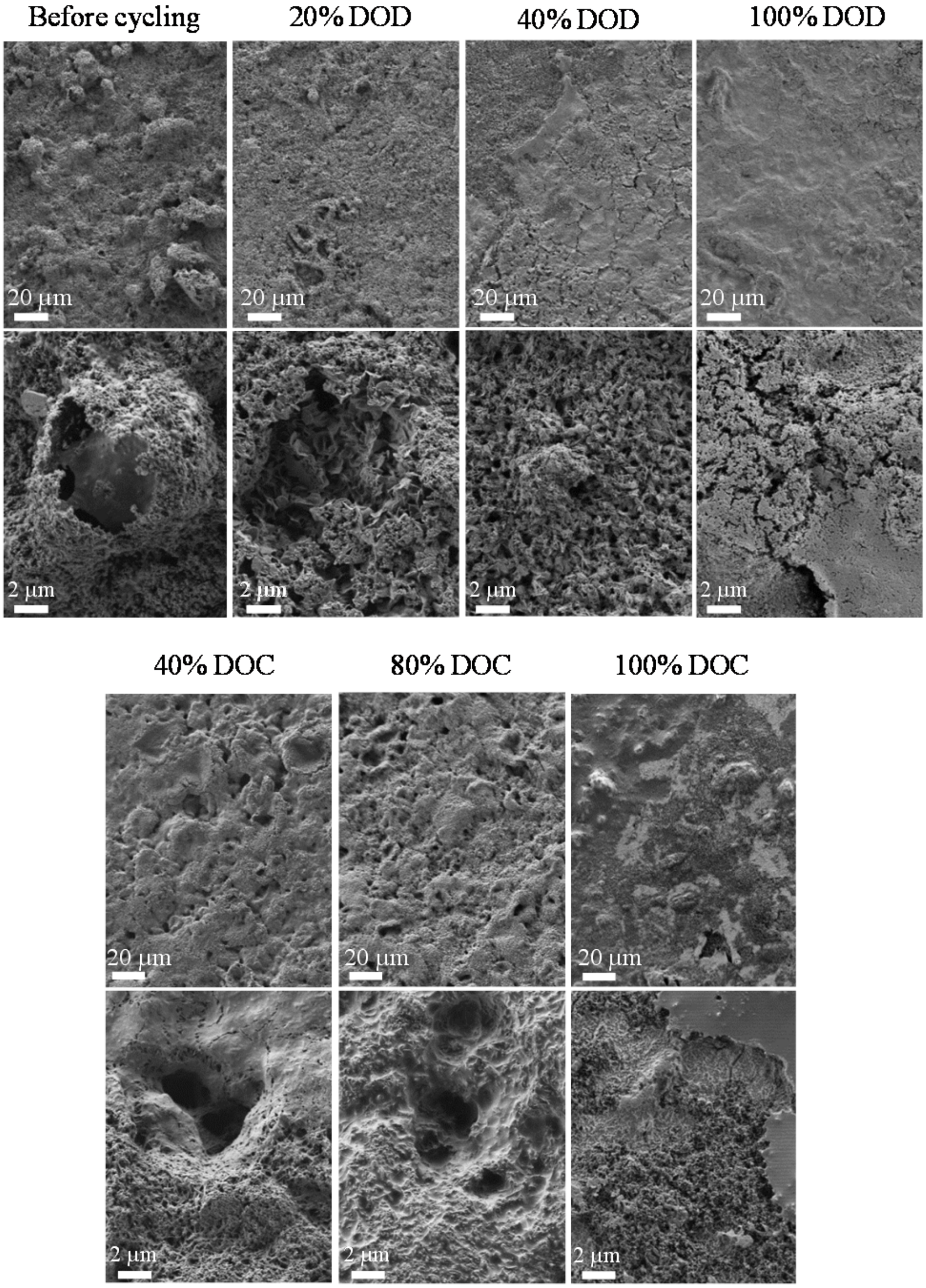
Before cycling
20% DOD
40% DOD
100% DOD
20 μm
20 μm
20 μm
20 μm
2 μm
2 μm
2 μm
2 μm
40% DOC
80% DOC
100% DOC
20 μm
20 μm
20 μm
2 μm
2 μm
2 μm

Figure 7.1: Ex–situ SEM micrographs of the cathode surface at different stages of discharge and charge (first cycle). Picture magnifications: 300x (top) and 3000x (bottom).The average discharge and charge capacity is 1276 and 1283 mAh g_{sulfur}^{-1} respectively [6]**.**

After the first half of the second discharge plateau, the cathode is partially covered by a solid layer. Small crystallites homogeneously are distributed on the surface layer can be also seen in the non–covered area of the cathode. These are probably related with the formation of Li_2S, as they have been already identified after the end of the first plateau (Figure 4.5). In addition, it is important to emphasize all the samples were measured *ex situ,* due to that, this layer or crystallites may be built up as a result of the decomposition of polysulfides and electrolyte compounds in air after dissembling the cell. It has been proven that Li_2S hydrolysis easily in air to form LiOH by the reaction: $Li_2S + 2\ H_2O \rightarrow 2\ LiOH + H_2S$ (see Figure 11.14). The images of fully discharged electrode exhibit a completely covered surface caused by the formation of the isolating reaction products. In addition, the observation of the deposition of solid isolating products on the surface can be correlated with the EIS results. In chapter 5.2.1, the process at middle frequencies ($R_3||CPE_3$) was associated with the formation and reaction of solid products. The resistance of this element increases dramatically at the end of discharge (Figure 5.6 (c)), and the SEM pictures confirm these results showing the formation of an isolating layer.

After 40% DOC, the cathode surface reveals some cavities, but the surface is still partially covered by the layer observed after discharge. At the beginning of the second charge plateau (80% DOC), the surface layer seems to disappear, and more cavities are present due to the complete reaction of solid Li_2S to soluble polysulfides. At this late state of charge, no peaks of crystalline sulfur are seen in the XRD spectra (Figure 4.6), but first after 90% DOD. Finally, once the battery is completely charged, the cavities on the cathode surface are filled with sulfur and the cathode is covered partially with a layer as well as with isolated sulfur particles. According to the results of XRD, the layer and the isolated particles of sulfur formed during charge disappear completely in the next discharge cycle. However, the deposited Li_2S reacts slower and has a lower dissolution in electrolyte (Figure 4.14).

It is worth mentioning that solid products remain not only over the cathode, but also some deposition of sulfur over the separator in the cathode and anode side is observed after dissembling the cell (Figure 11.6). The study of morphological changes under *ex situ* conditions, in contact with air, reveals the main transformations occurring in the electrode surface. However, to study the real formation and distribution of Li_2S, *in situ* measurements under argon atmosphere are needed.

7.2.2 Formation of isolating layers (AFM)

The electrical conductivity of the cathode was evaluated on the surface of the cathode before cycling, after the 1st discharge and the 1st charge. The samples were analyzed in three different positions and scanned over an area of 3 x 3 μm on the cathode surface. AFM images of the topography and the current distribution of the cathode can be seen in Figure 7.2 (a–f). The current measured between cathode surface and sample holder is directly proportional to the electrical conductivity of the path between them. This is influenced amongst others by the composition of the sample (percentage of non–conductive material), homogeneity of the sample, distribution of non–conductive particles in the bulk material, and formation of non–conductive surface layers. If an isolating surface layer is present, no current can be measured, and the percentage of non–conductive area can be quantified. The percentage of non–conductive area at different stages of the cell is displayed in (Figure 7.3).

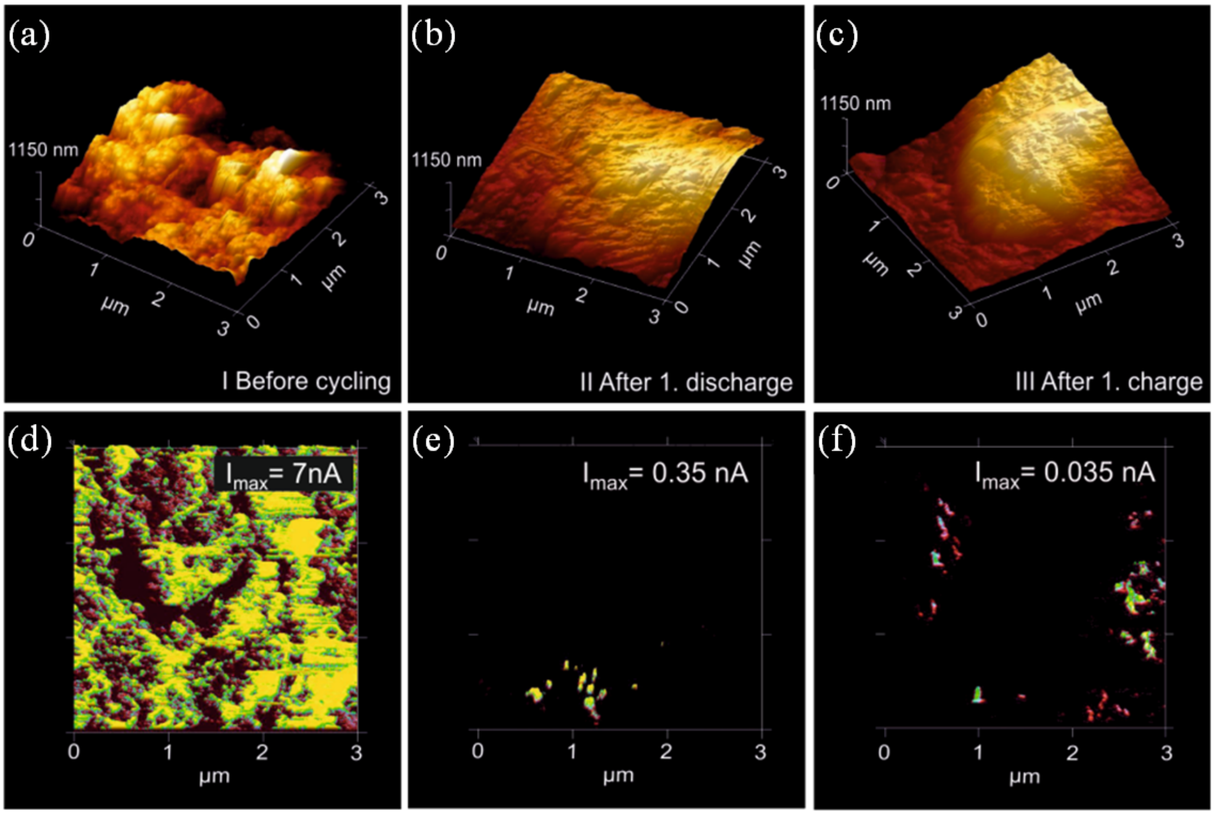

Figure 7.2: AFM topography images (b–d) and AFM current images (e–g) of the cathode surface before cycling (I), after first discharge (II) and after first charge (III) [7].

Topography images of the samples show smoother surfaces of the cathode after cycling (Figure 7.2 (a–c)). This is explained by the dissolution of micro–sized sulfur particles during discharge and the formation of a thinner layer instead. Before cycling, the cathode has a homogeneous surface covered mainly with carbon black (Figure 7.2 (d)). The non–conductive surface area rises to 28% (Figure 7.3). After the first discharge, the sample is covered with an isolating film, which reduces the conductive area to less than 1%. The film is accumulated during the last period of discharge and consists mainly of non–conductive Li_2S. As already mentioned before, LiOH is present instead of Li_2S, which is also non–conductive but stable under *ex situ* conditions. Thus, instead of the insulating Li_2S layer, the insulating LiOH layer is detected using AFM. The isolating property of this layer reconfirms the pronounced increase of charge resistance R_3 observed by the EIS measurements. After charge, the cathode has a high percentage of non–conductive area (93%) and an inhomogeneous surface caused by the formation of sulfur. Similar tendencies toward conductivity changes on cathode surfaces were also reported by Elazari and coworkers using AFM measurements under Ar atmosphere [122].

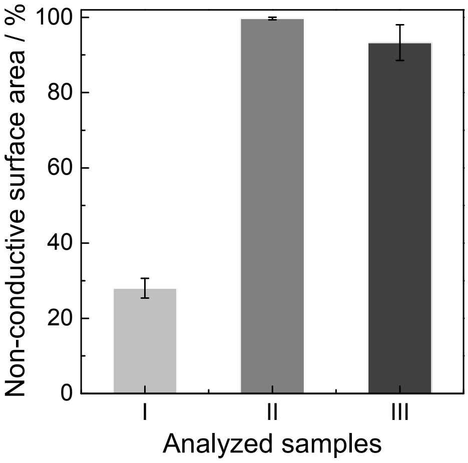

Figure 7.3: Non–conductive surface area (%) at different position of the sample before cycling (I), after first discharge (II) and after first charge (III).

7.2.3 Stability of the binding between particles (DSC–MS)

Characteristic temperatures and enthalpies of cathode components

The thermal behavior was analyzed for each component of the cathode separately to determine the characteristic temperatures of transformation or oxidation (Figure 7.4, Figure 7.5, Table 8). The samples were measured using DSC under air and argon atmosphere.

At standard conditions sulfur is commonly found in the orthorhombic form as cyclo–octa–S molecule, also called α–sulfur. While increasing the temperature until 95 °C, this phase converts into monoclinic β–sulfur which melts at 119.6 °C. The DSC curves of sulfur under both atmospheres show peak I at 109 °C and peak II at 122 °C, which correspond to the melting points of α–S and β–S respectively (Figure 7.4); therefore no changes in the TG curves are observed at these temperatures. Under air atmosphere, sulfur starts loosing mass at 140 °C due to an exothermic process. The well–defined peak IIIa may be associated with the oxidation of one phase of sulfur, because some mass loss occurs at the same temperature range. After this, the oxidation seems to be retarded by a transformation process, probably the endothermic process of vaporization. Subsequently, by 275 °C the oxidation rate increases and several sharp exothermic peaks appear. The sum of these (IV) by 275–325 °C is related to the oxidation of different sulfur phases. Sulfur polymerization may not occur under air atmosphere due to the earlier oxidation process. The theoretical temperature for sulfur polymerization is 169.5 °C [165].

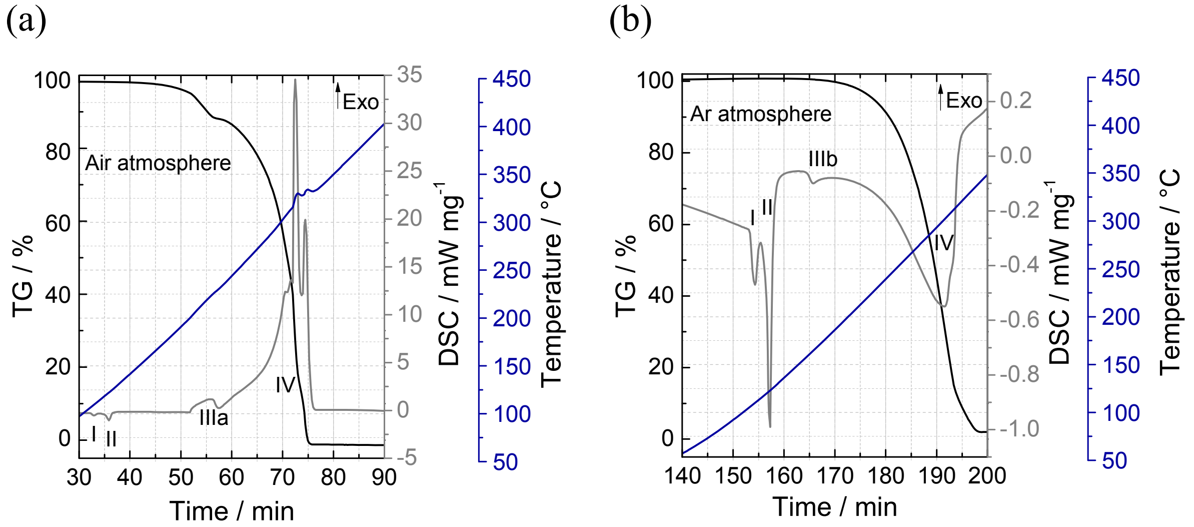

Figure 7.4: TG and DSC curves for sulfur under air (a) and under argon (b) atmosphere.

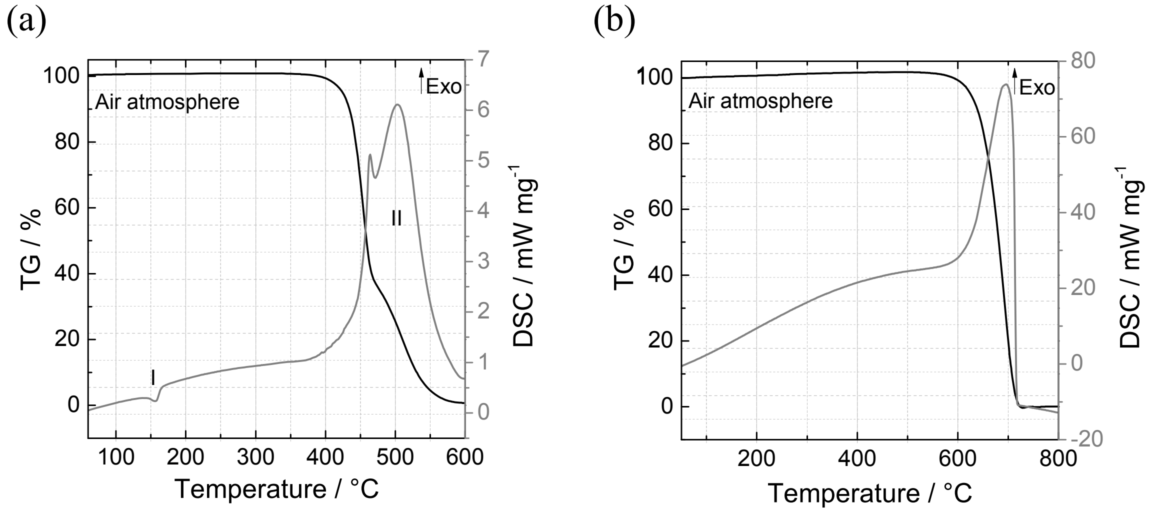

Figure 7.5: TG and DSC curves for PVDF (a) and CB (b) under air atmosphere.

Under argon atmosphere (Figure 7.4 (b)), the polymerization of sulfur can be observed by peak IIIb at 165.86, where no change of mass occurs. The non–symmetrical form of the peak is caused by the overlapping of vaporization process starting at around 165 °C. The vaporization occurs at a middle temperature of 300 °C, and the energy absorbed by the system is only slightly higher than the theoretical melting energy. Between 200–1000 °C vapor sulfur is composed of molecules with 2 – 10 atoms [173]. The energy curve keeps decreasing until 325 °C creating an asymmetrical peak (IV). This may be attributed to a partial oxidation of sulfur caused by a non–totally hermetical sealing of the furnace.

Table 8: Characteristic temperatures and enthalpies of S, PVDF, and CB. Exothermic process (positive sign) and endothermic process (negative sign). The values between parenthesis are from literature [165]**.**

Material	Atmosphere	Characteristic T (°C)	Enthalpy (J g^{-1})	Process
Sulfur	Ar /Air	109 (109.85)	–11	Melting of α–S
	Ar/ Air	122 (119.75)	–38	Melting of β–S
	Ar	300 (444.67)	–150	Evaporation
	Air	325	7868	Oxidation
PVDF	Air	156	–2	Melting
	Air	498	11312	Oxidation
CB	Air	696	14341	Oxidation

PVDF starts to melt at 156 °C (theoretical 168 °C), initiates decomposition at 380 °C, and oxidizes at a middle temperature of 498 °C (Figure 7.5 (a)). This last process leads to formation of several gaseous products like H_2O, CO_2, CO, responsible for the high value of energy released. The DSC diagram of CB shows an exothermic process related the oxidation to CO_2 at a middle temperature of 696 °C.

Cathode before cycling

TG curves of the cathode before cycling are shown in Figure 7.6. The measurements were carried out under air atmosphere to detect CB and PVDF up to 800 °C, and repeated for three samples. The first mass loss at 150 °C is related to sulfur oxidation, the slight decrease at around 400 °C to PDVF degradation, and at around 650 °C the oxidation of the carbon black particles occurs. The oxidation temperature of transformation is in all cases lower than the characteristic temperature obtained for the components measured separately as a powder. This is explained by the fact that reactions occur at a slower rate in the cathode due to the binding between particles.

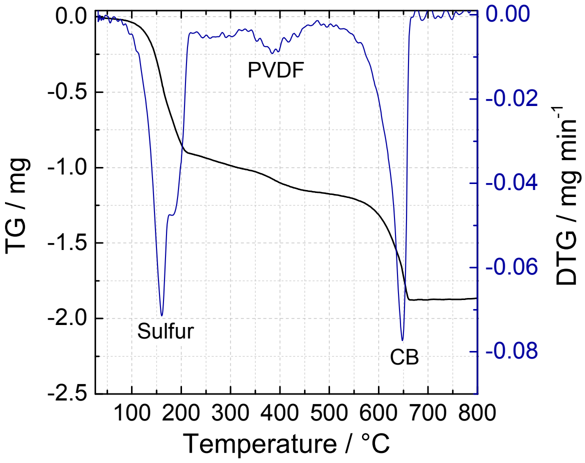

Figure 7.6: Typical TG curve of a cathode before cycling.

Table 9 summarizes the mass loss averages and corresponding standard deviations calculated for three cathodes measured before cycling. This confirms that the cathodes fabricated have a homogenous thickness (weight) and uniform distribution of the sulfur particles in the layer. Furthermore, it is important to mention that TG analysis is a trustful method to quantify the active material in the cathode, which is necessary for an exact calculation of specific capacity of battery during testing. Problems in the reproducibility of the electrochemical testing are often caused by a wrong quantification of the active material of the cell.

Table 9: Composition of cathode estimated using TGA. The average and standard deviation were calculated for three samples.

Mass	Sulfur	PVDF	CB	Total
mg	0.91 ± 0.03	0.21 ± 0.04	0.71 ± 0.02	1.83 ± 0.07
wt.%	49.73 ± 0.45	11.48 ± 1.66	38.8 ± 1.57	

Changes after cycling

TG curves for cathodes after 1, 10, 50, and 100 cycles are illustrated in Figure 7.7. As a complementary analysis to TG, the gas evolved during heating of sample was investigated with MS (Figure 7.7). The evolution of the mass number 64 (SO_2), 44 (CO_2), and 19 (F) is displayed below the TG curves.

After cycling, the mass loss of sulfur occurs at lower temperature, SO_2 forms between 100–150 °C instead of 250–300 °C (before cycling). The shift of the oxidation of sulfur from 219 °C before cycling to ca. 120 °C after cycling is explained by the reduction of the crystallite size and structure after cycling, already revealed in chapter

2.2.2, which increased the surface area of reaction. Furthermore, the crystallization of sulfur on the surface of the cathode and not in the bulk material may facilitate the reaction of sulfur with oxygen.

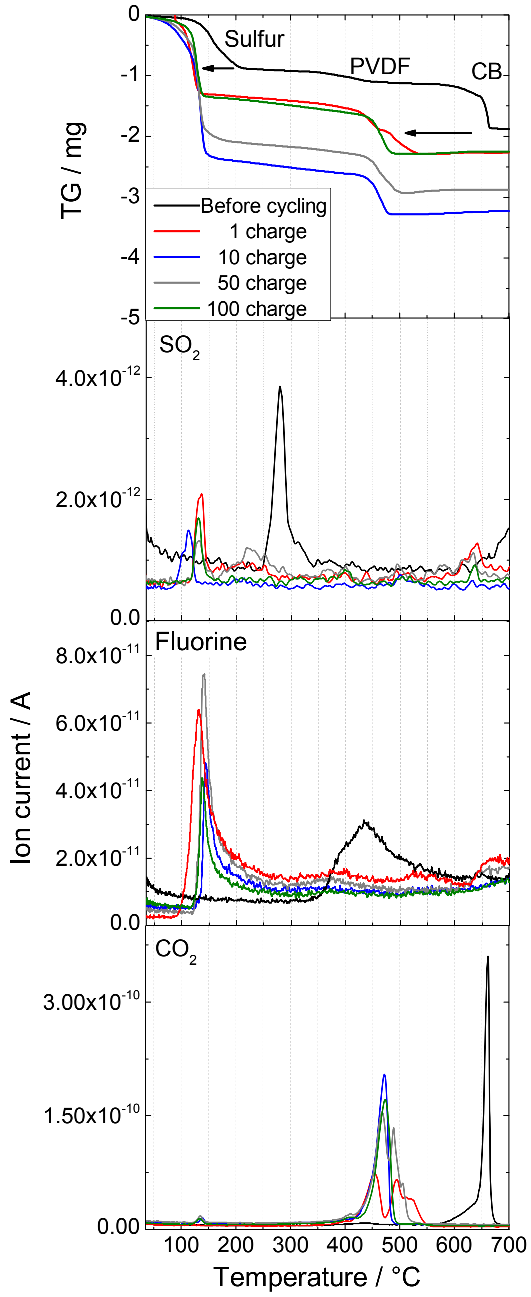

Figure 7.7: TG before cycling and after 1, 10, 50 and 100 cycles with the evolved gas analysis of SO_2, fluorine, and CO_2.

The increase in mass after cycling is related not only to the mass of sulfur, but also to reaction products of electrolyte in air. This was proved by measuring a cathode after drying with electrolyte (Figure 11.16). For this reason the sulfur content after cycling cannot be precisely determined using the TG analysis. However, the results of the mass spectroscopy show the decrease of the peak area of SO_2 which correlates with the content of sulfur in the cathode. The loss of active material is caused by the incomplete reaction of polysulfides to sulfur during charge, as well by the loss of sulfur which deposits in the separator surface.

The TG peak of PVDF is not distinguishable anymore after cycling. Moreover, the results of the MS reveal that the fluorine signal detected at around 400 °C for the cathode before cycling can no longer be detected after cycling. This may be a result of the decomposition of the binder by reaction with polysulfides during cycling.

For the cathode before cycling, CB particles oxidizes first slowly (small shoulder at 600 °C) and then rapidly (sharp peak) at the temperature range of 600–700 °C. Contrary, for the cathodes after cycling, oxidation reaction occurs at lower temperature: 660 °C for cathodes before cycling and 469 °C for cathodes after cycling (Table 10). These results suggest that the structure of CB is affected by the electrochemical cycling of the cathode; the binding of the CB particles in the structure may be partially destroyed, and this facilitates the oxidation process. In addition, the oxidation process after cycling occurs in some cases in several steps: see double peaks i.e. cycle 1 and 50 (Figure 7.7 (c)). Nevertheless, the appearance of one or several peaks could not be attributed to a specific cycle of the battery´s life.

Table 10: Changes in oxidation temperature of cathode components.

Material	Oxidation temperature (°C)		Oxidation range (°C)	
	Before cycling	After cycling	Before cycling	After cycling
Sulfur (SO_2)	219	130	146	97
PVDF	378	–	126	–
CB	660	469	170	98
(CO_2)	660	469	170	98

7.3 Conclusions

The dissolution and reaction of solid products during the first cycle affects drastically the morphology of the cathode. The formation of isolating layers at the end of the charge and discharge is inevitable using the present cathode and cell configuration. The low retention of active material in the bulk of the electrode was confirmed by the formation of sulfur deposition over the cathode and separator surfaces. The change in structure of sulfur already shown using XRD, it is confirmed in the TG curves: the formation of smalls crystallite or deposition of active material on the surface shift the oxidation process from 219 to 130 °C. In addition, the degradation of the PVDF binder, which was not detected in the TG curves after cycling, is one of the causes that affect the binding between the CB and S particles during cycling. An extreme reduction of the oxidation temperature of CB from 660 to 469 °C reveals that the conductive material is also affected by the electrochemical cycling. This reduction may well be explained by the destruction of the CB structure, which is important for the electron transport in the cell.

8 Simulations

Advances in new materials and concepts will potentially improve the performance of Li–S batteries in the next decades. However, the fundamental understanding of the physico-chemical processes is still the basis for its optimal design. As already shown in the last chapters, by the use of *in situ* and *ex situ* characterization methods more information can be gained about the system. However, to maximize the optimization of the battery, this information should be incorporated into models, which can reveal additional understanding and predict the behavior over a full range of battery operation under different conditions.

The first mathematical model for a complete Li–S battery was presented by Kumaresan and colleagues [140]. The model comprises electrochemical and chemical reactions, transport of species in the electrolyte, and charge transfer within and between solid and liquid phases. They simulated the two–staged discharge profile, analyzed the average concentration of polysulfides, and explained the physical reasons for the typical discharge profile obtained for lithium–sulfur cell. In this chapter, a more extended physicochemical model for Li–S batteries, developed by D. Fronczek et al. [174], is presented. The model allows simulating not only discharge profiles but also charge profiles at different C–rates, as well as electrochemical impedance spectra. Simulations were carried out for the Li–S cell configuration used in the experimental work and the output was compared with the experimental findings obtained from the electrochemical characterization, XRD, EIS and UV–vis spectroscopy described in the preceding chapters. Some of the results presented in this chapter were published in [8].

8.1 Description of the model

The model uses a continuum scale, physicochemical modeling framework called DENIS [175,176]. With this, differential equations can be solved, which describe transport in the liquid electrolyte, electrochemical kinetics, electrical properties of the cell, and the evolution of solid phases and their surfaces on a 1D–grid. In this model eight reactions among ten species are considered. They include dissolved polysulfides as well as solid products of discharge and charge, Li_2S and S_8, respectively. Figure 8.1

shows the assumed cell layout and reaction mechanism. Here, the domain of the model is illustrated and described by three layers: the lithium metal, a porous membrane filled with electrolyte and a cathode. Each of these layers comprises a number of bulk phases with one or more chemical species each. The following assumptions are considered: a) the cell is homogenous and infinite in parallel direction to the separator, b) the electrolyte is in contact with all of the solid components, c) the oxidation of lithium is not restricted, d) the overpotential in the negative electrode is insignificant, e) no other reaction occurs in the anode, f) all reactions occur at interfaces, and temperature and pressure are constant (T = 298 K, p = 101.325 Pa).

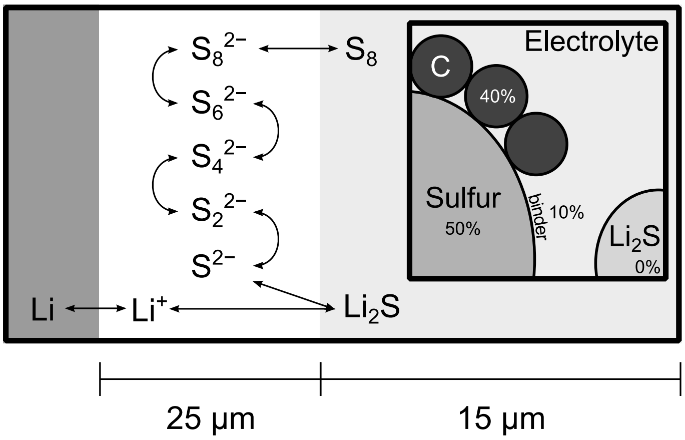

Figure 8.1: Geometry, reaction mechanism and initial cathode composition of the simulated cell.

The model is described by equations related to the mass and charge transport in the liquid electrolyte, the cell voltage and current, as well as the electrochemistry and multi–phase management in the cathode. This system of equations was evaluated on a 1D–grid with 45 equally sized and spaced control volumes. The meaning and units of the symbols used in the subsequent equations are provided in Table 16. The mass and charge transport of the species in the liquid electrolyte is described by dilute solution theory. The Nernst–Plank equation defines the continuity of the species i in the electrolyte according to:

$$\frac{\partial(\varepsilon_i c_i)}{\partial t} = \frac{\partial J_i}{\partial y} + \sum_m A_m^V \dot{s}_{i,m} \tag{8.1}$$

Here $\dot{s}_{i,m}$ is the chemical production rate of species i in reaction m and A_m^V the volume–specific surface area. The flux of the species J_i is dependent on the effective transport coefficient $D_{i,eff}$, the gradient of concentration c_i, and the gradient of the electrical potential ϕ_{elyt}.

$$J_i = -D_{i,eff}\frac{\partial c_i}{\partial t} - \frac{z_i F}{RT} c_i D_{i,eff} \frac{\partial \Phi_{elyt}}{\partial y} \tag{8.2}$$

It is assumed that electroneutrality holds for all control volumes, i.e. there is no charge separation at the length scale of the discretization (8.3). The total current density i (8.4) results from the current produced by charge transfer reactions (Faradaic reactions) i_f (8.5) and charge/discharge processes of an electrochemical double layer i_{dl} located at the surface of the electrodes (8.6). The potential between the components of the batteries are described by (8.7) and (8.8).

$$0 = \sum_m z_i F\, A_m^V \dot{s}_{i,m} - \sum_i z_i F \frac{\partial J_i}{\partial y} \tag{8.3}$$

$$i = \int_{y=0}^{l_{electrode}} \left(i_F + i_{dl}\right) dy \tag{8.4}$$

$$i = \sum_m F A_m^V \dot{s}_{electron,m} \tag{8.5}$$

$$i_{dl}(t) = A_{dl} C_{dl} \frac{\partial(\Delta\emptyset)}{\partial t} \tag{8.6}$$

$$\Delta\phi = \phi_{electrode} - \phi_{electrolyte} \tag{8.7}$$

$$E = \phi_{ca} - \phi_{an} \tag{8.8}$$

An elementary kinetic approach is used in this model for the surface reactions. The chemical production rate of species i in a reaction m is described by the mass action kinetics [177]. The Arrhenius rate law describes the forward reaction (8.10) while the reverse rate constant can be calculated by the law of mass action (8.11). Activation energies are assumed zero, and temperature constant; since no temperature–dependent kinetic coefficients are available.

$$\dot{s}_i = \nu_i \left(k_\mathrm{f} \prod_i c_i^{\nu_i'} - k_\mathrm{r} \prod_i c_i^{\nu_i''} \right) \tag{8.9}$$

$$k_\mathrm{f} = k_0 \exp\left(-\frac{E_\mathrm{f}^\mathrm{act}}{RT} \right) \exp\left(-\frac{\alpha z F}{RT} \Delta\phi \right) \tag{8.10}$$

$$\frac{k_\mathrm{f}}{k_\mathrm{r}} = \exp\left(-\frac{\Delta G}{RT} \right) \tag{8.11}$$

A multi–phase management is necessary for modeling the evolution of the bulk volume fractions in time and space. Changes in volume fraction are caused by the formation or reaction of a phase or a phase transition. The set of equations for the multi–phase management is described by the continuity equation for the bulk phases (8.12), in which the mass conservation is defined in terms of the mass density ($\varepsilon\rho$); and the dependence of diffusion coefficients on bulk (8.13). All equations are solved numerically using time–dependent boundary conditions which correspond to the experimental protocol.

$$\frac{\partial(\varepsilon_i \rho_i)}{\partial t} = M_i \sum_m A_m^\mathrm{V} \dot{s}_{i,m} \quad \text{with} \quad \sum_i \varepsilon_i = 1 \tag{8.12}$$

$$D_{i,\mathrm{eff}} = D_i \frac{\varepsilon_\mathrm{electrolyte}}{\tau_\mathrm{electrolyte}^2} \tag{8.13}$$

8.1.1 Model parameters

Mechanisms of reaction

Several mechanisms of reaction have been proposed in the last years for the Li–S system [12–17]. This was summarized in additional information (section 11.4.1). The reactions proposed in this model are presented below. Contrary to Kumaresan [140], no precipitation was considered for the polysulfides S_8^{2-}, S_6^{2-}, S_4^{2-}, and S_2^{2-}. Only the end products of charge $S_{8(s)}$ and discharge $Li_2S_{(s)}$ precipitates in the electrode, as already confirmed experimentally using XRD [6] (chapter 4).

$$S_{8(s)} \rightleftarrows S_{8(diss)} \tag{8.14}$$

$$\tfrac{1}{2}\, S_{8(diss)} + e^- \rightleftarrows \tfrac{1}{2}\, S_8^{2-} \tag{8.15}$$

$$S_6^{2-} + e^- \rightleftarrows \tfrac{3}{2}\, S_4^{2-} \tag{8.16}$$

$$\tfrac{1}{2}\, S_4^{2-} + e^- \rightleftarrows S_2^{2-} \tag{8.17}$$

$$\tfrac{1}{2}\, S_2^{2-} + e^- \rightleftarrows S^{2-} \tag{8.18}$$

$$2\, Li^+ + S^{2-} \rightleftarrows Li_2S_{(s)} \tag{8.19}$$

Initial concentration values of species are presented in Table 17. Prior to the actual transient simulation the initial concentrations of dissolved species are determined as follows: first, concentrations are set to arbitrary, but consistent (e.g. electroneutral) values. Then a simulation is run, where the electrical current is assumed to be zero and the volumes of all phases constant. Over time, the system will minimize its free energy by equilibrating species concentrations. Once a stable equilibrium is reached, these concentrations will be used as the initial values for the real transient simulation.

Low rate constants were considered for the reactions that involve solid products. The low dissolution of sulfur in the electrolyte is a limiting step for the following reduction reactions, once dissolved, the reactions to S_8^{2-} and to lower order polysulfides are considered to be faster. The crystallization of $Li_2S_{(s)}$ is a determining process during discharge: as already observed in the XRD analysis, $Li_2S_{(s)}$ reacts slowly during discharge and is responsible for the extension of the second plateau at around 2.1 V. A very low concentration of $Li_2S_{(s)}$ is assumed to be present in the cathode at the beginning of the discharge to obtain better numerical stability. A nucleation process is considered in the model to describe the transition from virtually no solid Li_2S (i.e. bulk activity equals zero) to a situation where there are solid Li_2S particles throughout the cathode (i.e. bulk activity equals one).

Further considerations and parameters

The model parameters are obtained from literature, assumed a priori or known from experiments. They are summarized in Table 11 and Table 17. Only the parameters in equations (8.20)–(8.22) were fitted in this study to match the experimental results. The parameters g_1–g_6 are geometrical fit parameters. ε'_{Li2S} and ε'_{S8} are the maximum volume fraction of Li_2S and S_8 respectively. These empirical expressions describe the dependence of the surface areas of bulk phases (carbon black, sulfur and Li_2S) on the bulk volume fraction ε. For S_8 and Li_2S a nucleation term of the form $1/(1 + e^{-\varepsilon})$ is included in the equations to describe the transition from the completely dissolved state to the solid bulk (equations (8.20) and (8.21)). Additionally, the S_8 phase contains a term of the form $\varepsilon^{3/2}$, which expresses the relation of surface area to volume for spherical bulk particles. A reduction of the electrochemically active carbon surface area is modeled to describe the deposition of Li_2S on this surface (8.22). Even though there is no direct experimental proof for either of these mechanisms, they allow describing both the formation of solid phases and the overpotential reasonably well without adding a complex 3D–resolved microstructure representation to the model. The specific surface area of the cathode was experimentally determined with Krypton adsorption measurements (BET) (see section 11.1.3).

$$A^{\mathrm{V}}_{\mathrm{S_8}} = A^{\mathrm{V}}_{\mathrm{S_8},0} \cdot \left\{ 1 + \exp\left(- \frac{\varepsilon_{\mathrm{S_8}} - \varepsilon'_{\mathrm{S_8}} / g_1}{\varepsilon'_{\mathrm{S_8}} / g_2} \right) \right\}^{-1} \cdot {\varepsilon_{\mathrm{S_8}}}^{3/2} \tag{8.20}$$

where, $g_1, g_2 = 50$

$$A^{\mathrm{V}}_{\mathrm{Li_2S}} = A^{\mathrm{V}}_{\mathrm{Li_2S},0} \cdot \left\{ 1 + \exp\left(- \frac{\varepsilon_{\mathrm{Li_2S}} - \varepsilon'_{\mathrm{Li_2S}} / g_3}{\varepsilon'_{\mathrm{Li_2S}} / g_4} \right) \right\}^{-1} \tag{8.21}$$

where, $g_3 = 3, g_4 = 5$

$$A^{\mathrm{V}}_{\mathrm{Li_2S}} = A^{\mathrm{V}}_{\mathrm{Li_2S},0} \cdot \left\{ 1 + \exp\left(- \frac{\varepsilon_{\mathrm{Li_2S}} - \varepsilon'_{\mathrm{Li_2S}} / g_3}{\varepsilon'_{\mathrm{Li_2S}} / g_4} \right) \right\}^{-1} \tag{8.22}$$

where, $g_5 = 0.5, g_6 = 256$

Table 11: Further parameters used for the model. Values are given for *T* = 298 K and *p* = 101325 Pa. Parameters are either known from experiments (†), known from literature (*) or assumed (°).

	Cathode		
Thickness:	15 µm†	Control volumes:	15
Bulk phases	Volume fraction (ε)		
Sulfur	0.0259† (= 50 wt. % of solids)		
Carbon	0.0259† (= 40 wt. % of solids)		
Binder (PVDF)	0.0071† (= 10 wt. % of solids)		
Electrolyte	0.8355† (= 84 % porosity)		
Lithium sulfide	$2.0 \cdot 10^{-4}$°		
Void space	0.1000°		
Interfaces	Specific area° (A_0^{V}) / $m^2\ m^{-3}$		
Sulfur–Electrolyte	$1.0 \cdot 10^{5}$		
Carbon–Electrolyte	$1.1 \cdot 10^{7}$		

Li_2S–Electrolyte	$1.0\cdot10^{5}$		
	Separator		
Thickness	25 µm†	Control volumes	25
Bulk phases	Volume fraction (ε)		
Electrolyte	0.41*		
Separator	0.59*		
	Anode		
Thickness	5 µm† (reactive top layer)	Control volumes	5
Bulk phases	Volume fraction (ε)		
Lithium	0.63°		
Electrolyte	0.37°		
Interfaces	Specific area° (A_0) / $m^2\ m^{-3}$		
Lithium–Electrolyte	$1.0\cdot10^{6}$		
	Reactions		
Chemical equation	Forward rate / $kmol\cdot m^{-2}\cdot s^{-1}$	Molar Gibbs free energy/$J\cdot mol^{-1}$	
$S_{8(s)} \rightleftarrows S_{8(diss)}$	$1.0\cdot10{-}5$°	16.5°	
$\frac{1}{2}\,S_{8(diss)} + e^{-} \rightleftarrows \frac{1}{2}\,S_8^{2-}$	$9.0\cdot10^{9}$°	−226.8°	
$\frac{3}{2}\,S_8^{2-} + e^{-} \rightleftarrows 2\,S_6^{2-}$	$1.0\cdot10^{11}$°	−188.3°	
$S_6^{2-} + e^{-} \rightleftarrows \frac{3}{2}\,S_4^{2-}$	$1.0\cdot10^{8}$°	−179.6°	
$\frac{1}{2}\,S_4^{2-} + e^{-} \rightleftarrows S_2^{2-}$	$4.0\cdot10^{11}$°	−132.3°	
$\frac{1}{2}\,S_2^{2-} + e^{-} \rightleftarrows S^{2-}$	$4.0\cdot10^{11}$°	−116.5°	
$2\,Li^{+} + S^{2-} \rightleftarrows Li_2S_{(s)}$	$1.0\cdot10^{16}$°	−149.1°	
$Li \rightleftarrows Li^{+} + e^{-}$	$1.0\cdot10^{-5}$°		

8.2 Simulations and correlation with experimental results

In this section, the results obtained using UV–vis spectroscopy, XRD and EIS during cycling of the cell are interpreted with respect to the simulated output of the model.

8.2.1 Discharge profile

First, the experimental discharge profile is compared to the simulation in Figure 8.2. The first cycle of the Li–S cell (Cathode II) shows a discharge specific capacity of ~1200 Ah kg^{-1} which corresponds to 72% of the theoretical value. This deviation from ideal behavior may be explained by two different effects: Either 28% of S_8 remains completely inactive during discharge or some S_8 is not entirely reduced to Li_2S. In the XRD experiments no crystalline sulfur was observed at the end of discharge. However, this does not exclude the possibility that sulfur is present as cyclic molecule dissolved in the electrolyte or that it reacts completely to polysulfides which do not react totally to Li_2S. In the simulation, virtually all sulfur is dissolved during the first stage of the discharge. The end of the discharge is triggered by an increasing overpotential at the cathode side due to Li_2S deposition on the electrochemically active surface. At the discharge cutoff voltage only 62% of the total sulfur is precipitated as Li_2S; the remainder is dissolved in the electrolyte either as neutral S_8 or as partly reduced charged polysulfides S_x^{2-}.

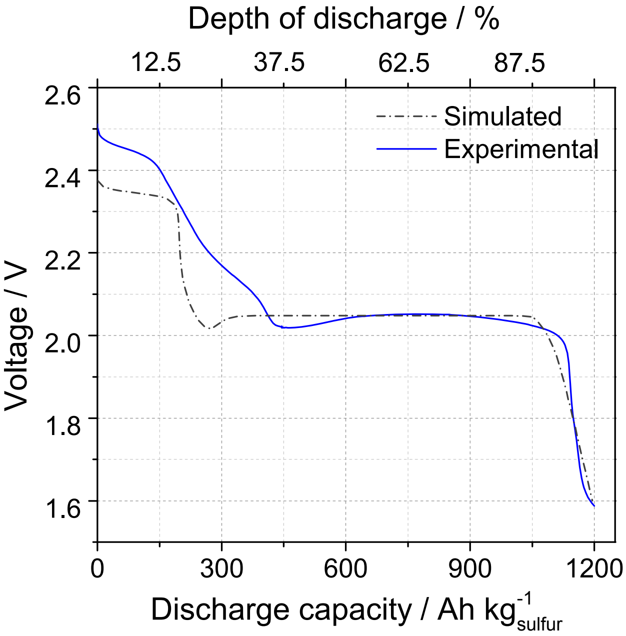

Figure 8.2: Experimental and simulated discharge profile at the first discharge.

While the experimental and simulated discharge profiles in Figure 8.2 look qualitatively similar, there are differences between the two datasets which can be attributed to the following effects: First, no explicit 3D–resolved model of the electrodes microstructure is included. While effective parameters, e.g. porosities, are chosen to be representative of the assumed microstructure, no extensive validation or fitting has been performed due to the lack of experimental evidence. Therefore, some important effects, e.g. nucleation and growth of solid particles can only be treated in a simplified fashion. Second, there are effects known to be present in the Li/S cell, which were excluded from the model, e.g. the polysulfide shuttle [18,178], disproportion reaction of polysulfides, and SEI formation [179,180]. While it is considered that these are important effects, they are not relevant to this study, which focuses on the reaction products and intermediates during discharge. Still there might be a visible impact on the discharge profiles.

8.2.2 Formation, dissolution and reaction of end products

In Figure 8.3, the volume fractions of solid S_8 and Li_2S in the porous cathode are plotted and compared to the results obtained by *in situ* XRD [6]. The relative integrated intensity of the Braggs peaks is directly proportional to the volume of the crystalline species in the sample. It is evident that, when starting from a fully charged cell, the two solid phases do not coexist during a discharge at a slow rate. This changes, however, if the rate of discharge is increased (Figure 8.4). The main difference is that significant amounts of both solid S_8 and Li_2S coexist during the intermediate discharge phase, which in turn affects the concentration of dissolved species. As a result, the dissolved polysulfides are either in equilibrium with the solid S_8 or Li_2S phase, but never both.

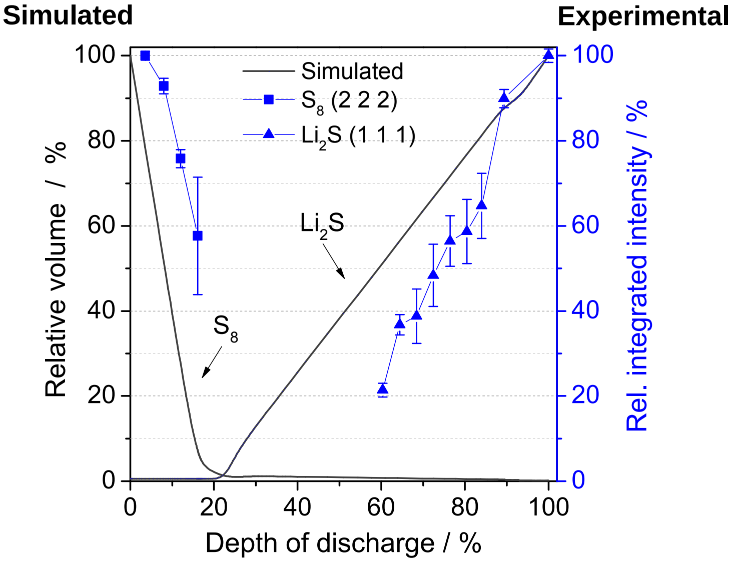

Figure 8.3: Relative volume of S_8 and Li_2S (simulated) compared with relative integrated intensity of the Bragg peaks S_8 (222) and Li_2S (111) obtained by *in situ* XRD [6] **during the first discharge.**

The belated onset of Li_2S formation as well as the discrepancy between the simulated and experimental results can be explained as follows: At the beginning of the discharge there is virtually no solid Li_2S in the cell, therefore no nuclei for crystallization are available. Only once the electrolyte becomes supersaturated with S^{2-}, crystallization is set off and solid Li_2S particles start to form. However, in the beginning these particles are nano–sized and the concentration is too low in order to be detected by XRD. Once the particles grow and fill more volume, they can be detected by XRD more readily.

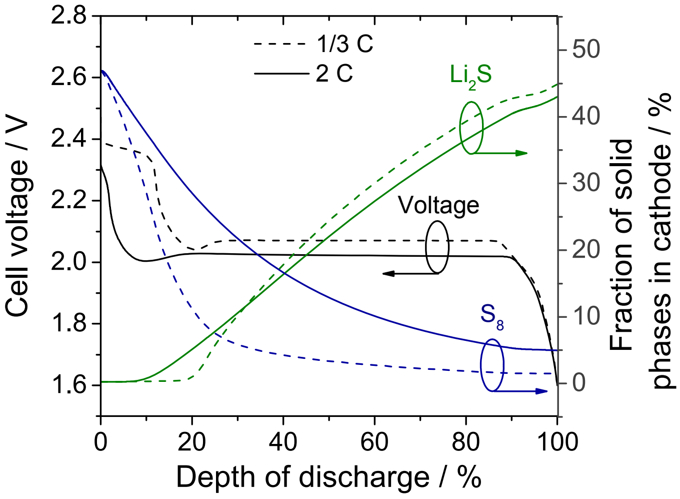

Figure 8.4: Simulated discharge of the cell at 2C and ⅓C rate. 100% (DOD) is defined as the maximal specific capacity reached in the simulation (not the theoretical specific capacity). In this case 100% DOD is 1130 Ah·kg$_S^{-1}$ for 2C and 1175 Ah·kg$_S^{-1}$ for 1/3C.

Assuming that Li_2S is built up homogenously on the surface of the CB particles, the film thickness of Li_2S (l) can be calculated using the simulated volume fraction of Li_2S (V_{Li2S}) with respect to the volume of carbon black (V_{CB}), and assuming spherical CB particles of 50 nm radius (r). Thus, l can be calculated as it follows:

$$\frac{V_{Li2S}}{V_{Li2S}+V_{CB}} = \frac{\frac{3}{4}\pi(R-r)^3}{\frac{3}{4}\pi R^3} \tag{8.23}$$

$$l = R - r = \frac{r}{\sqrt[3]{1-\frac{V_{Li2S}}{V_{Li2S}+V_{CB}}}} - r \tag{8.24}$$

where R= radius of the CB particle including the Li_2S layer

The growth of the Li_2S film thickness during discharge is displayed in Figure 8.5 (a). Up around 20% DOD the formation of Li_2S starts. However, it was already shown that the crystalline Li_2S is detected first up to 60% DOD using XRD while an amorphous phase is identified before. The reaction of polysulfides to Li_2S is limited by the formation of this isolating layer, thus when a 17 nm thick film of Li_2S is formed over the CB particles, electrons cannot be transferred anymore from the CB surface to the polysulfides located on the Li_2S. Thus, the potential reduces, and the battery cannot discharge further. In addition, the formation of this layer is observed also by the EIS results of represented by the R_3 element.

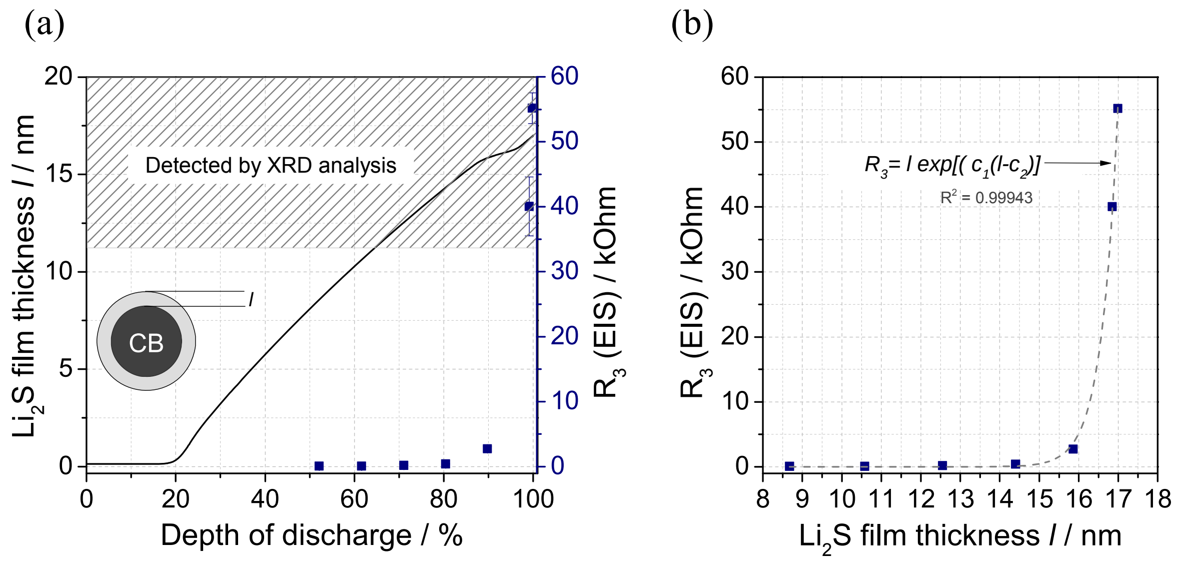

Figure 8.5: Concentration of polysulfides during discharge.

As it can be seen in the left axis of Figure 8.5 (a), this increases exponential during discharge. The empirical equation $R_3 = l \exp[c_1 (l - c_2)]$, was presented by Albertus and coworkers [181] to describe the dependence of the resistance with the layer thickness (*l*), where c_1 and c_2 are constants. In this work, this was used to fit the experimental (R_3) and simulated (*l*) results. In Figure 8.5 (b) the dependence of R_3 with the calculated film thickness is displayed and the fitted curve is shown as dotted line. The value of the constants c_1 and c_2 were estimated to be 2.34 and 16.48 respectively, where *R* is in kOhm and *l* in nm.

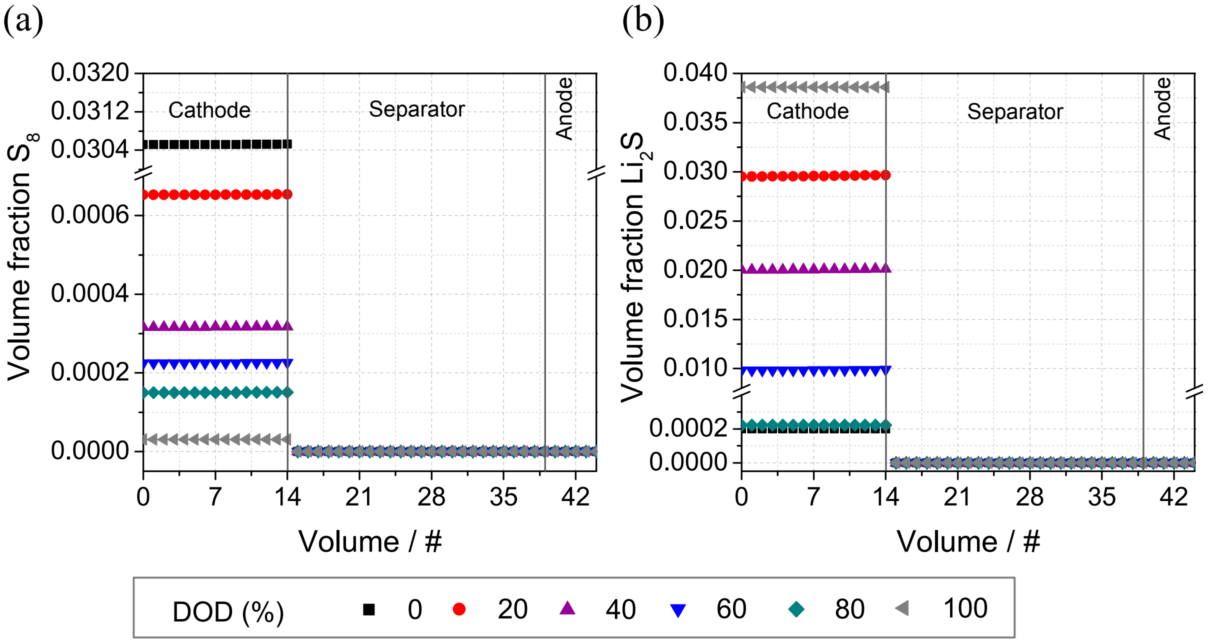

Figure 8.6: Concentration profile across the cell of volume fraction of S_8 and Li_2S (simulated).

In this model the formation of solid species and crystallite growth occur only in the bulk of the cathode and the volume fraction is stable through the whole volume when the rate of discharge is low as it can be seen in Figure 8.6.

8.2.3 Formation and reaction of intermediate products

Figure 8.7 compares the results of UV–vis spectroscopy with EIS [7] and the outcome of the simulation. The anode charge resistance as determined by EIS increases rapidly during discharge, reaching a maximum at around 35% DOD, after which it decreases continuously until the end of discharge.

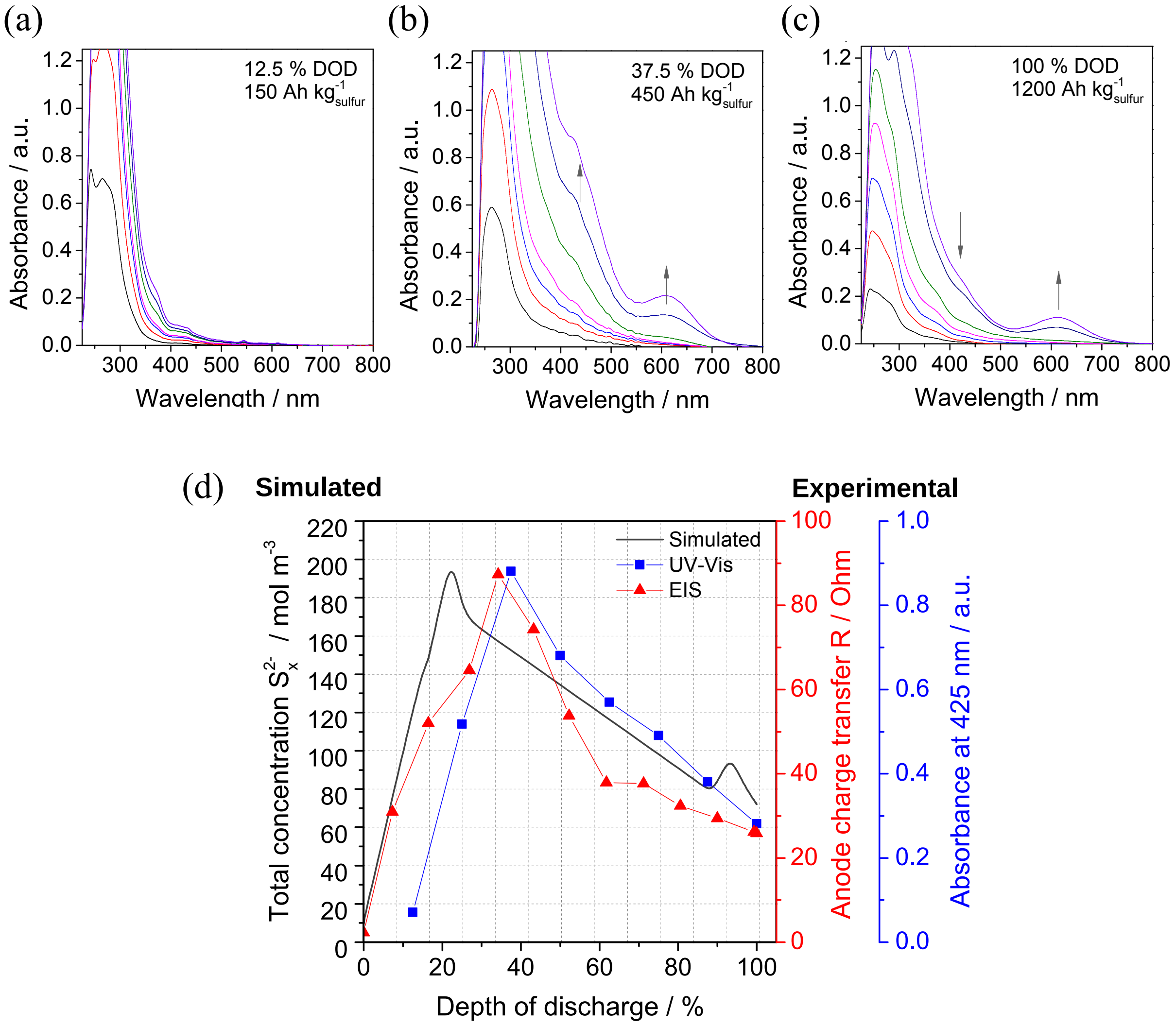

Figure 8.7: Total concentration of S_x^{2-} species (simulated) compared with the absorbance at 425 nm (UV–vis spectroscopy), and the anode charge transfer resistance (EIS) (d). Selected spectra to show the behavior of the absorbance bands (a–c).

The charge resistance at the anode side is directly proportional to the concentration of polysulfides. This has previously been confirmed by evaluating the electrolyte resistance, which has a similar behavior during cycling [7]. Comparing these results with the absorbance at 425 nm, a clear correlation can be seen, which confirms the maximum concentration of polysulfides right at the beginning of the second plateau (~37% DOD). Unlike with experiments, all internal states of the battery are directly accessible in the simulated results. Therefore, the concentrations of polysulfide can be studied at all times during the simulated discharge (Figure 8.8). Indeed the results qualitatively confirm that the polysulfide concentration is highest early during discharge; right after all sulfur has been dissolved. Also, it can be seen that the total concentration of dissolved polysulfides varies to a great extent during the discharge. As discussed above, a significant portion of polysulfides is still dissolved in the electrolyte at the end of discharge; this is reflected in the simulation results as well as in the UV–vis spectra (Figure 8.7 (c)).

In Figure 8.8 the variation on concentration of the polysulfide species is represented during discharge. S_8^{2-} starts forming right at the beginning of the cycle, reaching a maximum at approx. 20% DOD. Then the concentration reduces, when the S_6^{2-} and S_4^{2-} begin to build up. The concentration of the species decreases continuously upon discharge, and at around 90% DOD a slight increase of concentration is observed for species S_6^{2-} and S_4^{2-}. This behavior at the end of discharge was observed experimentally for anion radical $S_3^{\bullet -}$, which increases the absorbance at the end of discharge (Figure 8.7 (c). This species is not considered in the model, because no dissociation reactions were included, but it is known as dissociation product of S_6^{2-} [13] and S_4^{2-} [12].

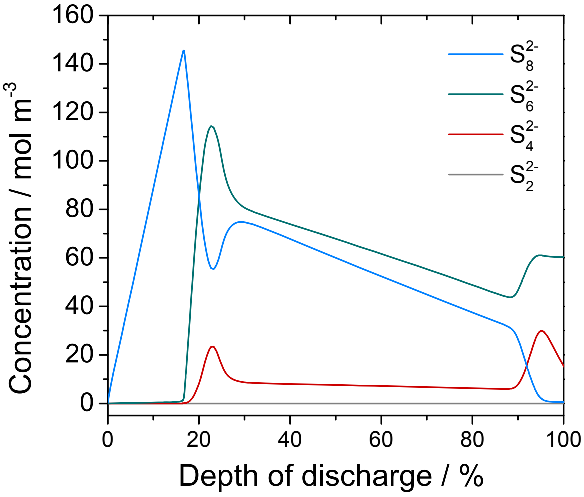

Figure 8.8: Concentration of polysulfides during discharge.

Figure 8.9 displays the concentration of the species Li$^+$, S_8^{2-}, S_6^{2-} and S_4^{2-} for all control volumes at different DODs. These profiles are highly dependent on the discharge rate as well as on the diffusion/reaction equilibrium, which changes considerably with the current.

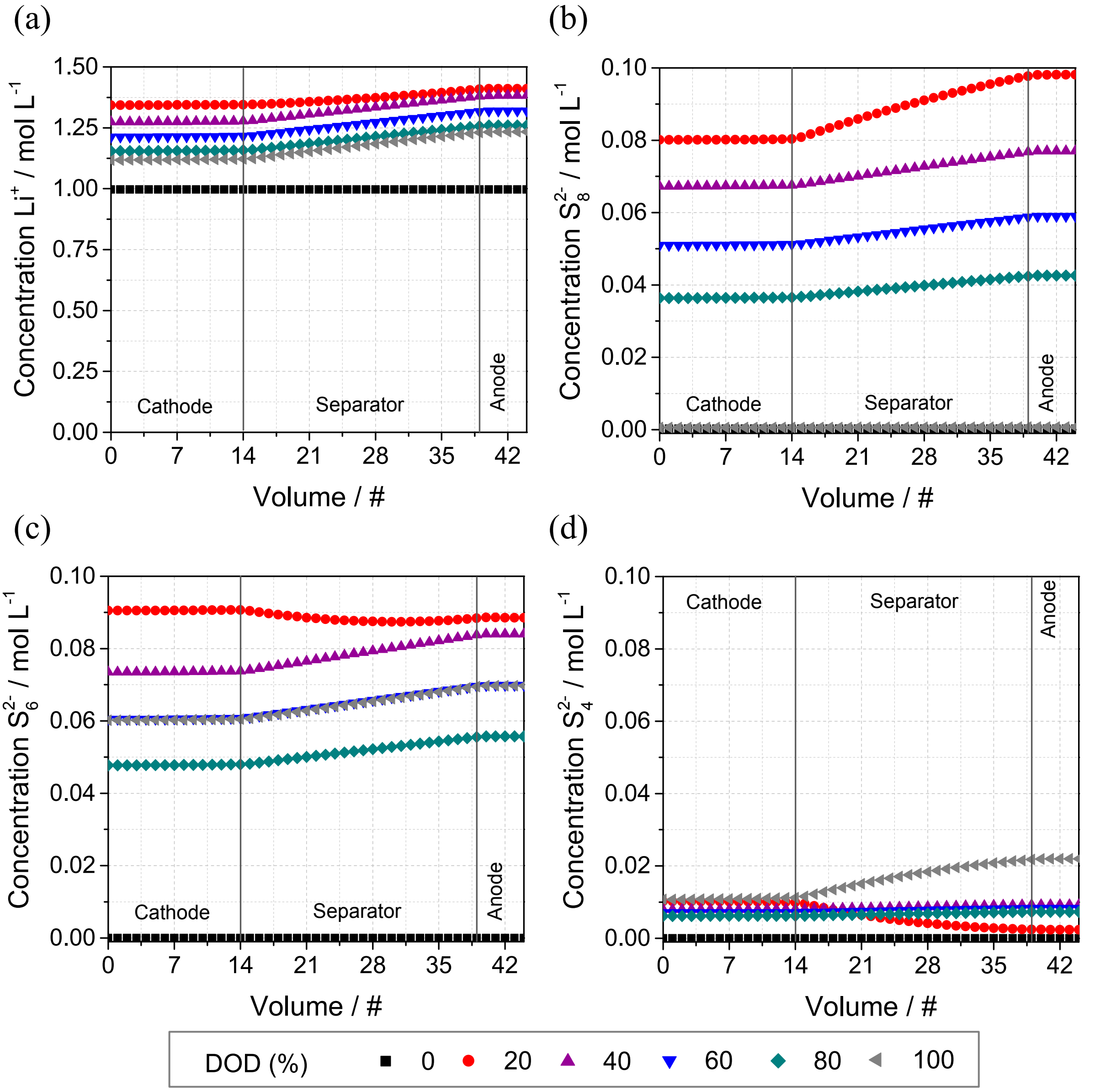

Figure 8.9: Concentration profile across the cell of Li$^+$, S_8^{2-}, S_6^{2-} and S_4^{2-} during discharge (simulated).

For the selected discharge current, the following behavior could be observed. The concentration of the species does not vary considerably throughout the cathode volume due to the low rate of discharge. However, concentration gradients are presented through the separator/electrolyte volume. The amount of Li$^+$ and S_8^{2-} species increases in direction to the anode surface during the discharge process. For S_6^{2-} the highest concentration is located in the cathode side at the beginning of discharge (20% DOD), while at higher DOD the concentration increases in direction to the anode side. At 20% DOD, the maximum concentration of S_4^{2-} is on the cathode side. Afterward, the concentration is almost constant through the separator, and at the end of discharge the profile in the cathode increases in direction to the anode surface. Although the reduction of sulfur species occur in the cathode by the acceptance of electrons, S_x^{2-} dissolves in the electrolyte and diffuses to the anode side due to the gradient of concentration. The model does not take in account reactions between polysulfides and the Li–anode, therefore, the different profiles obtained for the polysulfides are dependent on the time of formation of each polysulfide and also on the different diffusion constants. The electrolyte immersed in the separator acts as a buffer for the chemical environment in the cathode, reducing the immediate effect of current changes (or voltage spikes) on the cell voltage.

8.3 Conclusions

A numerical simulation of the discharge process was performed for the Li–S battery using the model developed by D. Fronczek [174]. The simulation output was validated with and compared to the results obtained experimentally using XRD, EIS, and UV–vis spectroscopy. Besides confirming the experimental findings, the model allows for the study of properties not easily accessible to experiments like concentrations of polysulfides. The model affirms that the polysulfide concentration is highest during discharge when all sulfur has been dissolved. Also, it can be concluded that a significant portion of polysulfides is still dissolved at the end of discharge. This seems to be of significant importance for improving the discharge capacity and cycling stability of lithium sulfur cells.

9 Summary and conclusions

Challenges facing the application of lithium–sulfur batteries were revealed throughout this work. New insights into the reaction and degradation mechanisms can contribute to the improvement of the capacity and stability of the battery at high discharge rate and prolonged cycle life. In this work, the use of several characterization techniques allowed the identification of several processes and confirmation of statements by comparing results from different sources. The following techniques were successfully applied on the study of Li–S batteries:

- *operando* X–ray diffraction (XRD) for detection and quantification of crystalline products Li_2S and S_8,
- electrochemical impedance (EIS) for analysis of electrolyte resistance, charge transfer resistance in the electrodes, and reaction and dissolution Li_2S and S_8,
- UV–vis spectroscopy for detection and quantification of dissolved species (mainly polysulfides),
- Atomic force microscopy (AFM) for surface analysis and formation of isolating layers,
- Scanning electron microscopy (SEM) for analyzing distribution of sulfur particles and CB and morphological changes during cycling, and
- Thermal analysis combined with mass spectroscopy (TG/DSC–MS) to study the degradation of components and morphological changes on the cathode.

In a sulfur composite cathode, micro–sized sulfur particles are surrounded by CB nanoparticles, this allows the electron transfer from the active material to the cathode collector into the electrical circuit. When the discharge starts, some of the sulfur is already dissolved in the electrolyte, the rest is continuously dissolved and reduced to S_8^{2-}. This process occurs in the first 20–30% DOD, which is represented in the first plateau of the discharge profile. The dissolution and reaction of sulfur reduces in 42% the charge transfer resistance in the cathode, enhancing in this way the further reduction of polysulfides in the surface of the carbon matrix. The cathode surface presents at this stage micro–cavities where the sulfur particles were located before. On the other side, the electrolyte resistance as well as the anode transfer resistance increases due to an increment of polysulfides dissolved in the electrolyte; polysulfides increase the viscosity of the electrolyte and can diffuse to the anode side. Mainly high order polysulfide (S_8^{2-}, S_6^{2-}, S_4^{2-}) and the product of its dissociation $S_3{\cdot}^-$ are presented in this stage. The reduction of polysulfides proceeds and a maximum is identified at the beginning of the second plateau in the discharge profile at around 40% DOD. At this stage, maximum values are obtained for the electrolyte resistance (EIS) and the absorbance of the electrolyte (UV–Vis). Moreover, no detectable crystalline phase is present, but probably amorphous Li_2S starts to build up. At 60% DOD nano crystalline Li_2S is formed in the cathode and increases until the end of discharge. A capacity of ca. 1200 Ah kg_S^{-1} is reached for the first discharge, which corresponds to 72% of the theoretical capacity. This 28% of missing capacity is not related to the low utilization of sulfur, which actually completely reacts to polysulfides, rather it is associated to the incomplete reaction of polysulfides to Li_2S. This is evidence by changes in the anode charge transfer resistance, before cycling: 2 Ohm and at 100% DOD: 19.1 Ohm (22% of the maximum value at ~40% DOD). The electrolyte resistance increases also in 15% after discharge due to remaining dissolved polysulfides and the absorbance band of the radical $S_3{\cdot}^-$ is still identified at the end of discharge. Thus, at the end of discharge, the cell consisted of amorphous Li_2S and nano–crystalline Li_2S in the cathode as well as the remaining soluble polysulfide in the electrolyte. The surface of the cathode is no longer conductive due to the formation of the isolating Li_2S film (<1% of conductive area).

Although a non–conductive film is build up after discharge, this does not inhibit the reaction of crystalline Li_2S to soluble polysulfide in the first charge and the further oxidation to solid sulfur. However, the amorphous phase remains inactive in the cathode during the further cycles, which is the main cause for the diminution of capacity in the first cycle. The formation of sulfur in the first charge is detected just at the end of discharge. Part of the sulfur crystallizes in oriented nano sized crystallites which arranges in large agglomerates in the cathode surface and over the separator. These crystallites can growth through the separator pores blocking probably the transfer of lithium ions between electrodes. The rest of the sulfur remains as amorphous phase.

The formation and reaction of sulfur and Li_2S during cycling affects extremely the morphology of the cathode. The formation of isolating layers at the end of the charge and discharge is inevitable using the present cathode and cell configuration. Low retention of active material in the bulk of the electrode was confirmed by sulfur depositions over the cathode and separator surfaces. Further degradation processes take place in the cell and they are related to the selected binder (PVDF) and the CB structure. The degradation of the PVDF binder, which was not detected in the TG curves after cycling, is one of the causes that affect the binding between the CB and S particles during cycling. An extreme reduction of the oxidation temperature of CB from 660 °C (before cycling) to 469 °C (after cycling) reveals that the conductive material is also affected by the electrochemical cycling. This reduction may well be explained by the destruction or modification of the CB structure, which is important for the electron transport in the cell.

Cathode with well–dispersed and small sulfur particles in the carbon matrix improves the sulfur utilization during the first cycles, which resulted in an increased of capacity from 275 to 528 Ah kg_S^{-1} after 50 cycles. However, the capacity fading of the battery was still high (47%) and could be improved by the utilization of $LiNO_3$ as co–salt in the electrolyte. With this cell configuration, discharge capacities of 800 Ah kg_S^{-1} were achieved (50 cycles, 0.18 C–rate). Nevertheless, the capacity fading of the battery is still high (35% between the 1st and 50th cycle). This simple but industrially viable cell configuration may be further improved by the utilization of Li ion conductive layers which can be located over the cathode to enhance retention of the active material in the bulk of the electrode.

This work emphasizes the importance of *in situ* studies to understand the structural modifications of Li–S batteries and the influence in the degradation behavior during cycling.

10 Outlook

The characterization techniques and the corresponding experimental set up presented in this work can be further used to evaluate and confirm improvement of materials or fabrication steps in Li–S battery, as well as in other electrochemical systems. Unfortunately, most of the publications related with improvements in Li–S batteries show less information regarding the state of the cell after cycling, which is important for confirming promising results in capacity and stability.

It has been shown that the formation of solid products S_8 and Li_2S originates undesirable changes in morphology, which increases the degradation of the battery. XRD analyses revealed that sulfur phase changes after the first cycle, with a reorientation of its particles and amorphization. This means that the preferred state of sulfur in the electrochemical cell sulfur is not the one expected under standard ambient temperature and pressure. Taking this into consideration, improvements on the cell capacity and stability maybe expected by introducing sulfur in amorphous state or as oriented particles in a conductive matrix, preventing in this way the formation of large particle or agglomerates of sulfur and Li_2S.

Further research into the identification and quantification of polysulfide in different solvents are needed for a better understanding of the reaction mechanisms in the cell. This may include the application of characterization techniques that complement the information obtained with UV–vis spectroscopy, like Raman spectroscopy and X–absorption spectroscopy.

The development of Li–S batteries is expected to continue in the next decades, probably in a rush way. In the last two years, important improvements on the sulfur cathode have been achieved. However, in the future, the battery safety and the impact of its components on the environment should not be compromised by battery performance. Approaches focused on replacing lithium anode by a safer material, like Si or Mg, should be fostered for the use of sulfur cathodes in mobile applications. By replacing the Li–anode, new challenges related with the cathode design and selection of electrolyte will come along. Moreover, developments of practical battery systems that can be fabricated in large–scale and at low cost are still important challenges in the development of cost–effective Li–S cells.

11 Additional information

11.1 Battery fabrication and electrochemical characterization

11.1.1 Swagelok® cells for electrochemical testing of Li–batteries

During this work, the materials and dimensions of the Swagelok® cells were modified. First, stainless steel fittings were used (Figure 11.1 (a)). In this case, an additional foil must be added in the internal wall of the cell to avoid short circuit. Although a metal cell is beneficial due to the high mechanical stability, the use of an additional foil increases the assembling time of the cell. Moreover, occasionally short circuits occurred due to displacement of the foil during assembling. Second, the cell body was replaced by Polytetrafluoroethylene (PTFE) fitting (Figure 11.1 (b)). Although here short circuits were avoided, this material degraded with the time when contact with Li, creating black deposition in the internal walls. Moreover, PTFE cells deformed after several uses and lost the hermetic sealing.

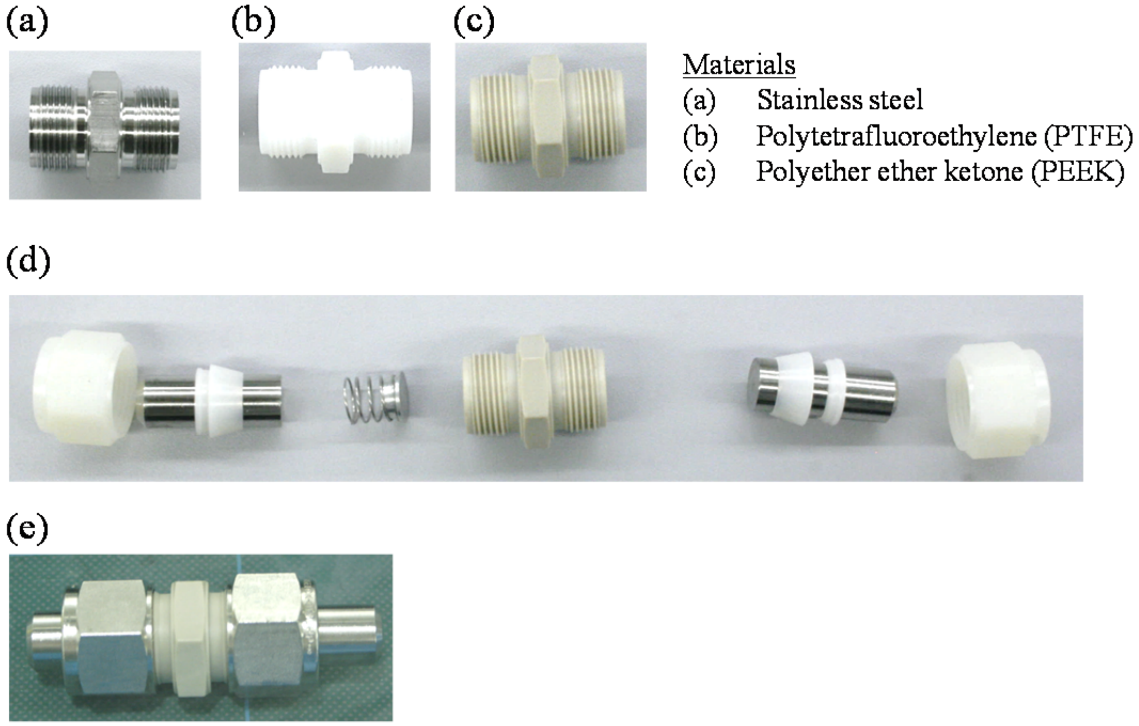
(a)
(b)
(c)
Materials
(a) Stainless steel
(b) Polytetrafluoroethylene (PTFE)
(c) Polyether ether ketone (PEEK)
(d)
(e)

Figure 11.1: Swagelok type cell and fittings for cell construction.

Finally, PEEK® was selected as material of the body (Figure 11.1 (c, d, e)). This material is stable chemically and mechanically, and it show good reproducibility of the cycling tests. Cells with the same material were made with larger size to test a larger electrode area (like the one used for TG/DSC measurements). Although, Swagelok® cells are well establish as testing cells in the battery labs. The use of coin cells is recommended for future work to test the performance of the cell in similar conditions as in the large scale fabrication.

11.1.2Images of cathodes and substrate

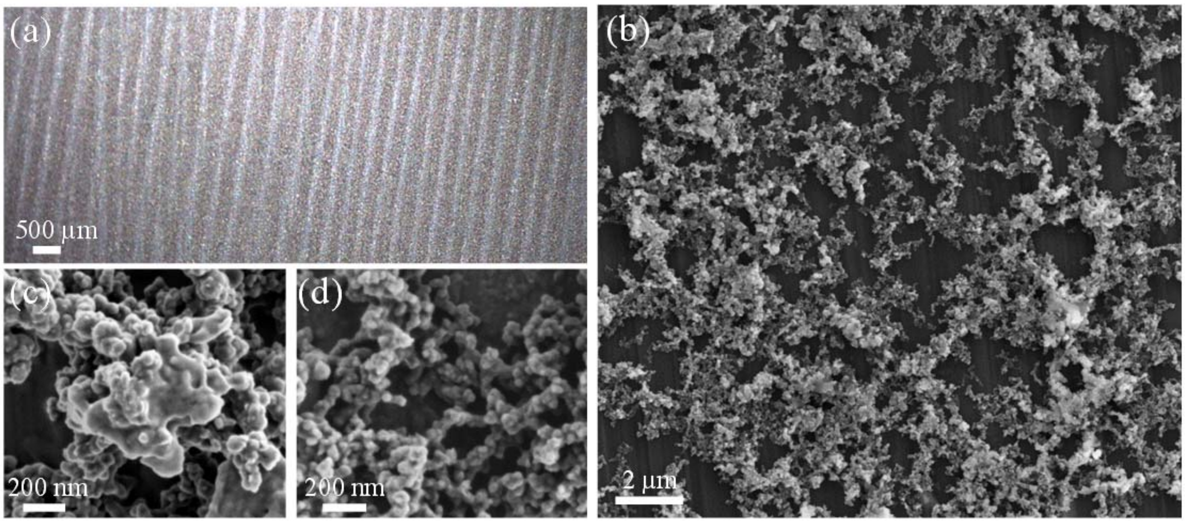

Figure 11.2: Showa Denko® substrate. (a) Microscopic picture. (b–d) SEM pictures.

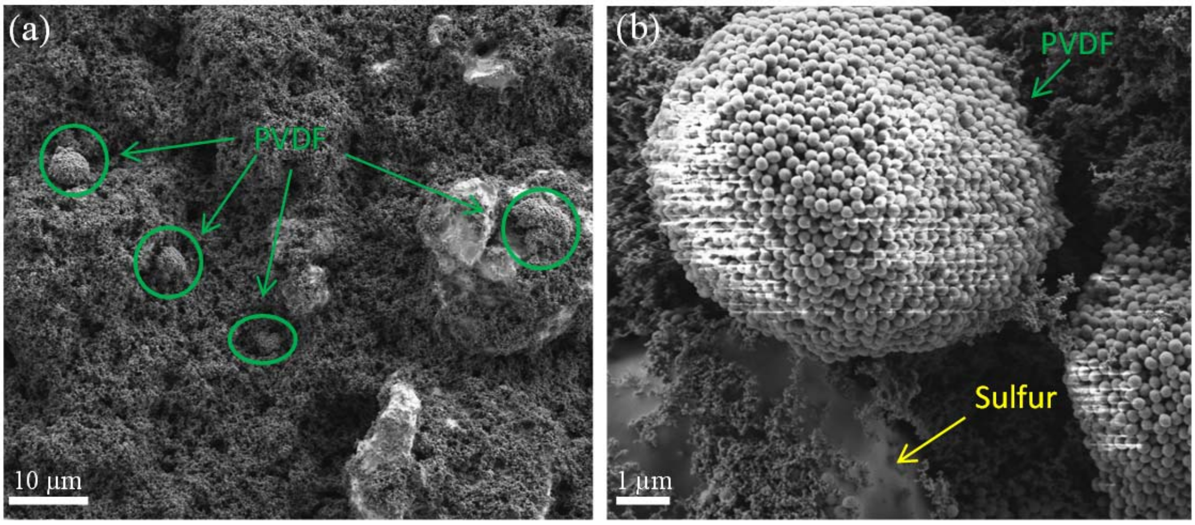

Figure 11.3: Non–dissolved PVDF particles on the surface of Cathode I.

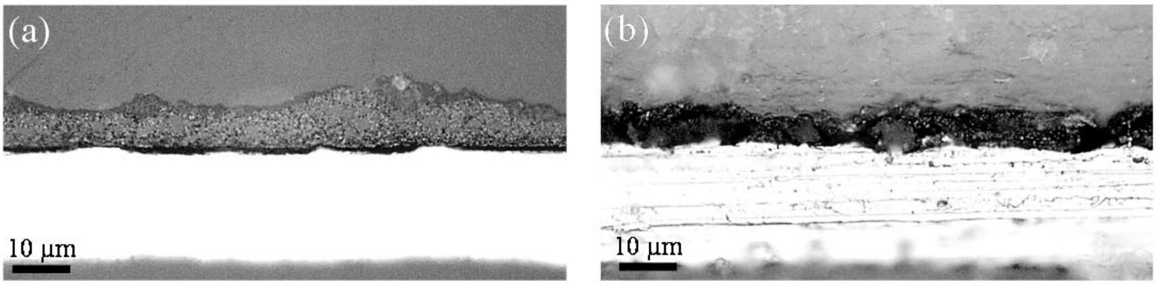

Figure 11.4: Microscopic pictures of cross section of the cathode layer over the aluminum collector.

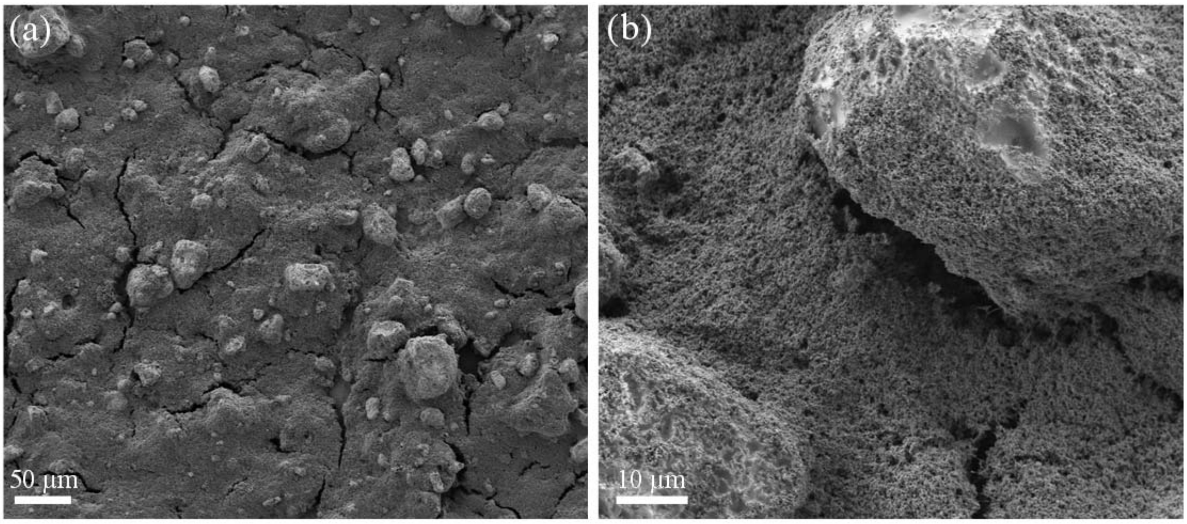

Figure 11.5: Cracks over the cathode surface cause by fast drying (Cathode I).

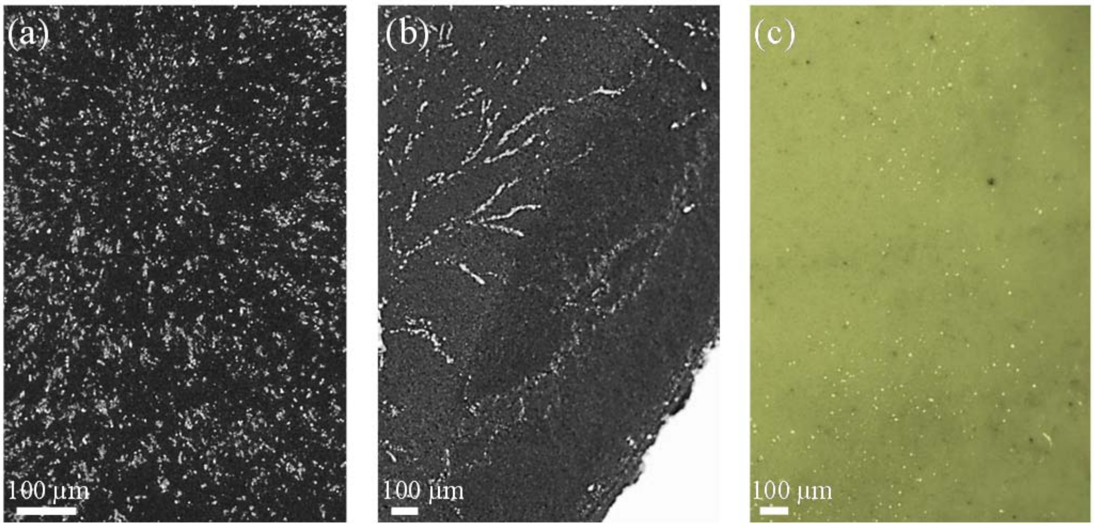

Figure 11.6: Microscopic pictures of cathode (a, b) and separator of a battery after its 1st charge (Cathode II, Electrolyte 1 M $LiPF_6$, 0.75 M $LiNO_3$ in TEGDME, Separator: Celgard 2500, anode: Lithium). End charge capacity ~1287 Ah kg_S^{-1}.

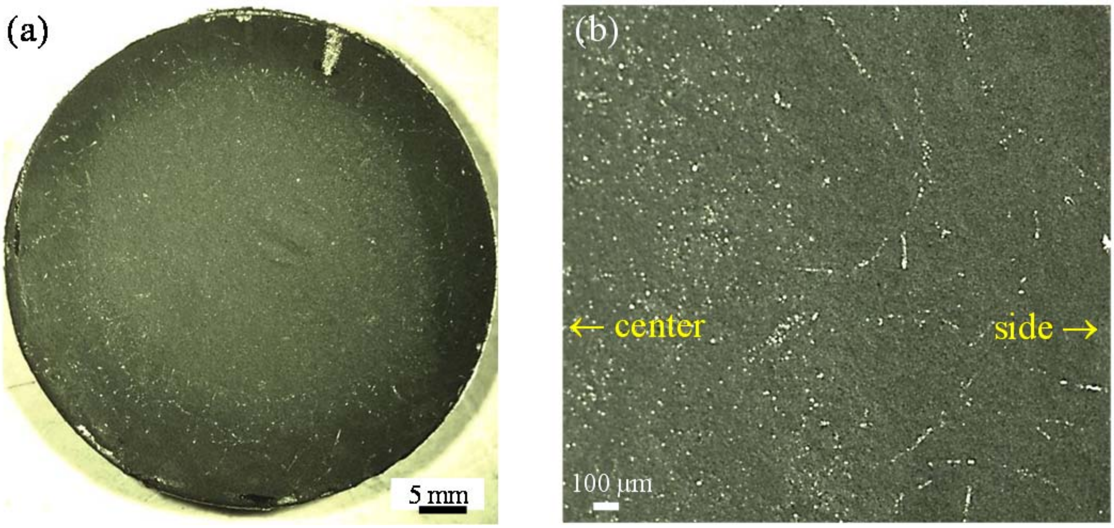

Figure 11.7: Microscopic pictures of cathode (a, b) and separator of a battery after its 5th charge (Cathode II, Electrolyte 1 M $LiPF_6$, 0.75 M $LiNO_3$ in TEGDME, Separator: Celgard 2500, anode: Lithium). End charge capacity ~1114 Ah kg_S^{-1}.

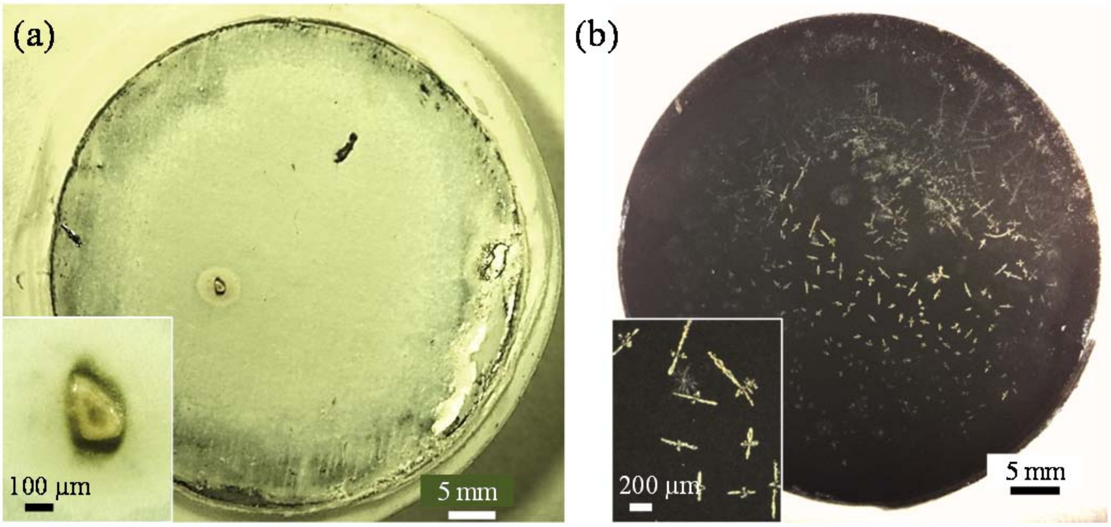

Figure 11.8: Microscopic pictures of cathode (a, b) and separator of a battery after its 11th charge (Cathode II, Electrolyte 1 M $LiPF_6$ in TEGDME, Separator: Celgard 2500, anode: Lithium). End charge capacity ~1211 Ah kg_S^{-1}.

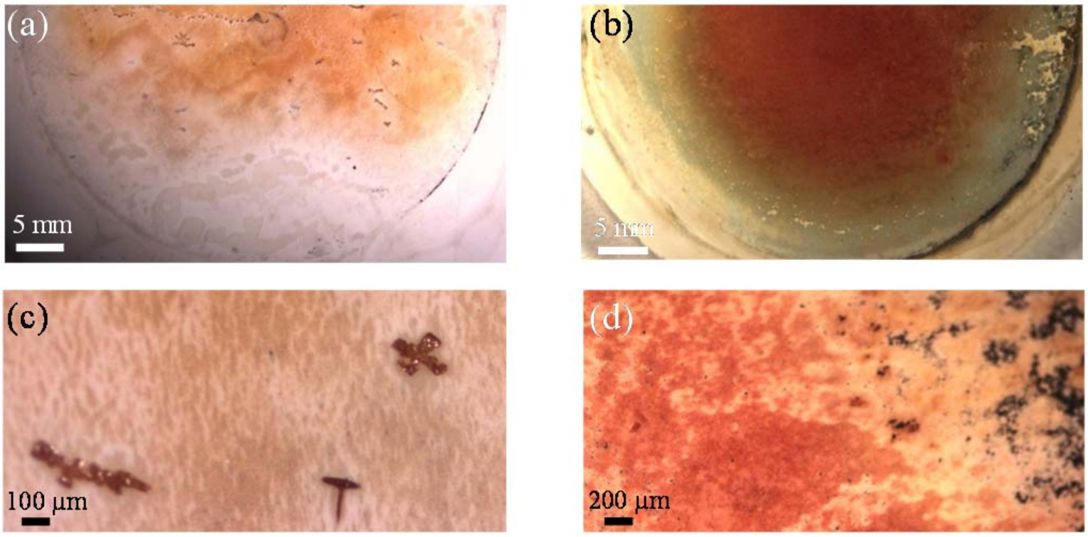

Figure 11.9: Microscopic pictures of cathode (a, b) and separator of a battery after its 64th charge (Cathode II, Electrolyte 1 M $LiPF_6$ in TEGDME, Separator: Celgard 2500, anode: Lithium). End discharge capacity ~500 Ah kg_S^{-1}. End charge capacity approx. 1155 Ah kg_S^{-1}.

11.1.3Krypton adsorption measurements

The specific surface area of CB and the cathode was measured using Krypton adsorption analysis (Figure 11.10, Figure 11.11). Krypton was used instead of nitrogen, because a low quantity of a thin cathode was measured. Since the total pore volumes and surface areas can be extremely small for such thin porous films, the pressure changes due to adsorption cannot be assessed with sufficient precision. Since the total pore volumes and surface areas can be extremely small for such thin porous films, the pressure changes due to adsorption cannot be assessed with sufficient precision and accuracy under said conventional conditions. When pore volume is reduced such as in thin films, gases with low sublimation capacity are needed to obtain more accuracy. The cathode samples consisted of the cathode layer (CB, PVDF and S) and the aluminum substrate. The specific area of carbon black is 60 $m^2\ g^{-1}$, while the specific area of the cathode was obtained subtracting the weight of the substrate and the specific area related to the substrate was considered negligible compared with the nano/micro–structured cathode layer. The specific area of the cathode layer measured is 10.45 ± 0.91 $m^2\ g^{-1}$.

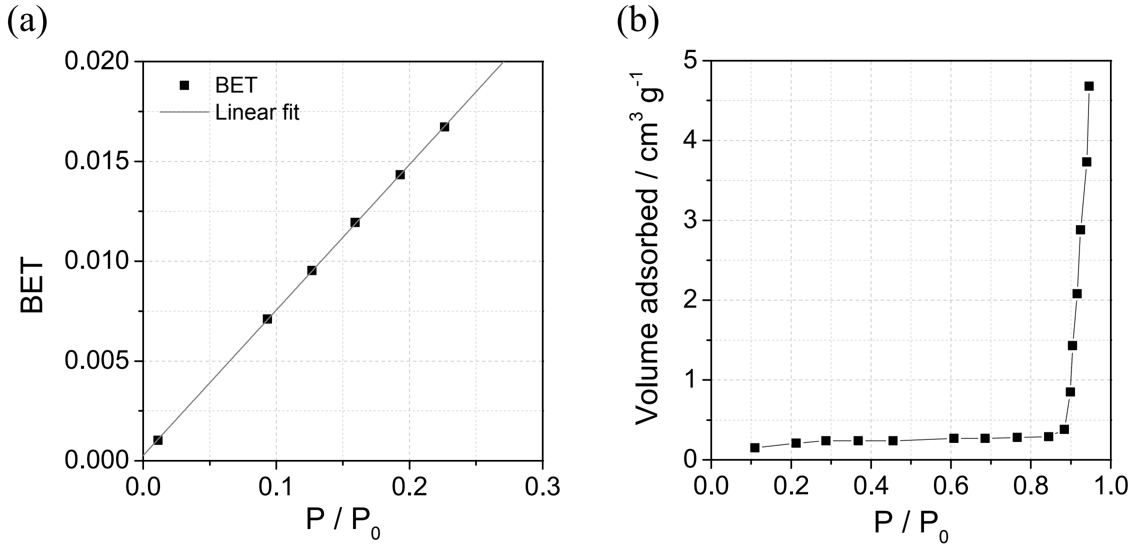

Figure 11.10: Krypton Adsorption analysis of Carbon black. (a) Adsorption/desorption (Ads/Des) isotherms and (b) BET plots.

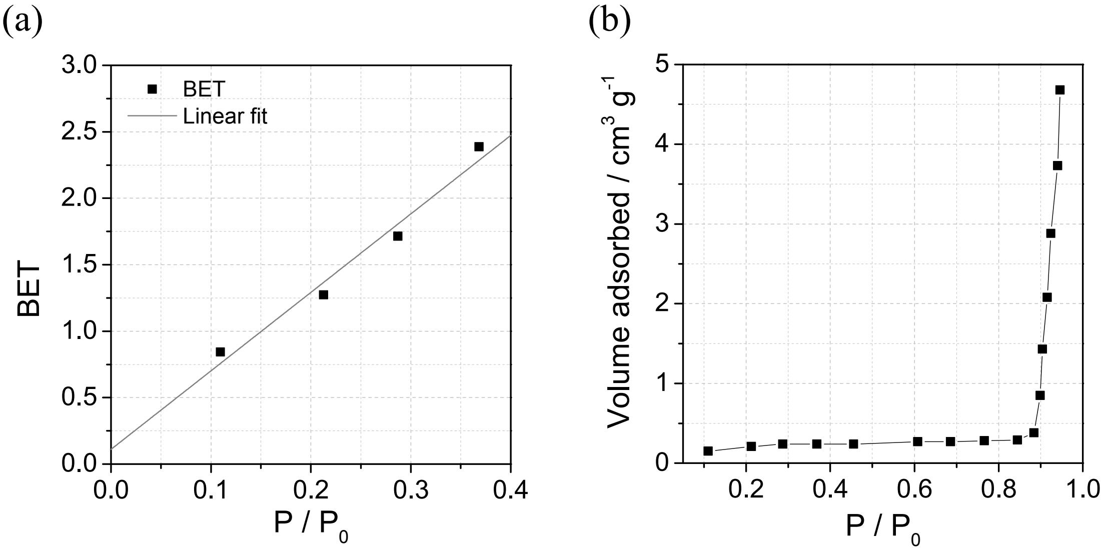

Figure 11.11: Krypton Adsorption analysis of cathode before cycling. (a) Adsorption/desorption (Ads/Des) isotherms and (b) BET plots.

11.1.4Influence of the temperature on the discharge capacity

Variation of the capacity (C) during prolonged cycling of the battery was observed as a small bump in the capacity curve vs time/cycle. Comparing the variation of temperature (T) with the capacity Figure 11.12 (a), a linear dependency was observed between ΔC and T (Figure 11.12 (b)), where ΔC= measured capacity (blue curve, Figure 11.12 (a)) expected capacity by linear interpolation (grey curve, Figure 11.12 (a)). Thus, the capacity increases in ca.12 Ah $\mathrm{kg_S}^{-1}$ per +1°C.

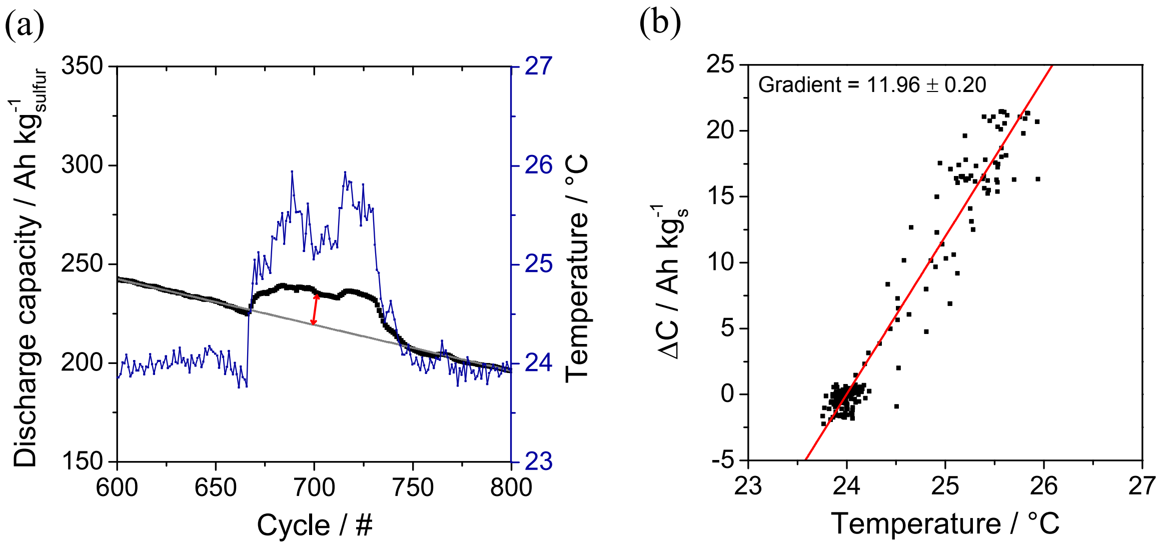

Figure 11.12: Influence of temperature on the capacity.

11.1.5Sulfur structure and Li_2S reactivity

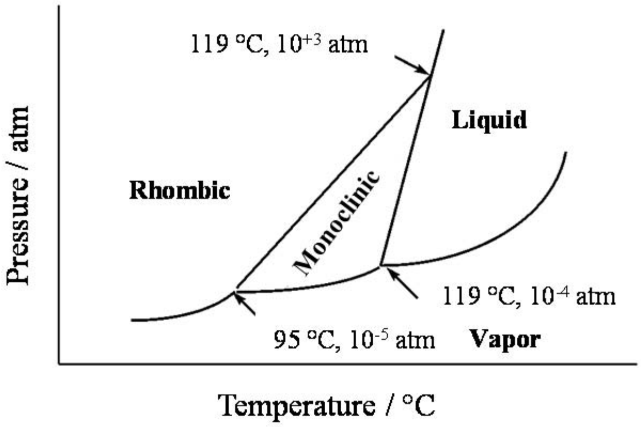
119 °C, 10^{+3} atm
Liquid
Rhombic
Monoclinic
119 °C, 10^{-4} atm
95 °C, 10^{-5} atm
Vapor
Pressure / atm
Temperature / °C

Figure 11.13: **Phase diagram of sulfur** [182].

Table 12: Structure parameters of α–S_8 at about 300 K (standard deviation in parenthesis). There are 16(4) molecules per unit primitive cell [134].

Crystal space group	FDDD–D_{2h} (70)
Lattice constants	
a (Å)	10.4646 (1)
b (Å)	12.8660 (1)
c (Å)	24.4860 (3)

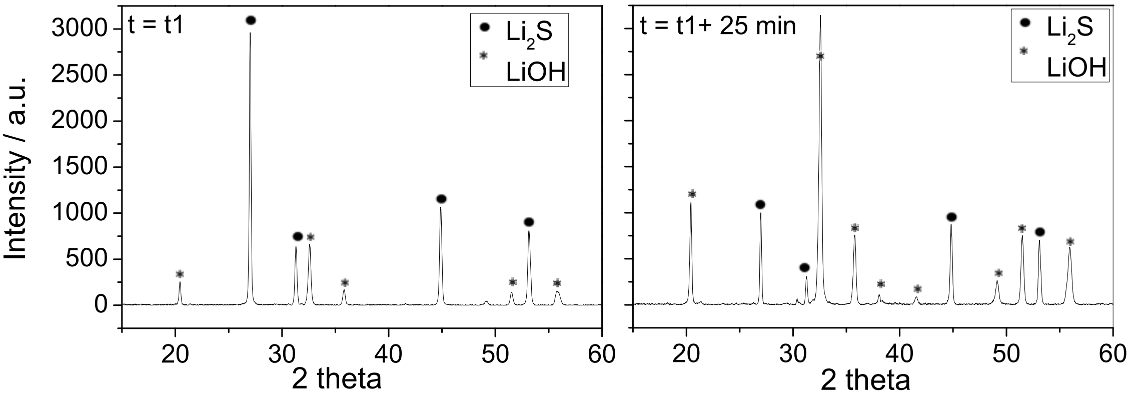

Figure 11.14: **X–ray pattern of the Li_2S sample before (t = t1) and after approximately 25 min in contact with air (t = t1 + 25 min).**

11.2 Electrochemical impedance spectroscopy

11.2.1Finite diffusion

The Nernstian diffusion impedance (Z_N), also called “General Warburg Impedance” describes a finite diffusion when the concentration at a certain distance to the electrode remains constant. Z_N consists of two terms: the Warburg parameter W (in $\Omega\ s^{-1/2}$) and a diffusion time constant (k_N) defined by the constant of diffusion (D_k) and diffusion layer thickness (d_N) [183]. The Nernst impedance is calculated by

$$Z_N = \frac{W}{\sqrt{j \cdot \omega}} \cdot \tan \sqrt{\frac{j \cdot \omega}{k_N}} \tag{11.1}$$

$$k_N = \frac{D_k}{{d_N}^2} \tag{11.2}$$

The high frequency part of the impedance spectra exhibits the same shape like the Warburg impedance (Special Warburg Impedance) whereas the low frequency part is similar to an R–C element. The Nernstian diffusion impedance can be also approximated by a R||CPE element.

When the diffusion length is finite due to a phase boundary located at a certain distance from the electrode, the diffusion is described by the “Finite diffusion impedance (Z_S)” with the transfer function given by

$$Z_S = \frac{W}{\sqrt{j \cdot \omega}} \cdot \coth \sqrt{\frac{j \cdot \omega}{k_S}} \tag{11.3}$$

$$\mathrm{k_S} = \frac{\mathrm{D_S}}{\mathrm{d_S}^2} \tag{11.4}$$

The high frequency part of the impedance spectra exhibits the same shape like the Warburg impedance (Special Warburg Impedance) whereas the low frequency part is similar to a capacity [183].

11.2.2EIS simulation results

Table 13, Table 14, and Table 15 show the simulation results for the EC elements of the EIS measured during the 1st discharge, during the 1st charge, and up to 50 cycles, respectively.

Table 13: Simulation results of the impedance spectra measured at different DOD for Li–S battery during the first cycle.

DOD / %	R_0 / Ohm	R_1 / Ohm	CPE_1 / nF	α	R_2 / Ohm	CPE_2 / µF	α
0	11.70 ± 0.42	2.25 ± 0.27	144.50 ± 20.8	0.49	1770.0 ± 20.35	0.85 ± 0.03	0.79
7	12.94 ± 0.11	31.0 ± 1.3	1854.0 ± 179.8	0.48	1143.0 ± 72.1	1.66 ± 0.06	0.79
16	17.79 ± 0.17	52.0 ± 3.6	662.4 ± 45.8	0.67	975.0 ± 6.0	1.70 ± 0.06	0.76
27	20.88 ± 0.16	64.6 ± 2.4	612.8 ± 40.2	0.66	952.8 ± 9.0	1.69 ± 0.02	0.75
34	22.90 ± 0.30	87.4 ± 3.8	551.2 ± 31.5	0.65	959.3 ± 14.1	1.61 ± 0.04	0.82
43	24.27 ± 0.49	74.3 ± 1.6	492.0 ± 31.4	0.67	695.0 ± 31.4	1.36 ± 0.01	0.79
52	22.47 ± 0.38	53.8 ± 1.4	544.2 ± 35.6	0.68	503.3 ± 8.2	1.41 ± 0.02	0.72
62	19.45 ± 0.19	37.9 ± 1.2	568.3 ± 30.3	0.70	462.2 ± 11.0	1.45 ± 0.02	0.70
71	17.60 ± 0.17	37.7 ± 0.7	526.8 ± 12.6	0.70	457.3 ± 3.5	1.27 ± 0.01	0.79
81	15.15 ± 0.18	32.40 ± 0.50	546.20 ± 5.90	0.69	436.90 ± 4.19	1.23 ± 0.00	0.77
90	13.94 ± 0.21	29.4 ± 0.8	533.4 ± 14.2	0.69	400.6 ± 3.8	1.19 ± 0.02	0.78
99	13.42 ± 0.24	21.8 ± 0.5	484.9 ± 19.9	0.72	450.7 ± 8.3	1.07 ± 0.02	0.73
100	13.50 ± 0.26	19.1 ± 0.7	435.9 ± 25.6	0.76	470.9 ± 8.5	0.99 ± 0.02	0.72

DOD / %	R_3 / Ohm	CPE_3 / µF	α	R_4 / Ohm	CPE_4 / µF	α
0						
7						
16	220 ± 4	18.1 ± 3.0	1.00			
27	174 ± 11	19.5 ± 4.8	1.00	242 ± 83	98.4 ± 0.5	0.60
34						
43						
52	73 ± 7	12.0 ± 0.3	1.00			
62	77 ± 8	8.6 ± 0.4	1.00	1021.0 ± 450.0	79.1 ± 4.0	0.6
71	187 ± 8	101.9 ± 11.0	0.79	783.6 ± 269.2	571.7 ± 0.8	0.8
81	392.20 ± 8.35	102.00 ± 6.42	0.82	1048.0 ± 359.8	407.7 ± 0.8	0.8
90	2737 ± 369	38.5 ± 1.6	0.73			
99	38640 ± 3284	79.1 ± 0.9	0.86			
100	55770 ± 3597	79.1 ± 1.0	0.86			

Table 14: Simulation results of the impedance spectra measured at different depth of charge for Li–S battery during the first charge.

DOC / %	R_0 / Ohm	R_1 / Ohm	CPE_1 / nF	α	R_2 / Ohm	CPE_2 / μF	α
0	14.65 ± 2.35	8.0 ± 0.7	335.1 ± 91.5	0.99	383.4 ± 10.7	913 ± 18	0.73
11	13.87 ± 2.21	9.8 ± 0.9	446.0 ± 102.0	0.97	280.3 ± 1.6	985 ± 28	0.77
23	14.73 ± 2.88	10.8 ± 1.3	380.0 ± 91.8	1.00	197.7 ± 0.8	1039 ± 41	0.79
34	15.81 ± 1.69	12.9 ± 1.0	332.3 ± 64.7	1.00	175.1 ± 1.0	1067 ± 43	0.79
45	16.98 ± 1.72	13.7 ± 1.0	309.8 ± 57.7	1.00	155.5 ± 1.1	1049 ± 45	0.79
56	18.16 ± 1.59	14.9 ± 1.1	297.5 ± 51.1	0.99	135.4 ± 1.4	1020 ± 46	0.80
66	17.16 ± 1.73	14.6 ± 1.1	318.2 ± 59.3	0.99	146.9 ± 2.0	1146 ± 56	0.79
76	14.64 ± 2.28	12.1 ± 1.1	385.6 ± 80.6	0.99	149.8 ± 1.0	1205 ± 57	0.77
86	11.98 ± 2.54	7.2 ± 0.8	497.7 ± 158.6	1.00	127.2 ± 1.8	1167 ± 55	0.76
96	10.54 ± 0.91	6.8 ± 1.1	820.4 ± 288.8	1.00	96.5 ± 1.4	1065 ± 59	0.84
100	9.99 ± 1.81	6.2 ± 1.2	1853.0 ± 658.7	1.00	122.2 ± 3.9	768 ± 5	0.77

DOC / %	R_3 / Ohm	CPE_3 / μF	α	R_4 / Ohm	CPE_4 / μF	α
0	39350 ± 10798	78.9 ± 2.2	0.83			
11	671 ± 25	52.3 ± 2.0	0.76	1002 ± 530	4.5 ± 0.5	0.91
23	340 ± 1	51.2 ± 1.3	0.74	362 ± 96	16.6 ± 0.6	1.00
34	229 ± 3	53.7 ± 1.0	0.76	278 ± 33	13.9 ± 0.5	1.00
45	184 ± 3	51.6 ± 1.7	0.75	217 ± 27	17.0 ± 0.9	0.99
56	177 ± 4	49.6 ± 2.5	0.74	204 ± 86	22.8 ± 1.2	1.00
66	106 ± 5	38.6 ± 5.5	0.67	144 ± 25	36.4 ± 3.2	1.00
76	63 ± 17	191.7 ± 50.9	0.43	77 ± 29	41.9 ± 2.5	0.96
86	63 ± 13	199.1 ± 31.8	0.46	65 ± 35	41.1 ± 2.3	0.94
96	69 ± 2	393.7 ± 4.8	0.70	394 ± 147	1.2 ± 0.1	0.78
100						

Table 15: Simulation results of the impedance spectra measured during cycling. The EIS were measured in discharge state until the 50th cycle.

Cycle	R_0 / Ohm	R_1 / Ohm	CPE_1 / nF	α	R_2 / Ohm	CPE_2 / μF	α
1	12.69 ± 0.80	10.0 ± 0.6	162.3 ± 9.5	0.91	399.1 ± 11.2	665 3 20	0.69
2	12.10 ± 0.23	13.0 ± 0.6	199.8 ± 6.6	0.95	338.6 ± 10.4	681 3 22	0.68
3	11.74 ± 0.29	10.4 ± 0.3	198.6 ± 8.7	1.00	318.1 ± 12.3	688 4 26	0.66
4	11.46 ± 0.39	8.0 ± 0.5	220.5 ± 14.8	1.00	306.6 ± 13.3	712 3 19	0.63
5	9.75 ± 0.49	6.6 ± 0.5	281.4 ± 24.9	1.00	255.1 ± 11.0	691 4 30	0.64
10	9.95 ± 0.51	7.7 ± 0.6	320.6 ± 46.8	1.00	200.3 ± 7.7	712 1 10	0.62
15	10.13 ± 0.47	9.1 ± 0.4	277.4 ± 44.1	1.00	172.7 ± 5.8	713 1 10	0.62
20	10.10 ± 0.50	9.3 ± 0.2	282.9 ± 27.1	1.00	145.6 ± 4.6	754 1 6	0.64
25	10.21 ± 0.55	9.5 ± 0.2	296.2 ± 46.7	1.00	137.3 ± 4.3	765 1 4	0.64
30	10.29 ± 0.48	9.4 ± 0.2	252.0 ± 27.9	1.00	131.3 ± 3.2	755 1 10	0.65
35	10.15 ± 0.48	9.2 ± 0.3	248.9 ± 28.8	1.00	127.8 ± 3.1	751 2 12	0.65
40	10.19 ± 0.47	10.4 ± 0.2	268.9 ± 25.1	1.00	126.8 ± 3.3	768 1 11	0.66
45	9.53 ± 0.44	9.7 ± 0.2	263.4 ± 25.0	1.00	119.3 ± 2.2	734 2 13	0.68
50	10.35 ± 0.49	10.7 ± 0.1	280.8 ± 33.6	1.00	114.6 ± 2.7	752 2 13	0.66

Cycle	R_3 / Ohm			CPE_3 / µF			α
1	31520	±	24422	74.1	±	1.3	0.83
2	23300	±	3747	76.5	±	1.9	0.83
3	20730	±	3599	75.0	±	2.4	0.82
4	20480	±	3971	71.9	±	1.6	0.82
5	19340	±	5170	71.2	±	2.2	0.81
10	17920	±	5007	72.4	±	1.9	0.81
15	19220	±	6345	67.6	±	2.0	0.80
20	21560	±	9827	63.0	±	2.3	0.78
25	22400	±	10409	62.5	±	1.9	0.78
30	25550	±	10971	53.3	±	2.2	0.75
35	24550	±	12152	52.0	±	2.0	0.75
40	24750	±	12405	52.7	±	1.8	0.75
45	26270	±	11393	50.7	±	1.5	0.73
50	25500	±	10126	49.6	±	0.5	0.70

11.3 Additional absorbance spectrum and TG analysis

The absorption spectrum of TEGDME is shown in Figure 11.15. This spectrum was used as reference and subtracted from the measured spectra of the electrolyte and polysulfide samples.

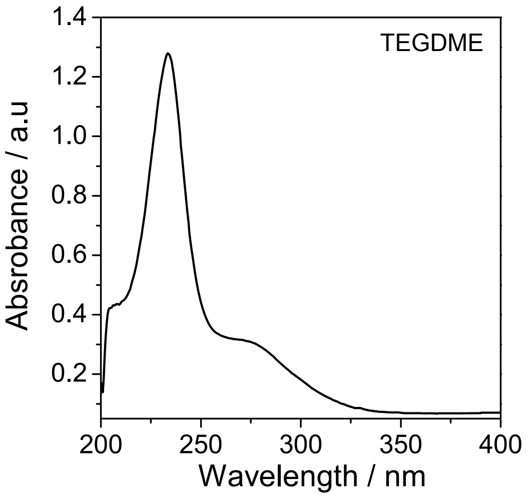

Figure 11.15: Absorption spectrum of TEGDME (UV–vis spectroscopy).

The cathode was immersed in the electrolyte, dried, and analyzed with TG. Figure 11.16 evidence that the electrolyte does not influence the degradation of PVDF and that the larger mass in detected in the region between 200 and 300 °C is caused by the reaction products of electrolyte.

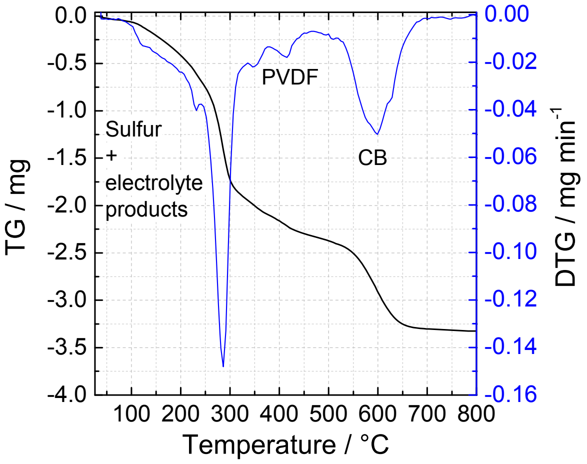

Figure 11.16: TG measurements of cathode, after drying the electrode immersed in electrolyte.

11.4 Reduction mechanisms of Li–S batteries and simulations

11.4.1 Review of sulfur reduction mechanisms for Li–S batteries

Mechanism proposed by Paris and Plinchon (1981) [13]**:**

$S_8 + 2e^- \rightarrow S_8^{2-}$

$S_8^{2-} \rightleftarrows 2S_3^{\bullet-} + \frac{1}{4} S_8$

$S_8^{2-} + 2e^- \rightleftarrows 2S_4^{2-}$

$S_4^{2-} + \frac{1}{4} S_8 \rightleftarrows S_3^{\bullet-}$

$S_3^{2-} + \frac{3}{4} S_8 \rightleftarrows 2S_3^{\bullet-}$

Mechanism proposed by Kim and Park (1993) [12]**:**

$S_8 + 2e^- \rightarrow S_8^{2-}$

$S_8^{2-} \rightleftarrows S_6^{2-} + \frac{1}{4} S_8$

$S_8^{2-} \rightleftarrows S_4^{2-} + \frac{1}{2} S_8$

$S_6^{2-} + S_8^{2-} \rightleftarrows \frac{3}{2} S_3^{2-} + S_8$

$S_6^{2-} \rightleftarrows S_3^{\bullet-}$

$S_8^{2-} + 2e^- \rightleftarrows S_8^{4-}$

$S_3^{\bullet-} + e^- \rightleftarrows S_3^{2-}$

$S_6^{2-} + 2e^- \rightleftarrows 2S_3^{2-}$

$S_8^{4-} \rightleftarrows 2S_4^{2-}$

$S_3^{2-} \rightleftarrows S_3^{\bullet -} + e^-$

$S_6^{2-} + S_3^{2-} \rightarrow S_3^{\bullet -} + 2e^-$

$S_4^{2-} + \rightleftarrows S_4^{\bullet -} + e^-$

Mechanism proposed by Levillain et al. (1997) [14]:

$S_{8c} + e^- \rightarrow S_{8c}^-$

$S_{8c}^- \rightleftarrows S_{8l}^-$

$S_{8l}^- + e^- \rightleftarrows S_{8l}^{2-}$

$S_{8l}^- + S_{8c}^- \rightleftarrows S_{8l}^{2-}$

$2S_3^{2-} \rightleftarrows S_2^{2-} + S_4^{2-}$

$2S_6^{2-} \rightleftarrows S_4^{2-} + S_8^{2-}$

$2S_6^{\bullet -} \rightleftarrows S_4^{\bullet -} + S_{8l}^-$

$S_3^{\bullet -} + S_4^{2-} \rightleftarrows S_4^{\bullet -} + S_3^{2-}$

$S_{8c} + S_6^{2-} \rightleftarrows S_6^{\bullet -} + S_{8c}^{2-}$

$S_{8l}^- + S_6^{2-} \rightleftarrows S_6^{\bullet -} + S_{8c}^{2-}$

Where subscript c: cyclic molecule, and l: linear chain

Mechanism proposed by Tobischima et al. (1997) [15]:

$\frac{1}{4} S_8 + S_4^{2-} \rightarrow S_6^{2-}$

$S_4^{2-} \rightleftarrows S_2^{\bullet -}$

$S_6^{2-} \rightleftarrows S_3^{\bullet -}$

$S_{8l}^- + S_{8c}^- \rightleftarrows S_{8l}^{2-}$

$S_x^{2-} \rightleftarrows S_x^{2-}$ $(x < 8)$

Mechanism proposed by Barchasz et al. (2012) [16]:

During first discharge plateau

$S_8 + 2e^- + 2Li^+ \rightarrow Li_2S_8$

$S_8^{2-} \rightarrow S_6^{2-} + \frac{1}{4} S_8$

$S_6^{2-} \rightarrow S_3^{\bullet -}$

$2S_6^{2-} \rightleftarrows S_5^{2-} + S_7^{2-}$

“middle” plateau

$2Li_2S_6 + 2e^- + 2Li^+ \rightarrow 3Li_2S_4$

$S_3^{\bullet -} \rightarrow S_6^{2-}$

$2S_6^{2-} \rightleftarrows S_5^{2-} + S_7^{2-}$

During second discharge plateau

$2Li_2S_4 + 2e^- + 2Li^+ \rightarrow 4Li_2S_3$

$2Li_2S_3 + 2e^- + 2Li^+ \rightarrow 3Li_2S_2$

$Li_2S_2 + 2e^- + 2Li^+ \rightarrow 2Li_2S$

Mechanism proposed by Yi–Chun Lu et al. (2014) [17]:

$S_8 + 2e^- \rightarrow S_8^{2-}$

$S_8^{2-} + 2e^- \rightarrow S_8^{4-}$

$S_8^{4-} \rightarrow S_4^{2-}$

$S_8^{2-} \rightarrow S_6^{2-} + \frac{1}{4} S_8$

$S_6^{2-} \rightleftarrows S_3^{\bullet -}$

$2S_4^{2-} \rightleftarrows S_8^{2-} + \frac{8}{7} S^{2-}$

11.4.2Parameters used in the simulation.

Table 16: Description of symbols and their units (chapter 8).

Symbol	Unit	Description
A_m^{V}	$\mathrm{m^{2}\ m^{-3}}$	Volume–specific surface area (surface at which reaction *m* happens)
A_{dl}	$\mathrm{m^{2}\ m^{-3}}$	Total volume specific area of an electrode
c_{i}	$\mathrm{mol\ m^{-3}}$	Concentration of species *i*
C_{dl}	$\mathrm{F\ m^{-2}}$	Area–specific double layer capacitance
D_i, $D_{i,\mathrm{eff}}$	$\mathrm{m^{2}\ s^{-1}}$	(Effective) transport coefficient of species *i*
E	V	Cell voltage
$E_{\mathrm{f}}^{\mathrm{act}}$	$\mathrm{J\ mol^{-1}}$	Activation energy of forward and reverse reactions phases
F	$\mathrm{As\ mol^{-1}}$	Faraday’s constant: 96485 $\mathrm{As\ mol^{-1}}$
g_{i}	$\mathrm{J\ mol^{-1}}$	Molar Gibbs free enthalpy of species *i*
ΔG	$\mathrm{J\ mol^{-1}}$	Molar Gibbs reaction enthalpy
i		Index of species and phases
i_{tot}, i_{dl}, i_{F}	$\mathrm{A\ m^{-3}}$	Volume–specific cell current density (indices: total current,

		double layer current, Faradaic current)
$\vec{J}_i$	mol m^{-2} s^{-1}	Flux of species *i*
k_f, k_r		Forward and backward rate constants
k_0		Pre–exponential factor in Arrhenius equation
m		Index of chemical reactions
M_i	kg mol^{-1}	Mean molar mass of phase *i*
R	J mol^{-1} K^{-1}	Ideal gas constant: 8.3145 J mol^{-1} K^{-1}
$\dot{s}_{i,m}$	mol m^{-2} s^{-1}	Chemical production rate of species *i* in reaction *m*
t	s	Time
T	K	Absolute temperature
y	m	Spatial position
z		Number of electrons transferred in charge–transfer step
α		Symmetry factor of charge transfer reactions. For all reactions in this work $\alpha = 0.5$
ε_i		Volume fraction of phase *i*
ε_i'		Maximum volume fraction of phase *i* (S atoms present in form *i*)
ϕ	V	Electric potential
Δϕ	V	Electric potential difference between electrode and electrolyte
ν_i		Stoichiometric coefficient of species *i*
ρ_i	kg ^{3}	Density of phase *i*
τ_i		Tortuosity of a porous phase *i*

The initial concentration assumed for the simulated cell as well as the diffusion coefficients are presented in Table 17. The dissolution of sulfur in TEGDME was calculated according to equation of Sciamanna et al.: wt.% sulfur =exp[–10.994(T_m/T) +12.584) [139].

Table 17: List of parameters used in the simulation. Values are known from calculation (†), literature (*), and assumed (°).

Species	Density / Initial	Diffusion coefficient /
$S_{8(s)}$	$2.07\cdot10^{3}\ \mathrm{kg\cdot m^{-3}}{*}$	–
C	$2.26\cdot10^{3}\ \mathrm{kg\cdot m^{-3}}{*}$	–
$(C_2H_2F_2)_n$	$1.78\cdot10^{3}\ \mathrm{kg\cdot m^{-3}}{*}$	–
$C_{10}H_{22}O_5$	$1.00\cdot10^{3}\ \mathrm{kg\cdot m^{-3}}{*}$	–
Li^{+}	$9.86\cdot10^{2}\ \mathrm{mol\cdot m^{-3\dagger}}$	$2.0\cdot10^{-11\circ}$
PF_6^{-}	$9.85\cdot10^{2}\ \mathrm{mol\cdot m^{-3\dagger}}$	$8.0\cdot10^{-11\circ}$
S^{2-}	$6.16\cdot10^{-20}\ \mathrm{mol\cdot m^{-3\circ}}$	$2.0\cdot10^{-11\circ}$
S_2^{2-}	$3.63\cdot10^{-14}\ \mathrm{mol\cdot m^{-3\circ}}$	$2.0\cdot10^{-11\circ}$
S_4^{2-}	$2.11\cdot10^{-2}\ \mathrm{mol\cdot m^{-3\circ}}$	$2.0\cdot10^{-11\circ}$
S_6^{2-}	$7.12\cdot10^{-4}\ \mathrm{mol\cdot m^{-3\circ}}$	$1.2\cdot10^{-10\circ}$
S_8^{2-}	$2.90\cdot10^{-1}\ \mathrm{mol\cdot m^{-3\circ}}$	$1.2\cdot10^{-10\circ}$
$S_{8(diss)}$	$9.33\cdot10^{2}\ \mathrm{mol\cdot m^{-3}}{*}$	$2.0\cdot10^{-10\circ}$
$Li_2S_{(s)}$	$1.64\cdot10^{3}\ \mathrm{kg\cdot m^{-3}}{*}$	–
Ar	–	–

Literature

[1] Deutsche Bundesregierung, German Federal Government's National Electromobility Development Plan, 2009.

[2] H. Danuta, U. Juliusz, D. Herbert, J. Ulam, Electric Dry Cells and Storage Batteries, US3043896A, 1962.

[3] P.G. Bruce, S.A. Freunberger, L.J. Hardwick, J.-M. Tarascon, Nat. Mater. 11 (2012) 19.

[4] Http://www.nissanusa.com/electric-Cars/leaf/features/ (2014).

[5] US Advanced Battery Consortium, Goals for Advanced EV Batteries, 2006.

[6] N.A. Cañas, S. Wolf, N. Wagner, K.A. Friedrich, J. Power Sources 226 (2013) 313.

[7] N.A. Cañas, K. Hirose, B. Pascucci, N. Wagner, K.A. Friedrich, R. Hiesgen, Electrochim. Acta 97 (2013) 42.

[8] N.A. Cañas, D.N. Fronczek, N. Wagner, A. Latz, K.A. Friedrich, J. Phys. Chem. C 118 (2014) 12106.

[9] R. Juza, W. Uphoff, Z. anorg. allg. Chem. 3 (1956) 113.

[10] H. Okamoto, J. Phase Equilibria 16 (1995) 94.

[11] P. Sonápearson, Thomas; Lucockárobinson, J. Chem. Soc. (1930) 413.

[12] B. Kim, S. Park, J. Electrochem. Soc. 140 (1993) 115.

[13] J. Paris, V. Plichon, Electrochim. Acta 26 (1981) 1823.

[14] P. Leghié, Lelieur; E., J.-P. Levillain, A. Lorriaux, New J. Chem. 20 (1996) 1121.

[15] S.-I. Tobishima, H. Yamamoto, M. Matsuda, Electrochim. Acta 42 (1997) 1019.

[16] C.C. Barchasz, F. Molton, C. Duboc, J.-C. Leprêtre, S. Patou, F. Alloin, J.-C. Leprêtre, S. Patoux, Anal. Chem. 84 (2012) 3973.

[17] Y.-C. Lu, Q. He, H.A. Gasteiger, J. Phys. Chem. C 118 (2014) 5733.

[18] Y. V. Mikhaylik, J.R. Akridge, J. Electrochem. Soc. 151 (2004) A1969.

[19] J. Shim, K.A. Striebel, E.J. Cairns, J. Electrochem. Soc. 149 (2002) A1321.

[20] X. Ji, K.T. Lee, L.F. Nazar, Nat. Mater. 8 (2009) 500.

[21] R.D. Rauh, K.M. Abraham, G.F. Pearson, J.K. Surprenant, S.B. Brummer, J. Electrochem. Soc. 126 (1979) 523.

[22] J.A. Dean, Lange's Handbook of Chemistry, 15th ed., 1999.

[23] X. He, J. Ren, L. Wang, W. Pu, C. Jiang, C. Wan, J. Power Sources 190 (2009) 154.

[24] Kiyoshi Kanamura, S. Shiraishi, H. Tamura, Z. Takehara, J. Electrochem. Soc. 141 (1994) 2379.

[25] J. Gao, M.A. Lowe, Y. Kiya, H.D. Abruna, D. Abru, J. Phys. Chem. C 115 (2011) 25132.

[26] S.-C. Han, M.-S. Song, H. Lee, H.-S. Kim, H.-J. Ahn, J.-Y. Lee, J. Electrochem. Soc. 150 (2003) A889.

[27] J.-W. Choi, G. Cheruvally, D.-S. Kim, J.-H. Ahn, K.-W. Kim, H.-J. Ahn, J. Power Sources 183 (2008) 441.

[28] J. Sun, Y. Huang, W. Wang, Z. Yu, A. Wang, K. Yuan, Electrochem. Commun. 10 (2008) 930.

[29] B. Zhang, C. Lai, Z. Zhou, X.P. Gao, Electrochim. Acta 54 (2009) 3708.

[30] D. Marmorstein, T.H. Yu, K.A. Striebel, F.R. Mclarnon, J. Hou, E.J. Cairns, J. Po 89 (2000) 219.

[31] C. Barchasz, J.-C. Leprêtre, F. Alloin, S. Patoux, J. Power Sources 199 (2012) 322.

[32] J.L. Wang, J. Yang, J.Y. Xie, N.X. Xu, Y. Li, Electrochem. Commun. 4 (2002) 499.

[33] J. Wang, L. Liu, Z. Ling, J. Yang, C. Wan, C. Jiang, Electrochim. Acta 48 (2003) 1861.

[34] L. Ji, M. Rao, H. Zheng, L. Zhang, Y. Li, W. Duan, J. Guo, E.J. Cairns, Y. Zhan, J. Am. Chem. Soc. 133 (2011) 18522.

[35] B. Ding, C. Yuan, L. Shen, G. Xu, P. Nie, Q. Lai, X. Zhang, J. Mater. Chem. A 1 (2013) 1096.

[36] B. Zhang, X. Qin, G.R. Li, X.P. Gao, Energy Environ. Sci. 3 (2010) 1531.

[37] X. Li, Y. Cao, W. Qi, L. V. Saraf, J. Xiao, Z. Nie, J. Mietek, J.-G. Zhang, B. Schwenzer, J. Liu, J. Mater. Chem. 21 (2011) 16603.

[38] V. Maurice, A.W. Hassel, P. Marcus, S.-R. Chen, Y.-P. Zhai, G.-L. Xu, Y.-X. Jiang, D.-Y. Zhao, J.-T. Li, L. Huang, S.-G. Sun, Electrochim. Acta 56 (2011) 9549.

[39] Z. Wang, S. Zhang, L. Zhang, R. Lin, X. Wu, H. Fang, Y. Ren, J. Power Sources 248 (2014) 337.

[40] N. Jayaprakash, J. Shen, S.S. Moganty, A. Corona, L.A. Archer, Angew. Chemie Int. Ed. 50 (2011) 5904.

[41] Z. Wei Seh, W. Li, J.J. Cha, G. Zheng, Y. Yang, M.T. McDowell, P.-C. Hsu, Y. Cui, Nat. Commun. 4 (2013) 1331.

[42] S.-E. Cheon, J.-H. Cho, K.-S. Ko, C.-W. Kwon, D.-R. Chang, H.-T. Kim, S.-W. Kim, J. Electrochem. Soc. 149 (2002) A1437.

[43] Y. Huang, J. Sun, W. Wang, Y. Wang, Z. Yu, H. Zhang, A. Wang, K. Yuan, J. Electrochem. Soc. 155 (2008) A764.

[44] Y. Wang, Y. Huang, W. Wang, C. Huang, Z. Yu, H. Zhang, J. Sun, A. Wang, K. Yuan, Electrochim. Acta 54 (2009) 4062.

[45] H. Schneider, A. Garsuch, A. Panchenko, O. Gronwald, N. Janssen, P. Novák, J. Power Sources 205 (2012) 420.

[46] Y. Yang, G. Yu, J.J. Cha, H. Wu, M. Vosgueritchian, Y. Yao, Z. Bao, Y. Cui, ACS Nano 5 (2011) 9187.

[47] M. Hagen, S. Dörfler, H. Althues, J. Tübke, M.J. Hoffmann, S. Kaskel, K. Pinkwart, J. Power Sources 213 (2012) 239.

[48] R. Elazari, G. Salitra, A. Garsuch, A. Panchenko, D. Aurbach, Adv. Mater. 23 (2011) 5641.

[49] L. Zhou, X. Lin, T. Huang, A. Yu, J. Mater. Chem. A 2 (2014) 5117.

[50] M. Hagen, S. Dörfler, P. Fanz, T. Berger, R. Speck, J. Tübke, H. Althues, M.J. Hoffmann, C. Scherr, S. Kaskel, J. Power Sources 224 (2013) 260.

[51] G.-C. Li, G.-R. Li, S.-H. Ye, X.-P. Gao, Adv. Energy Mater. 2 (2012) 1238.

[52] L. Wang, X. He, J. Li, J. Gao, M. Fang, G. Tian, J. Wang, S. Fan, J. Power Sources 239 (2013) 623.

[53] X. Zhou, J. Xie, J. Yang, Y. Zou, J. Tang, S. Wang, L. Ma, Q. Liao, J. Power Sources 243 (2013) 993.

[54] X. Wang, Z. Wang, L. Chen, J. Power Sources 242 (2013) 65.

[55] Q. Tang, Z. Shan, L. Wang, X. Qin, K. Zhu, J. Tian, X. Liu, J. Power Sources 246 (2014) 253.

[56] J. Scheers, S. Fantini, P. Johansson, J. Power Sources 255 (2014) 204.

[57] S.S. Zhang, D.T. Tran, J. Power Sources 211 (2012) 169.

[58] S. Evers, T. Yim, L.F. Nazar, J. Phys. Chem. C 116 (2012) 19653.

[59] S. Zhao, C. Li, W. Wang, H. Zhang, M. Gao, X. Xiong, A. Wang, K. Yuan, Y. Huang, F. Wang, J. Mater. Chem. A 1 (2013) 3334.

[60] N. Brun, K. Sakaushi, L. Yu, L. Giebeler, J. Eckert, M.M. Titirici, Phys. Chem. Chem. Phys. 15 (2013) 6080.

[61] Y.-J. Choi, Y.-D. Chung, C.-Y. Baek, K.-W. Kim, H.-J. Ahn, J.-H. Ahn, J. Power Sources 184 (2008) 548.

[62] Y.-J. Choi, K.-W. Kim, H.-J. Ahn, J.-H. Ahn, J. Alloys Compd. 449 (2008) 313.

[63] H.S. Ryu, Z. Guo, H.J. Ahn, G.B. Cho, H. Liu, J. Power Sources 189 (2009) 1179.

[64] C. Barchasz, J.-C. Lepretre, S. Patoux, F. Alloin, J. Electrochem. Soc. 160 (2013) A430.

[65] D.-R. Chang, S.-H. Lee, S.-W. Kim, H.-T. Kim, J. Power Sources 112 (2002) 452.

[66] J.-W. Choi, J.-K. Kim, G. Cheruvally, J.-H. Ahn, H.-J. Ahn, K.-W. Kim, Electrochim. Acta 52 (2007) 2075.

[67] J.H. Shin, E.J. Cairns, J. Electrochem. Soc. 155 (2008) A368.

[68] J. Wang, S.Y. Chew, Z.W. Zhao, S. Ashraf, D. Wexler, J. Chen, S.H. Ng, S.L. Chou, H.K. Liu, Carbon 46 (2008) 229.

[69] E. Peled, Y. Sternberg, A. Gorenshtein, Y. Lavi, J. Electrochem. Soc. 136 (1989) 1621.

[70] J. Hassoun, B. Scrosati, Adv. Mater. 22 (2010) 5198.

[71] H.-S. Ryu, H.-J. Ahn, K.-W. Kim, J.-H. Ahn, J.-Y. Lee, J. Power Sources 153 (2006) 360.

[72] B.H. Jeon, J.H. Yeon, I.J. Chung, J. Mater. Process. Technol. 143-144 (2003) 93.

[73] K. Jeddi, M. Ghaznavi, P. Chen, J. Mater. Chem. A 1 (2013) 2769.

[74] L.X. Yuan, J.K. Feng, X.P. Ai, Y.L. Cao, S.L. Chen, H.X. Yang, Electrochem. Commun. 8 (2006) 610.

[75] J. Wang, S. Chou, S. Chew, J. Sun, M. Forsyth, D. Macfarlane, H. Liu, Solid State Ionics 179 (2008) 2379.

[76] J.-W. Park, K. Yamauchi, E. Takashima, N. Tachikawa, K. Ueno, K. Dokko, M. Watanabe, J. Phys. Chem. C 117 (2013) 4431.

[77] A. Unemoto, H. Ogawa, Y. Gambe, I. Honma, Electrochim. Acta (2014).

[78] S. Xiong, K. Xie, E. Blomberg, P. Jacobsson, A. Matic, J. Power Sources 252 (2014) 150.

[79] J.-W. Park, K. Ueno, N. Tachikawa, K. Dokko, M. Watanabe, J. Phys. Chem. C 117 (2013) 20531.

[80] J.-W. Park, K. Yamauchi, E. Takashima, N. Tachikawa, K. Ueno, K. Dokko, M. Watanabe, J. Phys. Chem. C 117 (2013) 4431.

[81] Y. Yang, M.T. McDowell, A. Jackson, J.J. Cha, S.S. Hong, Y. Cui, Nano Lett. 10 (2010) 1486.

[82] J. Hassoun, Y. Sun, B. Scrosati, J. Power Sources 196 (2011) 343.

[83] Z. Yang, J. Guo, S.K. Das, Y. Yu, Z. Zhou, H.D. Abruña, L. a. Archer, J. Mater. Chem. A 1 (2013) 1433.

[84] S. Jeong, D. Bresser, D. Buchholz, M. Winter, S. Passerini, J. Power Sources 235 (2013) 220.

[85] F. Wu, A. Magasinski, G. Yushin, J. Mater. Chem. A 2 (2014) 6064.

[86] T. Takeuchi, H. Sakaebe, H. Kageyama, H. Senoh, T. Sakai, K. Tatsumi, J. Power Sources 195 (2010) 2928.

[87] M. Nagao, A. Hayashi, M. Tatsumisago, J. Mater. Chem. 22 (2012) 10015.

[88] Y.S. Nimon, M.-Y. Chu, S.J. Visco, Coated Lithium Electrodes, US 6,537,701, 2003.

[89] S. Liu, J. Yang, L. Yin, Z. Li, J. Wang, Y. Nuli, Electrochim. Acta 56 (2011) 8900.

[90] S.J. Visco, E. Nimon, S. Yevgeniy, B. Katz, Ionically Conductive Compossites for Protection of Active Metal Anodes, US 7,282,296 B2, 2004.

[91] A. Hayashi, R. Ohtsubo, T. Ohtomo, F. Mizuno, M. Tatsumisago, J. Power Sources 183 (2008) 422.

[92] M. Armand, J.-M. Tarascon, Nature 451 (2008) 652.

[93] L.P. Lossius, F. Emmenegger, Electrochim. Acta 41 (1996) 445.

[94] H.S. Kim, T.S. Arthur, G.D. Allred, J. Zajicek, J.G. Newman, A.E. Rodnyansky, A.G. Oliver, W.C. Boggess, J. Muldoon, Nat. Commun. 2 (2011) 427.

[95] Z. Zhao-Karger, X. Zhao, D. Wang, T. Diemant, R.J. Behm, M. Fichtner, Adv. Energy Mater. 2 (2014) 20861.

[96] Z. Zhao-Karger, J.E. Mueller, X. Zhao, O. Fuhr, T. Jacob, M. Fichtner, RSC Adv. 4 (2014) 26924.

[97] B. Duan, W. Wang, A. Wang, Z. Yu, H. Zhao, Y. Yang, J. Mater. Chem. A 2 (2014) 308.

[98] L. Spieß, R. Schwarzer, H. Behnken, G. Teichert, Moderne Röntgenbeugung Röntgendiffraktometrie Für Materialwissenchaftler, Physiker Und Chemiker, 1st ed., Teubner, Illmenau, 2005.

[99] J.-K. Park, Principles and Applications of Lithium Secondary Batteries, 1. ed., Wiley-VCH, Weinheim, 2012.

[100] H.M. Rietveld, Acta Crystallogr. 22 (1967) 151.

[101] H.M. Rietveld, J. Appl. Crystallogr. 2 (1969) 65.

[102] R. Allman, Röntgen-Pulverdiffraktometrie - Rechnergestützte Auswertung, Phasenanalyse Und Strukturbestimmung, 2nd ed., Springer, Heidelberg, 2003.

[103] J.I. Langford, J. Appl. Crystallogr. 11 (1978) 10.

[104] P. Suortti, M. Ahtee, L. Unonius, J. Appl. Crystallogr. 12 (1979) 365.

[105] B. AXS, Topas 4.2 Technical References, Bruker AXS GmbH, Karlsruhe, Germany, 2009.

[106] Z.B. Stoynov, D.E. Vladikova, in:, J. Garche (Ed.), Encycl. Electrochem. Power Sources, Elsevier, 2009, pp. 632–642.

[107] E. Barsoukov, J.R. Macdonald, Impedance Spectroscopy Theory , Experiment, and Applications, 2nd ed., John Wiley & Sons, 2005.

[108] C. Ben Faust, Modern Chemical Techniques, 3rd ed., The Royal Society of Chemistry, 1997.

[109] W.F. Hemminger, H.. Cammenga, Methoden Der Thermischen Analyse, 1st ed., Springer Berlin / Heidelberg, 1989.

[110] (2014).

[111] F. Wu, J. Chen, R. Chen, S. Wu, L. Li, S. Chen, T. Zhao, J. Phys. Chem. C 115 (2011) 6057.

[112] H.S. Ryu, H.J. Ahn, K.W. Kim, J.H. Ahn, K.K. Cho, T.H. Nam, Electrochim. Acta 52 (2006) 1563.

[113] Y. V. Mikhaylik, Electrolytes for Lithium Sulfur Cells, US7842421 B2, 2008.

[114] S. Xiong, K. Xie, Y. Diao, X. Hong, Electrochim. Acta 83 (2012) 78.

[115] X. Liang, Z. Wen, Y. Liu, M. Wu, J. Jin, H. Zhang, X. Wu, J. Power Sources 196 (2011) 9839.

[116] M. Hagen, E. Quiroga-González, S. Dörfler, G. Fahrer, J. Tübke, M.J. Hoffmann, H. Althues, R. Speck, M. Krampfert, S. Kaskel, H. Föll, J. Power Sources 248 (2014) 1058.

[117] S. Xiong, K. Xie, Y. Diao, X. Hong, J. Power Sources 246 (2014) 840.

[118] H.S. Kim, T. Jeong, N. Choi, Y. Kim, Ionics (Kiel). 19 (2013) 1795.

[119] D. Aurbach, E. Pollak, R. Elazari, G. Salitra, C.S. Kelley, J. Affinito, J. Electrochem. Soc. 156 (2009) A694.

[120] Y.-S. Su, A. Manthiram, Nat. Commun. 3 (2012) 1166.

[121] Z. Lin, Z. Liu, W. Fu, N.J. Dudney, C. Liang, Adv. Funct. Mater. 23 (2012) 1064.

[122] R. Elazari, G. Salitra, Y. Talyosef, J. Grinblat, C. Scordilis-Kelley, A. Xiao, J. Affinito, D. Aurbach, J. Electrochem. Soc. 157 (2010) A1131.

[123] J.R. Dahn, M.A. Py, R.R. Haering, Can. J. Phys. 60 (1982) 307.

[124] T. Gustafsson, J.O. Thomas, R. Koksbang, G.C. Farrington, Electrochim. Acta 37 (1992) 1639.

[125] X.Q. Yang, X. Sun, J. McBreen, Electrochem. Commun. 1 (1999) 227.

[126] G.A. Roberts, K.D. Stewart, Rev. Sci. Instrum. 75 (2004) 1251.

[127] S. Misra, N. Liu, J. Nelson, S.S. Hong, Y. Cui, M.F. Toney, ACS Nano 6 (2012) 5465.

[128] J. Nelson, S. Misra, Y. Yang, A. Jackson, Y. Liu, H. Wang, H. Dai, J.C. Andrews, Y. Cui, M.F. Toney, J. Am. Chem. Soc. 134 (2012) 6337.

[129] S.-E. Cheon, K.-S. Ko, J.-H. Cho, S.-W. Kim, E.-Y. Chin, H.-T. Kim, J. Electrochem. Soc. 150 (2003) A800.

[130] L. Yuan, H. Yuan, X. Qiu, L. Chen, W. Zhu, J. Power Sources 189 (2009) 1141.

[131] R. Steudel, B. Eckert, Top. Curr. Chem. 230 (2003) 1.

[132] R.F. Bacon, R. Fanelli, Ind. Eng. Chem. 34 (1942) 1043.

[133] Brucker AXS Topas, (n.d.) 2009.

[134] S.J. Rettig, J. Trotter, Acta Crystallogr. Sect. C 43 (1987) 2260.

[135] R.W.G. Wyckoff, in:, Anti-Fluorite Struct. Cryst. Struct. 1, Interscience Publishers, New York, 1963, pp. 239–444.

[136] B.E. Warren, in:, Proc. First Second Conf. Carbon, Buffalo, New York, 1956, pp. 49–58.

[137] International Center for Diffraction Data (ICDD), PDF-2 Release 9, 2009.

[138] B.E. Warren, J.T. Burwell, J. Chem. Phys. 3 (1935) 6.

[139] S. Sciamanna, Steven F.; Lynn, Ind. Eng. Chem. Res. 27 (1988) 485.

[140] K. Kumaresan, Y. Mikhaylik, R.E. White, J. Electrochem. Soc. 155 (2008) A576.

[141] S. Waluś, C. Barchasz, J.-F. Colin, J.-F. Martin, E. Elkaïm, J.-C. Leprêtre, F. Alloin, Chem. Commun. 49 (2013) 7899.

[142] Y.M. Lee, N.-S. Choi, J.-K.H. Park, J. Power Sources 119-121 (2003) 964.

[143] J. Hassoun, M. Agostini, A. Latini, S. Panero, Y.-K. Sun, B. Scrosati, J. Electrochem. Soc. 159 (2012) A390.

[144] Y. Fu, A. Manthiram, J. Phys. Chem. C 116 (2012) 8910−8915.

[145] J. Wang, J. Chen, K. Konstantinov, L. Zhao, S.H. Ng, G.X. Wang, Z.P. Guo, H.K. Liu, Electrochim. Acta 51 (2006) 4634.

[146] F. Zhang, Y. Dong, Y. Huang, G. Huang, X. Zhang, L. Wang, J. Phys. Conf. Ser. 339 (2012) 012003.

[147] Y.-S. Su, A. Manthiram, Electrochim. Acta 77 (2012) 272.

[148] D. Aurbach, K. Gamolsky, B. Markovsky, Y. Gofer, M. Schmidt, U. Heider, Electrochim. Acta 47 (2002) 1423.

[149] B. Jin, J.-U. Kim, H.-B. Gu, J. Power Sources 117 (2003) 148.

[150] L. Yuan, X. Qiu, L. Chen, W. Zhu, J. Power Sources 189 (2009) 127.

[151] Y. Li, H. Zhan, S. Liu, K. Huang, Y. Zhou, J. Power Sources 195 (2010) 2945.

[152] V.S. Kolosnitsyn, E. V. Kuz'mina, E. V. Karaseva, S.E. Mochalov, Russ. J. Electrochem. 47 (2011) 793.

[153] R.P. Martin, W.H. Doub, J.L. Roberts, D.T. Sawyer, Inorg. Chem. 12 (1973) 1921.

[154] R. Bonnaterre, G. Cauquis, J. Chem. Soc. Chem. Commun. (1972) 293.

[155] T. Chivers, I. Drummond, Inorg. Chem. 141 (1972) 18.

[156] W.F. Giggenbach, Inorg. Chem. 13 (1974) 1724.

[157] F. Seel, H.-J. Güttler, Angew. Chemie Int. Ed. 12 (1973) 420.

[158] R.D. Rauh, F.S. Shuker, J.M. Marston, S.B. Brummer, J. Inorg. Nucl. Chem. 39 (1977) 1761.

[159] D.-H. Han, B.-S. Kim, S.-J. Choi, Y. Jung, J. Kwak, S.-M. Park, J. Electrochem. Soc. 151 (2004) E283.

[160] N.S.A. Manan, L. Aldous, Y. Alias, P. Murray, L.J. Yellowlees, M.C. Lagunas, C. Hardacre, J. Phys. Chem. B 115 (2011) 13873.

[161] E. Levillain, F. Gaillard, P. Leghie, a. Demortier, J.P. Lelieur, J. Electroanal. Chem. 420 (1997) 167.

[162] C. Barchasz, F. Molton, C. Duboc, J.-C. Leprêtre, S. Patou, F. Alloin, Anal. Chem. 84 (2012) 3973.

[163] M.U.M. Patel, R. Demir-Cakan, M. Morcrette, J.-M. Tarascon, M. Gaberscek, R. Dominko, ChemSusChem 6 (2013) 1177.

[164] D. Marmorstein, Solid State Lithium/sulfur Batteries for Electric Vehicles: Electrochemical and Spectroelectrochemical Investigations, University of California, Berkeley, 2002.

[165] B. Meyer, Chem. Rev. 76 (1976) 367.

[166] A.M. Bass, J. Chem. Phys. 21 (1953) 80.

[167] M. V. Merritt, D.T. Sawyer, Inorg. Chem. 9 (1970) 211.

[168] F. Seel, H.-J. Güttler, Angew. Chem. Internat. 12 (1973) 420.

[169] D.R. Salahub, A.E. Foti, V.H. Smith, J. Am. Chem. Soc. 100 (1978) 7847.

[170] W. Giggenbach, J. Inorg. Nucl. Chem 55 (1968) 3189.

[171] R. Hiesgen, S. Helmly, I. Galm, T. Morawietz, M. Handl, K. Friedrich, Membranes (Basel). 2 (2012) 783.

[172] R. Hiesgen, S. Sörgel, R. Costa, L. Carlé, I. Galm, N. Cañas, B. Pascucci, K.A. Friedrich, Beilstein J. Nanotechnol. 4 (2013) 611.

[173] R. Steudel, Y. Steudel, M.W. Wong, Top. Curr. Chem. 230 (2003) 117.

[174] D.N. Fronczek, W.G. Bessler, J. Power Sources 244 (2013) 183.

[175] J.P. Neidhardt, D.N. Fronczek, T. Jahnke, T. Danner, B. Horstmann, W.G. Bessler, J. Electrochem. Soc. 159 (2012) A1528.

[176] W.G. Bessler, S. Gewies, M. Vogler, Electrochim. Acta 53 (2007) 1782.

[177] P.W. Atkins, J. De Paula, Physical Chemistry, 8th ed., University Press, New York, 2006.

[178] A.F. Hofmann, D.N. Fronczek, W.G. Bessler, J. Power Sources 259 (2014) 300.

[179] M.B. Pinson, M.Z. Bazant, J. Electrochem. Soc. 160 (2012) A243.

[180] S. Xiong, K. Xie, Y. Diao, X. Hong, J. Power Sources 236 (2013) 181.

[181] P. Albertus, G. Girishkumar, B. McCloskey, R.S. Sánchez-Carrera, B. Kozinsky, J. Christensen, A.C. Luntz, J. Electrochem. Soc. 158 (2011) A343.

[182] Michigan State University, Principle of Chemistry II (2014). http://www.cem.msu.edu/~mantica/cem152/prep1/sulfurphasediagram.html.

[183] N. Wagner, Bulg. Chem. Commun. 44 (2012) 371.

List of figures

Figure 1.1: Battery systems: comparison of practical specific energy, mileage and cost [3]. The mileage are based on the minimum specific energy for each system and scaled to the specific energy of Li–ion cells (140 Wh kg^{-1}) and driving range of the Nissan Leaf (160 km) [4]. The cost for technologies under development are targets of the US Advanced Battery Consortium [5]. 2

Figure 1.2: Organization of the thesis, main focus and interconnection of the chapters…..... 3

Figure 2.1: Illustration of the Li–S battery components. 5

Figure 2.2: Schematic discharge (a) and charge (b) profile expected for a fully cycled Li–S battery. 6

Figure 2.3: (a) Schematic representation of the spectrum emitted by an X–ray tube: the smooth continuous curve is due to bremsstrahlung and the spikes are characteristic k lines. (b) Elastic scattering of X–ray in the lattice of a crystalline solid. 14

Figure 2.4: Energy levels of bonding orbitals and electron transitions in UV–vis spectroscopy [108]. 21

Figure 2.5: Schematic of AFM instrument. PZT: piezoelectric tube. 22

Figure 2.6: Schematic of SEM instrument and signals generated by the interaction of electron beam and sample [99] 23

Figure 2.7: (a) TG and DSC configurations. (b) Schematic determination of the enthalpy by measuring the temperature of the sample (T_s) and the reference (T_r). 24

Figure 3.1: Raw materials (a) sulfur, (b) PVDF and (c) CB. SEM pictures, SE detector, EHT: 1 kV, 0.5 kV (PVDF). 27

Figure 3.2: Wet–powder spraying system for cathode fabrication. 30

Figure 3.3: Cathode after spraying and drying (a) and after individual cathodes were punched out for cell preparation (b). Microscopic picture of the cathode surface (c), where the white spots are the non–totally covered sulfur particles. 31

Figure 3.4: (a) Scheme of Swagelok®–cell with inside view of the battery components. (b) Components of the battery and dimensions......................................32

Figure 3.5: Surface of cathodes fabricated using different fabrication procedure. (a, c, e) Cathode I (initial procedure) and (b, d, f) Cathode II (new procedure). 33

Figure 3.6: Cyclability of batteries using Cathode I and Cathode II. (a) Discharge capacity vs cycle. (b) Coulombic efficiency. The average and error bars are calculated based on the results of 3 tested batteries..34

Figure 3.7: Discharge and charge profiles for cathode I (a,b) and cathode II (b,c). Cycling was performed between 1.5 and 2.8 V and current density of 300 A kg_S^{-1} (0.18 C). 36

Figure 3.8: Self discharge of Li–S batteries. 36

Figure 3.9: Influence of concentration of $LiNO_3$ in the capacity fading of batteries after 50 cycles (a) and the Coulombic efficiency (b). *Calculated between cycle 1 and 50. The average and error bars are calculated based on the results of 3 tested batteries……..38

Figure 3.10: Improvements on the cyclability of the cell by modification of cathode and electrolyte. The average and error bars are calculated based on the results of 3 tested batteries. 38

Figure 3.11: (a) Discharge capacity and Coulombic efficiency of Li–S batteries at 0.18 C and 2 C. (b) Comparison of discharge profile between batteries tested at 0.18 C and 2 C. (c) Specific energy density based on the cathode mass for cycle 1, 50, and 1000. 40

Figure 4.1: Exploded illustration of the *in situ* XRD cell. Components: 1) Anode plate, 2) polymer gasket, 3) insulator plastic tube, 4) spring, 5) stainless steel anode collector, 6) anode, 7) separator, 8) cathode, 9) cathode plate, 10) Al–window, and 11–12) holes for connecting the banana jacks...46

Figure 4.2: Configuration of the *in situ* XRD experimental set–up. The radiant tube and the VÅNTEC detector are shown. The *in situ* cell is mounted on a motorized goniometric head and connected to the potentiostat, in which the electrochemical experiment is controlled by the cycling program (Thales)...47

Figure 4.3: Diffractograms of the raw materials as powder: carbon black (a), PVDF (b) and sulfur (c). 49

Figure 4.4: Diffractogram of the cathode before cycling. The aluminum reflexes correspond to the aluminum collector. 50

Figure 4.5: *In situ* XRD data collected during discharge of Li–S battery at a rate of 300 A kg_s^{-1} (0.18 C). Background was subtracted for clarity, original XRD diffractograms can be seen in Figure 4.8. Three different regions are shown: (a) reaction of sulfur to high order polysulfides (blue), (b) reactions of high order polysulfides (gray), and (c) formation of Li_2S (red). The discharge curve is shown on the top. The average discharge capacity is 1276 Ah kg_S^{-1}. 51

Figure 4.6: *In situ* XRD data collected during charge of Li–S battery at a current density of 300 A kg_S^{-1} (0.18 C). Three different regions are shown: (d) reaction of Li_2S (blue), (e) reactions of high order polysulfides (gray), and (f) formation of sulfur (red). The charge curve is shown on the top. Charge capacity: 1283 Ah kg^{-1}. 52

Figure 4.7: *In situ* XRD data collected during the second cycle. (a) 2nd discharge and (b) 2nd charge of Li–S battery at a current density of 300 A kg_S^{-1} (0.18 C). 53

Figure 4.8: *In situ* XRD data collected before cycling, after the 1st discharge, after the 1st charge, after the 2nd discharge, and after the 2nd charge. 54

Figure 4.9: Schematic raster grid for analyzing 10 mm diameter cathodes. 13 target positions were selected. 55

Figure 4.10: Spatial distribution of the sulfur crystalline phase after charge (1st cycle)…... 56

Figure 4.11: Diffraction data of the cathode before cycling, after the 1st, 25th, and 100th cycle for the positions 1, 3, 7, 11 and 13 56

Figure 4.12: Measured and refined diffractogram for cathode before cycling (a), after 1st charge (b), and after 1st discharge. The subtracted curve between measured and calculated diffractogram is the grey curve in the bottom). 57

Figure 4.13: SEM micrographs of a separator section viewed from the cathode side (a–d) and of cathode after charge (e). 58

Figure 4.14: Semi–quantitative X–ray analysis for the first two discharges (a) and charge cycles (b) of a Li–S battery 60

Figure 5.1: Discharge curve of a Li–S battery; each point represents an EIS measurement (a). Selected Nyquist plots in the frequency range of 60 mHz–1 MHz at different depths of discharge, DOD (b). Experimental and fitting results at 27% (c), 52% (d), and 90% DOD (e). The high frequency regions of the spectra are amplified on the right. 65

Figure 5.2: Charge curve of a Li–S battery; each point represents an EIS measurement (a). Selected Nyquist plots in the frequency range of 60 mHz–1 MHz at different depths of charge, DOC (b). Experimental and fitting results at 100% DOD (c), 22% DOC (d), and 65% DOC (e). The high frequency regions of the spectra are amplified on the right. 66

Figure 5.3: Nyquist plot of a Li–S Battery, frequency range: 1 mHz–1 MHz (a) with magnification in the frequency range: 72 mHz–1 MHz (b). 68

Figure 5.4: Equivalent electrical circuit of a Li–S battery used to fit the experimental data. 68

Figure 5.5: Nyquist plot of the impedance response of the battery at 81% DOD. The blue semicircles are schematics to clarify the domain of each EC element. The high frequency region of the spectrum is magnified at the top. 69

Figure 5.6: Changes of charge transfer resistances during first discharge (a–c) and first charge (d–f) of the Li–S battery. 71

Figure 5.7: Cycle performance of a Li–S battery at room temperature for up to 50 cycles. 74

Figure 5.8: Charge transfer resistances calculated by modeling of the impedance spectra up to 50 cycles (a–c) and Nyquist plots of the corresponding frequency regions (d–f). 75

Figure 5.9: Relative values of the charge transfer resistance related to the electrolyte (R_0), anode charge transfer resistance (R_1), and cathode charge transfer resistance (R_2). 76

Figure 6.1: Set–up for UV–vis spectroscopic measurements......................................80

Figure 6.2: (a) Absorption spectra of S_8 dissolved in TEGDME, (b) the 2nd derivative spectra, and (c) changes in absorbance at λ_{max} with concentration 82

Figure 6.3: (a) Absorption spectra of Li_2S dissolved in TEGDME, (b) the 2nd derivative of the absorbance, and (c) changes in absorbance at λ_{max} with concentration..82

Figure 6.4: Absorption spectra of polysulfide solutions at different concentration Small insets show the visible color of the concentrated polysulfide solutions. 84

Figure 6.5: Example of fitted spectra at different wavelength regions with Gaussian functions to estimate the absorption maxima. 86

Figure 6.6: (a) Spectra of polysulfide solutions at the lowest concentration. The grey arrow indicates the changes in $\lambda_{max.}$ (b) Changes in absorbance of polysulfide solutions at 425 nm and 615 nm for the different polysulfide solutions relative to maximum absorbance at 265 nm; and (c) changes in the absorbance ratio between the bands at 615 nm and 425 nm in the concentration range of 0.45 – 1.47 mM. 86

Figure 6.7: UV–vis spectra of cathode samples at different depths of discharge. 88

Figure 6.8: Discharge profiles of batteries used for the *ex situ* measurements. 89

Figure 6.9: Changes of absorbance area (left axis) and maximal wavelength λ_{max} (right axis) during discharge at lowest concentration (0.67 $mmol_{initialS}L^{-1}$). 90

Figure 6.10: Absorbance changes in the bands at 425 and 615 nm at the highest concentration (9.12 $mmol_{initialS8}L^{-1}$). 91

Figure 7.1: Ex–situ SEM micrographs of the cathode surface at different stages of discharge and charge (first cycle). Picture magnifications: 300x (top) and 3000x (bottom).The average discharge and charge capacity is 1276 and 1283 mAh g_{sulfur}^{-1} respectively [6]. 95

Figure 7.2: AFM topography images (b–d) and AFM current images (e–g) of the cathode surface before cycling (I), after first discharge (II) and after first charge (III) [7]. 97

Figure 7.3: Non–conductive surface area (%) at different position of the sample before cycling (I), after first discharge (II) and after first charge (III). 98

Figure 7.4: TG and DSC curves for sulfur under air (a) and under argon (b) atmosphere. 99

Figure 7.5: TG and DSC curves for PVDF (a) and CB (b) under air atmosphere. 99

Figure 7.6: Typical TG curve of a cathode before cycling. 101

Figure 7.7: TG before cycling and after 1, 10, 50 and 100 cycles with the evolved gas analysis of SO_2, fluorine, and CO_2. 102

Figure 8.1: Geometry, reaction mechanism and initial cathode composition of the simulated cell. 106

Figure 8.2: Experimental and simulated discharge profile at the first discharge. 112

Figure 8.3: Relative volume of S_8 and Li_2S (simulated) compared with relative integrated intensity of the Bragg peaks S_8 (222) and Li_2S (111) obtained by *in situ* XRD [6] during the first discharge. 113

Figure 8.4: Simulated discharge of the cell at 2C and ⅓C rate. 100% (DOD) is defined as the maximal specific capacity reached in the simulation (not the theoretical specific capacity). In this case 100% DOD is 1130 $Ah{\cdot}kg_S^{-1}$ for 2C and 1175 $Ah{\cdot}kg_S^{-1}$ for 1/3C. 114

Figure 8.5: Concentration of polysulfides during discharge. 115

Figure 8.6: Concentration profile across the cell of volume fraction of S_8 and Li_2S (simulated). 115

Figure 8.7: Total concentration of S_x^{2-} species (simulated) compared with the absorbance at 425 nm (UV–vis spectroscopy), and the anode charge transfer resistance (EIS) (d). Selected spectra to show the behavior of the absorbance bands (a–c). 116

Figure 8.8: Concentration of polysulfides during discharge. 117

Figure 8.9: Concentration profile across the cell of Li^+, S_8^{2-}, S_6^{2-} and S_4^{2-} during discharge (simulated). 118

Figure 11.1: Swagelok type cell and fittings for cell construction. 127

Figure 11.2: Showa Denko® substrate. (a) Microscopic picture. (b–d) SEM pictures........ 128

Figure 11.3: Non–dissolved PVDF particles on the surface of Cathode I. 128

Figure 11.4: Microscopic pictures of cross section of the cathode layer over the aluminum collector. 129

Figure 11.5: Cracks over the cathode surface cause by fast drying (Cathode I). 129

Figure 11.6: Microscopic pictures of cathode (a, b) and separator of a battery after its 1st charge (Cathode II, Electrolyte 1 M $LiPF_6$, 0.75 M $LiNO_3$ in TEGDME, Separator: Celgard 2500, anode: Lithium). End charge capacity ~1287 Ah kg_S^{-1}. 129

Figure 11.7: Microscopic pictures of cathode (a, b) and separator of a battery after its 5th charge (Cathode II, Electrolyte 1 M $LiPF_6$, 0.75 M $LiNO_3$ in TEGDME, Separator: Celgard 2500, anode: Lithium). End charge capacity ~1114 Ah kg_S^{-1}..................... 130

Figure 11.8: Microscopic pictures of cathode (a, b) and separator of a battery after its 11th charge (Cathode II, Electrolyte 1 M $LiPF_6$ in TEGDME, Separator: Celgard 2500, anode: Lithium). End charge capacity ~1211 Ah kg_S^{-1}. 130

Figure 11.9: Microscopic pictures of cathode (a, b) and separator of a battery after its 64th charge (Cathode II, Electrolyte 1 M $LiPF_6$ in TEGDME, Separator: Celgard 2500, anode: Lithium). End discharge capacity ~500 Ah kg_S^{-1}. End charge capacity approx. 1155 Ah kg_S^{-1}. 131

Figure 11.10: Krypton Adsorption analysis of Carbon black. (a) Adsorption/desorption (Ads/Des) isotherms and (b) BET plots. 132

Figure 11.11: Krypton Adsorption analysis of cathode before cycling. (a) Adsorption/desorption (Ads/Des) isotherms and (b) BET plots. 132

Figure 11.12: Influence of temperature on the capacity. 133

Figure 11.13: Phase diagram of sulfur [182]. 133

Figure 11.14: X–ray pattern of the Li_2S sample before (t = t1) and after approximately 25 min in contact with air (t = t1 + 25 min). 134

Figure 11.15: Absorption spectrum of TEGDME (UV–vis spectroscopy). 137

Figure 11.16: TG measurements of cathode, after drying the electrode immersed in electrolyte. 138

List of tables

Table 1: Unit area peak types for the Gaussian, Lorentzian and Pseudo Voigt symmetric functions [105]. fwhm is the full width at half maximum, $x = 2\theta - \theta_k$, and η: mixing parameter. 17

Table 2: Circuit components, their respective symbols and impedance equations. On the right a schematic explanation of the behavior of the impedance for each element. (W: Warburg parameter). 19

Table 3: Comparison of mixing, coating and drying procedures. 29

Table 4: Structure parameters refined with Rietveld–method for diffractograms before and after cycling: crystallite size, cell volume, and lattice parameter a, b, c, for the orthorhombic structure of sulfur (phase group: Fddd) and Li_2S (phase group: Fm-3m) . 58

Table 5: Assignment of processes to the elements of the EC. 69

Table 6: Summary of absorption maxima estimated in the literature for polysulfides and radicals. 83

Table 7: Absorbance bands assigned to S_8, Li_2S and various polysulfides in TEGDME. 87

Table 8: Characteristic temperatures and enthalpies of S, PVDF, and CB. Exothermic process (positive sign) and endothermic process (negative sign). The values between parenthesis are from literature [165]. 100

Table 9: Composition of cathode estimated using TGA. The average and standard deviation were calculated for three samples. 101

Table 10: Changes in oxidation temperature of cathode components. 103

Table 11: Further parameters used for the model. Values are given for $T = 298$ K and $p = 101325$ Pa. Parameters are either known from experiments (†), known from literature (*) or assumed (°). 110

Table 12: Structure parameters of α–S_8 at about 300 K (standard deviation in parenthesis). There are 16(4) molecules per unit primitive cell [134]. 133

Table 13: Simulation results of the impedance spectra measured at different DOD for Li–S battery during the first cycle. 135

Table 14: Simulation results of the impedance spectra measured at different depth of charge for Li–S battery during the first charge...136

Table 15: Simulation results of the impedance spectra measured during cycling. The EIS were measured in discharge state until the 50th cycle. 136

Table 16: Description of symbols and their units (chapter 8). 140

Table 17: List of parameters used in the simulation. Values are known from calculation (†), literature (*), and assumed (°)...142

Publications

Part of the work presented in this thesis was already published in peer review journals and presented at conferences as oral presentation or poster.

Papers

- N. A. Cañas, S. Wolf, N. Wagner, K. A. Friedrich. “In–situ X–ray diffraction studies of lithium–sulfur batteries”. J. of Power Sources, 226 (2013) 313–319.
- N. A. Cañas, K. Hirose, N. Wagner, B. Pascucci, N. Wagner, K.A Friedrich, R. Hiesgen, “Investigations of lithium–sulfur batteries using electrochemical impedance spectroscopy”. Electrochim. Acta, 97 (2013) 42–51.
- N. A. Cañas, D. N. Fronczek, N. Wagner, A. Latz, K. A. Friedrich “Experimental and Theoretical Analysis of Products and Reaction Intermediates of Lithium–Sulfur Batteries”. J. Phys. Chem. C, 118 (2014) 12106–12114.
- N.A. Cañas, A. L. P. Baltazar, M. A. P. Morais, T. Oliver Freitag, N. Wagner, K. A. Friedrich. "Fabrication of sulfur cathodes by wet–powder spraying and the understanding of degradation". Electrochim. Acta, 157 (2015) 351-358.
- R. Hiesgen, S. Sörgel, R.Costa, L.Carlé, I. Galm, N. Cañas, B. Pascucci and K. A. Friedrich. “AFM as an analysis tool for high-capacity sulfur cathodes for Li–S batteries”. Beilstein J. of Nanotechnology, 4 (2013) 611–624.

Oral presentations

- N. Wagner, R. Hiesgen, N. A. Cañas. Zyklenstabilität von Lithium–Schwefel–Hochenergie–Batterien für die Elektromobilität. Presentation of Aversumsprojekt 2010/2011 February 19th 2013, Stuttgart, Germany.
- N. Wagner, N. A. Cañas, K. Hirose, K. A. Friedrich. “In–situ XRD and electrochemical characterization of cathodes for Li–sulfur batteries”, International Workshop on Impedance Spectroscopy. September 26–28 2012, Chemnitz, Germany.
- N. A. Cañas, K.A. Friedrich, N. Wagner, B. Pascucci, R. Hiesgen. Investigation of rechargeable lithium–sulfur batteries by in situ techniques.

224th ECS Meeting, 27 October –1. November 2013, San Francisco, United States of America.

- N. A. Cañas, N. Wagner, K.A. Friedrich. Importance of in situ techniques in the investigation of rechargeable lithium–sulfur batteries 2nd workshop on Lithium sulfur batteries, 6–7 November 2013, Dresden, Germany.
- N. A. Cañas, N. Wagner, K.A. Friedrich. Important Aspects on the Fabrication and Characterization of Lithium–Sulfur. 65th Annual Meeting of the International Society of Electrochemistry, 3rd September 2014, Lausanne, Switzerland.
- K. A. Friedrich, N. A. Cañas, N. Wagner, B. Pascucci. "Lithium-Sulfur Batteries: New insights and developments". World of Energy Solutions/battery storage, 06.-08. Okt. 2014, Stuttgart.
- K. Andreas Friedrich, N. A Cañas, T. O. Freitag, N. Wagner. "On the Improvement of High Capacity Lithium-Sulfur Batteries and the Understanding of Degradation". MRS Spring Meeting & Exhibit. 6. April 2015, San Francisco, United States of America.
- Norbert Wagner, N. A. Cañas, D. Wittmaier, K. A. Friedrich. "Post Li-ion batteries". 5th Regional Symposium on Electrochemistry South-East Europe, 7.-11. Juni 2015, Pravets, Bulgaria.

Posters

- N. A. Cañas, S. Wolf, N. Wagner, K. A. Friedrich. "In–situ XRD and electrochemical characterization of cathodes for Li–sulfur batteries", 16th International Meeting on Lithium Batteries, 17–22 June 2012, Jeju, Südkorea.
- N. A. Cañas, K. Hirose, N. Wagner, S. Sörgel, K. A. Friedrich. "In–situ XRD and electrochemical characterization of cathodes for Li–sulfur batteries", 2nd Ertl Symposium on Surface and Interface Chemistry, 24–27 June 2012 in Stuttgart. *"Best Poster Award".*
- N. A. Cañas, K. Hirose, N. Wagner, S. Sörgel, K. A. Friedrich. "In–situ XRD and electrochemical characterization of cathodes for Li–sulfur batteries". Electrochemistry 2012, 17–19 September 2012 in München.

- N. A. Cañas, N. Wagner, K. A. Friedrich. “Investigations of lithium–sulfur batteries using electrochemical impedance spectroscopy”. 6th International Conference on Polymer Batteries and Fuel Cells, 3–7 June 2013 in Ulm, Deutschland.
- N. A. Cañas, N. Wagner, K. A. Friedrich, “Investigations of lithium–sulfur batteries using electrochemical impedance spectroscopy”. 9th International Symposium on Electrochemical Impedance Spectroscopy, Okinawa, 16–21 June 2013 in Okinawa, Japan.
- N. A. Cañas, K. Hirose, B. Pascucci, N. Wagner, K. A. Friedrich, R. Hiesgen. Investigation of rechargeable lithium–sulfur batteries by *in situ* techniques. 13th International Conference on Electrified Surfaces, 30 June –5 July, 2013.
- N. Wagner, N. A. Cañas, R. Hiesgen, B. Pascucci, K. A. Friedrich. Herstellung und Charakterisierung von Li–Schwefel–Kathoden durch *in situ* XRD, Impedanzspektroskopie und AFM–Messungen. Wissenschaftsforum Chemie 2013, 1–4 September, Darmstadt.
- N. A. Cañas, K. A. Friedrich, K. Hirose, N. Wagner, B. Pascucci, R. Hiesgen. Investigation of rechargeable lithium–sulfur batteries by *in situ* techniques: Insight into interfacial processes. 64th Annual Meeting ISE, Santiago de Querétaro, Santiago de Querétano, Mexico, 8-13 September 2013.
- N. A. Cañas, D. N. Fronczek, N. Wagner, A. Latz, K. A. Friedrich. “Experimental and Theoretical Analysis of discharge process in Lithium–Sulfur Batteries”. 65th Annual Meeting of the International Society of Electrochemistry, 2nd September 2014, Lausanne, Switzerland.

Acknowledgements

This PhD thesis was carried at the department of Electrochemical Energy Technology at the Institute of Engineering Thermodynamics, German Aerospace Center (DLR) between December 2010 and Januar 2014.

Foremost, I would like to express my sincerely gratitude to my *Doktorvater* Prof. Dr. K. Andreas Friedrich for giving me the opportunity to carry out my PhD thesis in the Battery Technology Group at DLR. I am very grateful for the interesting and fruitful scientific discussions, for his continuous support and thoughtful guidance during this time.

I owe particular thanks to Prof. Dr. Maximilian Fichtner for being the second advisor of my thesis.

I would like to thank Norbert Wagner for supporting my ideas and giving me freedom to find my own path during this work.

Special thanks are dedicated to David Fronczek for providing the model, for supporting me with the simulations and the interpretation of results. For the interesting discussions on Li-S batteries and the excellent working atmosphere, my best thanks!

I want to thank Werner Seybold for supporting me with the fabrication of *in situ* cells and for being always willing to help me with technical issues. I enjoyed immensely working with you Werner!

I thank Steffen Wolf for introducing me to the world of X-ray diffraction and assisting me with the interpretation of results. To Ina Plock, thanks for the very nice and numerous SEM pictures of the challenging sulfur-composite cathode.

I want to thank my students for their great support with the experimental work: Kei Hirose, Ana Baltazar and Micael Morais. It was a pleasure working with you!

I am grateful to the members of the Battery Group, who were always willing to help me, hear me and advise me, especially when things were not going very well. For the very nice time with you, I thank you a lot! I also want to thank the colleagues at DLR, the ones who support my work and with whom I shared very nice moments.

Quisiera agradecer a toda mi familia, especiamente a mis padres, quienes me han apoyado en todas las decisiones que he tomado y que me han lllevado a lograr este doctorado. Por darme la educación que me dieron en Argentina y por su apoyo incondicional, no tengo palabras para agradecerles! A Fede, Flor, Fer, Fabi y Sole, que cerca o a la distancia siempre me apoyan y están presentes, muchas gracias!

A Fer, Aitor y Fede por leer capítulos de mi tesis y ayudarme con su correción.

Finally, I would like to express my deepest gratitude to Ingo Gräf, he has been a constant source of strength and inspiration. He stood by me and shared with me the good and difficult moments of the last years.

Curriculum vitae

Natalia Andrea Cañas

Born 3rd February 1983 in Córdoba, Argentina

Education

03/1996–12/2000	High school at the Instituto La Inmaculada, Córdoba, Argentina. (Equivalent certificate to enroll the university)
03/2001–06/2007	Diploma in chemical engineering at the National Technological University (Universidad Tecnológica Nacional, UTN), Córdoba, Argentina. Title: Ingeniera química (equivalent to Dipl.-Ing.).
09/2008–08/2010	Double–Master in Advanced Materials Science and Engineering (AMASE) at the Universiy of Saarland, Saarbrücken and the Technical University in Luleå, Sweden. Title: Master of Science (M. Sc.).

Work Experience

12/2007–07/2008	Internship at the Institute for Thermal Process Engineering, University of Karlsruhe (TH).
12/2007–07/2008	Trainee–Program at Kraft Foods, Buenos Aires, Argentina.
11/2010–12/2013	Researcher at the University of Stuttgart, Institute for Thermodynamic and Thermal Engineering with activities at the German Aerospace Center (DLR), Institute for Technical Thermodynamics, electrochemical energy technology, Battery technology.
01/2014–now	Researcher at the German Aerospace Center (DLR), Institute of Engineering Thermodynamics, Electrochemical Energy Technology, Battery Technology.